Multi-wavelength Observations of High-Accretion Rate Type 1 Active Galactic Nuclei and Other Super Soft X-ray Sources

A thesis submitted for the degree of
Doctor of Philosophy
at the University of Leicester.

by

Mark Simpson

X-ray & Observational Astronomy Group
Department of Physics & Astronomy
University of Leicester

December 2009

Declaration

I hereby declare that no part of this thesis has been previously submitted to this or any other University as part of the requirement for a higher degree. The work described herein was conducted by the undersigned, except for contributions from colleagues as acknowledged in the text.

Mark Simpson

December 2009

Multi-wavelength Observations of High-Accretion Rate Type 1 Active Galactic Nuclei and Other Super Soft X-ray Sources

Mark Simpson

ABSTRACT

The study of X-ray emission from AGN allows the investigation of the inner regions of their central engine. By understanding the processes taking place within AGN, many other areas of research will benefit, such as accretion and the formation and evolution of galaxies.

This thesis begins by investigating the background AGN population of the serendipitous sources detected in a deep-look (~ 500 ks) of the *XMM-Newton* field of view surrounding 3C 273. The deep-look is created by mosaicing *XMM-Newton* EPIC calibration observations of 3C 273. Time averaged spectra of the 17 brightest X-ray sources are analysed. Cross-correlation of the X-ray sources with catalogues at other wavelengths is performed and unique candidate counterparts proposed. Classification of the X-ray sources is attempted and the background AGN population is discussed.

A number of AGN have shown evidence of high-ionisation, high-velocity outflows in their X-ray spectra. These sources are believed to have a high-accretion rate at or near the Eddington limit. Six suspected high-accretion rate narrow line AGN observed with *XMM-Newton* are analysed and inspected for the presence of these outflows. No such outflows are detected. However, three of the targets did show evidence of mass loss in the form of a warm absorber. In addition, all of the sources appear to have a soft excess below ~ 2 keV.

Finally, a search for the AGN population of super soft X-ray sources (SSXs) in the first and second *XMM-Newton* catalogues is performed. Hardness ratios are used to search for SSXs, which are defined as having a characteristic temperature, kT$\lesssim 100$ eV. Cross-correlation of the selected SSXs with catalogues at other wavelengths is performed, returning both Galactic and extragalactic candidate counterparts. For a small number of SSXs with previously unclassified optical candidate counterparts, optical spectroscopic observations were acquired. The analysis of these observations identified 5 previously unclassified AGN.

Other Publications

Watson, M.G., Schröder, A.C., Fyfe, D., Page, C.G., Lamer, G., Mateos, S., Pye, J., Sakano, M., Rosen, S., Ballet, J., Barcons, X., Barret, D., Boller, T., Brunner, H., Brusa, M., Caccianiga, A., Carrera, F.J., Ceballos, M., Della Ceca, R., Denby, M., Denkinson, G., Dupuy, S., Farrell, S., Fraschetti, F., Freyberg, M.J., Guillout, P., Hambaryan, V., Maccacaro, T., Mathiesen, B., McMahon, R., Michel, L., Motch, C., Osborne, J.P., Page, M., Pakull, M.W., Pietsch, W., Saxton, R., Schwope, A., Severgnini, P., Simpson, M., Sironi, G., Stewart, G., Stewart, I.M., Stobbart, A.-M., Tedds, J., Warwick, R., Webb, N., West, R., Worrall, D., Yuan, W., 2009 **"The XMM-Newton serendipitous survey. V. The Second XMM-Newton serendipitous source catalogue"**, A&A, 493, 339

Simpson, M., & O'Brien, P.T., 2006, **"Outflows from High-Accretion Rate AGN"**, in 'The X-ray Universe 2005', ed. A. Wilson, ESA Special Publication, 604, 667

Bode, M.F., O'Brien, T.J., & Simpson, M., 2004, **"Echoes of an Explosive Past: Solving the Mystery of the First Superluminal Source"**, ApJ, 600, L63

Contents

List of Figures

List of Tables

Chapter 1

Introduction

1.1 Active Galactic Nuclei

Active Galactic Nuclei (AGN) are sources of extreme energetic radiation in the nuclei or central regions of galaxies, which cannot be solely attributed to stellar emission. Galaxies that harbour AGN are known as active galaxies. AGN are the most luminous continuously emitting objects in the Universe. Their luminosities cover a large range, between $10^{40} - 10^{48}$ erg s^{-1}, which are sustained throughout their lifetimes ($\sim 10^7$ years). Phenomena such as supernova and γ-ray bursts may briefly outshine them immediately after the initial explosion, but fall to sub-AGN luminosities within days. AGN often appear as point-like sources, out-shining their host galaxies by up to a factor of ~ 100. AGN also emit radiation across all wavelengths.

The commonly accepted process used to explain the observed abundant electromagnetic (EM) radiation from AGN is matter accreting onto a super-massive black hole (SMBH). As the matter is accreted by the SMBH, the gravitational potential energy of the matter is converted into the observed radiation. This is a result of the frictional processes taking place within the in-falling matter and also within the disc surrounding the SMBH from where the matter is accreting (Rees, 1984).

Even though the study of AGN is diverse, many questions remain unanswered, leaving an incomplete picture. However, just as diverse are the applications of AGN studies. Knowledge of the morphology and processes within AGN can contribute towards the further understanding of accretion processes, black holes (BH), general relativity, formation and characteristics of galaxies, evolution of the early Universe and the intergalactic medium, to name a few. Thus, a complete picture of AGN would be extremely informative. This will only occur with further observations and continuing theoretical work. Observatories such as *XMM-Newton* and *Chandra* have contributed considerably to the current understanding of AGN. Future missions, such as the *International X-ray Observatory* (IXO[1]) that will carry instruments with improved spatial and spectral resolution compared to *XMM-Newton* and *Chandra*, will begin to probe the inner regions of AGN.

This chapter begins by discussing the inner regions of AGN. A description of their continuum emission follows, with a brief summary of the observational properties of the various classes of AGN. A detailed discussion of the X-ray emission from the AGN environment is then given along with an introduction to X-ray emitting processes. The instrumentation used to obtain the data reported within this thesis is then described and finally, the aims of this thesis are given. It should be noted that the study of AGN is vast and out of necessity the following introductions to certain aspects of AGN are by no means comprehensive.

1.1.1 Central Engine

The commonly accepted morphology of the central engine of an AGN is an accreting SMBH that resides at or close to the centre of the host galaxy's potential well. The source of the accreted matter is the accretion disc, which surrounds the SMBH. The gravitational

[1] http://ixo.gsfc.nasa.gov/index.html

potential energy of the in-falling matter is converted into the observed EM radiation via frictional processes that take place both within the accretion disc and during the accretion process. Orbiting the SMBH, outside the plane of the accretion disc, are dense clouds (or clumps) of matter that are virialised in the potential well of the SMBH. The region in which these dense clouds reside is known as the broad line region (BLR). The BLR is highly ionised and has a high density ($n_{\rm e} \sim 10^9$ cm^{-3} or higher; Peterson, 1997). The term BLR is used to reflect the observed properties of the optical emission lines, which are thought to originate from this region. Permitted optical emission lines, e.g., $\rm H\beta$, that are Doppler broadened, resulting in lines with broad bases and full width half maximum (FWHM) values up to $\sim 10^4$ km s^{-1}, are observed in some types of AGN. A dusty torus is thought to surround the accretion disc and BLR. Depending on its orientation relative to the line of sight of the observer, the dusty torus can block the optical emission from the broad line clouds (Section 1.1.4). Lying just beyond the BLR and outside the dusty torus is the narrow line region (NLR), where low density ($n_{\rm e} \sim 10^3 - 10^6$ cm^{-3}; Peterson, 1997), low ionisation clouds of matter orbit the SMBH. Once again, Doppler broadened optical emission lines are thought to originate from these clouds. However, these lines are narrower (FWHM $\approx$ few$\times 10^3$ km s^{-1}) than the BLR lines. Also, due to the low density of the clouds, forbidden emission lines such as [O III] can be seen, since the required transitions are not de-excited via collisions.

This is the most simplistic view of the central engine. Refinements to this picture, such as radio emission, mass loss and other factors can also be observed. However, they are beyond the scope of this introduction.

The description given here of the central engine is shown in Figure 1.1. The suspected morphology of the various subclasses of AGN (Section 1.1.3) is also shown, a topic that is closely related to the unification of AGN (Section 1.1.4).

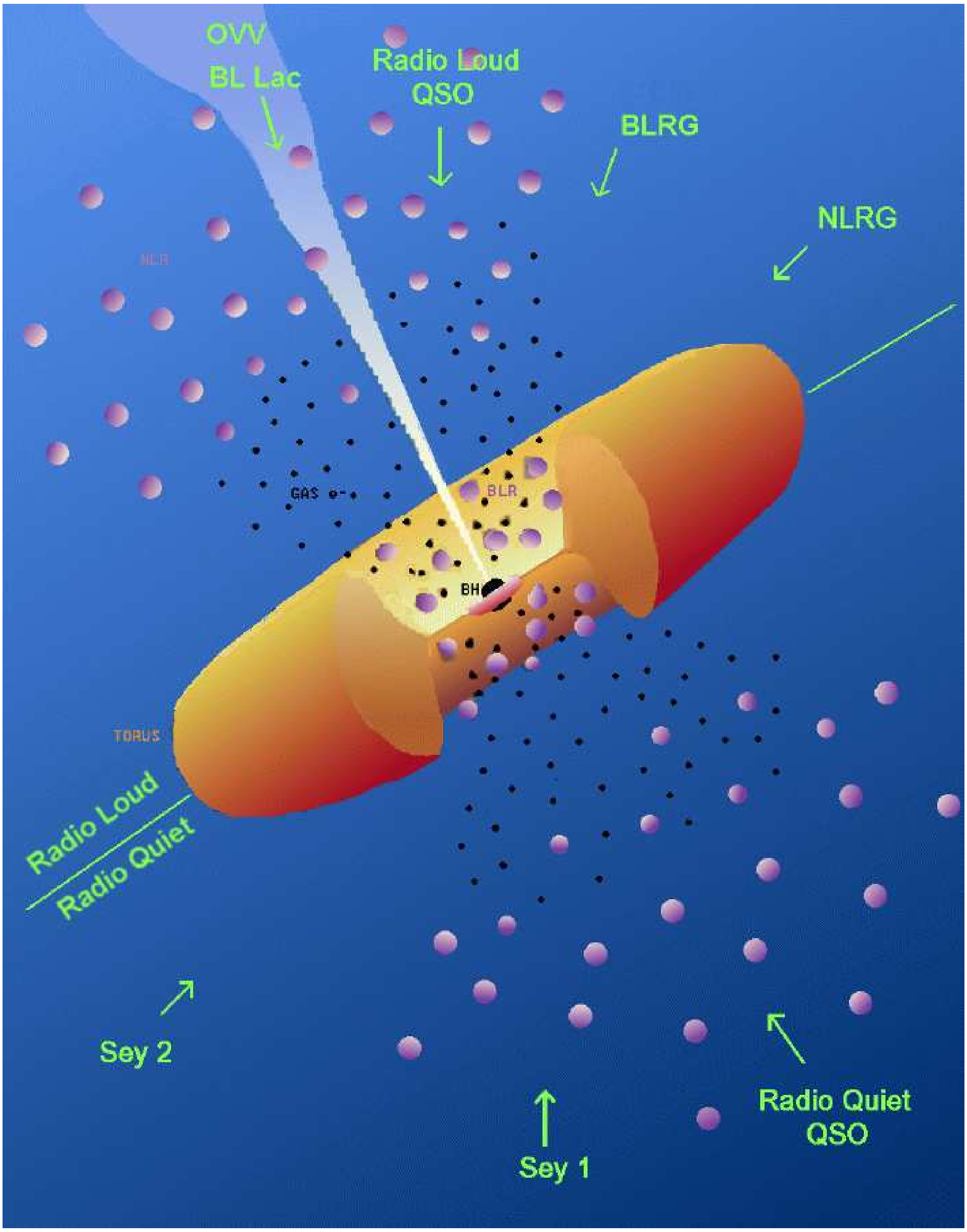

FIGURE 1.1: Schematic of the suggested morphology for the unification of the various subclasses of AGN, including radio loud and radio quiet AGN. Image taken from http://www.asdc.asi.it/bepposax/calendar/

The Accretion Disc

It is believed that accretion onto a SMBH is the main power source of AGN (Section 1.1). Accretion is one of the most efficient processes involved in the production of EM radiation within the Universe and is ~ 10 times more efficient than nucleosynthesis. Accretion can be studied locally in the form of Galactic BHs, e.g., Cyg X-1. Regardless of this, the processes involved are not well understood and it is not clear whether Galactic BH systems can be scaled up to describe the accretion process in AGN (Done and Gierliński, 2005).

The principal behind an accretion disc is the dissipation of a particle's angular momentum, allowing it to be accreted by the BH. This will occur via viscous drag if differential rotation is assumed. The drag force will not only dissipate the particle's angular momentum but it will also release energy in the form of heat (cf. the virial theorem). The released energy heats up the accretion disc giving it a characteristic temperature, T,

$$T = \left(\frac{G\, M_{\rm BH}\, \dot{M}}{4\, \pi\, \sigma\, r^3} \right)^{1/4} \qquad [\mathrm{K}] \tag{1.1}$$

where $M_{\rm BH}$ is the mass of the BH, $\dot{M}$ is the accretion rate of the BH, σ is the Stefan-Boltzmann constant and r is the distance from the BH.

Equation 1.1 assumes that the disc is geometrically thin and optically thick (Peterson, 1997) and that the dissipated heat is radiated locally as black body radiation. However, these assumptions simplify the processes involved within the accretion disc. When the viscous method of dissipation is taken into account and for masses appropriate to AGN, the equation can be rewritten as

$$T \simeq 6.3 \times 10^5 (\dot{M}/\dot{M}_{\rm Edd})^{1/4}\, M_8^{-1/4} \left(\frac{r}{R_{\rm S}} \right)^{-3/4} \qquad [\mathrm{K}] \tag{1.2}$$

where $\dot{M}_{\rm Edd}$ is the Eddington accretion rate, M_8 is the mass of the BH in units of 10^8 $\mathrm{M}_\odot$ and $R_{\rm S} = (2\, G M_{\rm BH}/c^2)$ is the Schwarzschild radius of the BH.

The true structure of an accretion disc is not clear as it depends on a number of parameters, such as M_{BH}, $\dot{M}$, magnetic field lines and viscosity, all of which are not well known or understood. It is also unclear what effect thermal instabilities might have on the disc, not to mention the exact nature of the viscosity involved and how it will shape the disc.

The characteristic temperature of the disc, T, is derived from the luminosity, L, of the central source. It is usual for the properties of the accretion disc to be described in terms of L relative to a theoretical limit. The rate of accretion of matter onto the BH, $\dot{M}$, can be found using the relation

$$L = \eta\, \dot{M}\, c^2 \tag{1.3}$$

leading to an accretion rate of

$$\dot{M} = 1.8 \times 10^{-3}\ (L_{44}/\eta) \qquad [\mathrm{M}_\odot\ \mathrm{yr}^{-1}] \tag{1.4}$$

where η is the efficiency factor ($\simeq 0.1$; Peterson, 1997) and L_{44} is the luminosity of the central source in units of 10^{44} erg s^{-1}. The theoretical limit of the maximum amount of energy that can be radiated away by a BH via accretion is known as the Eddington luminosity, L_{Edd}, and is given by

$$L_{\mathrm{Edd}} = \frac{4\,\pi\, G\, c\, m_{\mathrm{p}}}{\sigma_{\mathrm{T}}}\, M_{\mathrm{BH}} \tag{1.5}$$

$$\Rightarrow L_{\mathrm{Edd}} \simeq 1.26 \times 10^{38}\, (M_{\mathrm{BH}}/\mathrm{M}_\odot) \qquad [\mathrm{erg\ s}^{-1}] \tag{1.6}$$

where m_{p} is the mass of a proton and σ_{T} is the Thompson scattering cross-section. From this definition, the Eddington accretion rate, $\dot{M}_{\mathrm{Edd}}$, which is a representation of the maximum theoretical accretion rate for a BH, can be estimated as

$$\dot{M}_{\mathrm{Edd}} = \frac{L_{\mathrm{Edd}}}{\eta\, c^2} \approx 2.2\, M_8 \qquad [\mathrm{M}_\odot\ \mathrm{yr}^{-1}] \tag{1.7}$$

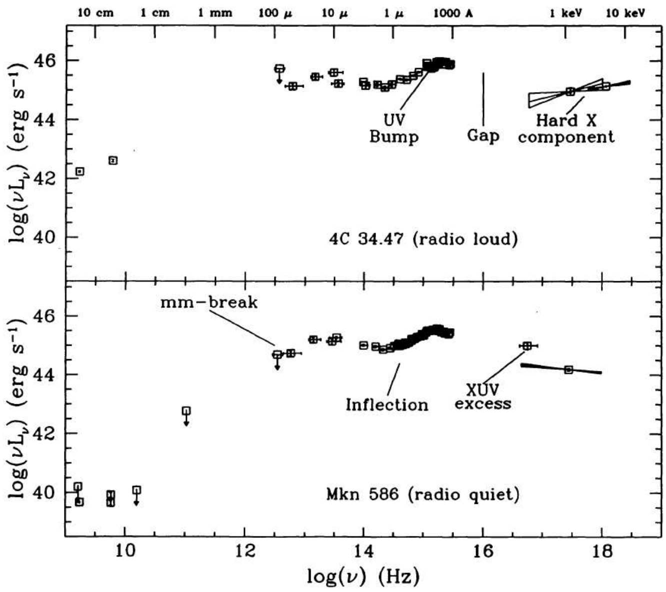

FIGURE 1.2: An SED plot taken from Elvis et al. (1994). The upper panel shows the SED of the radio loud AGN 4C 34.37. The lower panel shows the SED of the radio quiet AGN Mkn 586.

The treatment of the Eddington accretion rate here assumes a spherical system, i.e., radiation is emitted spherically. If instead the radiation is orientated along the disc axis, the Eddington luminosity could easily be exceeded. It is thought that the Eddington luminosity is exceeded in a subclass of AGN known as Narrow Line Seyfert 1 galaxies (NLS1s; Section 1.1.5).

1.1.2 Continuum Emission

AGN show continuum emission across the entire EM spectrum, as shown in the spectral energy distribution (SED) plot of 4C 34.37 and Mkn 586, a radio loud and radio quiet AGN, respectively (Figure 1.2; Elvis et al., 1994). Figure 1.2 shows that AGN emit the majority of their radiation between sub-mm and γ-ray wavelengths, with some emission in the radio, dependent on their radio properties.

Starting at radio wavelengths, AGN can be classified as radio quiet or radio loud.

Approximately 10% of AGN are radio loud (Stocke et al., 1992). The definition of radio loudness is given as a radio (5 GHz) to optical (B-band) flux ratio of $\gtrsim 10$. Even when classed as radio loud, the contribution to the bolometric luminosity by radio emission is small. The origin of the apparent dichotomy is unclear. Recent large scale studies have begun to question whether there is a true dichotomy, since more and more AGN show intermediate radio loudness (Sikora et al., 2007, and references therein). It is believed that the observed radio emission is produced by synchrotron radiation (Section 1.2.1).

Originally thought to be an extension of the radio emission, the infrared (IR) continuum seen from AGN is now thought to be thermal in origin. The IR continuum extends down to $\sim 200\mu$m after which there is a steep downturn in the SED, known as the sub-mm break. The spectral index, α, of the downturn is too steep ($\alpha \lesssim -2.5$) to be consistent with non-thermal synchrotron radiation (Wilkes, 2001). The IR SED from Seyfert galaxies (Section 1.1.3) has maxima at 16μm, 60μm and 150μm. The 16μm feature is attributed to hot dust irradiated by the central source. The other two features are associated with cooler dust from star formation and interstellar processes in the host galaxy (Prieto et al., 2001). This dust is likely to have a temperature $\lesssim 2000$ K, since dust grains sublime above this temperature (Peterson, 1997). This fact is capable of explaining the weakest portion of the IR spectrum, which is found in the near-IR.

The dominant feature in the UV/optical continuum is the big blue bump (BBB) (Peterson, 1997). The BBB is thought to originate from thermal emission ($T \approx 10^{5\pm1}$ K) from the accretion disc itself, while other theories suggest its origin in BH winds (Pounds et al., 2003a; King and Pounds, 2003).

AGN are luminous in X-rays (Elvis et al., 1978; Tananbaum et al., 1979) and can also be observed well into the γ-ray regime. The likely origin for the X-ray emission is either from the inner regions of the accretion disc or from the putative hot corona above the accretion disc, where comptonisation of the UV/optical photons takes place (Section 1.2.1). The higher energy γ-ray photons are thought to be produced in a similar fashion.

1.1.3 Taxonomy

The taxonomy of AGN can be difficult as the underlying physics of AGN is not well understood. The subclasses of AGN are defined mainly by their observed luminosities and optical properties, a number of which are attributed to orientation effects (Section 1.1.4). The following subsections give an introduction to the various subclasses of AGN.

Seyfert Galaxies

Originally classified by Carl Seyfert (Seyfert, 1943), Seyfert galaxies are radio quiet, low luminosity galaxies with an absolute B-band magnitude, $\mathrm{M}_B > -21.5 + 5\log h$, where h is the Hubble parameter, H_0, in units of 100 km s^{-1} Mpc^{-1} (Peterson, 1997). Seyfert galaxies appear in the sky as a star superimposed on a normal galaxy. The host galaxies tend to be spiral galaxies.

Seyfert galaxies can be divided into two distinct subclasses, known as type 1 and type 2. This further classification was first proposed by Khachikian and Weedman (1974). The distinguishing feature between the two subclasses is the presence (type 1) or absence (type 2) of broadened permitted optical emission lines (Section 1.1.1). However, the exact origin of the difference between the two types is not certain and is discussed further in Section 1.1.4.

Type 1 Seyfert galaxies contain two sets of emission lines superimposed upon one another. The first set consists of broad permitted emission lines originating in the BLR, while the second set consists of narrow (some forbidden) emission lines emitted within the NLR (Section 1.1.1).

Within the type 1 Seyfert subclass there is a type of object known as Narrow Line Seyfert 1 galaxies (NLS1s). They are similar to type 2 Seyfert galaxies as they have narrow permitted emission lines that are only slightly broader than the forbidden emission lines (Section 1.1.1). However, they also show some of the characteristics used to define type 1 Seyfert galaxies. It is believed that NLS1s are high-accretion rate, low mass BH systems (Pounds et al., 1995). NLS1s will be discussed in more detail in Section 1.1.5.

Type 2 Seyfert galaxies mainly differ from type 1 Seyfert galaxies due to the presence of only narrow optical emission lines (some forbidden) in their optical spectra. A second difference is that the ratio of the [O III] $\lambda\,5007$ emission line to the H_{β} emission line is less than three for type 2 Seyfert galaxies (Shuder and Osterbrock, 1981). Also, type 2 Seyfert galaxies show a difference in the strength of the Fe II (or higher ionisation) emission lines when compared to type 1 Seyfert galaxies; they are weaker in type 2 Seyfert galaxies.

Quasars

Quasars are believed to be the more luminous counterparts to Seyfert galaxies, with an absolute B-band magnitude, $\mathrm{M}_B < -21.5 + 5\,\log h$ (Peterson, 1997). In fact, it is likely that Seyfert galaxies and quasars are from the same population, with observational biases forming the dichotomy observed. Unlike Seyfert galaxies, the narrow optical emission lines in quasars are, in the most part, weaker relative to the observed broadened optical emission lines. In the radio regime, quasars tend to be type FR-II[2] objects (Fanaroff

[2]Extended (resolvable) radio sources can be divided into two separate classes (Fanaroff and Riley, 1974). Class I objects, FR-I, are the weaker of the two radio sources and are core dominated, with their surface brightness decreasing with distance from the core. In contrast, class II objects, FR-II, are limb-brightened and are stronger radio emitters than FR-I objects.

and Riley, 1974), showing extended radio emission, sometimes with asymmetrical radio jets. Approximately $5-10\%$ of quasars are radio loud (Stocke et al., 1992), where the radio loud quasars (RLQs) are ~ 100 times brighter in the radio than radio quiet quasars (RQQs).

LINERs

LINERs are Low Ionisation Nuclear Emission Region galaxies, which show relatively strong, low ionisation lines, e.g., [O I] $\lambda\,6300$ and [N II] $\lambda\lambda\,6548, 6583$. With the exception of these low ionisation lines, LINERs resemble type 2 Seyfert galaxies spectroscopically but are less luminous. In fact, LINERs are the least luminous subclass of AGN. It is thought that LINERs are common and may exist in nearly half of all spiral galaxies (Ho et al., 1995).

Blazars

The term Blazar encompasses two types of object, both of which are radio sources; BL Lacs (FR-I) and Optically Violent Variables (OVV; FR-II). Blazars show unusually large variations in their continuum emission on short time scales, e.g., $\Delta m > 0.1$ mag at visible wavelengths on time scales of one day (Peterson, 1997). Along with their large variations in flux over short time scales, their optical emission show signs of being strongly polarised when compared to other AGN subclasses, a property that varies with wavelength in both magnitude and position angle.

It is thought that Blazars are galaxies viewed along a relativistic, strongly beamed radio jet close to the line of sight of the observer. Their continuum emission comprises solely of a power-law function and has no thermal component. However, the distinguishing feature between BL Lacs and OVV is that BL Lacs do not have strong emission or absorption lines within their spectra, unlike OVV.

Radio Galaxies

There are two types of radio loud galaxies that can be classed as a subset of AGN. They are broad line radio galaxies (BLRGs) and narrow line radio galaxies (NLRGs) and are thought to be the radio loud counterparts of type 1 and type 2 Seyfert galaxies, respectively. However, they still have a number of differences from their radio quiet counterparts, for example, they are typically found in elliptical galaxies (Peterson, 1997).

1.1.4 Unification

As discussed in Section 1.1.1, the current AGN paradigm is that of a SMBH residing at the centre of the gravitational potential well of its host galaxy (Rees, 1984). The SMBH is surrounded by an accretion disc and fast moving non-coplanar clouds at varying distances in the BLR and NLR. Although there are a number of different subclasses of AGN (Section 1.1.3), a lot of work has gone into unifying them. Much of the unification work is based on the morphology of the central engine and trying to use as few parameters as possible (cf. Occam's Razor). The leading theory was proposed by Antonucci (1993). Antonucci suggested that the presence of a dusty torus (Section 1.1.1) would account for the observed differences at optical and X-ray wavelengths between type 1 and type 2 AGN. In this scenario, the observer's line of sight to the central source determines which type of AGN is seen. At low angles of inclination type 1 AGN are seen and at high angles of inclination type 2 AGN are seen (Figure 1.1).

The main difference between type 1 and type 2 AGN is the presence or absence of broadened optical emission lines like those found in type 1 Seyfert galaxies and missing from type 2 Seyfert galaxies (Section 1.1.3). The major piece of evidence for the orientation solution to this dichotomy lies in the discovery of broad optical emission lines found in the polarised optical light from the archetypal type 2 Seyfert galaxy NGC 1068 (Antonucci and Miller, 1985) and other type 2 AGN (e.g., Tran et al., 1992).

A similar morphology can be applied to radio loud AGN. High angles of inclination show type 2 radio loud AGN, which are lobe dominated, e.g., NLRGs. Low angles of inclination show type 1 radio loud AGN, which are core dominated, e.g., BL Lac objects.

This morphological explanation goes a long way to unify the various subclasses of AGN, but does not explain the apparent dichotomy in radio loudness, nor the range in intrinsic luminosities. There are other intrinsic features of AGN, e.g., broad absorption lines and warm absorbers, that have not been mentioned here. However, it is required that they are included in any unifying theories (see Elvis, 2000). These other intrinsic features are discussed in more detail in Chapter 3.

1.1.5 NLS1s

Another type of AGN that must be incorporated into the unification model are NLS1s (Section 1.1.3). They belong to type 1 Seyfert galaxies but have characteristics not too dissimilar to type 2 Seyfert galaxies (Bian and Zhao, 2003a).

NLS1s are defined by the properties of their optical emission lines. These objects have narrow H_β lines (FWHM $\leqslant 2000$ km s^{-1}; Osterbrock and Pogge, 1985; Bian and Zhao, 2003b), which are only slightly broader than the forbidden optical emission lines present in their spectra, making them similar to type 2 Seyfert galaxies. However, the similarities end there. NLS1s have a ratio of [O III]/$H_\beta > 3$ and show strong emission lines from Fe II and Fe III, comparable to type 1 Seyfert galaxies.

In X-rays, NLS1s are extreme and have been dubbed ultra-soft Seyfert galaxies in some cases. They often show a large soft excess (Section 1.2.2) and their hard X-ray spectrum tends to be steep (soft) with a photon-index, Γ (Section 1.2.2), $\sim 2.0-2.3$, compared to normal type 1 Seyfert galaxies, which have $\Gamma \sim 1.7-1.9$. NLS1s also show very rapid X-ray variability (Leighly, 1999*a*; Leighly, 1999*b*), especially in the soft-band of their X-ray spectrum (Pounds and Vaughan, 2000).

The leading explanation as to the nature of NLS1s is that a lower mass BH resides at their centre and is accreting at a higher fraction of its Eddington luminosity than would normally be expected (Boroson and Green, 1992; Pounds et al., 1995; Boller et al., 1996). The narrow emission lines can be explained by a higher luminosity resulting from a higher accretion rate. The higher luminosity would increase the radiation pressure on the BLR clouds, forcing them further away from the BH, decreasing the effects of Doppler broadening (Section 3.2). The increased luminosity could also explain the extreme soft excesses observed in their X-ray spectra (Section 1.2.2).

1.2 X-ray Mechanisms

The principal research reported in this thesis is based on X-ray observations of AGN. With that in mind, a brief discussion of the observed X-ray properties of AGN and a summary of X-ray emitting processes follows.

1.2.1 X-ray Processes

There are a number of mechanisms that emit X-rays. The first mechanism to be discussed is Bremsstrahlung radiation. Bremsstrahlung, or free-free radiation, is the result of interactions between electrons and the electrostatic (Coulomb) fields of nuclei. This free-free radiation is optically thin and thermal in nature. It is likely to occur in hot ionised gas, e.g., the central regions of AGN or within the corona of stars.

The second process is synchrotron radiation. Synchrotron radiation is caused by the rotation of electrons around magnetic field lines. As the electrons rotate they are accelerated and radiation is emitted. The speeds at which this process occurs are likely to be relativistic and as a result preferential beaming of the emitted radiation along the direction of motion will take place. This will focus the emitted radiation within a cone with a half angle of $1/\gamma$, where the Lorentz factor $\gamma = (1 - v^2/c^2)^{-1/2}$, for a given velocity v. If the energy distribution of the electrons is power-law in form, then the observed spectrum will also take the form of a power-law. This is generally the case for AGN.

The next process is comptonisation. In astrophysical terms, comptonisation is actually inverse-comptonisation; a process where photons gain energy after being scattered (accelerated) within the electromagnetic field of an energetic electron. The process can become saturated if enough scatterings have taken place to up-scatter all of the photons. It is believed that UV and optical photons emitted thermally from the accretion disc as part of the BBB get up-scattered to X-ray energies by energetic electrons in a hot corona that exists above the disc in close proximity to the BH.

The final process is a result of atomic transitions. The term atomic transitions covers a number of processes, which include ionisation, recombination and excitation of an atom, generally within a plasma. These transitions can be complex, e.g., dielectric recombination, and become more complex when the properties of the plasma are incorporated, i.e., whether the plasma is photoionised or collisionally ionised. A prime example of the production of X-rays from atomic transitions is the Fe K-shell fluorescence emission line that is a result of inner-shell transitions within Fe.

Analysis of the X-ray emission lines produced by photoionised or collisionally ionised plasmas allow certain parameters of the plasma to be obtained, e.g., density, abundance, temperature and ionisation parameter. The values obtained can then be used to determine other global parameters of the observed AGN. The study of atomic physics is vast and a full description of the physics and processes involved is well beyond this introduction. Reviews by Paerels and Kahn (2003) and Crenshaw et al. (2003) go some way to introduce the subject.

1.2.2 The X-ray Properties of AGN

AGN are bright in X-rays (Elvis et al., 1978; Tananbaum et al., 1979) and their X-ray spectra, to first approximation, can be described by a power-law, $F(\nu)$, that extends out to ~ 300 keV. The power-law is thought to originate from the comptonisation of UV/optical photons emitted from the accretion disc. The power-law can be described using either the photon-index, Γ, or the energy-index, α, in the form

$$F(\nu) \propto \nu^{-\alpha} \tag{1.8}$$

where $\alpha = \Gamma - 1$. The typical value of Γ for AGN is 1.9 (Nandra and Pounds, 1994).

There are a number of commonly seen spectral features that can be superimposed onto the initial power-law. Figure 1.3 shows a schematic X-ray spectrum of these features. In the hard-band $\gtrsim 2$ keV, additional Fe emission line features from neutral Fe (6.4 keV) or ionised Fe (6.7 keV) can be seen in X-ray spectra of some AGN. Both of these lines can be broadened depending upon the geometry and location of the emitting region. Absorption features such as Fe edges can also be present in AGN X-ray spectra around 7.1 keV and higher. In fact, they are expected in the case of fluorescence emission from neutral Fe. Additional absorption features can also be seen in the hard-band as result of high-ionisation, high-velocity X-ray outflows (Chapter 3). Beyond that, the power-law is flattened (hardened) by the presence of a Compton reflection bump above

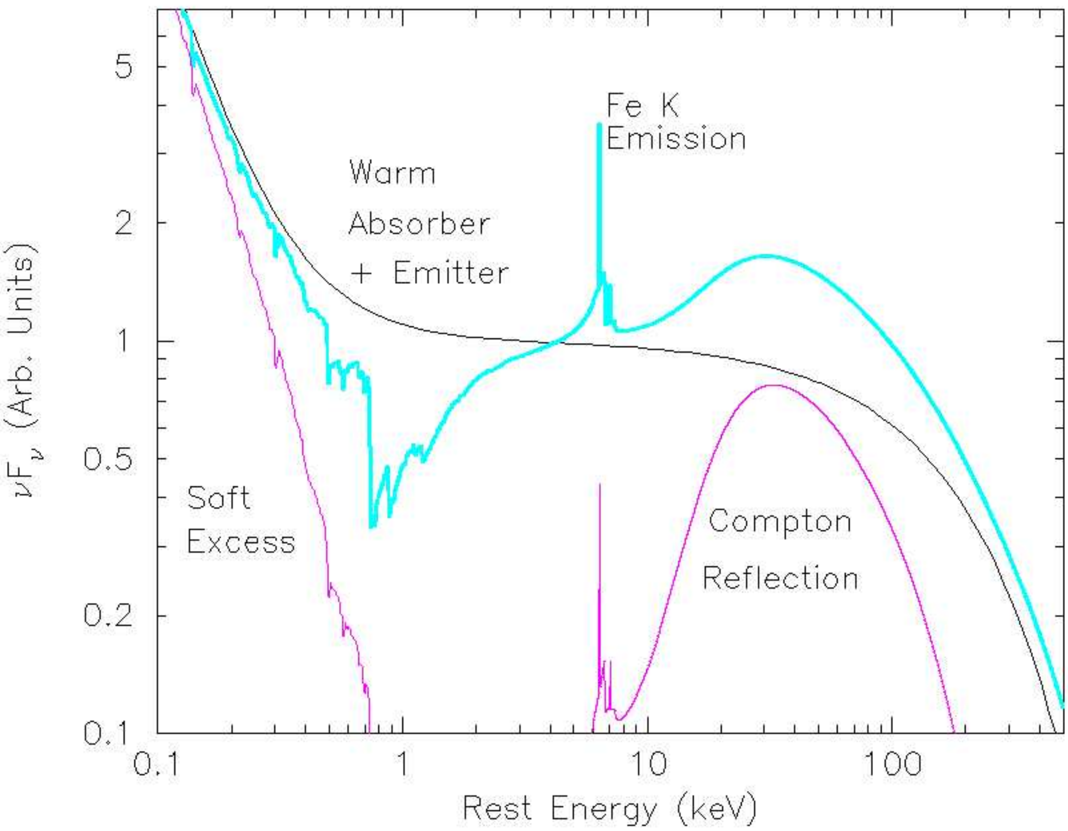

FIGURE 1.3: A schematic of the X-ray emission from an AGN. Image taken from http://www.jca.umbc.edu/~george/html/science/seyferts/seyf1_warmabsorber.shtml.

~ 10 keV. This is the result of soft X-ray photons being absorbed by the disc and harder photons being scattered back out of the disc.

Below 2 keV (soft-band) there are many features that can be present in the spectra of AGN. They can range from narrow emission lines from photoionised plasma (seen in high resolution spectra), to absorption from warm absorbers (Section 3.1.1), to the complete suppression of the soft X-ray continuum emission in type 2 AGN. The soft-band features of AGN are complex and cannot always be simply described by a power-law nor the comptonisation of UV/optical photons. It is likely that atomic physics play an important role at these energies.

Soft Excess

One feature that is present in the majority of type 1 AGN is a soft excess (Turner and Pounds, 1988). Soft excess is the term used to describe the excess emission seen below 2 keV when the initial hard-band ($2-10$ keV) power-law fit is extrapolated to lower energies. Some of the features described earlier can also be found superimposed on the soft excess, although generally the soft excess is seen as a smooth growth from the power-law. The ratio of the soft excess to the power-law fit can be large, approximately ten times larger at low energies (~ 0.3 keV) if not more in some extreme cases.

The study of the origin of the soft excess has become quite intense due to recent studies that have produced some intriguing results. The soft excess is usually parameterised using black body (BB) emission components during modelling. As the number of occurrences of sources with soft excesses increases (due to the ongoing missions of *XMM-Newton* and *Chandra*), the BB parameters of the soft excess have become reasonably well defined.

Large samples of sources with soft excesses ranging in luminosity and mass return BB temperatures in a well defined range of $0.1-0.2$ keV. Thus, the origin of the soft excess is likely to be the same regardless of the intrinsic parameters of the AGN. Initially it was suggested that the origin of the soft excess was a result of thermal emission from the comptonised accretion disc (e.g., Page et al., 2004, and references therein), although recently, as a result of the constant BB temperatures reported, this origin has been contested. Atomic physics has been invoked to explain soft excesses by a number of authors. Gierliński and Done (2004; 2006) suggest that partially ionised atomic absorption from a disc wind creates the soft excess, whereas Ballantyne et al. (2001) suggest emission from partially ionised material as the origin. Finally, Crummy et al. (2006) theorise that the soft excess is a result of reflection from a photoionised disc. Although there are a number of suggestions there is one common theme. In all cases, strong relativistic blurring (i.e., close proximity to the BH) is needed to produce the smooth appearance of the soft excess.

Unfortunately, all three models fit the current observational data well (Sobolewska and Done, 2007) and no one solution is discernible. Future missions such as the IXO will hopefully improve this situation. However, it is likely that the soft excess is an amalgamation of more than one process.

1.3 *XMM-Newton* Observatory

The majority of the data analysed within this thesis were obtained by the X-ray Multi-Mirror observatory, *XMM-Newton* (Jansen et al., 2001). *XMM-Newton* was developed principally by the European Space Agency (ESA) and launched in December 1999. Its mission is to obtain high quality X-ray imaging and spectroscopic data of celestial objects in order to explore their high-energy emission. One way in which *XMM-Newton* is able to achieve this goal is due to its highly elliptical (perigee $7{\times}10^7$ m, apogee $1.14{\times}10^9$ m) 48 hour orbit. Also, its inclination of 40° relative to the equator minimises the time spent in the van-Allen radiation belts and the Earth's shadow, allowing lengthy, continuous observations of targets.

XMM-Newton has a large energy bandpass of 0.2 to 12 keV ($0.3-10$ keV is the commonly used range during analysis) and an angular resolution (FWHM) of ~ 6 arc seconds maintained over a large field of view (FOV) with a diameter of ~ 30 arc minutes. Coupled with its vast effective collecting area (~ 1000 cm^2 at 1 keV, ~ 300 cm^2 at 10 keV) and a flux detection limit of $\sim 1.4\times 10^{-15}$ ergs cm^{-2} s^{-1} over the $2-10$ keV bandpass (Hasinger et al., 2001), *XMM-Newton* is one of the most powerful X-ray telescopes in orbit to date. A consequence of the size of the FOV and its large effective collecting area is that *XMM-Newton* detects approximately $50-100$ serendipitous X-ray sources in a typical 40 ks observation, making *XMM-Newton* ideal for large X-ray surveys (Watson et al., 2001).

Aboard *XMM-Newton* there are three Wolter type-1 telescopes, each with an European Photon Imaging Camera (EPIC) in their focal plane. Two of the EPIC cameras are EMOS detectors (EMOS1 and EMOS2; Turner et al., 2001) and the third is a PN detector (PN; Strüder et al., 2001). All three can be used for imaging and spectral analysis of X-ray sources. Between the EMOS detectors and their mirror assemblies lie the Reflection Grating Spectrometers (RGS; RGS1 and RGS2) transmission gratings (den Herder et al., 2001). By using the transmission gratings to divert $\sim 50\%$ of the light focused towards each EMOS detector onto the respective RGS detectors, the RGS are able to perform simultaneous high resolution spectroscopy ($\Delta E/E = 100-500$ across $0.3-2.1$ keV) of sources within the RGS FOV.

Also aboard *XMM-Newton* aligned with the three main telescopes is the Optical Monitor (OM; Mason et al., 2001), which has a FOV of 17×17 arc minutes^2. The OM allows simultaneous UV and optical ($\sim 1700-6000$ Å) observations of X-ray sources, making *XMM-Newton* an extremely versatile multi-wavelength observatory.

1.3.1 Data Reduction with SAS

The general techniques used during the reduction of *XMM-Newton* data are given below. The majority of the data reduction is performed using the Science Analysis Software (SAS), which was specifically written for this task. To begin the data reduction process, observational data files (ODF) are downloaded from the XMM Science Archive website[3]. These files are 'ingested' using the task ODFINGEST and calibration files are created with

[3]http://xmm.esac.esa.int/external/xmm_data_acc/xsa/index.shtml

the task CIFBUILD. Event lists for the EMOS, PN and RGS cameras are created using the tasks EMCHAIN, EPCHAIN and RGSPROC, respectively.

In the case of the EPIC cameras, a high-energy ($10-15$ keV) light curve of the entire FOV is produced for each detector and are used to create good time interval (GTI) tables. The GTI tables are then used to filter the event lists for any high-energy background flaring events that may affect the analysis of the target sources.

Images are then created from the filtered event lists using XMMSELECT. Pixel PATTERN values of $0-12$ for the EMOS detectors and $0-4$ for the PN detector and an energy range of $0.3-10$ keV are used. To create a sky image with pixels that have an area of $\sim 4\times 4$ arc seconds^2, the tangential sky plane (X,Y) is binned using a binning value of 80×80.

Regions are then selected for the extraction of source and background information, which will be used in the creation of spectra and light curves. The source region is centred on the target and its size optimised by the software. Background regions are offset from, but still close to, the source region, preferably on the same chip for the EMOS cameras or a similar distance from the centre line for the PN camera. The background regions are chosen such that no contamination from the source or other objects in the observation is present. The size of the background extraction region is the same or larger than the source extraction region. XMMSELECT extracts the relevant temporal and spectral information and creates the response matrix files (RMF) and ancillary response files (ARF) using RMFGEN and ARFGEN, respectively. The RMF files contain the energy distribution for each detector and the ARF files contain the physical characteristics of the source region on the detector, for example, quantum efficiency and effective area.

The light curves are binned in 100 second bins, where both the source and the background files have the same start and stop times in each camera.

Background subtracted source spectra and light curves are then created by subtracting the area-scaled background files from the source files. The background subtracted spectra are then binned with a minimum of 20 counts per bin, using the FTOOL *grppha*, which allows the use of Chi-squared statistics during modelling in XSPEC.

For the RGS cameras, a background light curve is created using EVSELECT and GTI tables are produced. The task RGSPROC is re-run to incorporate the GTI tables, which returns a high-energy background filtered event list. RGSPROC also creates the background subtracted source spectra and associated RMF files. Once again the spectra are binned with a minimum of 20 counts per bin.

1.4 William Hercshel Telescope and ISIS Instrument

A small amount of the data reported within this thesis was obtained using the Intermediate dispersion Spectrograph and Imaging System (ISIS) on the William Herschel Telescope (WHT). The WHT is situated at a latitude of $28^{\circ}\,45'\,38.3''$ N and a longitude of $17^{\circ}\,52'\,53.9''$ W, at the Rogue de Los Muchachos Observatory, La Palma, Spain. The WHT is an alt-azimuth mounted telescope with a 4.2 m primary mirror and a focal length of 10.5 m ($f/2.5$). The observatory is at a height of 2345.4 m above sea level.

The ISIS instrument is a double armed, moderate resolution ($8-120$ Å/mm) optical spectrograph, capable of long-slit spectroscopy, spectropolarimetry and imaging polarimetry observations. The introduction of a dichroic filter at the point of beam splitting allows simultaneous observations to be taken at both blue and red wavelengths. Along with the various dichroic filters available, there are a number of transmission gratings available for each arm. This variety allows observations of a range of spectral characteristics and wavelengths.

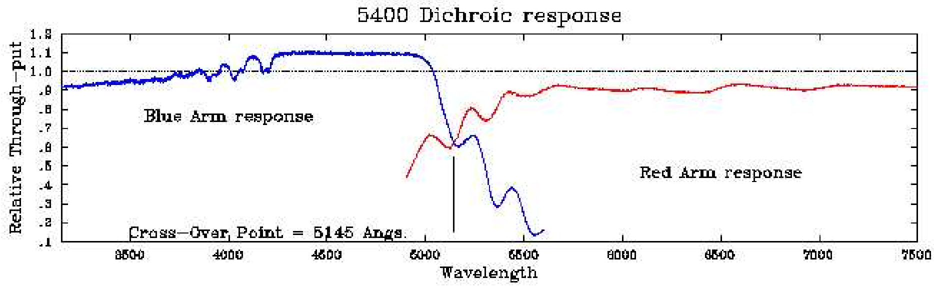

FIGURE 1.4: Plot of the 5400 dichroic response used during observations with the ISIS instrument on the WHT. Image taken from: http://www.ing.iac.es/Astronomy/instruments/isis/isis_dich.html.

For the observations reported within this thesis a long-slit of 2 arc seconds with the 5400 dichroic slide was used. The R300B and R158R gratings were used for the blue and red arms, respectively. This particular set-up gave a resolution of ~ 120 Å/mm for both arms and the observed wavelength range covered was $\sim 3300 - 8500$ Å. The wavelength dependent response of the 5400 dichroic slide is given in Figure 1.4.

1.5 Thesis Overview and Aims

Having given a brief introduction to AGN, particularly at X-ray wavelengths, along with the instrumentation and software used within this thesis, the aims of this thesis are now given. This thesis looks at AGN in extreme regions of parameter space, in particular, super soft X-ray AGN, suspected high-accretion rate AGN and the AGN population of faint background X-ray sources.

Chapter 2 describes the study of a deep-look (~ 500 ks) of the *XMM-Newton* FOV around the famous quasar 3C 273. The deep-look is created by mosaicing the many *XMM-Newton* EPIC calibration observations of 3C 273. Source detection is performed on the deep-look and the analysis explores the background population of AGN whilst looking at the EPIC spectra of the brighter sources within the FOV.

Chapter 3 looks at high-accretion rate AGN and their role within the little understood phenomenon of high-ionisation, high-velocity X-ray outflows detected in a small number of AGN. Specifically, six targets suspected of having a high-accretion rate were observed with *XMM-Newton* and analysed to search for the presence of high-ionisation, high-velocity X-ray outflows.

Chapter 4 uses the first and second releases of the *XMM-Newton* EPIC Source Catalogues to search for super soft X-ray sources (SSXs). The AGN population of SSXs are likely to be high-accretion rate objects, e.g., NLS1s, producing an excess of photons in the soft X-ray regime. The search for SSXs is not limited to AGN, as soft X-ray emitters can be found within our own Galaxy, e.g., cataclysmic variables and isolated neutron stars. Cross-correlation and classification of SSXs is performed and the global parameters of the AGN population explored.

Finally, Chapter 5 concludes this thesis with a summary and discussion of the work reported, allowing conclusions to be made and future work to be proposed for each topic.

Chapter 2

A Deep X-ray View of the *XMM-Newton* Field Surrounding 3C 273

2.1 Introduction

The *XMM-Newton* observatory has been observing the sky since its launch in 1999. The data obtained with *XMM-Newton* have vastly improved our understanding of high-energy phenomena. However, these advances would not be possible without the ongoing efforts of the people involved with the maintenance and calibration of the detectors aboard *XMM-Newton*. One of the ways in which the EPIC cameras are calibrated is to observe the famous quasar 3C 273 on a regular basis.

Regular observations and the impressive observing power of *XMM-Newton* (Section 1.3) allow a unique opportunity to monitor bright sources within the field of view (FOV) around 3C 273. Transient X-ray sources in the 3C 273 field can also be detected using these observations. In addition, a deep-look at the 3C 273 field can be created by stacking the images from all of the observations. It is the latter of these opportunities that is the main focus of this chapter. By creating a deep-look image, faint background X-ray sources that contribute to the cosmic X-ray background (CXB) can be probed.

This chapter begins by summarising the observations of the 3C 273 field taken with *XMM-Newton*. The techniques used to reduce the data are then described. Cross-correlation and the results from the spectral analysis follow. Using this information, classification of the X-ray sources is attempted. Finally, the results obtained within this chapter are discussed and summarised.

2.2 Observations

Since its launch in 1999, *XMM-Newton* has observed the quasar 3C 273 on many occasions. The observations of 3C 273 used to calibrate the EPIC detectors are taken at regular intervals of approximately $6-12$ months. There were also some scientific observations made on more frequent timescales as part of the monitoring campaign of 3C 273. The exposure times of these observations range from a few ks to ~ 60 ks. Table 2.1 lists the observations of 3C 273 that are used in this chapter. Included in Table 2.1 are the observation identification number (OBS_ID), revolution number (REV), date of observation, instrument used (INST), exposure identification number (EXP_ID) and good time interval (GTI) exposure time for each observation. As 3C 273 is such a bright X-ray source, the majority of the observations taken with the EPIC PN (EPN) camera on-board *XMM-Newton* were made in small window mode. In this mode, only a small square region (63×64 pixels) on CCD1, encompassing the bore sight of the EPN camera, is actively reading data. This allows a quick readout (5.7 ms) of events, reducing the amount of pile-up that occurs during the EPN observations of 3C 273. Thus, only data from the EPIC MOS (EMOS) cameras are used in this chapter to analyse the serendipitous sources within the *XMM-Newton* FOV around 3C 273. The data sets for each observation were obtained from the XSA website[1]. The calibration observations were public at

[1]http://xmm.esac.esa.int/xsa/

Table 2.1: Information for the *XMM-Newton* Observations of the 3C 273 Field

OBS_ID	REV	DATE	EMOS1		EMOS2	
			EXP_ID	GTI [s]	EXP_ID	GTI [s]
0126700301	0094	2000 − 06 − 14	001	57297	002	57400
0126700601	0095	2000 − 06 − 15	001	24892	002	24892
0126700701	0095	2000 − 06 − 16	001	18792	002	19892
0126700801	0096	2000 − 06 − 18	001	42597	002	43597
0136550101	0277	2001 − 06 − 13	001	41433	002	41435
0136550101	0277	2001 − 06 − 13	014	43958	015	44455
0112770201	0373	2001 − 12 − 22	002	5299	003	5559
0137551001	0382	2002 − 01 − 09	004	1939	004	1947
0137551001	0382	2002 − 01 − 09	007	7088	005	4307
0137551001	0382	2002 − 01 − 09	008	9160	008	8908
0112770601	0472	2002 − 07 − 07	–	–	002	1597
0112770801	0554	2002 − 12 − 17	002	3891	003	4746
0136550501	0563	2003 − 01 − 05	001	8654	002	8654
0112770701	0563	2003 − 01 − 05	002	4888	003	5141
0112771001	0645	2003 − 06 − 18	002	5400	003	5659
0112770501	0655	2003 − 07 − 08	002	6330	003	7711
0112771101	0735	2003 − 12 − 14	002	8401	003	8662
0136550801	0835	2004 − 06 − 30	001	15104	002	49891
0136550801	0835	2004 − 06 − 30	017	17630	–	–
0136550801	0835	2004 − 07 − 01	018	17707	–	–
0136551001	1023	2005 − 07 − 10	001	27751	002	27670
0414190101	1299	2007 − 01 − 12	001	59873	002	56265
0414190301	1381	2007 − 06 − 25	001	28506	002	26108
0414190401	1465	2007 − 12 − 08	001	34462	002	30365
0414190501	1649	2008 − 12 − 09	001	31806	002	27211

OBS_ID, REV, DATE, EXP_ID and GTI are the observation identification number, revolution number, date of observation, exposure identification number and good time interval exposure time, for each *XMM-Newton* observation of the 3C 273 field, respectively. EMOS1 and EMOS2 refer to the EPIC MOS1 and MOS2 cameras, respectively. Observations are ordered by revolution. GTI times are the exposure time after filtering for high-energy flaring. Only observations that were used in the analysis described in this chapter are shown here.

the time of analysis and the data sets from the monitoring campaign were obtained with permission from Dr. Martin Stuhlinger.

2.3 Data Reduction

Due to the large number of data sets, scripts were created to automate the data reduction process, where possible. These scripts use standard Science Analysis Software (SAS) tasks (version 9.0.0) to reduce the data sets and extract the final source products (Section 2.3.4). The following subsections describe the various steps taken during the data reduction process.

2.3.1 Reduction

Reduction of the data sets was performed in the usual way (Section 1.3.1). The downloaded observation data files (ODF) were 'ingested' using ODFINGEST and standard calibration files for each observation were constructed using CIFBUILD. Event lists for the EMOS detectors in use during each observation were produced with EMCHAIN.

High-energy ($10 - 15$ keV) light curves for the entire FOV of each camera from each observation were created with EVSELECT using a FLAG value of 0 and PATTERN values of $\leqslant 12$ (Section 1.3.1). From these high-energy light curves, GTI tables were produced with a standard RATE limit of $\leqslant 0.3$ counts s^{-1}, using the task TABGTIGEN. These GTI tables were then used to filter the event lists for high-background flaring, such that only the time periods defined by the GTI tables were to be used during future analysis. Only event lists with GTI exposure times greater than 1500 s were kept for analysis (Table 2.1). The event lists are filtered further so that only events with PATTERN $\leqslant 12$ and a FLAG value of 0 remained. The final stage of filtering involved removing the events from the central CCD (CCD1). This only removed events that originated from 3C 273, as 3C 273 dominated the chip due to its brightness and the observing mode of the cameras (small window or timing modes). Removing the events from CCD1 allowed for a better contrast when viewing serendipitous sources in the FOV. The term "event lists" now refers to these filtered event lists. The total GTI exposure times for EMOS1 and EMOS2 are $522{,}858$ s and $512{,}072$ s, respectively.

Six sky images and six exposure maps were produced per event list based on the second *XMM-Newton* Serendipitous EPIC Source Catalogue (2XMM; Watson et al., 2008; Watson et al., 2009) energy bands; $0.2-0.5$ keV (b1), $0.5-1$ keV (b2), $1-2$ keV (b3), $2-4.5$ keV (b4), $4.5-12$ keV (b5), $0.2-12$ keV (b6; broad-band). In addition, broad-band images and exposure maps were created in detector coordinates (DETX/Y) for each event list. The detector images and exposure maps were used to assist with verifying source extraction regions during the data products extraction (Section 2.3.4). An example broad-band image and exposure map for the EMOS1 camera from the 0126700601 observation are shown in Figure 2.1.

To create the deep-look towards 3C 273, the images in each band were stacked. This was achieved by mosaicing the images and exposure maps in each band using the task EMOSAIC. Essentially, EMOSAIC co-adds the images with reference to their world coordinate system (WCS) and were not averaged in any way. The EMOSAIC task uses the WCS reference values (pixel values and celestial coordinates) and the pixel scale (4 arc seconds) from the first image supplied to the task as the WCS and pixel scale for the output mosaiced image. The task then determines the bounds of the output image (using its WCS) by projecting the corners of each input image into the output frame. After this, the size of the output image in pixels is calculated using these bounds and the pixel size. Finally, each pixel in the output image has its coordinates projected into the frame of each input image and the corresponding pixel is sampled and written to the output pixel. This mosaicing procedure was done for the EMOS1 and EMOS2 cameras separately. A total of twelve images and exposure maps, one per band per camera, were created and used for source detection.

In addition to the images and exposure maps, a detector mask for each camera was created from each of the mosaiced broad-band exposure maps. These masks were created using the task EMASK. The detector masks are used by the source detection software to determine the regions to search in each of the images.

The broad-band mosaiced images and exposure maps for the two cameras were themselves mosaiced. The final mosaiced exposure map is shown in Figure 2.2. From these final two mosaiced files a broad-band exposure-corrected image was created and "smoothed" using ASMOOTH. This final image is to be used later for display purposes only. Within ASMOOTH, adaptive smoothing was set, which uses a total of 50 normalised Gaussian convolvers, with widths between 0 and 10 pixels, to smooth the image. This smoothed image is shown in Figure 2.3 and has a combined exposure time of ~ 1 Ms.

2.3.2 Source Detection

Source detection was performed on the twelve mosaiced images concurrently. Also used were the twelve mosaiced exposure maps and the newly created detection masks for each camera. During source detection, the calibration files from the latest EMOS1 observation (REV 1649) were used.

Source detection began by running EBOXDETECT in local detection mode using the supplied images and exposure maps. EBOXDETECT uses a window of 3×3 pixels to search the images for sources. The background is determined by the average number of counts in a 7×7 pixel region centred on the source pixel box that does not include the source box itself. EBOXDETECT searches the images three times, doubling the size of the box on each iteration, allowing the detection of extended sources. The result of this is an initial list of sources (boxlist1) that have a minimum detection likelihood value, MLMIN $\geqslant 8$.

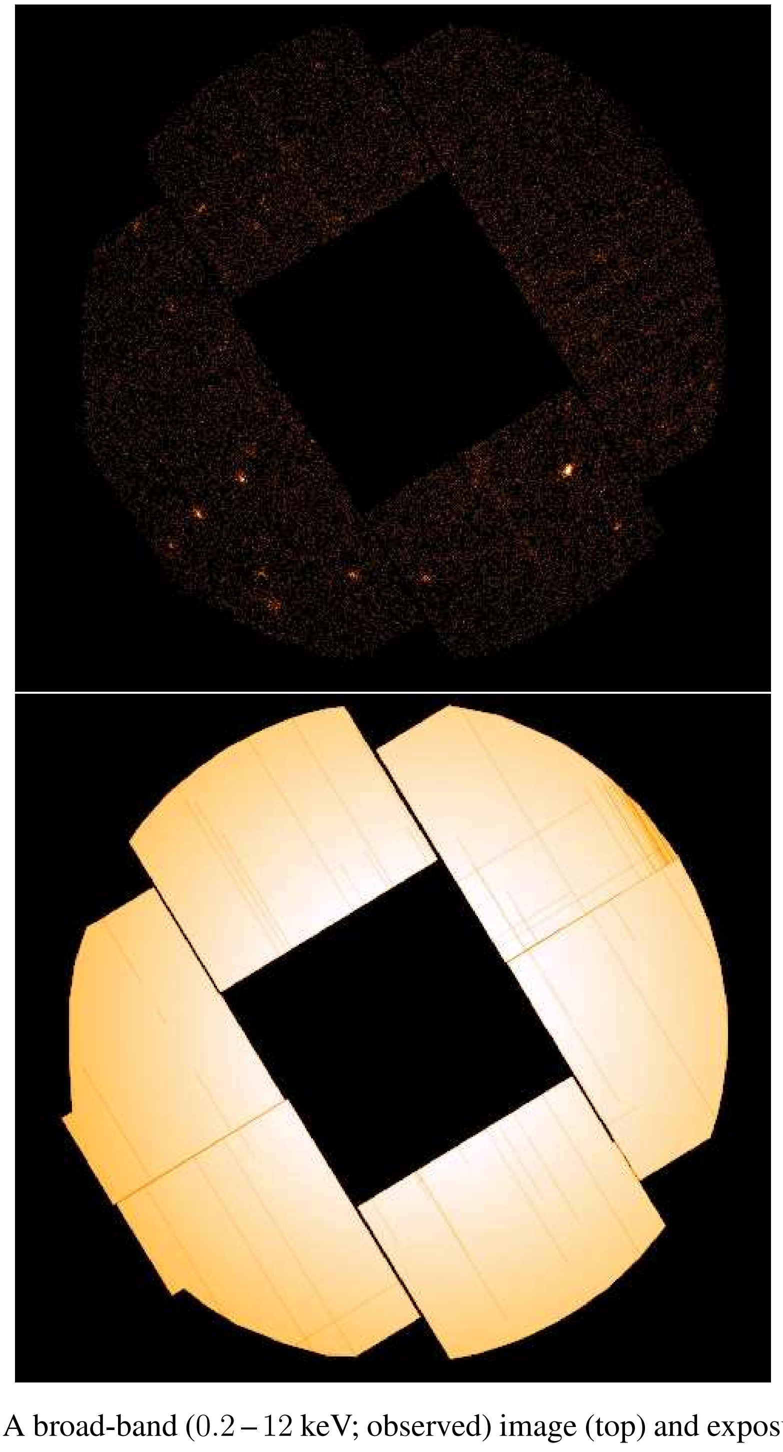

FIGURE 2.1: A broad-band ($0.2 - 12$ keV; observed) image (top) and exposure map (bottom) for the EMOS1 observation 0126700601.

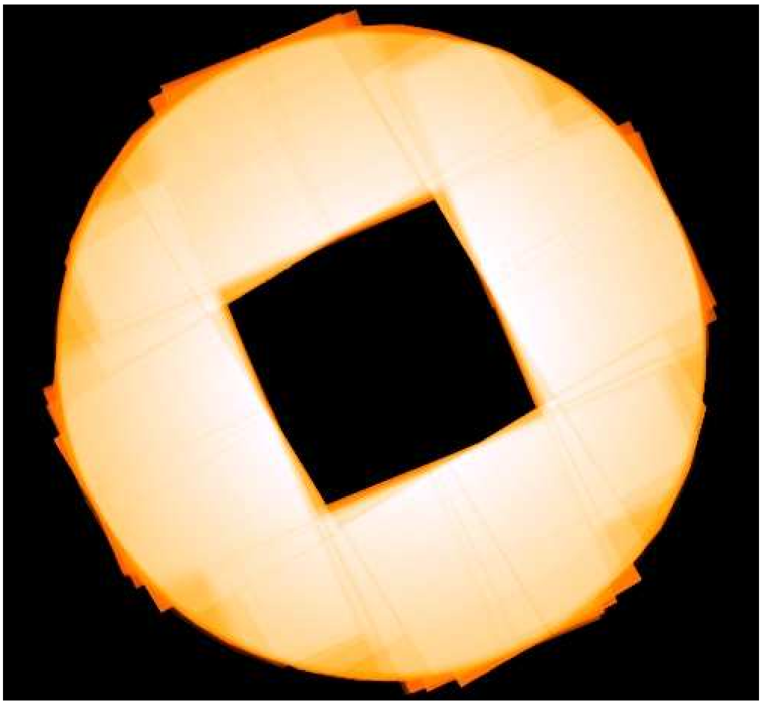

FIGURE 2.2: The final broad-band ($0.2 - 12$ keV; observed) mosaiced exposure map containing all the exposure maps for all the EMOS1 and EMOS2 observations listed in Table 2.1.

The task ESPLINEMAP is then run to construct background maps for the supplied images. ESPLINEMAP removes the sources listed in boxlist1 using the source parameters (e.g., source position, extent and counts) contained within that list and a suitable point spread function (PSF) to determine an appropriate extraction region. Once this is complete, ESPLINEMAP re-bins the image to a grid with 16×16 nodes. These images are then exposure corrected and a two-dimensional spline fit is applied. This fit is performed iteratively three times to remove any significant residuals present during fitting.

EBOXDETECT is then re-run in map mode. The detection method used in map mode is identical to that used in local mode, except the background is now taken from the newly created background maps. This results in improved source parameterisation and sensitivity. Once again, a MLMIN value of $\geqslant 8$ was used. The outcome of this task is a refined source list (boxlist2).

The final SAS task to be used during source detection is EMLDETECT. Using the source coordinates from boxlist2, EMLDETECT performs simultaneous maximum likelihood PSF fits to each source in all bands. Using the source location, assumed shape (Gaussian) and source count rates in each band, the fit calculates the total source count rate, minimum likelihood of detection (DET_ML; total and per band) and the likelihood of whether the source is extended. A DET_ML value of 12 ($> 4\sigma$ detection) was used as the minimum cut value, resulting in a better parameterised source list that contains fewer spurious sources.

The last step in the source detection process is to visually inspect each source. The source positions were plotted over the smoothed exposure corrected image for each band (Figure 2.3), allowing the small number of spurious sources (4) to be removed from the final source list. The parameters of the final 136 sources can be found in Table 2.2. The hardness ratios[2] ($\mathrm{HR}_{<\mathrm{band}>}$) reported in this table are the average of the individual hardness ratios for that band determined for each camera. The energy conversion factors (ecf) used to convert the RATE of a source into flux (flux=RATE/ecf) were the same as those used for the 2XMM catalogue. The ecf values were calculated assuming an absorbed power-law with a photon-index, $\Gamma = 1.7$ and a Galactic absorbing column, $N_{\mathrm{H}} = 3 \times 10^{20}$ cm^{-2}. The ecf values for EMOS1 in the bands b1, b2, b3, b4, and b5, were 1.6015, 1.82853, 2.01594, 0.7378 and 0.143131×10^{11} counts cm^2 erg^{-1}, respectively. The ecf values for EMOS2 in the bands b1, b2, b3, b4, and b5, were 1.6067, 1.83088, 2.01594, 0.741687 and 0.15056×10^{11} counts cm^2 erg^{-1}, respectively. The b6 flux values are the sum of the flux values from bands $1-5$ for each camera.

[2]Hardness ratio defined as: $\mathrm{HR_i} = \frac{\mathrm{C_{i+1} - C_i}}{\mathrm{C_{i+1} + C_i}}$ where $\mathrm{C_i}$ and $\mathrm{C_{i+1}}$ are the counts in the bands $\mathrm{b_i}$ and $\mathrm{b_{i+1}}$, respectively.

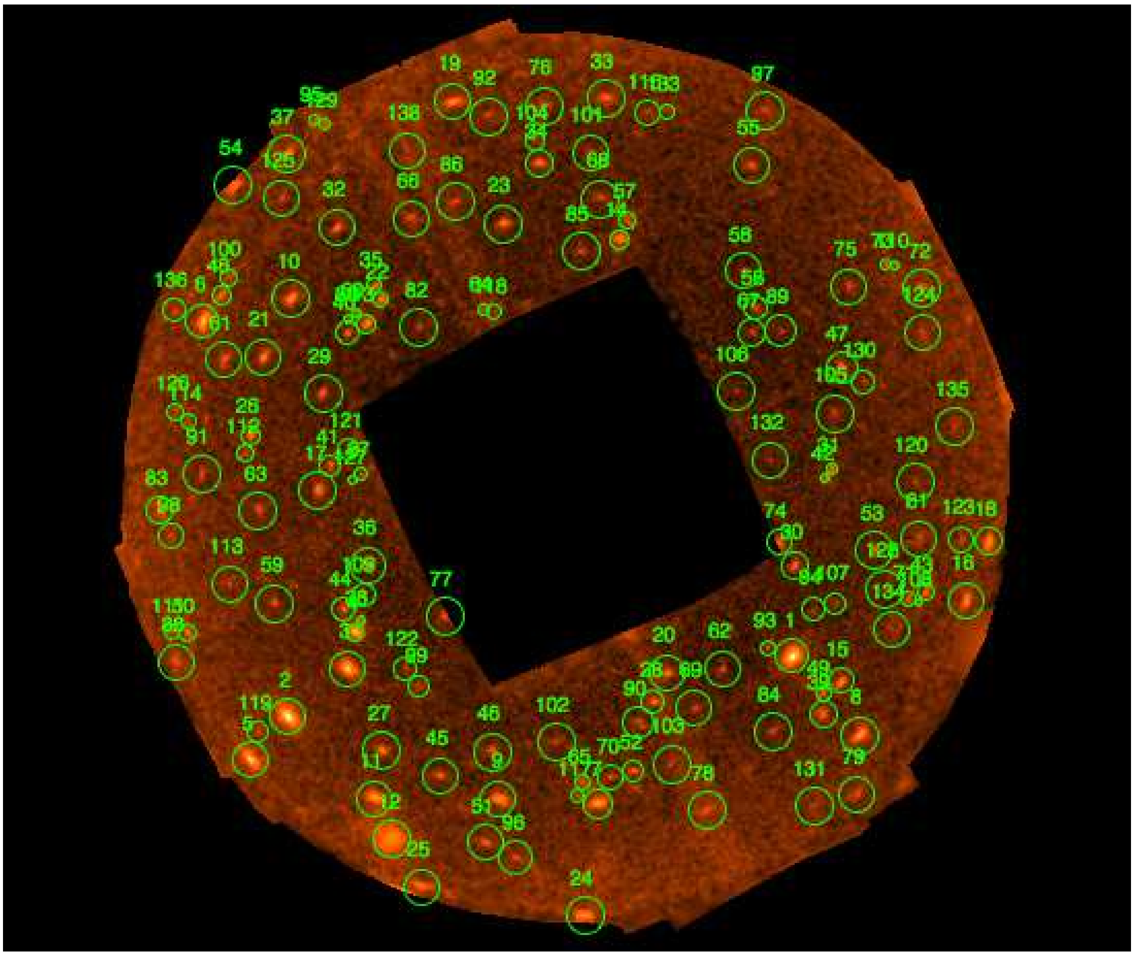

FIGURE 2.3: The final mosaiced and smoothed broad-band ($0.2 - 12$ keV; observed) image of the *XMM-Newton* FOV surrounding 3C 273. The image contains the data from all the EMOS1 and EMOS2 images listed in Table 2.1. Overlaid in green are the source regions centred on the source positions, labelled with the source ML_ID, that were used to extract data products. The maximum radius of the source extraction regions is 35 arc seconds. The exposure time for this image is ~ 1 Ms. The diameter of the *XMM-Newton* footprint in this image is 28.6 arc minutes.

2.3.3 X-ray Positional Errors

The X-ray source positions (R.A., Dec) given in Table 2.2 have been corrected and the positional error (POSERR) incorporates the errors from the source detection and errors introduced by certain steps of the data reduction process. To correct the X-ray source positions, determined by EMLDETECT, the X-ray source positions are cross-correlated with optical source positions from the USNO B1.0 catalogue. This is performed by the task EPOSCORR. The task requires the X-ray source position list and a list of USNO B1.0 optical source positions for the FOV. The optical source list is obtained from the pipeline products (pps; downloaded from the XSA website) for that observation. If the results of the cross-correlation are statistically reliable, as calculated by EVALCORR, then the systematic error (SYSERR) introduced by the EPOSCORR task is set to 0.35 arc seconds. This is in-line with the SYSERR values set for the 2XMM catalogue.

Unfortunately, the RADEC_ERR (from EMLDETECT) and SYSERR errors are not the only factors that need to be incorporated when calculating the X-ray source position errors. The way in which the images used for source detection were created will introduce an additional error to the X-ray source position. As EMOSAIC uses the WCS and pixel scale from the first input image to describe the WCS and pixel scale for the output image, when the pixels from the output image are mapped onto an input image other than the first input image, counts from the pixels within the input image may not be recorded in the correct pixel in the output image. This is a result of the differing WCS values for each input image, since the pixel scales are the same. If this does happen then the maximum offset from the “correct” output pixel should be no more than one pixel in all directions. This would lead to a “smearing” of the source counts around the “correct” pixel. Assuming that there are enough images contributing to the final mosaiced image then the smearing affect will average out. In addition, this effect is taken into account in

Table 2.2: Parameters of the Serendipitous X-ray Sources in the *XMM-Newton* Field Around 3C 273

R.A. [Deg]	Dec [Deg]	RADEC ERR [″]	POS ERR [″]	ML ID	DET ML	SCTS	FLUX $\times10^{-14}$ [erg s^{-1} cm^{-2}]	RATE $\times10^{-3}$ [cts s^{-1}]	HR1	HR2	HR3	HR4
187.154945	1.956113	0.1	2.6	1	21411.0	11651±127	13.62±0.21	43.19±0.47	0.45±0.01	−0.24±0.01	−0.76±0.01	−0.77±0.07
187.426923	1.923318	0.1	2.6	2	16966.3	9663±116	13.73±0.23	46.90±0.57	0.49±0.01	−0.04±0.01	−0.67±0.01	−0.76±0.05
187.394593	1.949333	0.1	2.6	3	6726.1	5438±91	5.90±0.14	20.60±0.34	0.10±0.02	0.10±0.02	−0.42±0.02	−0.61±0.04
187.390503	1.969331	0.1	2.6	4	4490.7	4420±85	4.59±0.12	15.12±0.29	0.20±0.03	0.17±0.02	−0.31±0.03	−0.48±0.04
187.447119	1.900431	0.2	2.6	5	3902.3	3426±73	6.07±0.18	20.93±0.45	0.07±0.03	0.11±0.03	−0.41±0.03	−0.57±0.06
187.472459	2.136719	0.5	2.6	6	2702.1	2870±69	4.92±0.16	15.80±0.38	0.19±0.03	0.11±0.03	−0.25±0.03	−0.57±0.06
187.259594	1.877113	0.2	2.6	7	1593.8	2141±63	2.64±0.11	9.24±0.28	0.63±0.05	0.30±0.03	−0.23±0.03	−0.70±0.06
187.118562	1.914050	0.2	2.6	8	1368.4	1514±53	2.67±0.14	8.51±0.31	0.42±0.04	−0.22±0.04	−0.88±0.05	−0.05±0.44
187.312965	1.879276	0.3	2.6	9	1298.2	1903±61	2.27±0.10	7.93±0.26	0.15±0.04	0.01±0.04	−0.41±0.05	−0.47±0.10
187.425226	2.149197	0.3	2.6	10	834.5	1400±54	1.93±0.10	6.32±0.24	0.14±0.06	0.23±0.04	−0.38±0.05	−0.53±0.11
187.380114	1.879924	0.3	2.6	11	1141.3	1754±58	2.78±0.12	8.83±0.30	−0.05±0.05	0.24±0.04	−0.29±0.05	−0.59±0.09
187.370717	1.857797	0.3	2.6	12	1875.5	2642±71	4.79±0.17	15.17±0.41	0.29±0.04	0.25±0.03	−0.42±0.03	−0.87±0.08
187.384502	2.135473	0.9	2.7	13	724.1	1343±54	1.54±0.09	5.16±0.21	0.25±0.06	0.22±0.05	−0.33±0.05	−0.54±0.10
187.247779	2.180733	0.4	2.6	14	716.0	1297±52	1.43±0.10	5.43±0.23	0.05±0.05	0.00±0.06	−0.32±0.07	−0.52±0.13
187.128604	1.942643	0.5	2.6	15	429.0	881±46	0.95±0.08	3.81±0.20	0.50±0.33	0.37±0.19	0.72±0.06	−0.28±0.05
187.061196	1.986160	0.5	2.6	16	634.1	1117±49	1.60±0.10	5.90±0.26	0.76±0.12	0.51±0.05	−0.09±0.05	−0.60±0.07
187.410455	2.045770	0.5	2.6	17	530.3	1197±54	1.19±0.07	4.04±0.18	0.48±0.09	0.35±0.05	−0.18±0.05	−0.58±0.09
187.049078	2.017649	0.6	2.6	18	603.1	902±42	2.45±0.12	6.58±0.37	−0.05±0.09	0.17±0.08	−0.49±0.09	−0.76±0.33
187.337890	2.254848	0.4	2.6	19	346.5	754±42	1.54±0.11	4.53±0.25	0.24±0.09	0.20±0.06	−0.30±0.07	−0.78±0.16
187.222539	1.947096	0.4	2.6	20	407.1	1038±51	1.04±0.07	3.20±0.16	0.24±0.07	0.15±0.06	−0.42±0.07	−0.41±0.15
187.440162	2.117072	0.4	2.6	21	454.9	934±46	1.22±0.08	3.95±0.20	0.11±0.06	0.02±0.06	−0.40±0.07	−0.68±0.20
187.376671	2.148334	0.5	2.6	22	424.0	957±48	1.20±0.08	3.79±0.19	0.37±0.09	0.34±0.05	−0.33±0.06	−0.58±0.13
187.310877	2.189595	0.5	2.6	23	321.6	816±46	0.87±0.07	3.12±0.18	0.35±0.08	0.11±0.06	−0.39±0.07	−0.46±0.17
187.266447	1.816738	0.4	2.6	24	305.8	607±37	5.69±0.67	16.56±1.28	0.47±0.13	0.31±0.08	−0.23±0.08	−0.52±0.14
187.355119	1.831499	0.5	2.6	25	252.8	540±34	1.17±0.10	4.46±0.29	0.00±0.27	0.94±0.09	0.32±0.07	−0.47±0.08
187.447060	2.075353	0.7	2.7	26	368.2	852±46	1.33±0.09	3.75±0.21	0.38±0.09	0.16±0.06	−0.26±0.07	−0.73±0.16
187.376172	1.905452	0.8	2.7	27	202.3	650±43	0.82±0.07	2.86±0.19	0.32±0.10	0.20±0.07	−0.33±0.08	−0.37±0.17
187.229578	1.931691	0.7	2.7	28	223.5	766±48	0.77±0.07	2.58±0.16	0.27±0.09	0.15±0.07	−0.31±0.08	−0.50±0.18
187.408273	2.097694	1.0	2.8	29	173.9	574±42	0.56±0.06	2.15±0.16	0.36±0.11	0.16±0.08	−0.34±0.09	−0.77±0.25
187.153722	2.004923	0.8	2.7	30	201.7	623±41	0.69±0.06	2.39±0.16	0.17±0.10	0.27±0.08	−0.33±0.08	−0.69±0.16
187.133925	2.056833	0.8	2.7	31	271.1	854±49	0.81±0.07	2.82±0.16	0.54±0.10	0.23±0.07	−0.23±0.07	−0.44±0.12
187.400450	2.187108	0.6	2.6	32	151.8	488±37	0.66±0.08	2.45±0.19	0.21±0.14	0.43±0.08	−0.34±0.08	−0.76±0.17
187.255344	2.256390	0.7	2.7	33	178.3	559±40	0.88±0.08	2.90±0.21	0.15±0.09	0.12±0.08	−0.49±0.10	−0.36±0.30
187.291353	2.221781	0.6	2.6	34	223.7	670±43	0.90±0.08	3.01±0.20	0.29±0.09	0.08±0.07	−0.37±0.09	−0.22±0.17
187.380211	2.155861	0.8	2.7	35	91.0	452±40	0.59±0.07	1.88±0.17	0.40±0.14	0.18±0.10	−0.21±0.11	−0.69±0.22
187.383401	2.005203	0.6	2.6	36	217.6	705±46	0.60±0.05	2.20±0.14	1.00±0.14	0.62±0.07	−0.25±0.07	−0.41±0.12
187.427670	2.226935	0.9	2.7	37	121.1	371±33	0.81±0.10	2.78±0.25	0.57±0.43	0.79±0.08	−0.26±0.09	−0.39±0.16
187.387617	1.975307	0.8	2.7	38	153.1	765±53	0.68±0.07	2.58±0.18	−0.02±0.17	0.47±0.11	0.12±0.08	−0.45±0.10
187.138688	1.924856	0.7	2.7	39	223.0	627±42	0.94±0.08	2.83±0.19	0.33±0.08	−0.11±0.07	−0.50±0.11	−0.23±0.34
187.394899	2.130272	0.6	2.6	40	150.8	530±40	0.58±0.07	2.09±0.16	0.31±0.11	0.09±0.09	−0.22±0.10	−0.74±0.20
187.403857	2.058990	0.8	2.7	41	160.3	633±46	0.65±0.06	2.05±0.15	0.23±0.13	0.33±0.08	−0.30±0.09	−0.52±0.21
187.136614	2.052195	0.9	2.7	42	102.2	488±43	0.46±0.06	1.57±0.14	0.31±0.23	0.50±0.09	−0.30±0.09	−0.82±0.23
187.082892	1.990565	0.9	2.7	43	119.2	493±40	0.65±0.08	2.28±0.19	0.37±0.17	0.38±0.09	−0.18±0.09	−0.42±0.17
187.396888	1.981551	0.7	2.7	44	126.2	538±42	0.53±0.06	1.87±0.15	0.00±0.00	0.82±0.11	0.18±0.08	−0.37±0.10
187.344673	1.891600	0.7	2.7	45	144.7	445±38	0.51±0.06	1.85±0.16	0.73±2.01	0.20±0.55	0.88±0.08	−0.37±0.08
187.316570	1.904969	1.0	2.7	46	96.1	434±39	0.46±0.06	1.73±0.16	0.14±0.12	0.09±0.11	−0.26±0.13	−0.81±0.31
187.128544	2.111747	0.6	2.7	47	245.1	762±46	0.77±0.07	2.77±0.17	0.43±0.10	0.26±0.07	−0.34±0.07	−0.38±0.15
187.462927	2.150436	0.8	2.7	48	97.3	438±38	0.64±0.09	2.52±0.23	−0.34±0.24	0.73±0.12	−0.04±0.10	−0.26±0.14
187.138504	1.936193	0.9	2.7	49	93.0	415±37	0.49±0.07	1.75±0.16	0.37±0.17	0.31±0.10	−0.31±0.10	−0.81±0.23
187.480940	1.968827	1.0	2.8	50	110.8	443±37	0.84±0.09	2.62±0.22	0.26±0.13	0.22±0.10	−0.28±0.11	−0.43±0.21
187.320442	1.855750	1.4	2.9	51	98.0	390±35	0.55±0.07	1.90±0.17	0.55±0.13	0.09±0.09	−0.49±0.12	−0.79±0.38
187.240113	1.894296	1.2	2.9	52	66.5	364±38	0.44±0.06	1.44±0.15	0.05±0.15	0.27±0.11	−0.47±0.15	−0.66±0.49

Table 2.2: Parameters of the Serendipitous X-ray Sources in the *XMM-Newton* Field Around 3C 273 (*Cont.*)

R.A. [Deg]	Dec [Deg]	RADEC ERR [$''$]	POS ERR [$''$]	ML ID	DET ML	SCTS	FLUX $\times 10^{-14}$ [erg s^{-1} cm^{-2}]	RATE $\times 10^{-3}$ [cts s^{-1}]	HR1	HR2	HR3	HR4
187.110231	2.013566	1.0	2.8	53	96.3	438±39	0.51±0.06	1.68±0.15	0.52±0.16	0.26±0.09	−0.44±0.11	−0.37±0.26
187.456417	2.210214	1.4	2.9	54	77.2	194±22	0.01±0.20	3.38±0.54	−0.06±0.16	0.01±0.17	0.19±0.16	−0.49±0.20
187.177009	2.220367	0.9	2.7	55	100.7	407±38	0.57±0.07	1.85±0.18	0.26±0.18	0.45±0.09	−0.50±0.11	−0.38±0.29
187.174463	2.143625	0.8	2.7	56	136.7	499±42	0.37±0.05	1.59±0.13	0.00±0.00	0.91±0.11	0.04±0.08	−0.54±0.12
187.243597	2.191444	0.7	2.7	57	244.3	555±41	0.70±0.08	2.31±0.17	0.74±0.06	−0.64±0.07	−0.72±0.21	−0.67±1.42
187.181084	2.163504	1.1	2.8	58	73.8	388±39	0.40±0.05	1.29±0.13	0.27±0.20	0.38±0.11	−0.11±0.11	−0.77±0.27
187.434179	1.985069	1.1	2.8	59	83.8	381±37	0.36±0.05	1.63±0.16	0.00±0.00	1.00±0.12	0.22±0.10	−0.30±0.12
187.389835	2.140437	1.2	2.8	60	60.4	360±38	0.38±0.06	1.43±0.16	0.53±0.50	0.74±0.15	0.01±0.11	−0.46±0.16
187.461198	2.115631	1.2	2.8	61	99.1	440±39	0.70±0.08	2.10±0.19	0.09±0.15	0.14±0.12	0.00±0.11	−0.79±0.20
187.192239	1.949430	1.0	2.8	62	51.7	349±40	0.28±0.05	1.14±0.13	−0.13±0.31	0.38±0.24	0.39±0.14	−0.37±0.15
187.442717	2.034690	1.0	2.8	63	88.4	427±40	0.52±0.06	1.75±0.17	0.50±0.19	0.33±0.10	−0.44±0.11	−0.11±0.23
187.321670	2.142919	1.2	2.8	64	103.9	531±46	0.61±0.06	1.81±0.16	0.22±0.13	0.11±0.11	−0.33±0.12	−0.39±0.24
187.267854	1.888225	1.2	2.8	65	55.8	371±40	0.40±0.06	1.50±0.16	0.16±0.39	0.42±0.23	0.38±0.12	−0.29±0.13
187.360269	2.191651	1.2	2.8	66	66.6	368±39	0.47±0.07	1.63±0.17	0.42±0.17	0.18±0.11	−0.39±0.14	−0.17±0.26
187.176502	2.130556	0.9	2.7	67	56.9	360±39	0.29±0.04	1.09±0.12	0.65±0.27	−0.15±0.24	0.59±0.14	−0.30±0.13
187.258463	2.202936	1.1	2.8	68	60.7	327±36	0.45±0.06	1.37±0.15	0.24±0.14	−0.01±0.13	−0.38±0.17	−0.63±0.35
187.207384	1.928223	1.0	2.8	69	47.5	315±39	0.34±0.05	1.10±0.14	−0.19±0.19	0.42±0.13	−0.61±0.17	−0.39±1.09
187.252900	1.891031	1.1	2.8	70	35.4	224±31	0.30±0.05	0.91±0.13	−0.23±4.14	0.90±0.17	0.09±0.13	−0.89±0.17
187.092278	1.987196	1.1	2.8	71	79.3	377±37	0.46±0.07	1.65±0.17	0.22±0.13	0.07±0.11	−0.38±0.14	−0.73±0.44
187.084903	2.154429	1.5	3.0	72	102.8	378±34	0.54±0.07	1.95±0.18	0.55±0.11	−0.12±0.09	−0.73±0.11	0.00±0.50
187.104236	2.167070	1.0	2.7	73	61.1	290±33	0.40±0.06	1.40±0.16	0.74±0.11	−0.25±0.12	−0.51±0.22	−0.39±0.52
187.162024	2.017055	0.9	2.7	74	70.9	242±26	1.03±0.17	3.26±0.36	0.16±0.15	0.04±0.13	−0.31±0.16	−0.48±0.27
187.124419	2.155253	1.0	2.8	75	67.8	348±36	0.47±0.06	1.42±0.15	0.41±0.14	−0.17±0.13	−0.09±0.17	−0.62±0.33
187.288730	2.252960	0.9	2.7	76	49.2	274±33	0.49±0.08	1.60±0.19	0.31±0.30	0.25±0.14	−0.11±0.15	−0.51±0.29
187.342587	1.977837	1.4	2.9	77	99.3	244±27	0.67±0.10	2.21±0.25	0.54±0.10	−0.82±0.11	0.17±3.46	−0.56±1.90
187.200977	1.873347	1.8	3.2	78	69.0	365±38	0.45±0.07	1.79±0.19	0.15±0.12	−0.12±0.12	−0.38±0.18	−0.68±0.51
187.119866	1.881887	1.4	2.9	79	43.5	242±31	0.49±0.08	1.54±0.20	0.41±0.20	0.18±0.13	−0.63±0.16	0.42±0.32
187.393827	2.138197	1.4	2.9	80	23.8	226±33	0.29±0.06	0.93±0.14	−0.10±0.24	0.47±0.16	−0.09±0.17	−0.59±0.28
187.085965	2.019673	1.5	3.0	81	65.1	340±37	0.38±0.07	1.48±0.16	0.35±0.14	−0.01±0.12	−0.71±0.18	0.00±0.63
187.356011	2.133596	1.3	2.9	82	30.6	262±35	0.31±0.05	0.92±0.12	−0.05±0.18	0.13±0.18	−0.07±0.18	−0.90±0.36
187.495748	2.034478	1.2	2.8	83	110.4	447±38	0.75±0.09	3.05±0.26	0.18±0.13	0.17±0.10	−0.33±0.12	−0.14±0.23
187.165257	1.915404	2.0	3.2	84	24.7	221±33	0.24±0.06	0.93±0.14	−0.33±0.26	0.34±0.21	−0.15±0.22	−0.52±0.34
187.268812	2.174786	1.0	2.7	85	56.2	371±39	0.39±0.06	1.30±0.14	0.11±0.16	0.12±0.13	−0.07±0.14	−0.62±0.23
187.337034	2.201112	2.3	3.5	86	48.6	299±36	0.31±0.06	1.33±0.16	0.00±0.00	0.71±0.36	0.28±0.15	−0.14±0.14
187.387165	2.053914	1.2	2.8	87	45.5	322±39	0.24±0.05	1.15±0.14	0.54±0.56	0.74±0.14	−0.42±0.13	−0.11±0.25
187.486838	1.952649	1.2	2.8	88	74.4	294±31	0.59±0.09	2.02±0.22	0.71±0.24	0.43±0.10	−0.42±0.11	−0.77±0.30
187.161178	2.131490	1.2	2.8	89	29.3	237±33	0.26±0.05	0.76±0.11	0.94±2.33	0.70±0.29	0.36±0.15	−0.62±0.17
187.237773	1.920423	1.0	2.8	90	54.3	372±41	0.44±0.06	1.29±0.14	0.51±0.19	0.10±0.12	−0.46±0.16	0.09±0.28
187.473316	2.054758	1.4	2.9	91	38.3	243±31	0.27±0.05	1.23±0.16	0.27±0.35	0.61±0.13	−0.27±0.14	−0.75±0.26
187.318683	2.247249	1.3	2.9	92	25.0	174±28	0.24±0.06	0.93±0.15	−1.00±5.93	1.00±4.95	0.58±0.13	−0.58±0.21
187.167817	1.960749	2.1	3.3	93	26.7	272±38	0.27±0.05	0.94±0.13	0.30±0.37	−0.04±0.33	0.46±0.21	−0.10±0.18
187.143247	1.981498	2.0	3.3	94	28.0	188±32	0.15±0.05	0.67±0.12	0.00±0.00	1.00±2.19	0.89±0.14	−0.55±0.18
187.411966	2.245001	1.6	3.0	95	42.9	208±26	0.74±0.11	2.29±0.29	1.00±0.55	0.72±0.17	0.05±0.14	−0.37±0.20
187.304088	1.847118	1.2	2.9	96	27.5	220±33	0.28±0.07	1.17±0.18	0.19±0.33	0.18±0.28	0.37±0.18	−0.49±0.24
187.169444	2.249749	1.3	2.9	97	28.1	198±28	0.33±0.06	1.34±0.20	0.29±0.24	0.22±0.16	−0.23±0.18	−0.86±0.37
187.489760	2.021165	1.6	3.0	98	24.3	198±30	0.39±0.08	1.13±0.17	0.19±0.18	−0.00±0.17	−0.65±0.23	−0.68±2.61
187.356294	1.940159	1.7	3.1	99	41.4	314±39	0.30±0.05	1.05±0.13	0.62±0.26	0.28±0.12	−0.65±0.13	0.21±0.32
187.458682	2.160359	1.5	3.0	100	40.2	233±30	0.43±0.08	1.45±0.19	0.63±0.28	0.57±0.13	−0.37±0.13	−0.72±0.34
187.263379	2.227307	1.4	2.9	101	22.3	200±31	0.19±0.05	0.92±0.14	0.75±0.54	0.53±0.23	0.08±0.16	−0.76±0.17
187.282413	1.910340	2.1	3.3	102	15.5	212±36	0.24±0.05	0.77±0.13	0.28±0.27	0.26±0.18	−0.48±0.22	−0.20±0.48
187.219625	1.898393	2.5	3.6	103	24.1	221±33	0.13±0.04	0.86±0.13	0.00±0.00	0.64±0.19	0.03±0.21	−0.83±0.38
187.293680	2.233871	1.3	2.9	104	19.5	178±30	0.21±0.05	0.85±0.14	0.00±0.00	1.00±0.39	0.65±0.21	−0.14±0.17

Table 2.2: Parameters of the Serendipitous X-ray Sources in the *XMM-Newton* Field Around 3C 273 (*Cont.*)

R.A. [Deg]	Dec [Deg]	RADEC ERR [″]	POS ERR [″]	ML ID	DET ML	SCTS	FLUX $\times 10^{-14}$ [erg s^{-1} cm^{-2}]	RATE $\times 10^{-3}$ [cts s^{-1}]	HR1	HR2	HR3	HR4
187.132030	2.087205	1.1	2.8	105	45.3	335±39	0.33±0.05	1.13±0.13	0.76±0.28	0.14±0.14	0.00±0.14	−0.32±0.21
187.185329	2.099216	1.7	3.1	106	16.6	215±37	0.14±0.04	0.59±0.10	0.28±0.25	0.12±0.18	−0.81±0.31	0.74±1.57
187.131586	1.984931	1.3	2.9	107	32.0	222±32	0.32±0.05	0.82±0.12	0.78±0.20	−0.21±0.20	−0.04±0.24	−0.92±0.45
187.086875	1.985667	2.2	3.4	108	24.2	239±35	0.34±0.07	1.08±0.16	−0.13±1.16	0.75±0.14	−0.14±0.15	−0.44±0.25
187.386563	1.989445	1.1	2.8	109	41.9	303±37	0.24±0.04	0.98±0.12	0.55±0.24	0.35±0.13	−0.23±0.13	−0.73±0.27
187.099340	2.167088	1.4	2.9	110	21.8	182±30	0.26±0.05	0.89±0.15	0.00±0.00	0.00±1.15	0.61±0.21	0.06±0.17
187.489364	1.969427	1.5	3.0	111	28.8	190±32	0.27±0.07	1.17±0.20	0.00±0.42	0.00±0.53	0.62±0.18	−0.54±0.22
187.449670	2.065511	2.0	3.3	112	22.1	252±37	0.40±0.07	1.08±0.16	−0.28±0.20	0.11±0.29	−0.06±0.28	0.05±0.33
187.458350	1.994874	1.5	3.0	113	17.5	202±33	0.28±0.06	0.95±0.16	1.00±0.37	0.35±0.25	0.13±0.21	−0.08±0.22
187.480452	2.082913	1.4	2.9	114	28.1	226±33	0.34±0.07	1.18±0.18	1.00±1.53	0.71±0.21	0.15±0.15	−0.41±0.21
187.232816	2.248677	1.8	3.2	115	14.1	183±31	0.19±0.05	0.86±0.15	0.50±0.26	0.18±0.24	0.09±0.20	−0.67±0.32
187.270593	1.881188	1.9	3.2	117	26.9	217±34	0.22±0.05	0.91±0.15	1.00±0.92	−0.36±0.66	0.85±0.17	−0.32±0.17
187.315838	2.141829	1.3	2.9	118	37.2	296±36	0.35±0.06	1.11±0.14	0.36±0.22	0.22±0.13	−0.37±0.16	−0.35±0.29
187.442798	1.914992	1.6	3.0	119	14.1	140±28	0.27±0.06	0.78±0.16	−0.19±0.20	0.03±0.28	−1.00±0.71	0.00±0.00
187.088608	2.050213	1.7	3.1	120	16.9	184±33	0.18±0.06	0.80±0.14	0.39±0.28	0.14±0.19	−0.43±0.23	−0.23±0.68
187.393835	2.067748	1.9	3.2	121	16.5	202±34	0.25±0.05	0.81±0.14	0.60±0.52	0.42±0.22	−0.24±0.19	−0.34±0.36
187.363394	1.949399	1.2	2.8	122	25.0	271±38	0.21±0.04	0.89±0.13	0.21±0.33	0.39±0.19	−0.05±0.16	−0.46±0.23
187.063652	2.019350	1.9	3.2	123	21.9	206±30	0.42±0.07	1.16±0.18	0.41±0.56	0.54±0.22	−0.32±0.20	−0.19±0.24
187.084896	2.130452	1.3	2.9	124	34.5	253±34	0.36±0.07	1.22±0.17	1.00±0.29	0.44±0.16	−0.12±0.14	−0.52±0.28
187.430181	2.203045	1.4	2.9	125	16.5	177±30	0.30±0.08	1.09±0.19	−0.31±0.44	0.64±0.19	−0.32±0.20	0.01±0.33
187.487416	2.088574	2.0	3.3	126	12.1	163±30	0.24±0.07	0.94±0.18	−0.05±0.29	0.38±0.20	−0.36±0.23	−0.56±0.67
187.391713	2.051016	1.5	3.0	127	14.7	210±36	0.16±0.04	0.64±0.11	−0.11±0.60	0.76±0.18	−0.39±0.19	−0.37±0.24
187.104990	1.993016	1.7	3.1	128	14.8	145±31	0.19±0.05	0.59±0.13	0.22±0.19	−0.63±0.27	−0.77±0.84	0.00±5.60
187.406781	2.242672	1.4	2.9	129	25.8	210±29	0.43±0.09	1.59±0.22	0.00±0.55	0.84±0.19	0.17±0.17	−0.05±0.18
187.116460	2.104188	1.6	3.0	130	20.5	194±35	0.22±0.05	0.74±0.13	0.93±0.37	0.19±0.17	−0.13±0.18	−1.00±0.65
187.143119	1.875892	2.2	3.4	131	17.9	145±28	0.31±0.07	0.82±0.16	0.36±49.1	0.84±0.37	0.41±0.21	−0.85±0.23
187.166735	2.061677	1.6	3.0	132	21.0	227±37	0.17±0.04	0.63±0.10	0.31±0.64	0.66±0.15	−0.21±0.15	−0.80±0.45
187.222121	2.249598	3.1	4.0	133	13.8	152±29	0.23±0.05	0.72±0.14	0.00±0.00	1.00±2.66	0.39±0.16	−0.69±0.23
187.101192	1.970853	1.6	3.0	134	23.7	217±34	0.26±0.06	0.94±0.15	−0.18±0.17	0.03±0.20	−0.89±0.38	0.00±1.62
187.067261	2.080253	1.9	3.2	135	19.3	198±32	0.25±0.06	0.97±0.16	0.03±0.34	0.20±0.20	−0.02±0.21	−0.71±0.35
187.488180	2.142182	1.6	3.1	136	14.8	161±29	0.46±0.09	1.20±0.22	0.28±0.27	0.07±0.27	−0.34±0.36	0.21±0.39
187.362608	2.228418	1.2	2.9	137	33.6	195±30	0.45±0.08	1.10±0.17	−0.01±0.15	−0.57±0.27	−0.35±0.39	0.04±1.09

The table is ordered by source identifier ML_ID; RA and DEC are in decimal degrees; RADEC_ERR and POSERR are the 1σ position errors returned by EMLDETECT and the final error calculation (Equation 2.1), respectively; DET_ML – Detection Minimum Likelihood value; SCTS - Source counts; FLUX is the X-ray flux ($0.2-12$ keV; observed) determined by EMLDETECT; RATE – Counts s^{-1}; HR1, HR2, HR3, and HR4 are the averaged EMOS1 and EMOS2 hardness ratios as defined in the text (Section 2.3.2).

the calculation of RADEC_ERR by EMLDETECT, since it is determined from the standard deviation of the distribution of counts within the detection cell.

The above discussion of the errors introduced by the task EMOSAIC assumes that the WCS are accurate for each input image, i.e., that the celestial coordinates recorded for the reference pixel are correct. However, this may not be the case as there is a known pointing error for each *XMM-Newton* observation. The pointing error for an individual observation is $\simeq 1.8$ arc seconds (r.m.s.[3]). As mosaicing is done on an image by image basis and one single WCS system is used for the output image, this means only two WCS are being compared at any one time. Therefore, the additional error introduced by the pointing error when using EMOSAIC, MOSAIC_ERR, will be a total of $1.8\sqrt{2}$ arc seconds. Therefore, the total error on the X-ray source position (POSERR) is,

$$\mathrm{POSERR}^2 = \mathrm{RADEC\_ERR}^2 + \mathrm{SYSERR}^2 + \mathrm{MOSAIC\_ERR}^2 \qquad [\text{arc seconds}^2] \quad (2.1)$$

where $\mathrm{SYSERR}^2 + \mathrm{MOSAIC\_ERR}^2 = 6.6025$ arc seconds^2.

2.3.4 Product Extraction

Using the complete source list, spectral information was extracted for each source in each observation. To begin with, a cut in the number of sources was made. Only sources with a total number of counts greater than 1000 had spectra extracted.

For products to be extracted, source and background regions had to be defined for all sources in all observations in each camera. This was achieved by using the SAS task REGION. This task was run in "batch" mode, creating a source region and a local background region pair, centred on the source coordinates, for each entry in the source list. The source regions are circular and initially set to have a radius of 35 arc seconds.

[3]Taken from the *XMM-Newton* calibration document CAL-SOC-CAL-TN-0018.pdf

The "shrinkconfused" parameter was set to "true", allowing the radii of overlapping source regions to be shrunk until they no longer did so.

The background regions were created from annuli centred on the source coordinates. The inner radius of the annulus was equal to 1 arc minute and the outer radius was equal to three times the inner radius. The inner radius was chosen based on the CUTRAD value determined by EMLDETECT. The CUTRAD parameter is the radius, in pixels, in which a PSF model fit is made to a source and is set such that it encompasses 68% of the calibration PSF. The CUTRAD value for all sources was 6.2 pixels, which equates to ~ 25 arc seconds. Thus, an inner radius of 1 arc minute will prevent any contamination from the source itself. It is likely, if not certain, that any background annulus will contain other sources. Therefore, a 1 arc minute radius exclusion region was centred on every source during the creation of the background annuli, so there was no contamination from source events.

Up to now, all information on source positions, parameters and extraction regions have been given in sky coordinates, which have been determined from the mosaiced images. However, the actual extraction of the source products were required to be performed on an individual basis for each camera for all of the observations. It was decided to convert the extraction regions into detector coordinates for use on individual observations in each camera. The reason for this decision was heavily influenced by the presence of light from 3C 273 that had been scattered by the RGS gratings onto the EMOS detectors. As the RGS gratings are aligned in a certain orientation relative to the EMOS detectors, light scattered by the gratings will fall on the same region in detector coordinates, irrespective of the sky coordinates of the observation. This region was defined for both the EMOS1 and EMOS2 detectors for later use during product extraction.

Extraction regions for each exposure in detector coordinates and exclusion regions to account for the scattered light from the RGS gratings allowed the data products to be extracted. Source and background spectra were extracted with EVSELECT using the criteria set out in the remainder of this paragraph. If the centre of the source extraction region was more than 0.5 times its radius from the edge of the FOV or from the inner edge of the detector, products were extracted for that particular source. For the sources that were to have spectra extracted, the location and extent of their extraction regions were compared to the determined RGS exclusion region for that detector. If no part of a source region, or its corresponding background region, fell within the exclusion region, no filtering of those regions took place. Also, in the case where the source region fell within the exclusion region, no filtering of either source or background region took place. If, however, only the background region overlapped the exclusion region, that part of the background region was excluded during extraction. It should be noted that for observations after REV 961, CCD6 of the EMOS1 detector was no longer operational. Thus, for sources that were mapped onto CCD6 for observations later than REV 961, no source spectra were created for those observations. During the creation of the source spectra, associated response matrix files (RMF) and ancillary response files (ARF) were created using RMFGEN and ARFGEN, respectively.

Spectra

After extracting source and background spectra for the sources in each exposure that met the selection criteria previously given, time averaged spectra were created for each source. These spectra were created using the FTOOL *mathpha*, which was used to sum the source spectra for a given source. This step was repeated for the background spectra. When using *mathpha*, Gaussian errors ($\sqrt{N}$, where N is the number of counts) were used and these errors were propagated through each pass. The associated RMF and ARF files were averaged using the FTOOLs *addrmf* and *addarf*, respectively, creating equivalent files that could be used with the final background subtracted source spectra. Each RMF and ARF file was weighted according to its exposure time. The weighting factor, W_i, is defined as

$$\mathrm{W}_i = \frac{T_i}{\sum_{i=1}^{n} T_i} \tag{2.2}$$

where T_i is the GTI exposure time for the i^{th} spectrum and n is the number of spectra for the source in question.

The summed background spectra were then scaled according to the ratio of the sum of the source region areas to the sum of the background region areas, A_{R}, which is given as

$$A_{\mathrm{R}} = \frac{\sum_{i=1}^{n} A_{\mathrm{src},i}}{\sum_{i=1}^{n} A_{\mathrm{bgd},i}} \tag{2.3}$$

where n is the number of exposures used to create the source and background spectra, A_{src} and A_{bgd} are the area in pixels of the source and background regions, respectively, calculated by the task BACKSCALE.

At this point, two versions of the final background subtracted source spectra were created. The first version was created by subtracting the area scaled, summed background spectra from the summed source spectra using *mathpha* for each source. These spectra were then binned using the FTOOL *grppha* such that each bin contained a minimum of 20 counts.

The second version of the final background subtracted source spectra was created by simply binning each of the summed source spectra into a minimum of 20 counts per bin using *grppha*. This allowed XSPEC to automatically subtract the summed background spectra during analysis. XSPEC does this by reading the binning information of the source spectrum and summing the appropriate channels in the source spectrum together. XSPEC then applies the same binning to the background spectrum and subtracts it from the source spectrum to create the background corrected source spectrum for analysis.

Using source 3 (ML_ID 3) as an example, the difference between the two types of final background subtracted source spectra are shown in Figure 2.4. Immediately, it is obvious that the XSPEC background corrected (*xbc*) spectrum covers all of the $0.3 - 10$ keV band, whereas the *mathpha* background corrected (*mbc*) spectrum stops at $\sim$ 8 keV. However, the data appear noisy in the *xbc* spectrum beyond ~ 5 keV. Inspection of the spectra in Figure 2.4, below an energy of 2 keV, suggests that the two methods are fairly similar for these energies, although there appears to be a discrepancy around the EMOS background Al K (1.5 keV) and Si K (1.7 keV) fluorescence line features.

The background spectra for the *xbc* and *mbc* methods are the same spectrum and it is shown in Figure 2.5. The Al K line is prominent in the background spectra, with the Si K line also evident. Figure 2.5 also shows evidence of two more features around ~ 0.55 and ~ 0.62 keV that are not reported in the calibration documentation. However, these new features do not appear to affect either of the final data sets (Figure 2.6).

To quantitatively decide which method to follow, XSPEC (version 12.5.1; Arnaud, 1996) was used to perform a number of Galactic absorbed power-law fits, *tbabs*$\times$*po*, to different energy bands in the *xbc* and *mbc* spectra, respectively. In each case the EMOS1 and EMOS2 data were modelled concurrently with the power-law photon-index, Γ (Section 1.2.2), tied between the two cameras. The FTOOL *nh* was used to calculate the Galactic absorbing column, N_{H}. As *nh* uses the Kalberla et al. (2005) HI map, which has a resolution of ~ 0.5 degrees, to calculate N_{H}, the same value of N_{H} (1.64×10^{20} cm^{-2}) will be used for every source that is modelled within XSPEC.

The first model fit was to the hard-energy band ($2 - 10$ keV) of the *xbc* and *mbc* spectra, as is standard practice for AGN. The resulting photon-indices and fit statistics (χ^2 statistic for a given number of degrees of freedom; d.o.f.) for the *xbc* and *mbc* model fits were $\Gamma = 2.44^{+0.36}_{-0.33}$, χ^2/d.o.f. $= 109.0/102$ and $\Gamma = 2.29^{+0.35}_{-0.33}$, χ^2/d.o.f. $= 32.1/35$,

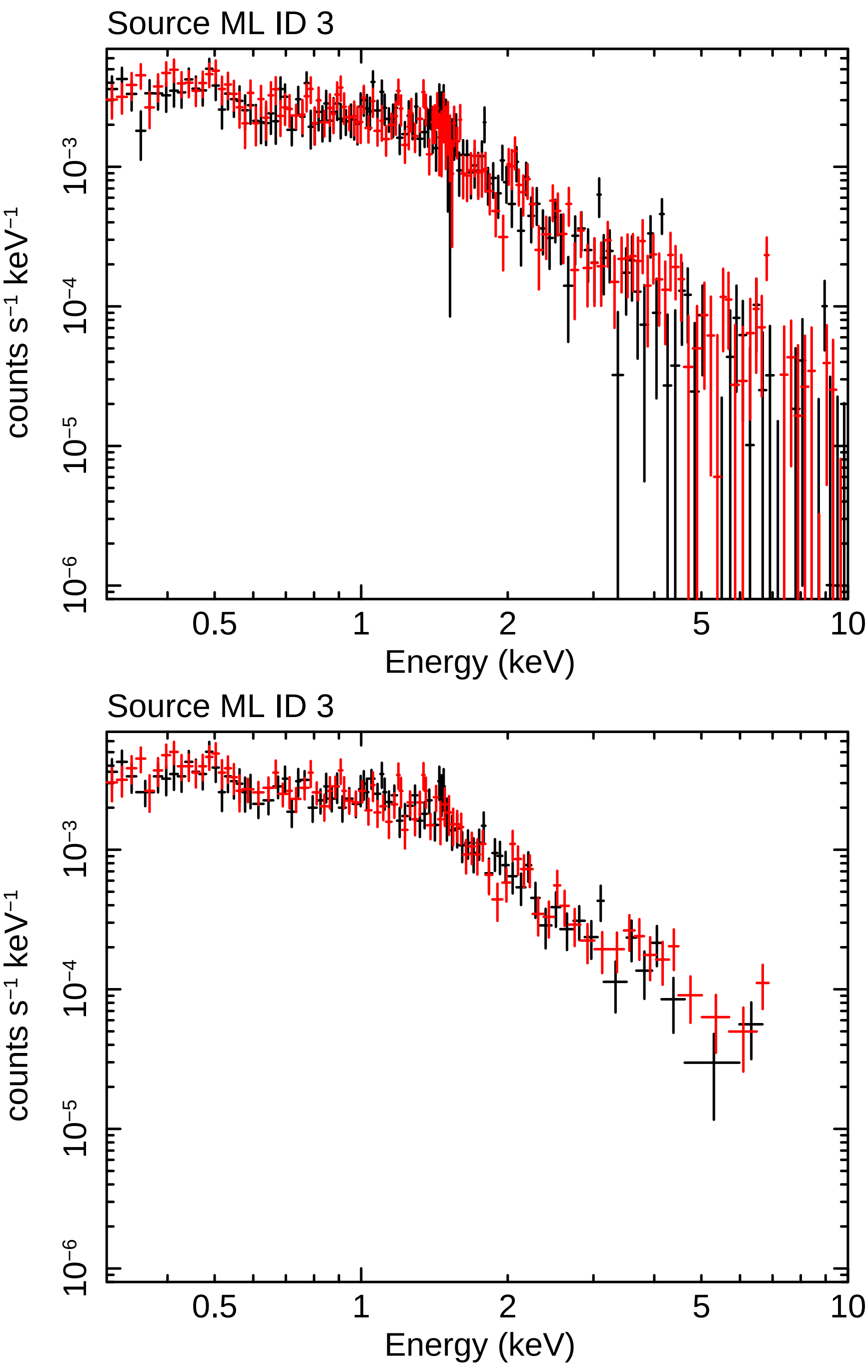

FIGURE 2.4: Background subtracted source spectra ($0.3-10$ keV; observed) of source 3 (ML_ID 3) produced during data reduction. Black and red points represent EMOS1 and EMOS2 data, respectively. Top: Background subtracted by XSPEC (*xbc*). Bottom: background subtracted using *mathpha* (*mbc*).

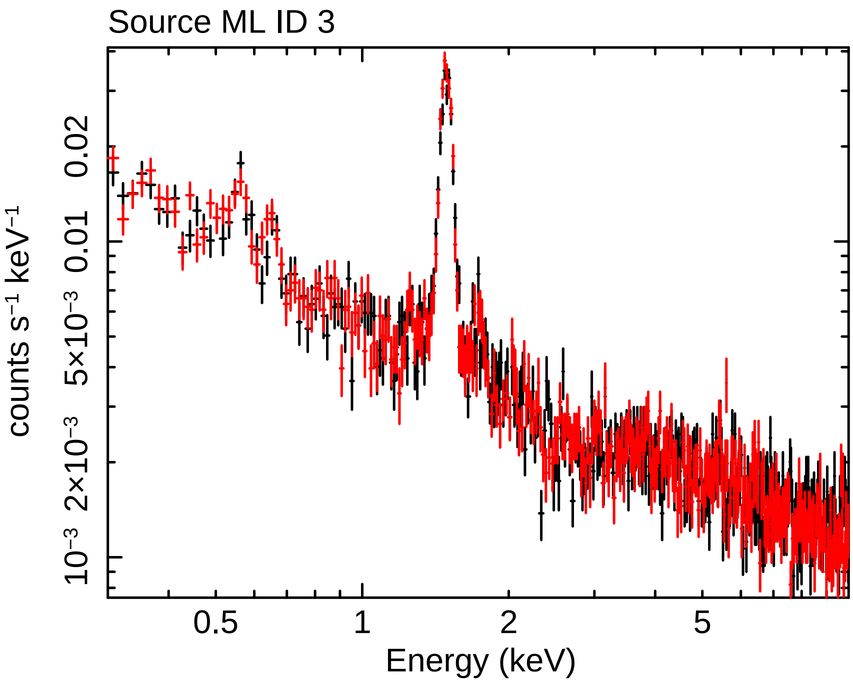

FIGURE 2.5: Background spectra ($0.3-10$ keV; observed) for source 3 (ML_ID 3) created during data reduction. Black and red points represent EMOS1 and EMOS2 data, respectively. The data have been re-binned within XSPEC for viewing purposes only, with a minimum significance of 5σ and a maximum number of 5 bins in each datum point.

respectively. The photon-indices agree within errors but the *xbc* data sets have three times the number of data bins, allowing for better parameterisation of Γ. Calculating the "goodness" of the fit, returns 48% and 26% for the *xbc* and *mbc* data sets, respectively. These results would suggest that the *xbc* method is the one to follow, although the $2-10$ keV model fit includes the noisy points of the *xbc* spectrum ($\gtrsim 5$ keV) and also includes the data-less section of the *mbc* spectrum ($\gtrsim 8$ keV). Thus, the model fits were repeated for only $2-5$ keV. The photon-indices and fit statistics were $\Gamma = 2.45^{+0.41}_{-0.38}$, $\chi^2/\text{d.o.f.} = 61.9/61$ and $\Gamma = 2.31^{+0.43}_{-0.41}$, $\chi^2/\text{d.o.f.} = 22.4/29$, for the *xbc* and *mbc* data sets, respectively. Again the *xbc* data sets have three times the number of data bins and the photon-indices match within errors between the two methods and between the two energy band fits. The latter point suggest that the $2-10$ keV model fit was dominated by

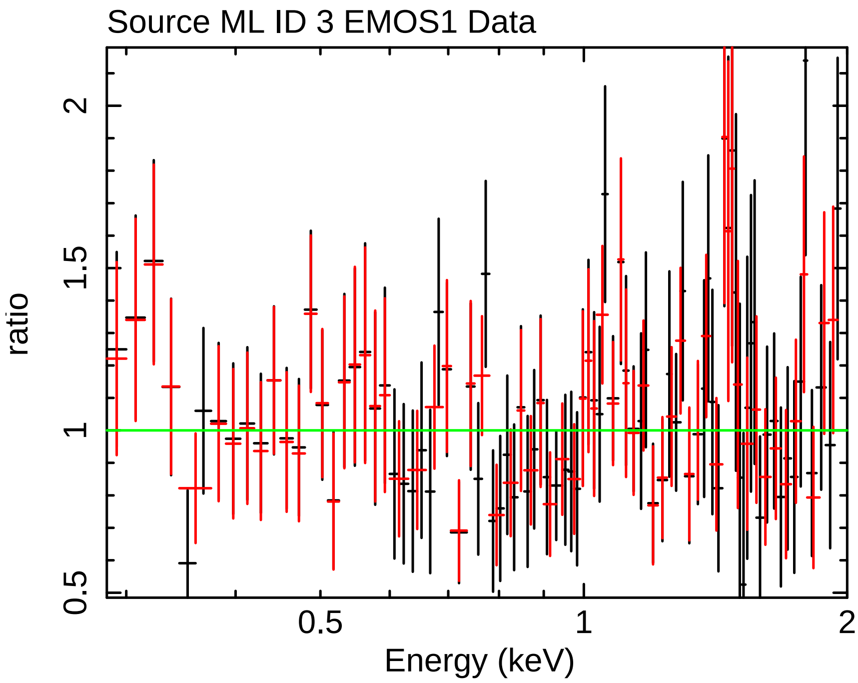

FIGURE 2.6: Ratio plot (data point to model line) of a Galactic absorbed power-law model fit, *tbabs*×*po*, to the EMOS1 data sets ($0.3-2$ keV; observed) of source 3 (ML_ID 3) created by the *xbc* and *mbc* methods. Black and red data points are the *xbc* and *mbc* methods, respectively.

$2-5$ keV data points as one would expect. Once more, the model fits suggest that the *xbc* method is the one to follow.

The final item to look at before making a decision are the energies below 2 keV. As stated earlier, below 2 keV, with the exception of the energies that enclose the Al K and Si K fluorescence lines, the data sets appear virtually identical (Figure 2.4). To see this visually in more detail, the EMOS1 data sets from the two methods were fit concurrently with a Galactic absorbed power-law model. This was not done to gain any fit parameters nor fit statistics but rather for illustrative purposes. The ratio (data/model) plot of this fit is shown in Figure 2.6 and it appears that the two data sets match fairly well. In conclusion, the *xbc* method will be used for all further analysis.

2.4 Cross-Correlation

As with any survey, the aim is to determine the nature of the sources that have been detected. For the work presented here, this began by cross-correlating the X-ray source positions with source positions in other survey catalogues. This task was performed before the analysis of the X-ray spectra, so that this information could assist with the X-ray analysis. The databases and catalogues searched during the cross-correlation were NED[4], SIMBAD[5] and the Sloan Digital Sky Survey Data Release 6 (SDSS DR6; Adelman-McCarthy et al., 2008).

Although rather large, a value of 10 arc seconds was chosen as the standard search radius during cross-correlation. This value was chosen based on the POSERR values for the X-ray sources. The minimum and maximum values of POSERR are 2.57 and 4.01 arc seconds, respectively. The mean POSERR value, $\mu_{\rm POSERR}$, and the standard deviation of POSERR, $\sigma_{\rm POSERR}$, were found to be 2.85 and 0.24 arc seconds, respectively. It is standard practice to use a search radius of 3 times the positional error. Thus, using $\mu_{\rm POSERR}$ as the standard positional error, calculating $3 \times \mu_{\rm POSERR}$ results in a value of 8.55 arc seconds. Therefore, a choice of 10 arc seconds radius search around the X-ray source positions is conservative but appropriate.

2.4.1 SDSS Results and Calculation of $P_{\rm id}$

Of the 136 X-ray sources detected in the deep-look of the *XMM-Newton* FOV around 3C 273, 99 had at least one SDSS optical candidate counterpart within 10 arc seconds selected from the source positions in the SDSS DR6 catalogue. Clearly, there is no guarantee that the SDSS optical source returned is a true counterpart to the X-ray source.

[4]http://nedwww.ipac.caltech.edu/
[5]http://simbad.u-strasbg.fr/simbad/

Therefore, in an attempt to identify the most likely counterpart to an X-ray source, a probability, $P_{\rm id}$, was calculated and assigned to each SDSS candidate source, describing the likelihood of it being a unique counterpart to the X-ray source. The calculation of $P_{\rm id}$ is taken from the reliability method presented by Rutledge et al. (2000) and was performed in conjunction with Dr. Rebecca Smith. A description of the probability analysis follows.

In addition to the 10 arc second radius searches around the X-ray source positions, 10 arc second radius background searches within the SDSS DR6 were carried out. A total of 727 background searches outside of, but still close to, the *XMM-Newton* FOV around 3C 273 were performed. This was done to sample the local optical background to create a background list of sources for comparison with the candidate optical counterparts.

For each source returned in each 10 arc second radius search (for all X-ray source position and background searches), a value, r, describing the offset of the optical source from the centre of the search area is calculated. Using this value of r and assuming a Gaussian distribution of true positional coincidence, along with the assumption that the likely optical counterpart is bright, the likelihood ratio for the ith source, LR_i, is given as

$$LR_i = \frac{e^{(-r_i^2\,/\,2\sigma_i^2)}}{\sigma_i\,\frac{N(<m_i)}{F_{\rm bgd}}} \tag{2.4}$$

where m_i is the apparent magnitude of the ith optical source, $N(<m_i)$ is the total number of background sources with an apparent magnitude, m, less than m_i, $F_{\rm bgd}$ is the number of background fields used and σ_i is the combined positional error of the X-ray source and the ith optical source. The value of σ_i is dominated by the X-ray positional errors and was set to $\mu_{POSERR} = 2.85$ arc seconds. This is similar to the determination of σ_i by Rutledge et al. (2000). For this analysis, the SDSS r-band magnitude was used for m and m_i.

Although the likelihood ratio for each optical counterpart has now been calculated, giving an indication of the most likely optical counterpart (the highest value of LR for each X-ray source), the probability of a unique match has not yet been calculated, since a reliability value must first be determined. The reliability value, $R(LR_i)$, is determined for each optical source and describes the binomial probability that a given optical and X-ray source pair with a specific value of LR are truly associated. However, this does not incorporate other optical sources that have been associated with that particular X-ray source. The value of $R(LR_i)$ is given as

$$R(LR_i) = \frac{\frac{N_{\rm src}}{F_{\rm src}} - \frac{N_{\rm bgd}}{F_{\rm bgd}}}{\frac{N_{\rm src}}{F_{\rm src}}} \tag{2.5}$$

where $F_{\rm src}$ is the number of source fields used (99), $N_{\rm src}$ and $N_{\rm bgd}$ are the number of candidate (true) and background (false) sources, respectively, that have a value of LR that lies between $10^{log(LR_i)-0.6}$ and $10^{log(LR_i)+0.6}$. This range of LR was chosen such that the number of objects used in Equation 2.5 is sufficient enough for $R(LR_i)$ to converge according to the central limit theorem.

Having calculated $R(LR_i)$, the probability, $P_{\rm id}$, that a given optical source is a unique match to the X-ray source is calculated. For each X-ray source there are a total of M optical sources returned from the 10 arc second radius search. This means that there are $M+1$ possible outcomes, which includes the possibility that none of the M candidate counterparts are a unique counterpart. As $R(LR_i)$ is a binomial probability, the probability that none of the optical sources are a unique match to the X-ray source, $P_{\rm no-id}$, is calculated as

$$P_{\rm no-id} = \frac{\prod_{j=1}^{M}(1-R_j)}{S} \tag{2.6}$$

where S is the normalisation, specific to each X-ray source. This then gives the probability that the X-ray source does have an optical counterpart, $1 - P_{\rm no-id}$. Thus, for each X-ray source, the probability, $P_{\rm id}$, that the ith optical source is uniquely associated with it is given as

$$P_{\mathrm{id},i} = \left[\frac{R_i}{1-R_i} \prod_{j=1}^{M} (1-R_j) \right] / S \qquad (j \neq i) \tag{2.7}$$

where the normalisation factor S is written as

$$S = \sum_{i=1}^{M} \left[\frac{R_i}{1-R_i} \prod_{j=1 \neq i}^{M} (1-R_j) \right] + \prod_{j=1}^{M} (1-R_j) \tag{2.8}$$

such that the following expression is satisfied

$$P_{\mathrm{no-id}} + \sum_{i=1}^{M} P_{\mathrm{id},i} = 1 \tag{2.9}$$

A candidate optical counterpart was assumed to be a truly unique association with an X-ray source if its calculated value of P_{id} was $\geqslant 0.95$. A number of X-ray sources (19) had a $P_{\mathrm{no-id}}$ value that was greater than the P_{id} values calculated for the candidate counterparts for that X-ray source. These X-ray sources were consequently removed from any further optical analysis. There were 68 X-ray sources that were deemed to have an unique optical counterpart as determined by the calculated P_{id} values. The 68 sources and their P_{id} values are listed in Table 2.3. Also given in Table 2.3 are the five SDSS magnitudes for the optical counterpart; the offset (in arc seconds) between the X-ray position and the optical source position; the SDSS Type ('T'), 'e' designates an extended source and 'p' designates a point source; the SDSS spectroscopic redshift, z_{SDSS}, where available; the X-ray flux to optical flux ratio, $\log_{10}(f_{\mathrm{X}}/f_{\mathrm{opt}})$; and finally the SDSS ObjID number.

The X-ray flux to optical flux ratio is calculated using the r-band flux, f_r, as the optical flux, f_{opt}. The ratio is calculated using the following equation, taken from Civano et al. (2005),

$$\log_{10}\left(\frac{f_{\mathrm{X}}}{f_r}\right) = \log_{10}(f_{\mathrm{X}}) + 5.5 + \frac{\mathrm{r}}{2.5} \tag{2.10}$$

where r is the SDSS r-band magnitude and f_X is the observed broad-band ($0.2 - 12$ keV) X-ray flux calculated by EMLDETECT.

Table 2.3: SDSS Cross-Correlation Results for X-ray Sources with an Optical Source Match with $P_{\rm id} \geqslant 95\%$

ML ID	Offset [arcsec]	$P_{\rm id}$	u [mag]	g [mag]	r [mag]	i [mag]	z [mag]	T	$z_{\rm photo}$	$z_{\rm SDSS}$	$\log_{10}(f_{\rm X}/f_{\rm opt})$	SDSS ObjID
1	1.6	1.000	17.28±0.02	14.69±0.02	13.50±0.01	13.52±0.01	12.15±0.02	p			−1.966±0.008	587726014535172228
2	1.0	1.000	14.57±0.02	13.10±0.00	13.77±0.00	13.29±0.00	12.23±0.01	p			−1.854±0.007	587726014535303221
3	0.7	0.998	18.63±0.03	18.71±0.02	18.78±0.02	18.55±0.02	18.41±0.03	p	$1.98^{+0.07}_{-0.12}$	1.922	−0.218±0.012	587726014535303212
4	1.0	0.998	22.49±0.41	22.01±0.09	20.98±0.05	20.46±0.05	19.83±0.10	e	$0.38^{+0.68}_{-0.03}$		0.552±0.023	587726014535303647
5	1.1	0.998	20.35±0.07	19.66±0.03	19.18±0.02	18.90±0.02	18.58±0.04	e	$0.28^{+0.38}_{-0.03}$		−0.046±0.015	587726014535303340
6	1.0	0.998	20.49±0.07	20.06±0.02	20.01±0.02	19.74±0.03	19.82±0.12	e	$0.23^{+0.02}_{-0.02}$		0.195±0.017	587726032251846784
8	1.2	1.000	14.49±0.02	12.96±0.00	13.05±0.00	13.19±0.00	12.11±0.02	p			−2.855±0.023	587726014535172176
9	0.9	0.998	20.45±0.08	20.29±0.03	19.99±0.03	19.91±0.03	19.89±0.11	p	$1.38^{+0.07}_{-0.27}$		−0.147±0.023	587726014535237854
10	2.0	0.987	21.15±0.11	21.06±0.04	21.18±0.06	20.75±0.06	20.57±0.23	p	$1.82^{+0.07}_{-0.07}$		0.255±0.033	587726032251781374
11	0.6	0.998	19.45±0.04	19.03±0.02	19.00±0.02	18.87±0.02	18.70±0.04	p	$2.23^{+0.02}_{-0.08}$	0.770	−0.456±0.020	587726014535303207
12	3.8	0.993	24.23±1.45	24.00±0.47	21.75±0.09	19.83±0.03	18.68±0.05	p	$5.38^{+0.03}_{-0.03}$		0.879±0.041	587726031714910413
13	1.1	0.998	22.17±0.26	22.38±0.12	22.06±0.12	21.74±0.14	21.03±0.35	p	$0.28^{+0.12}_{-0.08}$		0.511±0.054	587726032251781511
14	0.8	0.998	21.94±0.24	21.48±0.06	21.09±0.05	20.86±0.07	20.29±0.17	p	$0.33^{+0.08}_{-0.08}$		0.093±0.037	587726032251715713
15	2.8	0.997	21.03±0.12	20.15±0.03	19.20±0.02	18.70±0.02	18.34±0.03	e	$0.23^{+0.47}_{-0.02}$		−0.845±0.035	587726014535172301
17	2.0	0.986	23.27±0.90	22.92±0.20	21.69±0.09	21.30±0.10	20.94±0.27	p			0.252±0.045	587726014535303689
18	1.0	0.998	22.49±0.41	21.61±0.06	21.39±0.07	20.93±0.07	21.11±0.32	e	$1.68^{+0.02}_{-0.03}$		0.443±0.034	587726014535172483
19	1.4	0.998	21.75±0.18	21.60±0.06	21.46±0.07	21.25±0.10	22.03±0.73	p	$1.52^{+0.58}_{-0.12}$		0.273±0.043	587726032251781357
20	1.1	0.998	21.34±0.16	20.89±0.04	20.80±0.05	20.86±0.07	20.38±0.16	p	$2.48^{+0.17}_{-0.27}$		−0.165±0.034	587726014535237950
21	1.0	0.998	22.77±0.44	22.47±0.13	22.34±0.15	21.58±0.13	21.21±0.40	e	$1.02^{+0.33}_{-0.27}$		0.522±0.068	587726032251781620
22	2.9	0.996	23.95±1.01	22.29±0.12	21.03±0.05	20.31±0.04	19.56±0.10	e	$0.53^{+0.38}_{-0.08}$		−0.008±0.036	587726032251781493
26	0.4	0.998	22.69±0.49	22.90±0.20	22.66±0.21	21.91±0.17	22.23±0.66	e	$1.68^{+0.02}_{-0.03}$		0.688±0.088	587726014535303743
27	0.1	0.998	22.07±0.29	23.56±0.33	22.44±0.18	22.55±0.29	21.72±0.51	p	$1.98^{+0.12}_{-0.18}$		0.392±0.081	587726014535303872
28	3.8	0.995	24.25±1.39	23.42±0.29	22.46±0.19	22.30±0.24	22.33±0.70	e			0.367±0.083	587726014535238432
29	0.5	0.998	22.12±1.06	21.95±0.09	22.05±0.12	21.93±0.17	21.32±0.44	p	$2.33^{+0.32}_{-0.43}$		0.071±0.065	587726032251781560
30	1.4	0.998	23.29±0.79	21.91±0.08	21.64±0.09	22.19±0.22	21.65±0.48	p	$2.92^{+0.23}_{-0.17}$		−0.003±0.053	587726014535172762
31	0.8	0.998	23.06±0.66	22.96±0.19	21.31±0.06	20.34±0.04	19.85±0.10	e	$0.68^{+0.12}_{-0.08}$		−0.066±0.043	587726014535172694
33	1.2	0.998	22.59±0.37	22.22±0.11	22.23±0.14	21.56±0.19	21.18±0.37	p	$1.88^{+0.07}_{-0.32}$		0.336±0.070	587726032251716064

Table 2.3: SDSS Cross-Correlation Results for X-ray Sources with an Optical Source Match with $P_{\rm id} \geqslant 95\%$ (*Cont.*)

ML ID	Offset [arcsec]	$P_{\rm id}$	u [mag]	g [mag]	r [mag]	i [mag]	z [mag]	T	$z_{\rm photo}$	$z_{\rm SDSS}$	$\log_{10}(f_{\rm X}/f_{\rm opt})$	SDSS ObjID
34	1.0	0.994	23.26±0.65	22.88±0.19	22.39±0.16	22.07±0.19	22.41±0.83	e	$0.03^{+1.48}_{-0.03}$		0.408±0.075	587726032251716151
37	1.4	0.998	23.97±1.05	22.98±0.21	22.05±0.12	21.33±0.10	21.26±0.42	e			0.231±0.072	587726032251781606
38	4.5	0.989	22.84±0.55	22.15±0.10	21.35±0.07	21.10±0.08	20.22±0.15	e	$0.38^{+0.98}_{-0.03}$		−0.124±0.052	587726014535303638
40	2.2	0.997	25.55±0.88	23.64±0.36	23.12±0.30	21.74±0.16	21.24±0.42	p			0.510±0.130	587726032251781963
41	0.9	0.998	25.60±1.02	23.16±0.24	22.12±0.13	21.04±0.08	20.38±0.16	e	$0.62^{+0.22}_{-0.03}$		0.163±0.066	587726014535303901
45	1.6	0.998	21.30±0.17	19.97±0.03	19.05±0.02	18.65±0.02	18.25±0.03	e	$0.17^{+0.08}_{-0.07}$		−1.176±0.052	587726014535303289
48	1.5	0.998	23.93±1.33	23.67±0.37	22.78±0.23	22.40±0.26	21.82±0.63	e			0.416±0.110	587726032251782048
49	2.0	0.995	24.89±1.44	23.27±0.24	22.55±0.20	21.61±0.14	21.50±0.43	e	$0.62^{+0.38}_{-0.07}$		0.207±0.099	587726014535172194
51	0.4	0.998	21.66±0.21	21.58±0.07	21.61±0.09	21.49±0.11	21.24±0.39	p			−0.117±0.065	587726031714910420
52	1.7	0.997	21.44±0.17	21.32±0.05	21.31±0.07	21.22±0.09	21.02±0.29	e	$1.52^{+0.03}_{-0.52}$		−0.336±0.069	587726014535237959
54	5.0	0.962	20.68±0.08	20.26±0.03	20.15±0.03	19.78±0.03	19.58±0.10	p			−2.405±8.126	587726032251781263
55	0.6	0.998	22.12±0.25	21.38±0.05	20.60±0.04	20.06±0.04	19.68±0.10	e	$0.23^{+0.78}_{-0.02}$		−0.504±0.053	587726032251715928
56	0.8	0.998	21.52±0.15	20.12±0.02	19.35±0.02	18.92±0.02	18.52±0.04	e	$0.12^{+0.08}_{-0.07}$		−1.187±0.055	587726032251715672
57	2.1	0.998	20.15±0.05	18.17±0.01	17.43±0.01	17.05±0.02	16.63±0.02	e		0.078	−1.683±0.048	587726032251715710
58	2.1	0.997	23.16±0.60	21.86±0.08	21.20±0.06	20.61±0.05	20.72±0.25	e	$0.17^{+0.08}_{-0.12}$		−0.423±0.060	587726032251715933
66	1.8	0.979	22.99±0.52	22.59±0.15	21.84±0.10	21.24±0.09	20.54±0.23	e	$0.38^{+0.98}_{-0.03}$		−0.094±0.078	587726032251781455
67	1.5	0.998	22.71±0.41	20.88±0.04	20.01±0.03	19.47±0.03	18.96±0.06	e	$0.12^{+0.08}_{-0.07}$		−1.032±0.066	587726032251715772
68	2.2	0.997	22.84±0.46	22.86±0.19	22.08±0.12	22.25±0.22	21.36±0.43	e	$0.33^{+0.27}_{-0.03}$		−0.017±0.078	587726032251716070
69	0.8	0.998	20.77±0.10	20.16±0.03	19.95±0.03	19.91±0.03	19.99±0.12	p			−0.992±0.072	587726014535237794
71	1.4	0.998	24.98±1.40	23.04±0.20	22.12±0.12	21.47±0.12	20.91±0.27	e	$0.17^{+1.02}_{-0.07}$		0.013±0.080	587726014535172585
72	2.1	0.997	20.54±0.07	19.12±0.02	18.51±0.01	18.12±0.02	17.81±0.02	e		0.158	−1.366±0.057	587726032251650141
73	1.6	0.998	22.90±0.56	19.89±0.02	18.46±0.01	17.33±0.02	16.70±0.02	p			−1.511±0.070	587726032251650170
74	2.2	0.981	23.09±0.68	22.34±0.10	21.82±0.10	21.21±0.09	21.40±0.44	e			0.241±0.083	587726014535172372
75	1.3	0.998	23.98±1.04	22.75±0.18	21.93±0.11	21.07±0.08	20.84±0.27	e	$0.62^{+0.32}_{-0.07}$		−0.056±0.072	587726032251650620
77	0.3	1.000	11.45±0.00	10.61±0.00	10.18±0.00	12.67±0.01	10.48±0.00	e			−4.600±0.062	587726014535303171
78	2.5	0.997	21.75±0.26	21.76±0.07	21.54±0.08	21.22±0.09	21.27±0.36	e	$1.68^{+0.02}_{-0.03}$		−0.228±0.076	587726014535237938
79	1.5	0.998	22.82±0.55	22.79±0.17	21.95±0.11	21.23±0.10	20.73±0.23	e	$0.62^{+0.43}_{-0.07}$		−0.029±0.083	587726014535172654
83	1.1	0.998	22.71±0.49	21.86±0.08	21.83±0.10	22.30±0.23	21.39±0.39	p	$2.42^{+0.33}_{-0.17}$		0.108±0.066	587726014535369051

Table 2.3: SDSS Cross-Correlation Results for X-ray Sources with an Optical Source Match with $P_{\rm id} \geqslant 95\%$ (*Cont.*)

ML ID	Offset [arcsec]	$P_{\rm id}$	u [mag]	g [mag]	r [mag]	i [mag]	z [mag]	T	$z_{\rm photo}$	$z_{\rm SDSS}$	$\log_{10}(f_{\rm X}/f_{\rm opt})$	SDSS ObjID
84	2.0	0.998	21.83±0.41	21.98±0.08	22.01±0.12	21.86±0.16	21.13±0.32	e	$1.57^{+0.03}_{-0.02}$		−0.322±0.113	587726014535172417
85	3.7	0.996	24.68±1.21	23.03±0.22	21.91±0.10	20.86±0.07	20.38±0.19	e	$0.62^{+0.28}_{-0.03}$		−0.140±0.077	587726032251716347
87	2.0	0.998	22.83±0.92	21.44±0.06	19.84±0.03	19.27±0.02	18.78±0.04	e	$0.38^{+0.32}_{-0.03}$		−1.189±0.094	587726014535303397
93	2.5	0.997	26.01±0.76	24.07±0.46	22.73±0.22	21.62±0.13	21.14±0.33	e	$0.68^{+0.07}_{-0.08}$		0.025±0.124	587726014535173111
98	1.0	0.999	21.51±0.17	18.61±0.02	17.08±0.01	15.67±0.02	14.91±0.01	p			−2.081±0.086	587726014535368843
107	1.2	0.998	20.06±0.06	19.20±0.02	18.71±0.02	18.30±0.02	18.03±0.03	e		0.159	−1.515±0.073	587726014535172302
110	1.7	0.989	21.85±0.19	20.01±0.03	19.00±0.02	18.51±0.02	18.02±0.03	e	$0.17^{+0.03}_{-0.07}$		−1.486±0.087	587726032251650158
114	3.5	0.996	23.81±0.98	24.54±0.66	22.65±0.20	21.98±0.18	20.51±0.22	e			0.097±0.118	587726032251847329
121	1.0	0.998	23.57±0.97	22.57±0.15	21.34±0.07	20.63±0.05	19.99±0.12	e			−0.559±0.096	587726014535303656
128	2.1	0.998	26.09±0.95	21.67±0.06	20.20±0.03	18.50±0.02	17.52±0.02	p	$5.42^{+0.03}_{-0.02}$		−1.145±0.122	587726014535172354
131	2.3	0.997	23.25±0.93	22.22±0.10	21.24±0.06	20.60±0.06	20.02±0.12	e	$0.28^{+0.92}_{-0.03}$		−0.520±0.098	587726014535172728
133	2.9	0.998	24.63±1.21	23.83±0.41	22.56±0.19	21.86±0.16	21.40±0.44	p			−0.121±0.125	587726032251716277
136	2.9	0.998	23.24±0.65	22.41±0.13	22.62±0.20	22.76±0.35	22.50±0.86	p			0.215±0.119	587726032251847028

ML_ID – X-ray source identifier; Offset – distance in arc seconds between X-ray source position and SDSS optical source position; $P_{\rm id}$ – probability of the correct optical source match; T – SDSS morphology description, e and p represent extended and point-like sources, respectively; $z_{\rm photo}$ – photometric redshifts; $z_{\rm SDSS}$ – SDSS spectroscopic redshifts; $f_{\rm opt} = f_r$ (Equation 2.10); SDSS ObjID – SDSS identifier of optical source.

2.4.2 SIMBAD and NED Results

From the SIMBAD searches, 18 of the X-ray sources returned at least one possible candidate counterpart within 10 arc seconds. 15 of the 18 X-ray sources returned a single candidate counterpart, 2 of the sources (ML_IDs 5 and 77) produced two candidates and the source ML_ID 85 returned 4 candidates. In the case of ML_ID 5, the two candidate sources returned by SIMBAD are given as a single source within the NED database. It is unclear as to whether the four sources given for ML_ID 85 are all unique. The results of the SIMBAD searches are shown in Table 2.4.

The NED searches resulted in 86 X-ray sources having at least one candidate counterpart within 10 arc seconds. However, the majority of these X-ray sources only had SDSS sources as possible counterparts. Since the SDSS DR6 catalogue was searched separately as part of this work (Section 2.4.1), if an X-ray source only had SDSS candidate counterparts returned in the NED search results, the X-ray source was not recorded in Table 2.4. For these X-ray sources, if one of their candidate SDSS counterparts had a $P_{\rm id}$ value $\geqslant 0.95$, the SDSS cross-correlation results for the X-ray source will have been recorded in Table 2.3. However, if an X-ray source had candidate counterparts returned in the SIMBAD searches results, the X-ray source was recorded in Table 2.4 even if the NED results for that X-ray source were all SDSS sources. In addition, X-ray sources with NED results that returned an alternative identifier to the SDSS name or contained a non-SDSS source are displayed in Table 2.4. Henceforth, the term 'NED results' shall refer to these filtered NED results, as shown in Table 2.4. It should be noted that all the unique SDSS candidate counterparts listed in Table 2.3 that have a spectroscopic redshift, $z_{\rm SDSS}$, and hence classification, can be found in the NED results in Table 2.4.

All 18 X-ray sources found to have candidate counterparts from SIMBAD also have at least one candidate counterpart from NED. There were an additional 12 X-ray sources that returned candidate counterparts only from NED. Thus, there are 30 X-ray sources with candidate counterparts in either NED or SIMBAD. A total of 25 of these 30 X-ray sources have an SDSS candidate counterpart with an associated $P_{\rm id}$ value $\geqslant 0.95$ (calculated in Section 2.4.1) and can be found in Table 2.3. This means 43 of the 68 X-ray sources (listed in Table 2.3) that were deemed to have an unique SDSS candidate counterpart, i.e., $P_{\rm id} \geqslant 0.95$, have no other identifier associated with them within NED or SIMBAD.

As previously stated, Table 2.4 records the SIMBAD and NED results returned by the 10 arc second radius searches. For both NED and SIMBAD candidates, the candidate 'NAME', 'Offset' in arc seconds (distance between X-ray and candidate counterpart source positions), candidate source 'Type' and, where possible, a redshift for the candidate counterpart, 'z', are given. If a NED candidate counterpart had an associated SDSS source, the 'SDSS NAME' (SDSS identification number) and 'SDSS Type' were recorded. When more than one candidate counterpart is returned, all candidates are displayed. If a NED source matches the SIMBAD source, an 'M' is placed in the same row as the NED source under the 'Match' column heading. Finally, under the SDSS column group heading, the number of sources returned by the SDSS DR6 10 arc second radius search is given, along with whether a given SDSS source (returned by NED) is uniquely associated with the X-ray source, i.e., $P_{\rm id} \geqslant 0.95$. If a unique SDSS association was found, a 'T' is placed in the same row as the SDSS source under the $P_{\rm id} \geqslant 0.95$ column. If no unique SDSS association was found, an 'F' is placed in that column for that X-ray source.

Of the 30 X-ray sources listed in Table 2.4, 15 can be said to have definite classifications. These classifications are based on the SDSS $P_{\rm id} \geqslant 0.95$ matches and their associated non-SDSS identifiers. These 15 sources fall into the following categories:

3 quasi-stellar objects (QSOs), 8 galaxies (Gal), 2 stars (*), 1 absorption lines system (AbLs) and 1 possible star/extended source (!*; ML_ID 77). The redshift range of these sources is $0 < z < 1.921$. In addition, source ML_ID 62 returns only a single possible candidate that is only known as a radio source (Rs) and has no possible candidate counterparts from the SDSS search.

There are a further 7 X-ray sources that had an SDSS $P_{\rm id} \geqslant 0.95$ match but also had a separate candidate X-ray source within the 10 arc second search radius from NED or SIMBAD. It is likely that the candidate X-ray source from NED or SIMBAD is the same X-ray source detected here. Therefore, it is likely that the candidate X-ray source is associated with the SDSS source ($P_{\rm id} \geqslant 0.95$) matched with the X-ray source detected here. There are a total of 3 X-ray sources (ML_IDs 7, 64 and 90) that have no SDSS $P_{\rm id} \geqslant 0.95$ matches but do have a known X-ray source within the search results of NED or SIMBAD.

Finally, there are three sources (ML_IDs 6, 85 and 99) that cannot be grouped as easily as those sources previously discussed. Source ML_ID 99 does not have an SDSS $P_{\rm id} \geqslant 0.95$ match nor any candidate X-ray sources, although all the candidates from the searches are classed as galaxies. Sources ML_ID 6 and ML_ID 85 do have SDSS $P_{\rm id} \geqslant 0.95$ matches. However, in the case of source ML_ID 85, there are multiple sources returned by the SIMBAD search that are not matched with the NED source that has the $P_{\rm id} \geqslant 0.95$ match. Although, once again, all the sources returned are galaxies. Source ML_ID 6 as stated has a SDSS $P_{\rm id} \geqslant 0.95$ match but also has a possible QSO candidate. As QSOs are normally bright in X-rays, it is possible that the X-ray source detected here could be associated with the candidate QSO (which itself has an associated SDSS source) suggesting a possible incorrect $P_{\rm id}$ association calculation. However, before commenting on the true nature of source ML_ID 6, modelling of the X-ray spectra will be performed.

Table 2.4: SIMBAD and NED Search Results

	SIMBAD				NED							SDSS	
ML ID	NAME	Offset [arcsec]	Type	z	NAME	Offset [arcsec]	Type	z	SDSS NAME	SDSS Type	Match	# of Results	$P_{\rm id}$ $\geqslant 0.95$
						1.11	*		J122837.14+015723.1	p			
1	GSC 00282-00187	1.47	*M2			2.01	*		J122837.20+015720.4	p		2	T
					CXOMP J122837.1+015720	1.19	*				M		
2	GSC 00282-00477	1.33	*G9		XBS J122942.3+015525	1.10	*		J122942.45+015524.9	*	M	2	T
3	2QZ J122934.7+015657	0.65	QSO	1.910	2QZ J122934.7+015657	0.40	QSO	1.921	J122934.72+015658.0	QSO	M	2	T
						6.96	Gal		J122935.07+015650.6	e			
5	[MWD93] 122713.78+021037.1	1.47	Gal	0.155	2dFGRS TGN388Z113	1.45	Gal	0.158	J122947.30+015402.6	Gal	M^{α}	2	T
	2dFGRS TGN388Z113	1.97	Gal	0.158									
						4.24	Gal		J122946.85+015405.3	e			
						0.75			J122953.32+020811.9	e			T
6	QSO B1227+0224	7.44	QSO	0.570		6.41			J122953.66+020806.0	e		4	
					1E 1227+024	6.33	QSO	0.570	J122952.80+020808.3	e	M		
7					[POS96] J122902.75+01	3.17	Xs					1	F
						2.75			J122901.73+015237.8	e			
						1.60			J122828.48+015449.4	p			T
8					1WGA J1228.4+0154	1.45	Xs					3	
						5.71			J122828.72+015444.6	p			
9	2QZ J122915.1+015244	2.74	QSO	1.220	2QZ J122915.1+015244	0.40	QSO	1.227	J122915.14+015244.5	QSO	M	1	T
11	2QZ J122931.2+015247	0.62	QSO	0.770	2QZ J122931.2+015247	0.30	QSO	0.770	J122931.19+015248.0	QSO	M	1	T
						3.93			J122929.06+015131.5	p			T
12						5.18			J122928.62+015132.7	e		4	
					[POS96] J122929.31+015134.6	7.07	Xs						
						2.85			J122928.32+015128.2	e			
14	[CME2001] 3C 273 2	0.61	Xs			0.46			J122859.52+021050.6	p		4	T
					CXOMP J122859.5+021050	1.20	Xs				M		
15	2dFGRS TGN387Z046	2.73	Gal	0.232	2dFGRS TGN387Z046	2.52	Gal	0.232	J122830.95+015631.1	Gal	M	2	T
						6.65			J122830.64+015640.2	e			
20					CXOMP J122853.4+015648	0.55	Xs		J122853.46+015648.8	UvEs		2	T
28					CXOMP J122855.0+01555	2.96	Xs					1	
						1.07			J122855.34+015553.6	e			T
45					APMUKS(BJ) B122649.35+021004.7	1.30	Gal		J122922.80+015330.7	Gal		2	T
						6.89			J122923.02+015322.5	e			
						0.64			J122857.73+015340.1	e			T
52					CXOMP J122857.7+015338	1.51	Xs					2	
						4.13			J122858.07+015336.2	p			
54	RX J122949+02126	6.03	XS			4.78			J122949.56+021231.7	UvEs		2	T
						6.18			J122949.12+021232.1	p			

Table 2.4: SIMBAD and NED Search Results (*Cont.*)

	SIMBAD				NED							SDSS	
ML ID	NAME	Offset [arcsec]	Type	z	NAME	Offset [arcsec]	Type	z	SDSS NAME	SDSS Type	Match	# of Results	P_{id} $\geqslant 0.95$
56					APMUKS(BJ) B122608.47+022512.4	0.24	Gal		J122841.92+020836.8	Gal		1	T
57	2dFGRS TGN387Z032	2.06	AbLs	0.078	2dFGRS TGN387Z032	2.27	Gal	0.078	J122858.44+021127.1	Gal	M	1	T
62	MRC 1226+022	4.39	Rs		MRC 1226+022	1.74	Rs				M	0	
64	[CME2001] 3C 273 12	3.90	Xs		[CME2001] 3C 273 12	2.98 5.12	Xs		 J122917.47+020830.2	 e	M	2	F
67					APMUKS(BJ) B122608.96+022425.1	0.32	Gal		J122842.45+020749.7	Gal		1	T
69					CXOMP J122849.8+015541	0.62 0.42 3.29	Xs		 J122849.82+015541.6 J122850.22+015544.3	 p e		2	T
72	[MWD93] 122546.88+022548.5	2.87	Gal	0.158	[MWD93] 122546.88+022548.5	2.04	Gal	0.158	J122820.34+020913.8	Gal	M	2	T
77	BD+02 2547 [SPB96] 1716	0.17 6.66	*F5 UVs		BD +02 2547	0.25	!*		J122922.20+015840.0	e	M	2	T
85	[GRN94] J122904.47+021033.2 [PBF95] W1-2 [GRN94] E [GRN94] J122904.44+021024.1	3.79 5.15 5.23 5.33	Gal Gal Gal		MDS W01-02	3.23	Gal		J122904.53+021025.5	Gal		1	T
90					CXOMP J122857.2+015516	2.57	Xs					2	F
99					APMUKS(BJ) B122651.97+021300.4	0.83 4.43 8.57	Gal		J122925.38+015624.2 J122925.55+015629.3 J122925.56+015616.0	Gal Gal Gal		5	F
107	2dFGRS TGN387Z041	0.35	Gal	0.159	2dFGRS TGN387Z041	1.25	Gal	0.159	J122831.62+015906.7	Gal	M	1	T
110	2dFGRS TGN387Z049	1.68	Gal	0.159	2dFGRS TGN387Z049	1.59	Gal	0.159	J122823.91+021000.1	Gal	M	2	T

The SIMBAD search results are under the SIMBAD column group heading and the NED search results are under the NED column group heading. In the case of the NED searches, only the results for sources that had either a SIMBAD match, an alternative identifier to an SDSS source name or returned a non-SDSS source are shown. For both sets of results the 'NAME', 'Offset' (distance between X-ray and candidate counterpart source positions in arc seconds), 'Type' and, where possible, redshift, 'z', of the candidate counterpart are given. If a NED source also had an SDSS identifier, the SDSS identifier is given under the 'SDSS NAME' column along with the 'SDSS Type'. An 'M' in the 'Match' column indicates that the NED source in that row matches the SIMBAD source returned for that X-ray source. The number of SDSS DR6 candidate counterparts returned by the 10 arc second radius search for each X-ray source is shown in the column headed '# of Results' under the SDSS group heading. If an SDSS source in the NED results has a $P_{\mathrm{id}} \geqslant 0.95$, a 'T' is shown in the same row in the '$P_{\mathrm{id}} \geqslant 0.95$' column. If a listed X-ray source does not have an SDSS candidate counterpart with $P_{\mathrm{id}} \geqslant 0.95$ an 'F' is recorded in the '$P_{\mathrm{id}} \geqslant 0.95$' column instead. The acronyms used for the 'Type' are: * – star; QSO – quasi stellar object; Gal – galaxy; AbLs – Absorption line system; Rs – Radio source; Xs – X-ray source; UVs – Ultraviolet source; UvEs – Ultraviolet excess source; and !* – possible star/extended source. a – The NED results for 2dFGRS TGN388Z113 indicates that it is the same source as the two sources returned by the SIMBAD searches.

The same applies to all of the X-ray sources that have more than 1000 source counts. Only after analysis of the X-ray spectra can a possible classification be made.

2.4.3 Photometric Redshifts

The results of the probability analysis of the SDSS DR6 cross-correlation (Section 2.4.1) were also used by Dr. Smith to perform photometric redshift, $z_{\rm photo}$, calculations on the unique optical counterparts. The colour-redshift relationship (CZR) method, taken from work by Weinstein et al. (2004), was used to calculate the photometric redshifts. Training sets of objects (QSOs and galaxies separately) with spectroscopic redshifts were taken from the SDSS DR6 to create the CZR. This CZR was then tested on optical data from the Lockman Hole. The accuracy of this particular CZR was calculated to be $\sigma_{\rm rms} = 0.224$ and is given by

$$\sigma^2_{\rm rms} = \frac{\sum_{i=1}^{N}\left(\frac{z_{{\rm phot},i}-z_{{\rm spec},i}}{1+z_{{\rm spec},i}}\right)^2}{N} \tag{2.11}$$

where $z_{{\rm phot},i}$ and $z_{{\rm spec},i}$ are the photometric and spectroscopic redshifts of the ith source, respectively, and N is the number of sources used to create the CZR. Within the work carried out by Dr. Smith, the photometric redshift of an optical source was only calculated if its $P_{\rm id}$ was $\geqslant 0.95$ and the probability of the photometric redshift being correct ($P_{\rm phot}$; see Weinstein et al., 2004, for more details) was $\geqslant 0.8$. In addition, sources with $\log_{10}(f_{\rm X}/f_{\rm opt}) \leqslant -1.5$ were not included in the calculation of $z_{\rm photo}$, since they are likely to be stars. The results for the 46 sources that matched the photometric redshift criteria are listed under the '$z_{\rm photo}$' column in Table 2.3.

2.5 Spectral Analysis

As described in Section 2.3.4, only sources with a total number of counts $\geqslant 1000$ had spectra extracted. There were a total of 17 sources that met this minimum count number

(ML_IDs 1–14, 16, 17 and 20). These sources, along with their exposure times, are listed in Table 2.5. The exposure times are not always the same due to whether the source spectrum was extracted for a particular exposure in the deep-look (Section 2.3.4). The extracted EMOS1 (black) and EMOS2 (red) spectra, as described in Section 2.3.4, for each of the 17 sources are shown in Figures 2.7, 2.8 and 2.9.

All spectral analysis was performed with XSPEC, version 12.5.1, with Wilms abundances set (Wilms et al., 2000). As stated in Section 2.3.4, a single Galactic absorbing column value, $N_{\rm H} = 1.64 \times 10^{20}$ cm^{-2}, was used for each source. The model component used to simulate Galactic absorption was *tbabs*. Analysis of the background-subtracted spectra was performed on a source by source basis. In the instances where a spectroscopic redshift was available, this was incorporated into the model fits, where appropriate. In some circumstances, it was required to ignore the energy range where the Al K fluorescence line feature, caused by the EMOS detector background, was present ($1.45 - 1.55$ keV) to assist with modelling. This is noted in Table 2.5.

Although the 17 sources modelled in this chapter are the brightest in the FOV around 3C273, it can be seen from Figures 2.7, 2.8 and 2.9 that the source spectra are noisy in places. This limited the complexity of the models used during spectral fitting for some of the targets. In some cases, the best fit model over-fits the data, which is most likely a result of over-estimation of the errors on the data.

For targets with a known classification, e.g., source ML_ID 1, the X-ray data was modelled with that classification in mind. In the instances where no classification was already known, modelling started with a Galactic absorbed power-law fit, *tbabs*$\times$*po*, to the hard-band ($2 - 10$ keV). Obvious features were modelled accordingly during the hard-band fit, e.g., emission lines were fitted using a Gaussian line component if required. This hard-band model was then extended down to 0.3 keV and the data (broad-band;

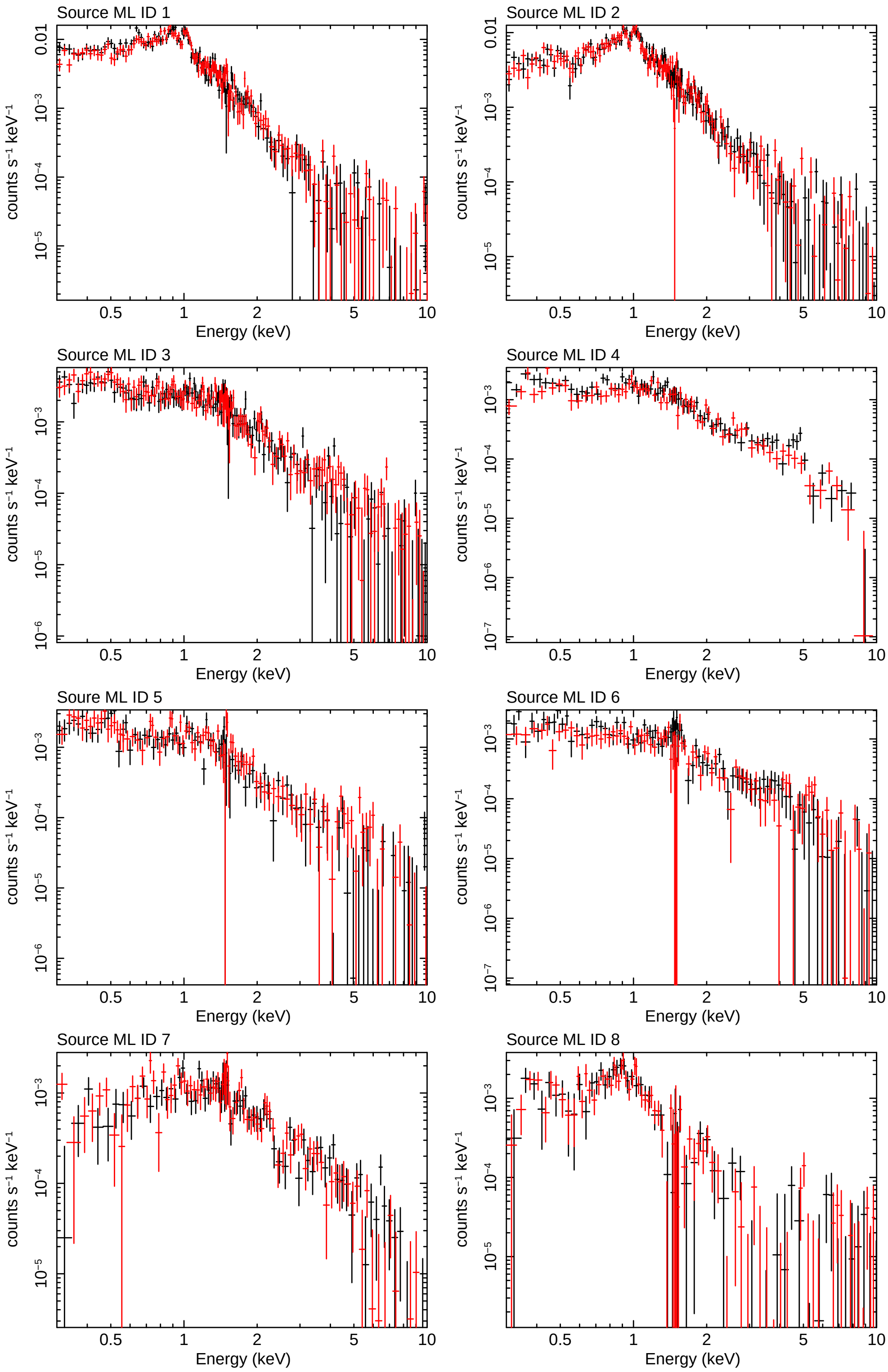

FIGURE 2.7: Spectra of the serendipitous sources within the *XMM-Newton* FOV around 3C 273 with $\geqslant 1000$ counts as detected by EMLDETECT. The source ML_ID number is given at the top of each spectrum. The black and red data points represent the EMOS 1 and EMOS 2 data, respectively.

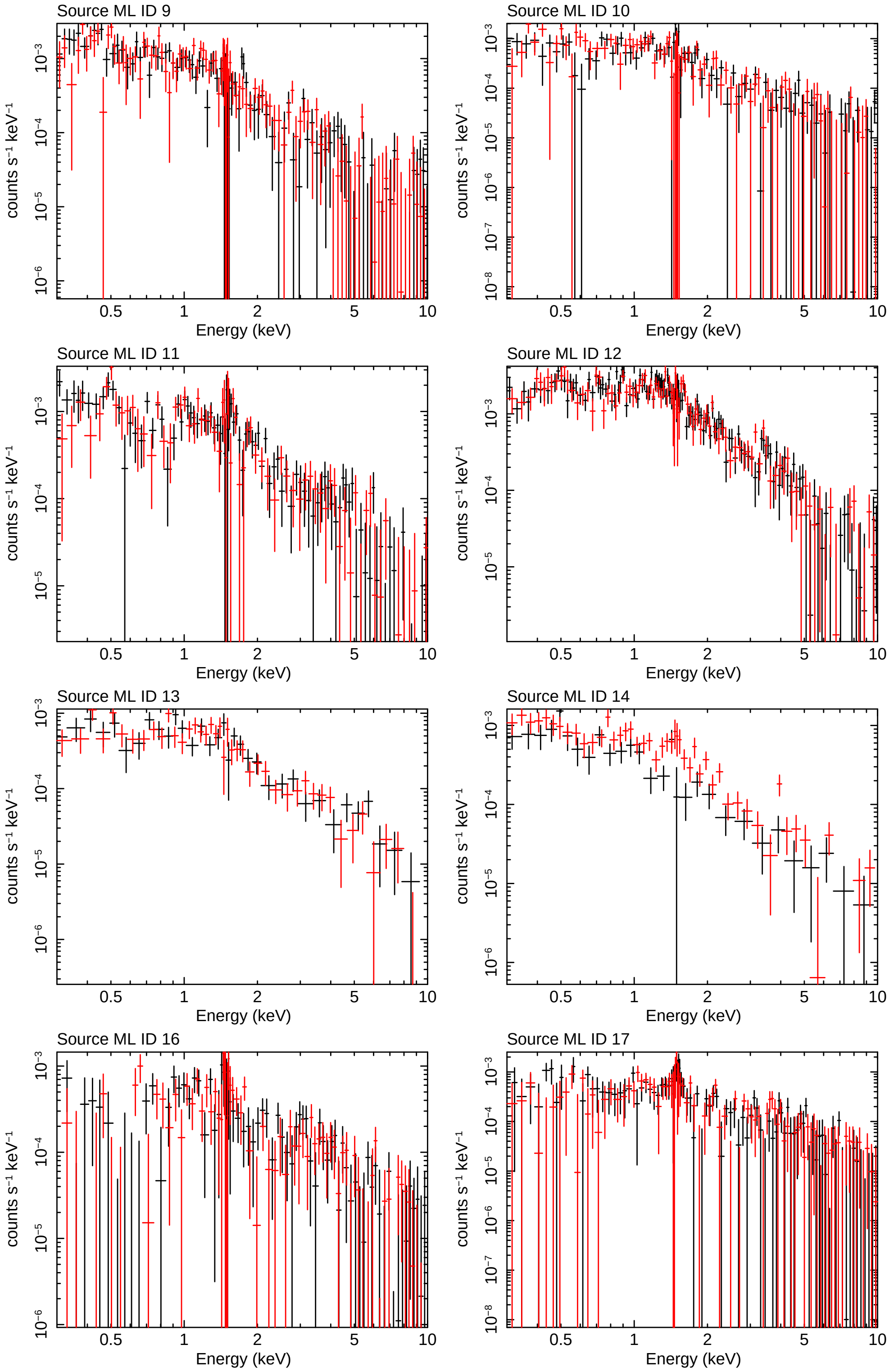

FIGURE 2.8: Spectra of the serendipitous sources within the *XMM-Newton* FOV around 3C 273 with $\geqslant 1000$ counts as detected by EMLDETECT. The source ML_ID number is given at the top of each spectrum. The black and red data points represent the EMOS 1 and EMOS 2 data, respectively.

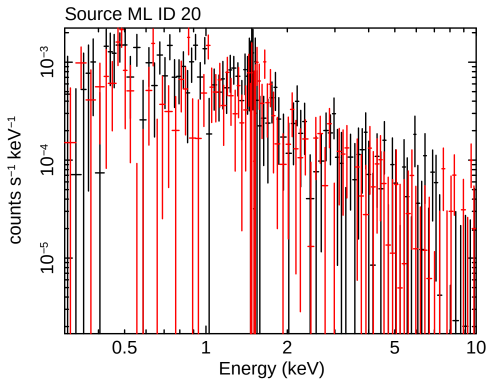

FIGURE 2.9: Spectra of the serendipitous sources within the *XMM-Newton* FOV around 3C 273 with $\geqslant 1000$ counts as detected by EMLDETECT. The source ML_ID number is given at the top of each spectrum. The black and red data points represent the EMOS 1 and EMOS 2 data, respectively.

$0.3 - 10$ keV) was fitted. Any excess or absorption, visible at lower energies, were modelled using a blackbody (BB) component and either *tbabs* (neutral absorption) or *absori* (warm absorber; WA), respectively. If the broad-band power-law fit (including any excess or absorption) was not acceptable, a *mekal* or *vmekal* model component was used to replace the power-law component. The *mekal* and *vmekal* components both simulate emission spectra from a hot diffuse gas. The only difference between the two components is that *vmekal* allows individual elemental abundances to be varied. Table 2.5 contains the information of the best-fitting models and includes the parameter values and fit statistics. In addition, the unabsorbed $0.3 - 10$ keV model X-ray fluxes are reported in Table 2.5.

The sources can be grouped by their best fitting models. Of the 17 sources modelled, 10 required only a power-law component, 1 a power-law and BB components, 1 a power-law including neutral absorption, 1 a power-law including a WA, 2 required two *vmekal* components, 1 required three *vmekal* components and the final source was modelled with a *cemekl* component, which models a multi-temperature plasma, based on the *mekal*

Table 2.5: Spectral Fitting Results for X-ray Sources with Total Counts $\geqslant 1000$

	0.3 – 10 keV *Power-law* Fits								GTI	Ignored
ML ID (1)	Γ (2)	kT [eV] (3)	$N_{\mathrm{h},1}$ [$\times 10^{22}$ cm^{-2}] (4)	$N_{\mathrm{h},2}$ [$\times 10^{22}$ cm^{-2}] (5)	ξ [erg s^{-1} cm^{-1}] (6)	χ^2 d.o.f. (7)	$\log_{10}(f_{\mathrm{X}})$ 0.3 – 10 keV (8)	$\log_{10}(f_{\mathrm{X}})$ 0.5 – 2 keV (9)	M1 [ks] M2 [ks] (10)	Low [keV] High [keV] (11)
3	$2.18^{+0.06}_{-0.06}$					272.5	$-13.07^{+0.02}_{-0.02}$	$-13.44^{+0.02}_{-0.02}$	516	
						280	$-13.07^{+0.02}_{-0.02}$	$-13.44^{+0.02}_{-0.02}$	504	
4	$1.81^{+0.05}_{-0.05}$					156.5	$-13.11^{+0.02}_{-0.02}$	$-13.57^{+0.02}_{-0.02}$	516	
						146	$-13.18^{+0.02}_{-0.03}$	$-13.64^{+0.02}_{-0.02}$	504	
5	$2.19^{+0.08}_{-0.08}$					212.4	$-13.10^{+0.03}_{-0.03}$	$-13.47^{+0.03}_{-0.03}$	516	
						194	$-13.13^{+0.03}_{-0.03}$	$-13.49^{+0.02}_{-0.03}$	504	
6	$1.50^{+0.11}_{-0.13}$	130^{+22}_{-22}				131.3	$-13.07^{+0.05}_{-0.05}$	$-13.57^{+0.03}_{-0.03}$	460	1.40
						153	$-13.10^{+0.05}_{-0.05}$	$-13.64^{+0.03}_{-0.03}$	506	1.60
7	$1.67^{+0.13}_{-0.11}$		$0.11^{+0.05}_{-0.05}$			181.7	$-13.14^{+0.03}_{-0.04}$	$-13.63^{+0.06}_{-0.05}$	461	
						163	$-13.16^{+0.03}_{-0.03}$	$-13.66^{+0.06}_{-0.05}$	506	
9	$2.20^{+0.12}_{-0.12}$					165.8	$-13.46^{+0.04}_{-0.04}$	$-13.82^{+0.04}_{-0.04}$	516	1.45
						174	$-13.48^{+0.04}_{-0.05}$	$-13.84^{+0.04}_{-0.04}$	506	1.55
10	$1.77^{+0.13}_{-0.13}$					131.5	$-13.44^{+0.06}_{-0.06}$	$-13.91^{+0.04}_{-0.05}$	517	1.45
						148	$-13.49^{+0.06}_{-0.06}$	$-13.96^{+0.04}_{-0.05}$	506	1.55
11	$2.23^{+0.43}_{-0.34}$			$0.93^{+0.40}_{-0.36}$	$3.65^{+15.72}_{-2.32}$	124.5	$-13.08^{+0.17}_{-0.11}$	$-13.44^{+0.20}_{-0.17}$	516	1.40
						135	$-13.15^{+0.17}_{-0.12}$	$-13.51^{+0.21}_{-0.18}$	361	1.80
13	$1.70^{+0.11}_{-0.11}$					55.6	$-13.57^{+0.05}_{-0.05}$	$-14.06^{+0.04}_{-0.05}$	392	
						73	$-13.57^{+0.05}_{-0.05}$	$-14.06^{+0.04}_{-0.04}$	506	
14	$2.16^{+0.13}_{-0.13}$					69.3	$-13.62^{+0.03}_{-0.03}$	$-14.00^{+0.03}_{-0.03}$	390	1.45
						68	$-13.62^{+0.03}_{-0.03}$	$-14.00^{+0.03}_{-0.03}$	506	1.55
16	$0.94^{+0.10}_{-0.11}$					139.1	$-13.26^{+0.08}_{-0.09}$	$-14.10^{+0.07}_{-0.08}$	517	1.45
						140	$-13.37^{+0.09}_{-0.10}$	$-14.21^{+0.07}_{-0.09}$	506	1.55
17	$1.24^{+0.08}_{-0.08}$					149.6	$-13.55^{+0.08}_{-0.09}$	$-14.24^{+0.07}_{-0.07}$	517	1.45
						170	$-13.56^{+0.08}_{-0.09}$	$-14.25^{+0.07}_{-0.08}$	504	1.55
20	$1.81^{+0.18}_{-0.17}$					152.5	$-13.63^{+0.07}_{-0.07}$	$-14.08^{+0.05}_{-0.06}$	461	1.45
						177	$-13.79^{+0.08}_{-0.09}$	$-14.24^{+0.06}_{-0.07}$	506	1.55

	0.3 – 10 keV *Vmekal* Fits											GTI	Ignored
ML ID (1)	kT$_1$ [keV] (12)	kT$_2$ [keV] (13)	kT$_3$ [keV] (14)	O [keV] (15)	Ne [$\times$solar] (16)	Mg [$\times$solar] (17)	Si [$\times$solar] (18)	Fe [$\times$solar] (19)	χ^2 d.o.f. (7)	$\log_{10}(f_{\mathrm{X}})$ 0.3 – 10 keV (8)	$\log_{10}(f_{\mathrm{X}})$ 0.5 – 2 keV (9)	M1 [ks] M2 [ks] (10)	Low [keV] High [keV] (11)
1	$2.218^{+1.183}_{-0.222}$	$0.096^{+0.018}_{-0.096}$	$0.617^{+0.024}_{-0.023}$	$1.31^{+0.45}_{-0.32}$	$1.35^{+0.44}_{-0.33}$	$0.61^{+0.29}_{-0.61}$	$0.80^{+0.36}_{-0.31}$	$0.29^{+0.11}_{-0.07}$	257.9	$-12.84^{+0.02}_{-0.02}$	$-13.00^{+0.01}_{-0.01}$	461	
									260	$-12.89^{+0.01}_{-0.02}$	$-13.05^{+0.01}_{-0.01}$	506	

Table 2.5: Spectral Fitting Results for X-ray Sources with Total Counts $\geqslant 1000$ (*Cont.*)

	0.3 – 10 keV *Vmekal* Fits											GTI	Ignored
ML ID (1)	kT_1 [keV] (12)	kT_2 [keV] (13)	kT_3 [keV] (14)	O [keV] (15)	Ne [×solar] (16)	Mg [×solar] (17)	Si [×solar] (18)	Fe [×solar] (19)	χ^2 d.o.f. (7)	$\log_{10}(f_X)$ 0.3 – 10 keV (8)	 0.5 – 2 keV (9)	M1 [ks] M2 [ks] (10)	Low [keV] High [keV] (11)
2	$1.613^{+0.321}_{-0.207}$	$0.670^{+0.035}_{-0.036}$		$0.72^{+0.25}_{-0.21}$	$1.58^{+0.40}_{-0.42}$	$0.63^{+0.29}_{-0.63}$	$0.56^{+0.29}_{-0.28}$	$0.31^{+0.07}_{-0.07}$	283.8 278	$-12.84^{+0.02}_{-0.02}$ $-12.86^{+0.02}_{-0.02}$	$-13.00^{+0.01}_{-0.01}$ $-13.02^{+0.01}_{-0.01}$	516 504	
8	$1.436^{+0.514}_{-0.302}$	$0.307^{+0.071}_{-0.053}$		$0.27^{+0.34}_{-0.20}$	$1.90^{+1.40}_{-0.82}$		$4.94^{+2.97}_{-2.52}$	$0.67^{+0.57}_{-0.30}$	121.9 199	$-13.53^{+0.05}_{-0.05}$ $-13.60^{+0.04}_{-0.04}$	$-13.68^{+0.04}_{-0.05}$ $-13.75^{+0.04}_{-0.04}$	315 506	1.45 1.55

	0.3 – 10 keV *Cemekl* Fits							GTI	Ignored
ML ID (1)	α (20)	T_{max} [keV] (21)	abund [×solar] (22)	redshift (23)	χ^2 d.o.f. (7)	$\log_{10}(f_X)$ 0.3 – 10 keV (8)	 0.5 – 2 keV (9)	M1 [ks] M2 [ks] (10)	Low [keV] High [keV] (11)
12	$1.46^{+0.92}_{-0.45}$	$11.5^{+4.8}_{-3.1}$	$0.98^{+0.50}_{-0.43}$	$0.966^{+0.021}_{-0.023}$	232.9 224	$-12.92^{+0.03}_{-0.03}$ $-12.97^{+0.03}_{-0.04}$	$-13.32^{+0.02}_{-0.02}$ $-13.37^{+0.02}_{-0.03}$	516 361	

The spectral $0.3-10$ keV best fit results for the 17 sources with total counts $\geqslant 1000$. The results are grouped by model type, *power-law*, *vmekal* and *cemekl*. Columns are as follows: (1) - Source ML_ID number; (2) - power-law index, Γ; (3) - BB temperature, kT; (4) - additional neutral absorbing column intrinsic to source, modelled by *tbabs*, $N_{\rm h,1}$; (5) - warm absorber column density intrinsic to source, modelled by *absori*, $N_{\rm h,2}$; (6) - warm absorber ionisation, modelled by *absori*, ξ; (7) - best fit model statistics, χ^2/d.o.f.; (8) - unabsorbed $0.3-10$ keV model flux in units of erg s^{-1} cm^{-2} (Top: EMOS1; Bottom: EMOS2); (9) - unabsorbed $0.5-2$ keV model flux in units of erg s^{-1} cm^{-2} (Top: EMOS1; Bottom: EMOS2); (10) - GTI exposure times for the extracted spectrum to the nearest ks for EMOS1 and EMOS2, respectively; (11) - if required, low and high energy range ignored during modelling, respectively; (12) - first *vmekal* component temperature, kT_1; (13) - second *vmekal* component temperature, kT_2; (14) - third *vmekal* component temperature, kT_3; (15 – 19) - O, Ne, Mg, Si and Fe *vmekal* elemental abundances relative to solar, tied between each *vmekal* component; (20) - *cemekl* power-law emissivity index function, α; (21) - *cemekl* maximum temperature, T_{max}; (22) - *cemekl* elemental global abundance relative to solar; (23) - *cemekl* redshift.

codes. Source ML_ID 12, modelled by the *cemekl* component, was identified as a possible galaxy cluster, XMMU J1229 + 0151, by Boehringer et al. (2005) as part of the *XMM-Newton* Distant Cluster Project. The X-ray spectral analysis of ML_ID 12 in this work also suggests that ML_ID 12 is a galaxy cluster with a redshift of $z = 0.97 \pm 0.02$. This redshift is consistent with the value of 0.97 obtained by Santos et al. (2009). The authors calculated the average redshift of optical sources spectroscopically identified as part of the cluster. It should be noted that Santos et al. (2009) also modelled the combined *XMM-Newton* EPIC MOS spectrum of XMMU J1229+0151 (reduced in a similar manner to the method used in this work) with a Galactic absorbed, single temperature *mekal* component. The authors cite a temperature of $6.4^{+0.7}_{-0.6}$ keV and an iron abundance relative to solar of $0.34^{+0.14}_{-0.13}$ for the best model fit. This is not consistent with the model fit and resulting parameters, $T_{\rm max} = 11.5^{+4.8}_{-3.1}$ keV and elemental global abundance relative to solar of $0.98^{+0.50}_{-0.43}$, calculated in this work.

2.6 Discussion

The aim of this chapter was to detect, classify and extract as much information as possible from the serendipitous sources in the 3C 273 field observed by *XMM-Newton*. The data analysed in this chapter were obtained by combining a number of EMOS exposures of the 3C 273 field into the equivalent of one long ~ 500 ks look. This is a considerable amount of observing time and was only made possible by the large number of calibration observations made of 3C 273. However, from an analysis view point, one long observation would reduce the errors in, for example, the background calculations, compared to the errors introduced by combining all of the shorter exposures.

After performing source detection on the *XMM-Newton* FOV around 3C 273, the X-ray source positions were cross-correlated with other survey catalogues, as described

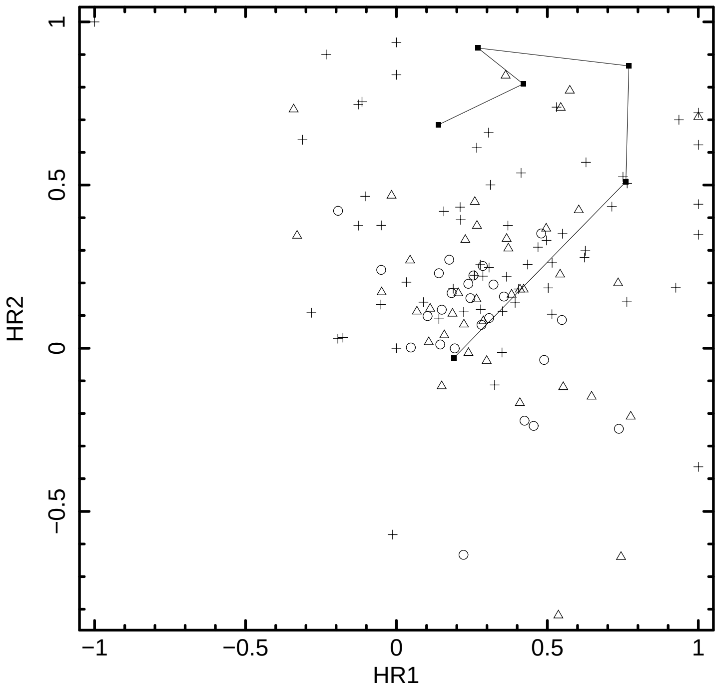

FIGURE 2.10: Hardness ratio plot, HR2 against HR1, for all 136 X-ray sources detected in the *XMM-Newton* EMOS FOV around 3C 273. Crosses represent X-ray sources without a candidate counterpart with $P_{\rm id} \geqslant 0.95$ from the SDSS. Circles represent X-ray sources with a candidate counterpart with $P_{\rm id} \geqslant 0.95$ from the SDSS that have been classified as point-like. Triangles represent X-ray sources with a candidate counterpart with $P_{\rm id} \geqslant 0.95$ from the SDSS that have been classified as extended. The filled squares and joining lines indicate expected HR values (taken from Watson et al., 2009) for a given power-law photon-index ($\Gamma = 1.9$) with varying amounts of absorption ($N_{\rm h} = 0.03, 0.4, 1, 5, 10, 50 \times 10^{22}$ cm^{-2}). The lower-left marker of the spectral track corresponds to the lowest $N_{\rm h}$ value.

in Section 2.4. In an attempt to draw more information from both the X-ray and optical data, a number of plots were created using each source's X-ray information and associated optical information from the SDSS DR6 searches. These plots are shown in Figures 2.10–2.19.

Figures 2.10, 2.11 and 2.12 show the X-ray HR plots of the 136 sources detected in the deep-look of the FOV surrounding 3C 273. HR tracks (taken from Watson et al., 2009) are plotted for a power-law with given photon-indices of 1.9, 1.7 and 1.4, in Figures 2.10, 2.11 and 2.12, respectively, with various amounts of absorption ($N_{\rm h} =$

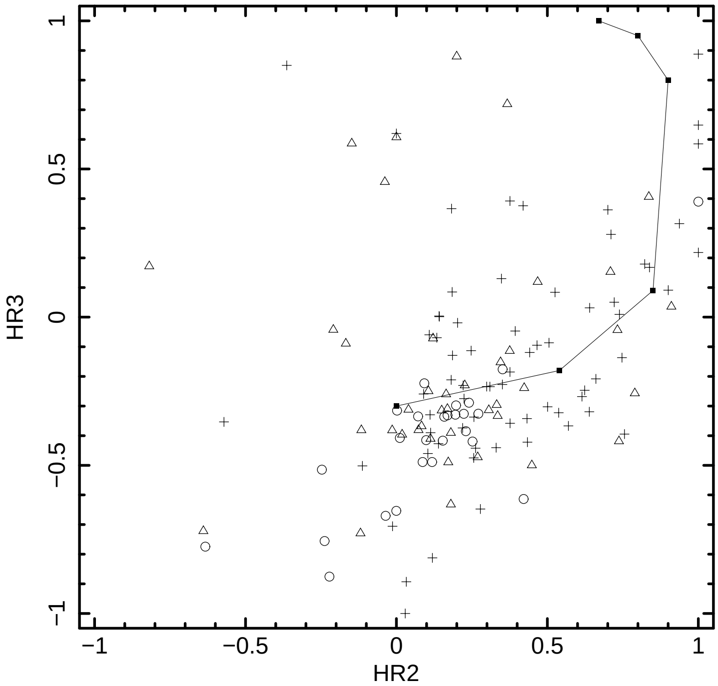

FIGURE 2.11: Hardness ratio plot, HR3 against HR2, for all 136 X-ray sources detected in the *XMM-Newton* EMOS FOV around 3C 273. The symbols are as defined in Figure 2.10. The filled squares and joining lines indicate expected HR values (taken from Watson et al., 2009) for a given power-law photon-index ($\Gamma = 1.7$) with varying amounts of absorption ($N_{\rm h} = 0.03, 0.4, 1, 5, 10, 50 \times 10^{22}$ cm^{-2}). The lower-left marker of the spectral track corresponds to the lowest $N_{\rm h}$ value.

$0.03, 0.4, 1, 5, 10, 50 \times 10^{22}$ cm^{-2}). The lower-left marker of each HR spectral track corresponds to the lowest $N_{\rm h}$ value.

Comparing the HR plots from this work to the HR plots of the sources detected in the *XMM-Newton* Bright Serendipitous Survey (BSS[6]; Della Ceca et al., 2004), it is possible to place loose limits on the types of sources present in the *XMM-Newton* FOV around 3C 273. The work presented by Della Ceca et al. (2004) uses the old 1XMM bands. The HR3′ against HR2′ plot (the prime represents 1XMM HRs; Figure 5 of Della Ceca et al., 2004) shown by the authors is the closest representation of the HR4 against HR3 plot presented in this work (HR4 $\equiv$ HR3′, HR2′ incorporates HR3). For a comparison

[6]The BSS is a flux limited, $f_{\rm X} \approx 7 \times 10^{-14}$ erg s^{-1} cm^{-2} ($0.5 - 4.5$ keV), survey for Galactic latitudes of $|b| \geqslant 20°$)

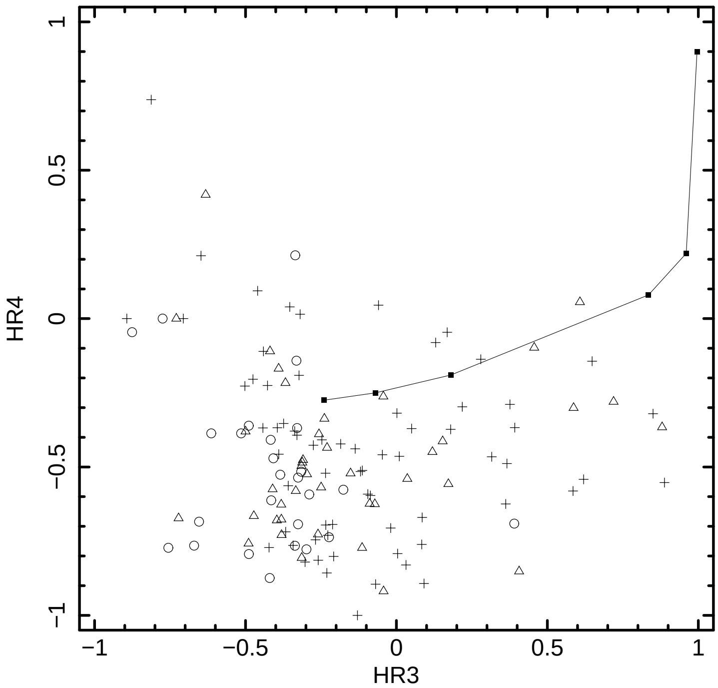

FIGURE 2.12: HR4 against HR3 hardness ratio plot for all 136 X-ray sources detected in the *XMM-Newton* EMOS FOV around 3C 273. Symbols are as defined in Figure 2.10. The filled squares and joining lines indicate expected HR values (taken from Watson et al., 2009) for a given power-law photon-index ($\Gamma = 1.4$) with varying amounts of absorption ($N_{\rm h} = 0.03, 0.4, 1, 5, 10, 50{\times}10^{22}$ cm^{-2}). The lower-left marker of the spectral track corresponds to the lowest $N_{\rm h}$ value.

of HR3 to HR2′, Figure 2.13 shows the HR3′ against HR2′ for the 136 sources detected in this work. Della Ceca et al. (2004) found that 90% of the optically classified type 1 (broad-line) AGN from the BSS fall between the values of $-0.75 \leqslant$ HR2′ $\leqslant -0.35$. These boundries are marked by dot-dashed lines on Figure 2.13. The authors also find that 96% of those source classified as coronal emitting stars lie below HR2′ $\leqslant -0.75$. In addition, Della Ceca et al. (2004) suggest that those sources with HR2′ $\geqslant -0.35$ are X-ray absorbed with $N_{\rm h}$ ranging from a few times 10^{21} to a few times 10^{23} cm^{-2}. Finally, the authors discuss the fact that type 2 (narrow-line) AGN are distributed over a large area of the HR3′ against HR2′ plot, covering both the broad-line AGN and X-ray absorbed source regions. Applying these limits to Figures 2.12 and 2.13, it can be seen

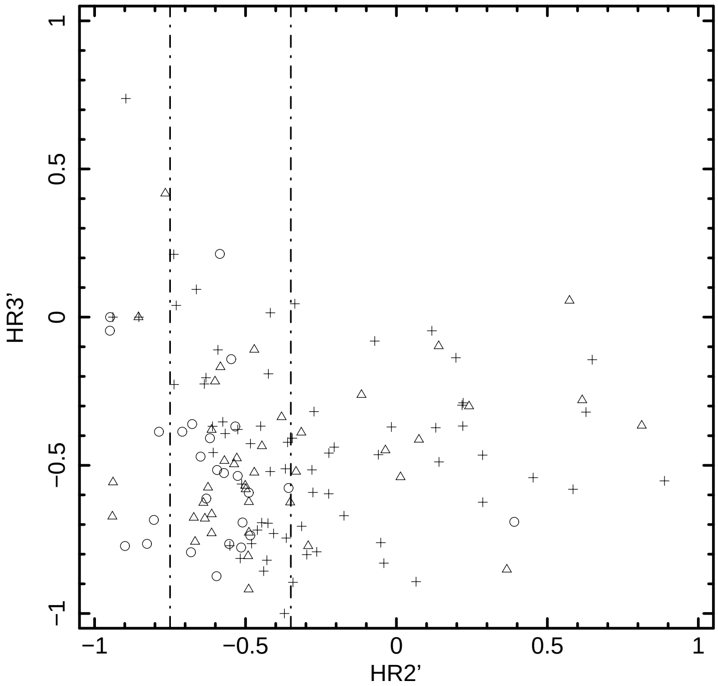

FIGURE 2.13: HR3′ against HR2′ plot hardness ratio plot for all 136 X-ray sources detected in the *XMM-Newton* EMOS FOV around 3C 273, using 1XMM bands. Symbols are as defined in Figure 2.10. The two dot-dashed lines represent the boundaries of constant HR2′ within which Della Ceca et al. (2004) found $\sim 90\%$ of the classified type 1 AGN from the BSS sample to be contained.

that the majority of the X-ray sources with an SDSS candidate counterpart lie in or very close to the broad-line AGN region, with nearly all of the point-like sources also lying in this range ($18/26$ in Figure 2.13). For those sources with HR3 $\geqslant -0.35$ and a candidate optical counterpart, most are classed by SDSS as being optically extended.

Only five of the 136 X-ray sources have SDSS spectral information (2 QSOs, 3 galaxies). However, based on the morphological properties and HR3 (HR2′) values of those X-ray sources with SDSS candidate counterparts, the results shown in Figure 2.12 (Figure 2.13) are consistent with those reported by Della Ceca et al. (2004). For the two QSO sources with an SDSS spectrum (ML_IDs 3 and 11), their HR2′ values lie between $-0.75 \leqslant$ HR2′ $\leqslant -0.35$. The same can be said for all the X-ray sources identified as QSOs in Table 2.4. In addition, all the X-ray sources classified as stars in Table 2.4 lie

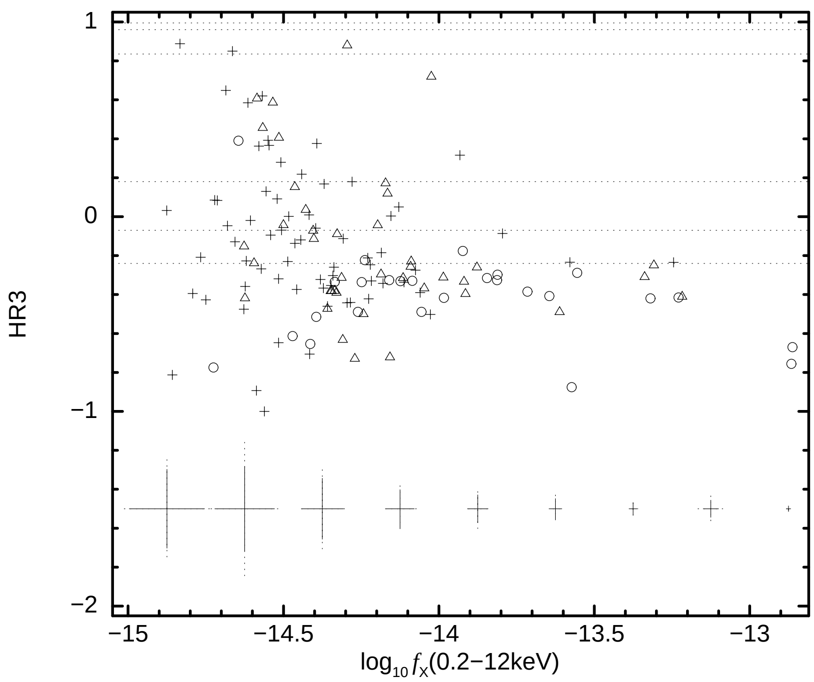

FIGURE 2.14: HR3 against observed $0.2-12$ keV X-ray flux for all 136 X-ray sources detected in the *XMM-Newton* EMOS FOV around 3C 273. Symbols are as defined in Figure 2.10. Dotted lines represent expected HR3 values (taken from Watson et al., 2009) for a given power-law photon-index ($\Gamma = 1.7$) with varying amounts of absorption ($N_{\mathrm{h}} = 0.03, 0.4, 1, 5, 10, 50 \times 10^{22}$ cm^{-2}). The absorption increases from bottom to top. The lower points at HR3 equal to -1.5 are representative errors for HR3 and observed X-ray flux, calculated for flux bins of 0.25 in log space. Solid lines indicate the mean error with the dotted (extended) portions of the lines showing the 1σ value of the distribution of the errors.

below HR2$' \leqslant -0.75$. Those sources classified as galaxies cover the full HR2$'$ range. It should be noted that there are a number of sources without candidate optical counterparts with HR2$' \geqslant -0.35$, which would suggest that these sources are optically absorbed. This is consistent with these sources also being X-ray absorbed. Infrared (IR) observations of these sources would be appropriate to determine their true nature.

Figure 2.14 shows the HR3 value for all 136 X-ray sources against the observed $0.2-12$ keV X-ray flux. For comparison, Figure 2.15 shows the HR2$'$ value against the observed $0.2-12$ keV X-ray flux. The dotted lines on Figure 2.14 indicate the expected

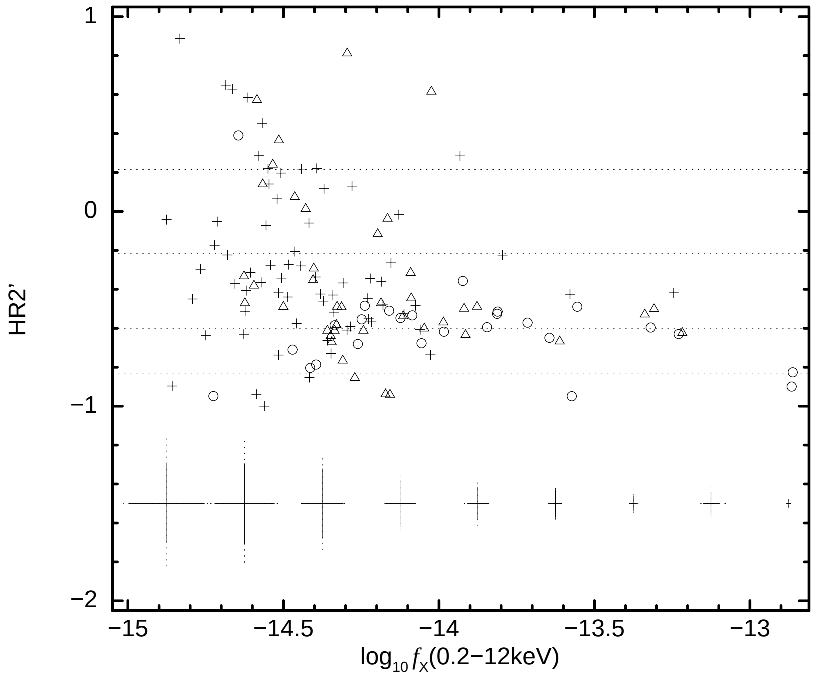

FIGURE 2.15: HR2′ against observed $0.2 - 12$ keV X-ray flux for all 136 X-ray sources detected in the *XMM-Newton* EMOS FOV around 3C 273. Symbols are as defined in Figure 2.10. Dotted lines represent expected HR3 values (taken from Della Ceca et al., 2004) for a given unabsorbed power-law photon-index ($\Gamma = 0, 1, 2, 3$). The photon-index increases from top to bottom. The lower points at HR2′ equal to -1.5 are representative errors for HR2′ and observed X-ray flux, calculated for flux bins of 0.25 in log space. Solid lines indicate the mean error with the dotted (extended) portions of the lines showing the 1σ value of the distribution of the errors.

HR3 values for an absorbed power-law with $\Gamma = 1.7$ and absorbing column values of $N_{\rm h} = 0.03, 0.4, 1, 5, 10, 50 \times 10^{22}$ cm^{-2}, respectively, from bottom to top (taken from Watson et al., 2009). Plotted on Figure 2.15 are dotted lines that indicate the expected HR2′ values for an unabsorbed power-law with a given photon-index of $\Gamma = 0, 1, 2, 3$, respectively, from top to bottom (taken from Della Ceca et al., 2004). As part of the *Chandra* Multi-wavelength Project, Green et al. (2004) performed an optical follow up of the *Chandra* serendipitous sources and produced a similar plot of hardness ratio against X-ray flux (Figure 15 of Green et al., 2004). When Figure 2.14 is compared to the Green et al. (2004) figure, a number of sources detected in this work show slight to

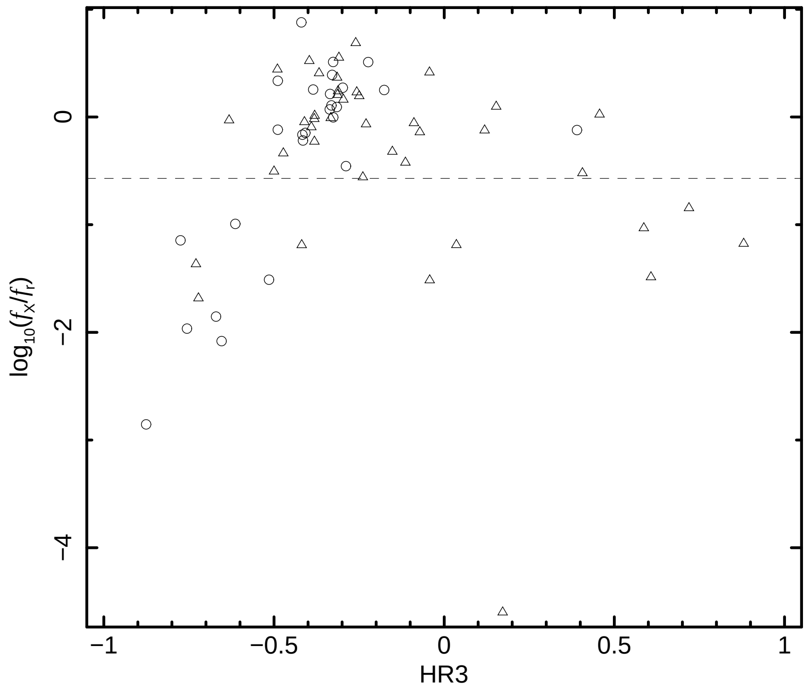

FIGURE 2.16: X-ray flux ($0.2-12$ keV; observed) to optical flux ratio, $\log_{10}(f_X/f_r)$, against HR3, for the 68 X-ray sources detected in the *XMM-Newton* EMOS FOV around 3C 273 with SDSS candidate counterparts with $P_{\rm id} \geqslant 0.95$, where $f_r = f_{\rm opt}$ (Equation 2.10). Symbols are as defined in Figure 2.10. The dashed line represents the typical mean value of optical to X-ray flux ratio index, $\alpha_{\rm o,x} = 1.5$, determined for optically selected AGN (Green et al., 1995). This corresponds to an X-ray to optical flux ratio of $\log_{10}(f_X/f_{\rm opt}) = -0.57$.

moderate absorption ($N_{\rm h} \leqslant 10^{22}$ cm^{-2}; $-0.7 \lesssim$ HR3 $\lesssim -0.3$). These sources cover the entire range of detected fluxes and are likely to be broad-line objects. In addition, a number of sources are heavily absorbed ($N_{\rm h} \geqslant 10^{22}$ cm^{-2}; HR3 $\gtrsim -0.3$) and have fluxes $\leqslant 10^{-14}$ erg s^{-1} cm^{-2}, again suggesting the presence of X-ray absorption.

Focusing on the 68 X-ray sources with an SDSS candidate optical counterpart with $P_{\rm id} \geqslant 0.95$, Figure 2.16 shows the observed $0.2-12$ keV X-ray to optical flux ratio, $\log_{10}(f_X/f_{\rm opt})$, plotted against HR3 for the 68 sources. The dashed line in Figure 2.16 represents the typical mean value of optical to X-ray flux ratio index, $\alpha_{\rm o,x} = 1.5$, determined for optically selected AGN (Green et al., 1995). This corresponds to an X-

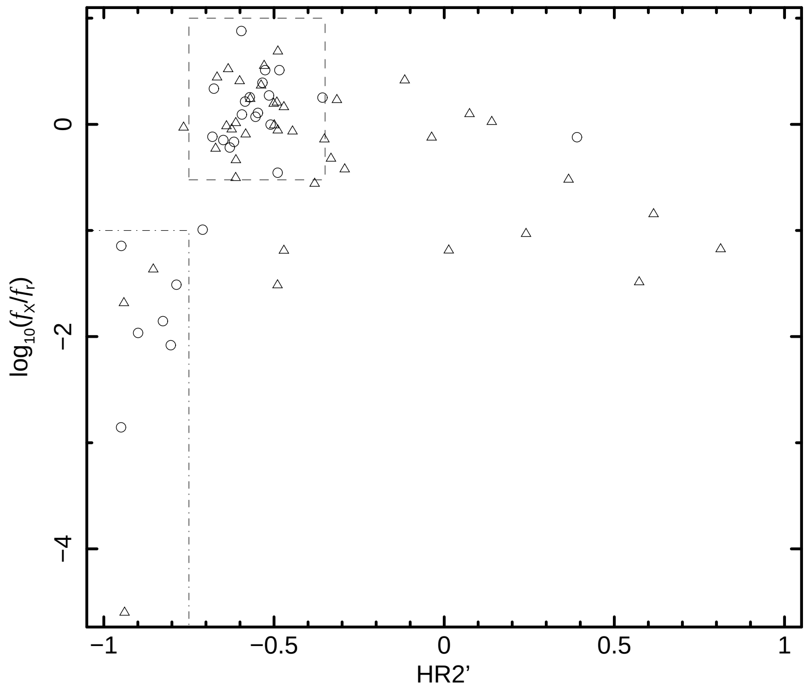

FIGURE 2.17: X-ray flux ($0.2-12$ keV; observed) to optical flux ratio, $\log_{10}(f_{\rm X}/f_r)$, against HR2$'$, for the 68 X-ray sources detected in the *XMM-Newton* EMOS FOV around 3C 273 with SDSS candidate counterparts with $P_{\rm id} \geqslant 0.95$, where $f_r = f_{\rm opt}$ (Equation 2.10). Symbols are as defined in Figure 2.10. The boxes defined in the above Figure are taken from Figure 15 of Green et al. (2004). They enclose $\sim 95\%$ (dot-dashed lines) and $\sim 85\%$ (dashed lines) of the optically identified coronal emitting stars and broad line AGN in the BSS, respectively.

ray to optical flux of $\log_{10}(f_{\rm X}/f_{\rm opt}) = -0.57$. Again, for comparison, Figure 2.17 shows the observed $0.2-12$ keV X-ray to optical flux ratio, $\log_{10}(f_{\rm X}/f_{\rm opt})$, plotted against HR2$'$. Figure 2.16 is similar to Figure 6 of the BSS work by Della Ceca et al. (2004), where $f_{\rm X}/f_{\rm opt}$ is plotted against HR2$'$. In the plot shown by Della Ceca et al. (2004), there appears to be distinct regions (recreated in Figure 2.17) for stellar objects ($f_{\rm X}/f_{\rm opt} \leqslant 0.1$, HR2$' \leqslant -0.75$; dot-dashed line) and broad-line AGN ($0.3 \lesssim f_{\rm X}/f_{\rm opt} \lesssim 10$, $-0.75 \leqslant$ HR2$' \leqslant -0.35$; dashed line), with narrow-line AGN covering a larger area ($0.002 \lesssim f_{\rm X}/f_{\rm opt}$, HR2$' \gtrsim -0.75$) that encompasses the broad-line region. Comparing these regions to Figure 2.16, there is a cluster of objects (containing most of the point-like sources) around HR3 ~ -0.4 and $\log_{10}(f_{\rm X}/f_{\rm opt}) \sim 0$, that is comparable to the broad-line region in the Della Ceca et al. (2004) work. Those sources in Figure 2.16 beyond HR3 ~ -0.3 that have $\log_{10}(f_{\rm X}/f_{\rm opt}) \gtrsim -1$ are likely to be narrow-line AGN, while those sources with $\log_{10}(f_{\rm X}/f_{\rm opt}) \lesssim -1$ are possible X-ray bright optically normal galaxies (XBONGs; e.g., Comastri et al., 2002; Civano et al., 2007). The source with $\log_{10}(f_{\rm X}/f_{\rm opt}) \approx -4.5$ and HR3 ≈ 0.2 is source ML_ID 77, which was optically matched with a known star BD$+$02 2547, of type F5. From Figure 2.3 it can be seen that source ML_ID 77 lies on a chip edge. It is possible that the X-ray flux values determined have been affected by this, as suggested by the errors on HR3 (± 3.5) and HR4 (± 1.9) in Table 2.2. However, looking at Figure 2.17, source ML_ID 77 now falls into the stellar region, as defined by Della Ceca et al. (2004), with HR2$'$ ≈ -0.94 and $\log_{10}(f_{\rm X}/f_{\rm opt}) \approx -4.5$. The remaining stars and all the QSOs previously classified in Table 2.4 fall within their respective HR2$'$ and $\log_{10}(f_{\rm X}/f_{\rm opt})$ limits. Interestingly, two of the X-ray sources, ML_IDs 57 and 72, classified as galaxies using SDSS spectra (ML_ID 57 is identified as an absorption line system galaxy), have HR2$'$ values of -0.94 ± 0.14 and -0.85 ± 0.17, and $\log_{10}(f_{\rm X}/f_{\rm opt})$ values of -1.89 ± 0.05 and -1.58 ± 0.06, respectively. This places these two sources firmly in the stellar region in Figures 2.13 and 2.17. In the work presented by Della Ceca et al., there is only one galaxy that falls in the stellar region.

The SDSS $(g - r)$ against $(u - g)$ and $(r - i)$ against $(g - r)$ colour-colour plots are shown in Figure 2.18. The X-ray sources plotted in the $(r - i)$ against $(g - r)$ colour–colour plot, cover the same range as those plotted in Figure 10 of Green et al. (2004). Also, shown in Figure 2.18 are quasars within the SDSS DR5 Quasar Catalogue (Schneider et al., 2007). The SDSS quasars are plotted in groups of redshift; light grey, light blue, green and dark blue points represent quasars with redshifts of $z < 3$, $3 \leqslant z < 3.5$, $3.5 \leqslant z < 4$ and $4 \leqslant z$, respectively. It can be seen in the $(g - r)$ against $(u - g)$ and

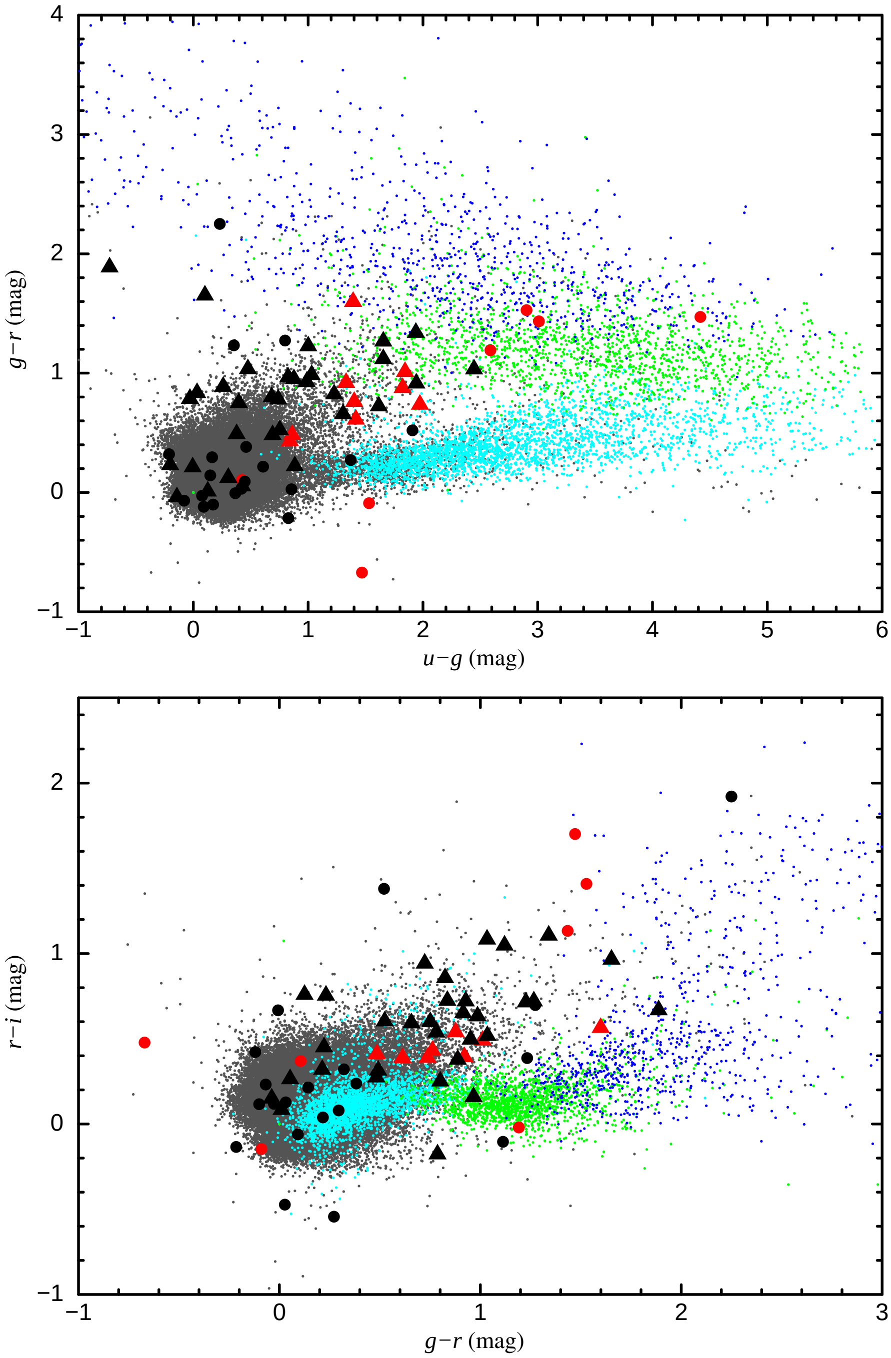

FIGURE 2.18: Colour–colour plots of the 68 X-ray sources with a candidate optical counterpart within the SDSS DR6 with $P_{\rm id} \geqslant 0.95$. Solid circles and triangles indicate candidate counterparts designated as point-like and extended by the SDSS, respectively. Red and black indicate candidate counterparts with $\log_{10}(f_{\rm X}/f_{\rm opt}) < -1$ and $\log_{10}(f_{\rm X}/f_{\rm opt}) \geqslant -1$, respectively. The light grey, light blue, green and dark blue points indicate quasars with redshifts of $z < 3$, $3 \leqslant z < 3.5$, $3.5 \leqslant z < 4$ and $4 \leqslant z$ in the SDSS Quasar Catalogue DR5 (Schneider et al., 2007), respectively.

$(r-i)$ against $(g-r)$ plots that it is only at a redshifts of $3\leqslant z$ and $3.5\leqslant z$, respectively, that quasars can be separated out from lower redshift quasars. From Figure 2.18, it can be suggested that the majority of sources designated as point-like by the SDSS and have $\log_{10}(f_{\rm X}/f_{\rm opt})\geqslant -1$ (filled black circles) are likely to be AGN, with $z<3$. In the top panel of Figure 2.18, there is a cluster of extended sources with $\log_{10}(f_{\rm X}/f_{\rm opt})\geqslant -1$ (filled black triangles) that lie above the $3\leqslant z<3.5$ quasar branch and to the right of the $z<3$ bulk of quasars; these sources are likely to be normal galaxies. This point can be seen again in the lower panel with the same sources lying above the $3.5\leqslant z<4$ quasar branch. Those sources that are extended and have $\log_{10}(f_{\rm X}/f_{\rm opt})<-1$ (filled red triangles) are likely to be emission line galaxies as suggested by the SDSS spectra of sources ML_IDs 57, 72 and 107. Finally, those sources designated as point-like with $\log_{10}(f_{\rm X}/f_{\rm opt})<-1$ (filled red circles) are likely to be stellar type objects, e.g., source ML_ID 1. Interestingly, the galaxy cluster XMMU J1229 + 0151, source ML_ID 12, which is designated as point-like with $\log_{10}(f_{\rm X}/f_{\rm opt})\geqslant -1$, $u-g=0.23\pm1.52$ mag, $g-r=2.25\pm0.48$ mag, and $r-i=1.92\pm0.09$ mag, lies in the $4\leqslant z$ quasar region in the two colour–colour plots. This indicates that optical spectroscopy of the candidate counterparts is required to definitively classify the X-ray objects detected in this work.

Finally, a plot of SDSS r magnitude against the observed $0.2-12$ keV X-ray flux for the 68 sources with candidate optical counterparts from the SDSS with $P_{\rm id}\geqslant 0.95$ is shown in Figure 2.19. Also plotted are lines of constant X-ray to optical flux ratios. The dot-dashed line labelled QSOsOS in Figure 2.19 represents the typical mean value of optical to X-ray flux ratio index[7], $\alpha_{\rm o,x}=1.5$, determined for optically selected AGN (Green et al., 1995). This corresponds to an X-ray to optical flux ratio of $\log_{10}(f_{\rm X}/f_{\rm opt})=-0.57$.

[7]The optical to X-ray flux ratio index, $\alpha_{\rm o,x}$, is defined as

$$\alpha_{\rm o,x}=\log\left[\frac{f_\nu\,(2\,{\rm keV})}{f_\nu\,(2500\,\text{Å})}\right]\div\log\left[\frac{\nu\,(2\,{\rm keV})}{\nu\,(2500\,\text{Å})}\right]$$

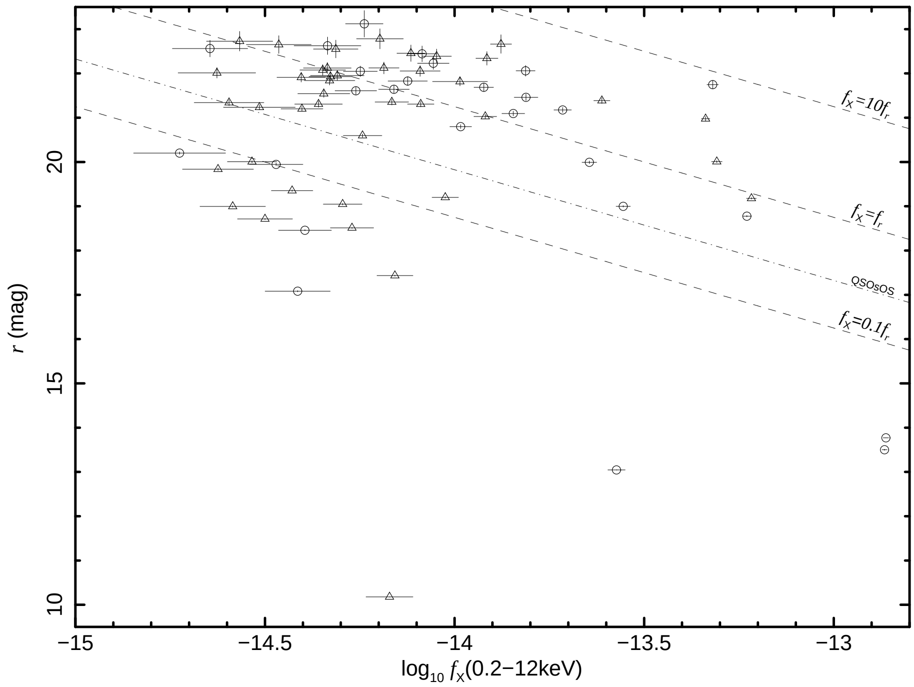

FIGURE 2.19: SDSS r magnitude against observed $0.2-12$ keV X-ray flux for the 68 sources with candidate optical counterparts from the SDSS with $P_{\rm id} \geqslant 0.95$. Symbols are as defined in Figure 2.10. The dashed lines represent constant X-ray to optical flux ratios, where $f_r \equiv f_{\rm opt}$ (Equation 2.10). The dot-dashed line labelled QSOsOS represents the typical mean value of optical to X-ray flux ratio index, $\alpha_{\rm o,x} = 1.5$, determined for optically selected AGN (Green et al., 1995). This corresponds to an X-ray to optical flux ratio of $\log_{10}(f_{\rm X}/f_{\rm opt}) = -0.57$.

Comparison of Figure 2.19 with Figure 5 from Green et al. (2004) would suggest that most of the sources that lie above the QSOsOS line are broad-line AGN. Sources that lie below this line are likely to be a mixture of narrow-line AGN, normal galaxies, XBONGS, stars and absorbed systems. Those sources with a $r \leqslant 15$ magnitude are most likely stars. However, the majority of sources in Table 2.4 that have previously been classified as a galaxy lie below the $f_{\rm x}/0.1f_r$ line. All the QSOs listed in Table 2.4 lie above the QSOsOS line. Source ML_ID 77 can be found at $\log_{10} f_{\rm X} \sim -14.2$ and $r \sim 10$ magnitude.

2.7 Conclusions

The analysis in this chapter has made use of *XMM-Newton* EMOS observations of 3C 273 to produce a deep-look (~ 500 ks) of the FOV surrounding 3C 273. The deep-look was created by mosaicing the individual observation images that were taken over a period of ~ 8 years. Source detection was then performed concurrently on the mosaiced EMOS1 and EMOS2 images. The serendipitous X-ray sources detected were cross-correlated with other catalogues, including the SDSS DR6. Of the 136 X-ray sources, 68 had a match in the SDSS with $P_{\rm id} \geqslant 0.95$. In addition, 15 of the 136 sources were found to be previously classified and included stars, galaxies and QSOs. The X-ray spectra of the brightest 17 X-ray sources were modelled in an attempt to corroborate previous classifications or to classify the unknown sources and place better constraints on their X-ray properties. In addition, initial crude classifications of sources were made from the observed properties of the X-ray sources and SDSS candidate optical counterparts. A number of different types of X-ray sources were detected in this work, as shown in the various plots that are consistent with the work of Della Ceca et al. (2004) and Green et al. (2004). For classification of all the X-ray sources detected, analysis of their optical spectra is required.

Chapter 3

Mass Loss from AGN

3.1 Introduction

As discussed in Section 1.1.1, the current AGN paradigm is that of a super massive black hole (SMBH) residing at the centre of the gravitational potential well of the host galaxy (Rees, 1984). The SMBH is surrounded by an accretion disc and fast moving clouds at varying distances known as the broad- and narrow-line regions (BLR and NLR). A dusty torus is often proposed to surround the system as a way of unifying the two types of optically defined AGN (Antonucci, 1993), explaining the evidence of, amongst others, emission from either the NLR or both the NLR and BLR. The activity and continuum radiation of AGN is a result of the in-fall of matter from the accretion disc onto the SMBH, converting gravitational potential energy into electromagnetic (EM) radiation.

Unfortunately, describing the true structure of AGN and their unification is not as clear cut as discussed in Section 1.1.3. The observed optical properties of AGN can be used to divide them into a number of subclasses. However, there are additional components found in the majority of these subclasses, which may be related through mass loss from the central engine.

3.1.1 Mass Outflows

There are a variety of examples of mass loss processes within AGN. The topic of interest in this chapter is specifically high-ionisation ($\log \xi \gtrsim 3$), high-velocity ($v_{\rm out} \sim 0.04-0.2c$) X-ray outflows. Such outflows have been claimed in a small number of sources, e.g., PDS 456 (Reeves et al., 2003; Reeves et al., 2009) and PG $1211+143$ (Pounds et al., 2003a; Pounds and Page, 2006; Pounds and Reeves, 2009), with the majority of these outflows showing evidence of high-density absorbing columns ($\sim 10^{23}-10^{24}$ cm^{-2}). This suggests a large loss of mass from the central engine. If the line identifications of the detected absorption features and therefore the related outflow velocities are correct, these outflows could provide a direct link between the SMBH and their host galaxies, for example, the regulation of the SMBH and galactic bulge growth (Silk and Rees, 1998; Fabian, 1999; King, 2003; Di Matteo et al., 2005; Murray et al., 2005), which could lead to the $M_{\rm BH}-\sigma_*$ relation (Section 3.2.1; Ferrarese and Merritt, 2000; Gebhardt et al., 2000a; Tremaine et al., 2002). The current generation of X-ray observatories, e.g., *XMM-Newton* and *Chandra*, do not have the resolving power to undeniably classify the absorption lines detected. Proposed future X-ray observatories such as the *International X-ray Observatory* (IXO[1]) will carry a number of next generation instruments that will have the ability to probe the inner regions of AGN with better clarity. For example, the IXO microcalorimeter spectrometer (XMS) will provide an increased spectral resolution (better than 10 eV at the Fe K line $\sim 6.4-6.7$ keV; 2.5 eV across $0.3-7$ keV), while the wide-field instrument aboard the IXO, which will provide a spatial and spectral resolution similar to the *XMM-Newton* EPIC instruments of ~ 5 arc seconds and $\Delta\mathrm{E} = 150$ eV, respectively, (within an 18 arc minute field of view, across $0.1-15$ keV), will have a throughput (3 m^2 at 1.25 keV) $\gtrsim 3$ larger than the throughput for the EPIC

[1]http://ixo.gsfc.nasa.gov/index.html

instruments. This will allow the detection of features that would go undetected by the EPIC instruments, which will place firm limits on parameters such as column density and ionisation, and would, amongst other things, lead to better constraints on the location of the outflow, its launch radius and observing angle. The IXO may also detect evidence of high-ionisation, high-velocity outflows in the X-ray spectra of fainter targets, placing limits on their frequency and, as a result, find possible common observable features that may be prerequisites for such outflows to exist. However, before discussing the properties of high-ionisation, high-velocity outflows and their implications, other forms of mass loss will be addressed to add perspective.

The various forms of mass loss have one aspect in common; they all take the form of material in an outflow, for example, a wind or jet-like structure. Mass loss is not limited only to AGN; systems such as Galactic black holes (BH) and young stellar objects can show evidence of winds or jets (e.g., Livio, 2003). Such phenomena are expected to carry both angular momentum and energy away from the accretion disc. Winds or jets are thought to be closely linked to the accretion of matter onto the BH (Balbus, 2003). The exact nature, origin and driving mechanisms of these outflows are unknown and are likely to vary between sources. A full discussion of the possible mechanisms that form and drive mass outflows is beyond the scope of this thesis. However, a brief synopsis is given in Section 3.1.2 following the discussion of the observational evidence for the presence of such outflows.

Radio jets

Large radio lobes, on kpc scales, are often found in radio loud AGN and are more common in FR-II sources. These radio lobes are attributed to a relativistic jet originating deep within the central region that expands into the inter-stellar medium (ISM) and beyond the limits of the host galaxy. The lobes are likely to be aligned along the magnetic fields within the central region (i.e., perpendicular to the accretion disc), which allows the jet to be collimated and accelerated to relativistic speeds. The jet transports energy and particles, and in the extended regions of the lobes a plasma is formed from which synchrotron radiation is emitted. It is this synchrotron radiation that allows the radio lobes to be observed. Often only one lobe is detected. When two lobes are detected either side of the central radio source, the second jet, moving away from the observer, is known as the "counter jet". This "counter jet" is generally the fainter of the two. The apparent difference in brightness of the two jets is due to preferential "Doppler beaming" of the jet approaching the observer.

Relativistic jets carry little mass and are described by high-energy phenomena. By applying energy and mass conservation constraints to the jet and then relating them to the accretion rate of the central BH, a relation between the mass loss from the central system and the BH mass can be determined (Falcke and Biermann, 1995; Falcke et al., 1995; Hubbard and Blackman, 2006).

The relation between the mass loss from the central system, known as the mass loading rate of the jet, $\dot{M}_{\mathrm{J}}$, and the luminosity of the jet, L_{J}, is given as $\dot{M}_{\mathrm{J}} = L_{\mathrm{J}}/\gamma c^2$, where γ is the jet's Lorentz factor[2]. For a given BH with a mass of M_{BH} and a corresponding Eddington luminosity of L_{Edd}, along with a conservative value for L_{J} of $0.1L_{\mathrm{Edd}}$, the corresponding value of $\dot{M}_{\mathrm{J}}$ is given as

$$\dot{M}_{\mathrm{J}} \simeq (2.2\,/\,\gamma)(M_{\mathrm{BH}}\,/\,\mathbf{M}_{\odot}) \times 10^{-10} \qquad [\mathbf{M}_{\odot}\,\mathrm{yr}^{-1}] \tag{3.1}$$

Thus, for a BH with a mass of 10^6 $\mathrm{M}_{\odot}$ and a jet with a γ of 2, the resulting value of $\dot{M}_{\mathrm{J}}$ is $\sim 10^{-4}$ $\mathrm{M}_{\odot}$ yr^{-1}, corresponding to approximately 1% of the BH accretion rate.

[2]The Lorentz factor is given as $\gamma = (1 - (v/c)^2)^{-1/2}$, for a given velocity v.

If this value is integrated over the expected lifetime of a jet ($\sim 10^7$ years), a mass of 10^3 $\mathrm{M}_\odot$ would be lost by the central system as a result of the jet.

Warm Absorbers

In the X-ray band, evidence of mass loss via winds on large scales within AGN can be found in the form of a warm absorber (WA). The term WA is applied to ionised gas seen along the observer's line of sight to the centre of the AGN. The ionised gas is adept at absorbing soft X-ray photons that are emitted from the central regions of the AGN. Since the first detection of a WA in QSO MR2251–78 with the *Einstein* observatory by Halpern (1984), the number of detected WAs has grown. The analysis of *Advanced Satellite for Cosmology and Astrophysics* (ASCA; Tanaka et al., 1994) data found that $> 50\%$ of nearby type 1 Seyfert galaxies showed evidence of a WA (Reynolds, 1997; George et al., 1998; Blustin et al., 2005, and references therein). With the new era of high resolution spectroscopy available with *XMM-Newton* and *Chandra*, the complexity of WAs has been revealed. WAs manifest themselves as narrow absorption lines in the soft X-ray spectrum of an object, usually blueshifted by a few hundred km s^{-1} (Kaastra et al., 2000; Kaspi et al., 2000a), with low to moderate ionisations[3] ($\log \xi \sim -1.4 - 1.0$) and a large range of column densities ($N_{\mathrm{h}} \sim 10^{20} - 10^{24}$ cm^{-2}; Kaastra et al., 2002; Crenshaw et al., 2003; McKernan et al., 2007). In addition to the narrow absorption lines, there is evidence of moderately ionised iron absorption. For example, the analysis of the *XMM-Newton* RGS spectra of IRAS 13349+2438 performed by Sako et al. (2001) found evidence of narrow absorption lines from L shell ions (Fe XVII-XX), along with the first detection of an unresolved transition array (UTA; $16 - 17$Å) of 2p-3d inner-shell

[3]The ionisation parameter ξ is a description of the ionisation state of a material, e.g., a cloud of gas, in which photons are either emitted or absorbed or most likely a combination of both. ξ is measured in units of erg cm s^{-1} and is defined as, $\xi = \frac{L}{nr^2}$, where L is the luminosity of the source ionising the material, n is the number density of the material and r is the distance of the material from the ionising source.

absorption by Fe M shell ions.

Work by Blustin et al. (2005) places the base of the WA outside of the BLR, as far out as the dusty torus, in agreement with the theoretical work carried out by Krolik and Kriss (2001). Krolik and Kriss (2001) suggest that the features observed from WAs are created in a multi-temperature wind that is fed by material evaporated from the inner edge of the torus by photoionisation. Blustin et al. go on to estimate the mass loss, attributed to a WA, from the central engine with a BH of mass 10^7 $\mathrm{M}_\odot$, using values taken from their sample. The authors assume a mass loss rate of ~ 0.3 $\mathrm{M}_\odot$ yr^{-1}, an accretion rate of ~ 0.04 $\mathrm{M}_\odot$ yr^{-1} and that the ratio of the mass loss rate to the accretion rate is approximately constant throughout the lifetime of the AGN (~ 0.3 Gyr, i.e., the time taken for the BH to grow to 10^7 $\mathrm{M}_\odot$). Using these values, the total mass ejected for a BH of mass 10^7 $\mathrm{M}_\odot$ during the lifetime of the AGN is $\sim 8 \times 10^7$ $\mathrm{M}_\odot$. This is considerably larger than the total mass accreted by the BH. The WA could, in theory, affect the inner regions of the host galaxy, providing a direct link between the SMBH of the AGN and its host galaxy.

Broad Absorption Line QSOs

Although mass loss due to WAs is sizeable, it is not extreme, nor are the physical properties of the outflow itself. The presence of extreme outflows in AGN has been known for some time. Evidence for these extreme outflows can be found within the UV spectra of certain quasars in the form of broad absorption lines (BALs). Quasars that exhibit these features are known as BALQSOs. The true fraction of QSOs that contain BALs is unknown and estimates of this fraction vary from $\sim 6-43\%$, determined from optically selected QSO samples. Gibson et al. (2009a), using the SDSS DR5 QSO catalogue (Schneider et al., 2007), found a BALQSO fraction of $16.4\pm0.6\%$. Other authors claim optically selected BALQSO fractions of $6 \pm 2\%$ (Brandt et al., 2000), $\approx 15\%$ (Tolea et al., 2002), $22 \pm 4\%$ (Hewett and Foltz, 2003), $13.4 \pm 1.2\%$ (Reichard et al., 2003), $\approx 26\%$ (Trump et al., 2006) and $\approx 11\%$ (Ganguly et al., 2007). Recent work by Allen et al. (2010) shows a strong redshift dependence of the intrinsic BALQSO fraction. Allen et al. calculate an intrinsic BALQSO fraction of $38.8 \pm 2.2\%$ for a redshift interval of $1.65 \leqslant z < 2.3$, which decreases by a factor of 3.5 ± 0.4 for the redshift interval of $3 \leqslant z < 4.5$. In addition to these optically selected samples, QSO samples selected at other wavelengths have been analysed to search for BALs. Becker et al. (2000) used QSOs selected from the VLA FIRST Survey (White et al., 2000; Gregg et al., 1996) and found a BALQSO fraction of $18 \pm 4\%$, whereas, Dai et al. (2008) found the BALQSO fraction of 2MASS detected QSOs in the SDSS DR3 QSO catalogue (Schneider et al., 2005) and the SDSS BALQSO catalogue (Trump et al., 2006) to be $43 \pm 2\%$.

Although the observed BALQSO fraction is still under debate, it is widely believed that all QSOs harbour BALs in one form or another (Becker et al., 2000). The prominent absorption features are generally from C IV (λ1549), N V ($\lambda\lambda$1238.8, 1242.8), Si IV ($\lambda\lambda$1393.8, 1402.8), Mg II ($\lambda\lambda 2796.3, 2803.5$), Al III ($\lambda\lambda 1854.72, 1862.79$) and H I Ly$\alpha$ ($\lambda 1215.7$), although a range of absorption features and ionisations can be present depending on the complexity of the velocity components within the outflow (Crenshaw and Kraemer, 1999). The absorption features observed are blueshifted with respect to the rest frame of the source and have widths ranging from a few thousand km s^{-1} to $\sim 0.3c$ in some instances (Weymann et al., 1991). These features are given a BALnicity index (Weymann et al., 1991) measured with respect to the C IV ($\lambda 1549$) emission line. Essentially, the BALnicity index is the width of the C IV ($\lambda 1549$) absorption feature found within the wings of the C IV ($\lambda 1549$) emission line, expressed in km s^{-1}. The

BALnicity index is only calculated for features that are a minimum of 2000 km s^{-1} in width and that are more than 3000 km s^{-1} blue-wards of the redshifted C IV emission line. However, this definition is very restrictive. Hall et al. (2002) extend this definition to incorporate low-ionisation species often found in mini-BALs, which share most if not all of the features of BALs but have widths in the range $300-2000$ km s^{-1} (Hamann et al., 2001).

BALs themselves can be split into three observationally determined subgroups (Hall et al., 2002, and references therein). First are the high-ionisation BALs (HiBALs), which show absorption from C IV ($\lambda\lambda1548.2$, 1550.8), N V ($\lambda\lambda1238.8$, 1242.8), Si IV ($\lambda\lambda1393.8$, 1402.8) and Lyα ($\lambda1215.7$). Secondly, there are low-ionisation BALS (LoBALs) which contain, in addition to the features in HiBALs, absorption from lower ionisation species, such as Mg II ($\lambda\lambda2796.3, 2803.5$), Al III and Al II. The third subset, known as FeLoBALs are rare. They are similar to LoBALs, however, they show evidence of additional absorption features due to Fe III and Fe II. It has been suggested that FeLoBALs are young objects (e.g., young QSOs) encased in a dust cocoon (Hall et al., 2002). Farrah et al. (2007) looked at mid/far-infrared (MIR/FIR) data of 9 infrared (IR) bright FeLoBALs and suggested that FeLoBALs are QSOs containing an extremely luminous starburst episode that is nearing the end of its life, with the central SMBH casting off its dusty cocoon, i.e., FeLoBALs may be a transition phase of an ultra-luminous IR galaxy (ULIRG) into a QSO.

The range of ionisation states needed to produce the observed absorption features for all types of BALs ($\log \xi \simeq -4-1$; Crenshaw et al., 2003) require that the outflows are shielded from the irradiating central source to some extent (Murray and Chiang, 1995; Murray and Chiang, 1997; Proga et al., 2000; Proga and Kallman, 2004). The determination of the column densities in BALs can be problematic due to the poor understanding of UV absorption. Using the values typically quoted ($\log N_{\rm h} \approx 18.0 - 21.5$; Crenshaw et al., 2003), the resulting mass loss rates due to the absorber, $\dot{M}_{\rm abs}$, are of the order of the BH accretion rates, $\dot{M}$, for these objects.

The study of the BAL phenomenon is vast and a full discussion of its intricacies is beyond the scope of this thesis. The reader is directed to the review by Crenshaw et al. (2003, and references therein), which contains a comprehensive discussion on intrinsic UV and X-ray absorption in AGN that covers both BALs and WAs. The unification of the observed properties of BALs, links with WAs and their ejection and driving mechanisms have not been discussed here. However, they will be touched upon in the mechanisms section (Section 3.1.2).

High-Ionisation, High-Velocity X-ray Outflows

High-ionisation, high-velocity X-ray outflows detected in certain AGN is the last form of mass loss to be discussed. The discovery of such outflows from AGN in recent years has been a source of great discussion within the field. The well known target PDS 456 (Reeves et al., 2002; Reeves et al., 2003; Reeves et al., 2009) is the best known high-luminosity candidate to exhibit such an outflow. This target shows clear evidence for outflowing material in the form of absorption features in both its X-ray and UV spectra (O'Brien et al., 2005). The UV spectrum is extreme and shows a broad Lyα absorption trough that is blueshifted between $14 - 24 \times 10^3$ km s^{-1}, but has no evidence of other BAL features. In the X-ray regime, PDS 456 is also extreme; the X-ray absorption is seen to vary between the observations of PDS 456 since it was first observed in 1998 (Reeves et al., 2009). Reeves et al. (2003) associated the absorption seen in the EPIC PN data from the *XMM-Newton* observation taken in February 2001 (Figure 3.1) with broadened ($v_{\rm turb} = 10^3$ km s^{-1}) Fe K & L shell absorption, resulting in an outflow velocity of $v_{\rm out} = 0.25^{+0.12}_{-0.04}c$. The absorbing column density and ionisation parameter required to produce this absorption were found to be $N_{\rm h} = 5.7^{+2.0}_{-2.5} \times 10^{23}$ cm^{-2} and $\log \xi = 2.5 \pm 0.3$, respectively. Reeves et al. (2009) then reported on a deep (~ 190 ks) *Suzaku* (Mitsuda et al., 2007) observation of PDS 456 from 2007. The authors confirm the presence of a high-ionisation, high-velocity outflow, identifying the absorption as broadened ($v_{\rm turb} = 10^4$ km s^{-1}) He-like resonance absorption by Fe XXVI (1s-2p). The outflow velocity, absorbing column density and ionisation parameter were then found to be $v_{\rm out} \approx 0.26 \pm 0.02c - 0.31 \pm 0.02c$, $N_{\rm h} \approx 0.22 - 2.1 \times 10^{24}$ cm^{-2} and $\log \xi \approx 4.5^{+1.3}_{-0.7}$, respectively. Using a conservative covering factor value of 10%, Reeves et al. estimate the mass outflow rate for each separate observation to be $\sim 10\,{\rm M}_{\odot}$ yr^{-1}. The mass of the (suspected Schwartzchild) BH at the centre of PDS 456 is $\log M_{\rm BH} = 9.3 \pm 0.4$ M$_{\odot}$. Combined with an efficiency $\eta = 0.06$, Reeves et al. estimate the Eddington limited accretion rate, $\dot{M}_{\rm Edd}$, to be ~ 50 M$_{\odot}$ yr^{-1}. Thus, the outflow mass is likely to be a substantial fraction of the actual accretion rate. The authors go on to estimate the kinetic energy contained within the outflow, $\dot{E} \approx 2 \times 10^{46}$ erg s^{-1} and the bolometric luminosity of PDS 456, $L_{\rm Bol} \approx 1.8 \times 10^{47}$ erg s^{-1}. This suggests that the kinetic energy of the outflow may be an appreciable fraction of the bolometric luminosity of PDS 456.

Along with PDS 456, there are a number of other targets that appear to manifest this type of outflow, albeit less extreme. Some examples are: PG 1211$+$143 (Pounds et al., 2003a; Pounds and Page, 2006; Pounds and Reeves, 2009, Figure 3.2), APM 08279$+$5255 (a BAL; Chartas et al., 2002; Hasinger et al., 2002; Chartas et al., 2009), PG 0844$+$349 (Pounds et al., 2003b), PG 1115$+$080 (a mini-BAL; Chartas et al., 2003), Mrk 509 (Dadina et al., 2005), MR 2251$-$178 (Gibson et al., 2005), IC 4329a (Markowitz et al., 2006), MCG$-$5-23-16 (Braito et al., 2007) and Ark 564 (Papadakis et al., 2007). These sources exhibit evidence of outflows with velocities of $\gtrsim 0.1c$, based on the identification

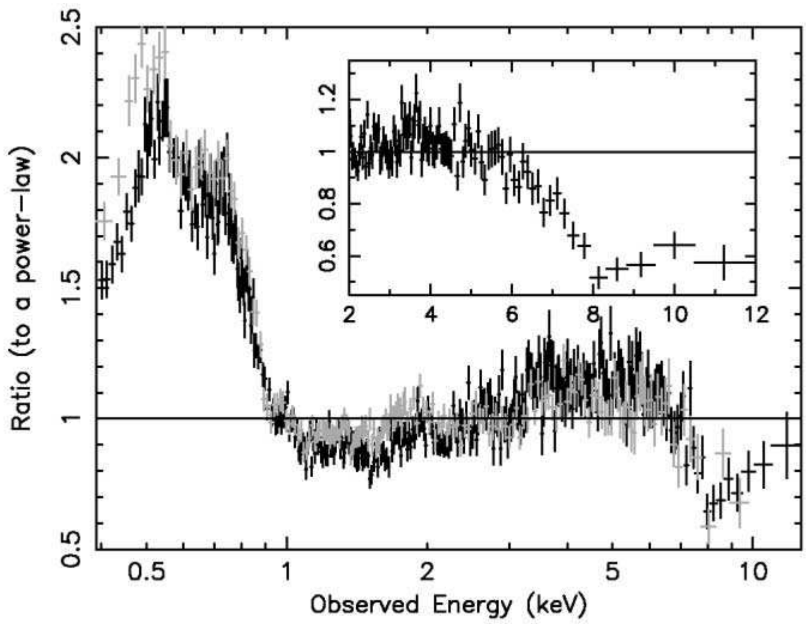

FIGURE 3.1: Ratio plot of the broad-band X-ray spectrum of PDS 456 to a simple Galactic absorbed power-law model (with $\Gamma = 2$). Black: PN data. Grey: MOS data. The inset shows a power-law fit to the $2-12$ keV PN data. This image is taken from Reeves et al. (2003, their Figure 1). Note the absorption due to the iron K shell band (~ 8 keV).

of absorption lines from H- and He-like species of Fe. Not all of the above authors give absorbing column densities or ionisations, but for those that do the cited numbers are $N_{\rm h} \gtrsim 1 \times 10^{22}$ cm^{-2} and $\log \xi \gtrsim 2.9$, respectively. APM 08279+5255 is an interesting case as Chartas et al. (2002; 2009) claim that there are two separate high-ionisation, high-velocity outflows detected in its *XMM-Newton* and *Chandra* X-ray spectra. Chartas et al. (2009) associate two detected absorption lines with the same species of iron (Fe XXV or Fe XXVI) but outflowing at different velocities. They calculate the outflow velocities to be $\sim 0.2c$ and $\sim 0.61c$ with an upper limit of $\sim 0.76c$ placed on the faster component. As with PDS 456, the mass loss rates of these other objects are of the order of the BH accretion rate, although the energy budgets involved are not as impressive. All are radio

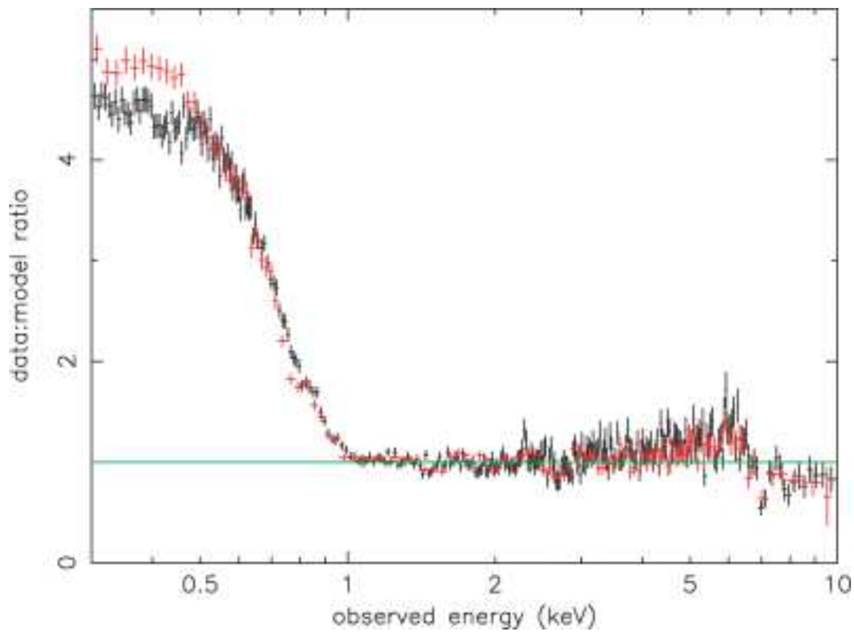

FIGURE 3.2: Ratio plot of $0.3-10$ keV EPIC data of PG 1211+143 to Galactic absorbed $1-10$ keV power-law fit. Black: PN data. Red: MOS data. Image taken from Pounds et al. (2003a, their Figure 3). Note the soft excess below 1 keV and the iron K shell absorption around ~ 7 keV.

quiet (RQ) and are thought to be accreting at a high rate around, or above, the Eddington limit.

Absorption features detected primarily in the hard-band of the X-ray spectra of these objects, at $\sim 7-8$ keV (intrinsic), suggest the presence of high-ionisation, high-velocity outflows, with other features found in high-resolution X-ray spectra below 2 keV. This is a result of the high-ionisation ($\log \xi \sim 3.5$ for the observed species of Fe) of the absorbing material along the line of sight of the observer. At this level of ionisation, elements in the absorbing material with small atomic numbers will be completely ionised. Those elements that are not completely ionised, such as oxygen and heavier elements up to iron, will have a deficit of electrons, potentially leaving them in H- and He-like states.

The large (trough-like) absorption features in the hard-band are most likely due to Fe K & L band electrons, e.g., Fe XVII-XXVI. Further evidence of ionised Fe ($\sim \lambda 12-13$ Å) can be seen as absorption lines in the soft X-ray spectra, often blended with K shell absorption from Ne IX-X. Other examples of ionic species that produce prominent absorption features are O VII-VIII (cf. the large jump in opacity often observed in type 1 AGN at $\sim 0.6-0.7$ keV; Turner and Pounds, 1988), Mg XII Lyα (~ 1.47 keV) and S XVI (~ 2.6 keV). The species listed here are only a handful of those found but they generally represent the final ionisation states for those atoms detected in the X-ray spectra. Analysis of high resolution spectra obtained with the *Chandra* low- and high-energy transmission gratings and with the RGS cameras aboard *XMM-Newton* show the presence of other transitional states from these ionic species, e.g., the Fe M Shell UTA (Sako et al., 2001).

As with the other forms of mass loss, the mechanisms behind these X-ray outflows are not well known, although a number of promising candidates will be discussed in Section 3.1.2. However, it should be noted that there have been attempts to disprove the outflow velocities cited, if not the presence of an outflow entirely. In the case of PG $1211+143$, Kaspi and Behar (2006), using a slightly different analysis methods to Pounds et al. (2003a), come to the conclusion that the outflow velocity is ~ 3000 km s^{-1} rather than $\sim 0.1c$ as cited by Pounds et al. (2003a). Kaspi and Behar suggest blueshifted absorption features attributed to Fe XXVI could be the result of absorption from several less ionised, consecutive Fe ions. They also find evidence of several broad (FWHM $\approx$ 6000 km s^{-1}) emission lines, e.g., N VI Lyα and O VII Lyα. Although Kaspi and Behar suggest a lower outflow velocity, they do concede that as a result of poor signal-to-noise, they cannot completely rule out a high velocity component within the outflow. More recently, Pounds and Page (2006; 2009) have now confirmed the presence of a high-velocity outflow in PG 1211 + 143.

PG 1211 + 143 has, along with PDS 456, also been scrutinised by McKernan et al. (2004) whilst the authors investigated O VII and O VIII absorption from within our own Galaxy. They suggest that absorption believed to be intrinsic to AGN may in fact result from absorption by hot, local gas. When taking into account the redshift of the sources and the cited outflow velocities (Pounds et al., 2003a), the resulting velocities at $z = 0$ are small ($cz \approx 3 \times 10^2$ km s^{-1}) and are consistent with rotational velocities associated with the Galaxy. However, work by Reeves et al. (2008), who look at the *XMM-Newton* and *Suzaku* observations of PG 1211+143 refutes the work of McKernan et al. (2004). Reeves et al. (2008) show that the variation in the observed 7 keV Fe K absorption line leads to a compact scale size for the absorber (a few parsecs) and that the surface brightness of the gas is too bright ($9 - 10$ orders of magnitude) to arise within our own Galaxy, the local group or from the warm/hot intergalactic medium (WHIM). In a similar fashion to McKernan et al., Brinkmann et al. (2006) re-analysed the MOS data for PG 0844 + 349. They concluded that they are unable to confirm the classification of the spectral features reported by Pounds et al. (2003b), claiming that the nature and position of the iron absorption feature around 7 keV is unclear and that the detected O VII absorption may be caused by incorrect modelling of the soft X-ray emission or by the uncertainties left from the calibration of the detector.

3.1.2 Mechanisms and Unification

Having discussed the observational evidence for the various forms of mass loss, an overview of the mechanisms suggested to explain such phenomena will now be provided. Much theoretical work is being carried out in an attempt to determine the processes involved in mass loss and, to some extent, provide a unification to the various outflows observed. If the unification paradigm (Antonucci, 1993) is to be believed, that type 1 and type 2 AGN are from the same parent population, the unification process must also take into account the various mass loss processes. Depending on a number of factors, including BH mass, accretion rate and composition of the material surrounding the BH, the mechanisms suggested for outflows must explain all forms of outflow (Elvis, 2000). It is likely that the properties of both the outflow and the central system are closely related (King, 2003). It is also possible that a source may exhibit a number of outflows throughout its lifetime (cf. FeLoBALs) or exist concurrently, e.g., radio-loud BALs (Becker et al., 2000), the BAL members of the X-ray sources exhibiting high-ionisation, high-velocity outflows (e.g., APM 08279+5255) and the recent discovery of high-ionisation, high-velocity X-ray outflows in a small number of BLRGs (Tombesi et al., 2010b).

The exact nature of outflows is not well defined, although in general, one of three main types of outflow model is invoked to explain the mass loss observed; thermal driving, radiation driving (line and continuum) and magnetic driving. The mechanisms themselves are poorly understood, particularly magnetic driving, and a large amount of on-going work is being carried out to better understand these processes.

Thermal driving is a result of irradiation of the outer parts of the accretion disc by the corona above it and the central source. The irradiation produces a pressure difference between the surface of the disc and the surrounding medium, resulting in material being driven to higher scale heights and gaining thermal velocity. At some radius, known as the launch radius, the thermal velocity will become greater than the escape velocity of the disc (Begelman et al., 1983; Krolik and Kriss, 1995). This leads to a thermal wind that carries mass away from the central system. However, these thermal winds will not reach the velocities of the observed outflows. An example of suspected thermal winds are galaxy wide superwinds, initiated by starburst or supernova events, e.g., the galactic wind seen in M82 (see Veilleux et al., 2005, for a review of galactic winds). These superwinds can enrich (with metals) and heat the interstellar, intracluster and intergalactic mediums, depending on their scale.

Radiation driving appears to be the most promising scenario to describe the mechanism involved in driving the outflows observed in AGN. After a wind is launched from the disc, e.g., by thermal driving, it can then be accelerated to greater speeds by radiation, increasing the mass loss rate considerably. Whether the outflow is driven by radiation pressure from emission lines (Murray and Chiang, 1995; Murray and Chiang, 1997; Proga et al., 2000; Proga and Kallman, 2004) or from continuum emission (Chelouche and Netzer, 2003; Everett and Ballantyne, 2004) is still under debate. A common difficulty is explaining the ionisation state of the wind. For instance, to observe the column densities and ionisation values quoted for BALs, the wind material must be, to some extent, partially shielded from the central source, otherwise the wind will become too ionised. This would effectively make it transparent to the radiation pressure and therefore unable to produce the observed velocities. In addition, if the wind material is completely un-shielded, the launch radius would have to be much further out and the wind much denser for the observed outflows to occur, properties which are not predicted by current radiation models.

Radiation driven winds, when used in conjunction with orientation effects, can be used to explain both the presence of BALs and the narrower absorption lines in WAs. Elvis (2000) proposed such a model for AGN that goes some way to provide unification between not only type 1 and type 2 AGN but also between the various types of outflows seen. The model proposed is fairly simple; it consists of a funnel-shaped, thin shell geometry (Figure 3.3) and removes the need for the dusty torus. With the addition of other parameters, such as dust and luminosity, this geometry can reproduce the observed properties in AGN. However, at the time of publication, high-ionisation, high-velocity X-ray outflows had not been proposed and are not covered by Elvis (2000). It is possible that high-ionisation, high-velocity outflows are only seen when viewed from a preferential viewing angle, in which the observer sees material close to the central engine, e.g., BALs, as shown in Figure 3.3. Reeves et al. (2009) place the base of the outflow seen in PDS 456 between $\sim 30 - 100$ gravitational radii ($r_{\rm g} = GM_{\rm BH}/c^2$; $\sim 1 - 3 \times 10^{16}$ cm). The lower estimate is based on the variation seen in the X-ray spectra on timescales of $20 - 30$ ks and assumes an inhomogeneous outflow consisting of clumpy material. The upper limit is based on a homogeneous spherical or bi-conical outflow. These estimates would place the start of the outflow at the base of the funnel where the cylindrical outflow starts to expand. At this location, the X-ray absorber could be protecting the material that would normally be viewed as a BAL and thus no BALs would be detected, which could be the situation in PDS 456. If this is the case, a high incidence of high-ionisation, high-velocity X-ray outflows would be expected. However, the detection of these outflows depends on data quality, meaning there could be a high incidence of high-ionisation, high-velocity X-ray outflows, they just have not been detected yet.

Along a similar theme, Pounds et al. (2003a; see also King and Pounds, 2003) showed that for the outflow found within PG $1211+143$, the required column densities were likely to be optically thick, almost Compton thick, to continuum emission at small radii. They believe it is inevitable that an object with a mass outflow rate, $\dot{M}$, similar to its Eddington accretion rate, $\dot{M}_{\rm Edd}$, will produce a photosphere that is optically thick to electron scattering as a result of a continuum driven wind. Pounds et al. (2003a) suggest that this photosphere could be used to produce the big blue bump (BBB) found in the UV regime of AGN spectral energy density (SED) plots. A similar approach can be taken with ultra-luminous X-ray (ULX) sources, where the photosphere could be the source of

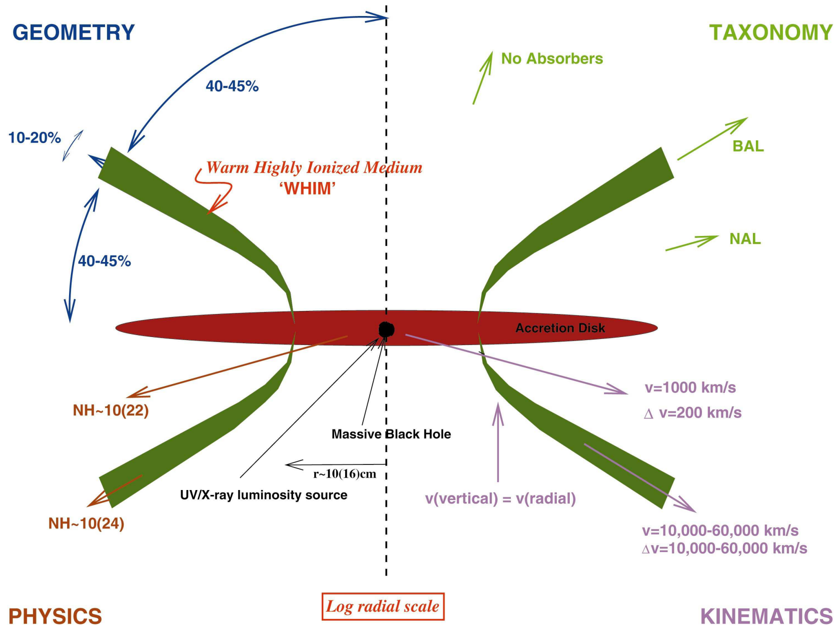

FIGURE 3.3: The structure of QSOs as proposed by Elvis (2000). This image is taken from Elvis (2000, their Figure 1). Depending on the orientation, different subclasses of QSO are seen.

the ultra-soft X-ray photons. In context with the model proposed by Elvis (2000), the photosphere could contribute towards the unification of AGN, removing the need for a dusty torus. However, it may prove difficult to use such a description for objects not accreting at or beyond the Eddington limit.

The final and least understood driving mechanism is magnetic field driving. This mechanism is believed to arise from rotating magnetic field lines that centrifugally transport and accelerate matter away from the disc. This method is often used to explain radio jets found within radio galaxies (Blandford and Payne, 1982). Even with the large amount of work in this field (Kato et al., 2004; Hawley and Krolik, 2006; Kato, 2007), current limitations in observational data prevent the determination of the true nature of magnetically driven winds. These winds are used to explain the X-ray outflow found within PDS 456, after extreme X-ray variability previously detected in PDS 456 was believed to be the result of magnetic flaring in the accretion disc (Reeves et al., 2002). Reeves et al. (2003) compare the magnetic wind to a radio jet, suggesting that the wind could be a failed radio jet. The authors suggest that this could be a result of less tightly wound magnetic field lines in the wind system when compared to the magnetic field lines in a radio jet. In this scenario, WAs could be failed or slower versions of the high-velocity outflows. Thus, depending on the evolution of the central region and the surrounding areas of an AGN, along with other intrinsic properties of the AGN, all forms of outflow may be present at some point throughout the lifetime of all AGN.

The processes behind outflows, in particular high-ionisation, high-velocity X-ray outflows, are likely to be a hybrid of the mechanisms discussed here, as described in work presented by Proga (2003) and Everett (2005). The combination of observations taken with future generations of X-ray and UV telescopes, which will lead to greater constraints on outflow properties, and the quickly developing theoretical work currently taking place, should lead to a better understanding of outflow mechanisms.

3.1.3 Relevance of Mass Loss

The study of high-ionisation, high-velocity outflows is one of great importance. The identification of the processes involved in these outflows and the reasons behind their formation are likely to be closely linked to the accretion process in AGN. High-ionisation, high-velocity outflows are also relevant on a larger scale, since they could provide a connection between the AGN and its host galaxy. They could also provide an explanation for the apparent dichotomy of radio loudness in AGN. If outflows are present for a large fraction, if not the entirety, of the lifetime of an AGN ($\sim 10^7$ yr), the amount of mass injected back into the surrounding area and host galaxy can be quite large (of the order of the mass of the SMBH). At high redshifts this outflow could have provided feedback on a galactic scale that could have given rise to the $M_{\rm BH} - \sigma_*$ relation (Ferrarese and Merritt, 2000; Gebhardt et al., 2000a; Tremaine et al., 2002), where σ_* is the stellar velocity dispersion of the host galaxy's bulge. The $M_{\rm BH} - \sigma_*$ relation takes the form

$$\log_{10}\left(M_{\rm BH}/{\rm M}_\odot\right) = \alpha + \beta \log_{10}\left(\sigma_*/\sigma_0\right) \tag{3.2}$$

where α and β are determined observationally and σ_0 is a reference value chosen by the observer, normally $\sigma_0 = 200$ km s^{-1}. The cited values of β vary between $3.75 - 5.3$ (Tremaine et al., 2002). The mass ejected is also likely to enrich the ISM with metals. If it interacts with the ISM or contains regions of high density, it is possible the outflow could trigger star formation (Blustin et al., 2005).

If mass outflows are common to all AGN, then why are they not observed in all AGN, or at least more frequently? Could viewing angle account for this? Could they be redshift dependent? In the case of high-ionisation, high-velocity X-ray outflows these questions are particularly important, as the number of objects showing evidence for these outflows is small (≈ 10 with $0.008 \lesssim z \lesssim 3.71$). It has been suggested that this type of outflow is linked to high-accretion rate objects ($\dot{M} \approx \dot{M}_{\rm Edd}$; Section 3.1.1; King, 2003). The remainder of this chapter focuses on a sample of suspected high-accretion rate AGN that were chosen as means of testing this assumption. The selection procedure, observations with *XMM-Newton*, data reduction, spectral analysis and results of this sample will now be discussed.

3.2 Sample Selection

The sample of objects to be examined for evidence of high-ionisation, high-velocity X-ray outflows was taken from the paper by Wang (2003). The author determines a limit relation between the mass of the central BH, $M_{\rm BH}$, and the full width half maximum of the Hβ line, $v_{\rm FWHM}({\rm H}\beta)$. A brief summary of the relation follows.

3.2.1 $M_{\rm BH}$ – Hβ Line Width Relation

The rate at which the SMBH at the centre of an AGN is accreting matter, $\dot{M}$, is thought to drive most of the observable features of AGN. Unfortunately, current observational limitations mean that $\dot{M}$ cannot be determined with any certainty. The theoretical limit at which an object can accrete matter, the Eddington rate ($\dot{M}_{\rm Edd}$), is thought to be exceeded in certain AGN (e.g., NLS1s; Section 1.1.5). However, there is no direct way of determining whether an object is accreting at a super-Eddington rate or not. It may be possible, using the limit relation between $M_{\rm BH}$ and $v_{\rm FWHM}({\rm H}\beta)$, to probe the inner regions of AGN and theorise whether they are accreting at super-Eddington rates.

The limit relation is based upon the established theoretical models of slim accretion discs (Abramowicz et al., 1988) and the empirical reverberation relation (Kaspi et al., 2000b). Reverberation mapping is the study of the response of BLR emission line widths to variations in the irradiating continuum source (Bahcall et al., 1972; Blandford and McKee, 1982; Peterson, 1993). Kaspi et al. (2000b) used this technique to study a sample of 34 AGN and reported that the size of the BLR, $R_{\rm BLR}$, is dependent on the luminosity of the source at a wavelength of 5100 Å, giving rise to the empirical reverberation relation

$$R_{\rm BLR} = R_0 \left(\frac{\lambda L_\lambda}{10^{44}\,{\rm erg\,s^{-1}}} \right)^{\beta} \quad \text{[light-days]} \tag{3.3}$$

where λL_λ is the continuum luminosity at 5100 Å, $R_0 = 32.9^{+2.0}_{-1.9}$ and $\beta = 0.7 \pm 0.003$. The exact values of R_0 and in particular β are still a matter of debate; values of β vary between 0.5 and 0.78 (Kaspi et al., 2000b; Vestergaard, 2002; Netzer, 2003; Peterson et al., 2004; Kaspi et al., 2005; Vestergaard and Peterson, 2006; Bentz et al., 2006; Bentz et al., 2008). There are a number of reasons that might explain the large scatter in the values obtained for β. The large range could be from an analytical point of view, i.e., line profiling, the statistical and error techniques used or even the form of cosmology used. Even though it is assumed that the optical continuum can be represented by a power-law ($L_{\rm opt} \propto \nu^{-\alpha}$; Netzer, 2003), this may not be an ideal description. On the other hand, the scatter in β could be more physically motivated, in that not all AGN are identical, e.g., their BLR geometries or spectral energy densities (SEDs) could vary. It addition, the value of β can also be affected by optical reddening within the host galaxy and by contamination from stellar light within the host galaxy. Recent work by Bentz et al. (2006; 2008), who looked at the reverberation mapping results of 35 AGN after removing the contaminating star light at $\lambda5100$ Å from the AGN host galaxies, determined β to be $0.519^{+0.063}_{-0.066}$. This is consistent with the value of $\beta = 0.5$, determined using the naive assumption that all BLR are identical, i.e., that they have the same geometry, composition, density, ionisation parameter etc, and that all AGN have the same SED, i.e., all AGN are scaled up or down versions of one another (Bentz et al., 2008). However, it should be noted that AGN have been shown to have different SEDs (e.g., Mushotzky and Wandel, 1989; Zheng and Malkan, 1993). The exact values of β and R_0 do not interfere with the derivation of the limit relation. However, they can have a large effect on the consequences of the limit relation, as discussed later in this section.

During the following discussion, it is assumed that the $\mathrm{H}\beta$ line is emitted within the BLR clouds of the AGN and that the BLR clouds are virialised in the gravitational potential of the central SMBH. If the continuum source of the AGN increases in luminosity then as a consequence of the empirical reverberation relation so must $R_{\rm BLR}$ increase. This implies $v_{\rm FWHM}(\mathrm{H}\beta)$ has a dependency on $\dot{M}$ in the sub-Eddington phase ($\dot{m} = \dot{M}/\dot{M}_{\rm Edd} < 1$). For the luminosity to increase $\dot{M}$ must increase. As $R_{\rm BLR}$ increases due to the increased luminosity, $v_{\rm FWHM}(\mathrm{H}\beta)$ must decrease due to $v_{\rm FWHM}(\mathrm{H}\beta)$ being inversely proportional to $R_{\rm BLR}$. This means that $v_{\rm FWHM}({\rm H}\beta)$ is inversely proportional to $\dot{M}$ in the sub-Eddington phase. However, it is in the super-Eddington ($\dot{m} > 1$) phase that the limit relation takes affect. In the standard model of a slim accretion disc ($\dot{m} < 50-100$; Abramowicz et al., 1988), the nature of the accretion disc emitting the continuum radiation, its resulting spectrum and variability are not well known (Wang et al., 1999; Mineshige et al., 2000; Wang and Netzer, 2003). In the standard accretion disc model (Shakura and Syunyaev, 1973), the regions close to the centre of the accretion disc are radiation dominated in the sub-Eddington phase. This is also true for a slim accretion disc with the exception that advection of energy to the centre of the accretion disc is efficient enough to limit the amount of radiation being emitted by the accretion disc (Chen and Taam, 1993). In effect, photon trapping takes place within the disc, altering the dependency of the disc's luminosity, $L_{\rm Disc}$, on $\dot{M}$ (Begelman, 1978; Begelman and Meier, 1982). In the sub-Eddington phase, $L_{\rm Disc}$ is strongly dependent on $\dot{M}$. In the super-Eddington phase, $L_{\rm Disc}$ is weakly dependent on $\dot{M}$, $L_{\rm Disc} \propto \log(\dot{M})$, and is instead linearly proportional to $M_{\rm BH}$ (Abramowicz et al., 1988; Wang and Zhou, 1999; Mineshige et al., 2000; Ohsuga et al., 2002). Thus, in the context of a slim accretion disc model, the output luminosity is limited. Work by Ohsuga et al. (2002) and Wang and Zhou (1999), calculate this limited luminosity to be roughly the Eddington luminosity. As a consequence of this limited luminosity, the dependency of $L_{\rm Disc}$ on $M_{\rm BH}$ in the super-Eddington phase and the empirical reverberation relation, a relationship between $M_{\rm BH}$ and $v_{\rm FWHM}({\rm H}\beta)$ is therefore expected.

If the continuum luminosity is limited at or around the Eddington luminosity, then from the empirical reverberation relation, $R_{\rm BLR}$ will also be limited. This is known as the Eddington size. At this radius, $v_{\rm FWHM}({\rm H}\beta)$ is known as the Eddington width (Wang, 2003). Thus, the $v_{\rm FWHM}({\rm H}\beta)$ is a measure of the gravitational potential of the central BH and hence a measure of $M_{\rm BH}$ itself. The derived Eddington limit relationship between $M_{\rm BH}$ and $v_{\rm FWHM}({\rm H}\beta)$ is

$$M_{\rm BH,6} = l_1\, v_{\rm FWHM,3}^{2/(1-\beta)} \tag{3.4}$$

where $M_{\rm BH,6}$ is the mass of the central BH in units of 10^6 $\rm M_\odot$, $v_{\rm FWHM,3}$ is the value of $v_{\rm FWHM}({\rm H}\beta)$ in units of 10^3 km s^{-1}. The constant l_1 is dependent on β and is defined as

$$l_1 = \left[\frac{\xi}{1.26}\left(\frac{10}{1.46\,R_0\,f^2}\right)^{\frac{1}{\beta}}\right]^{\frac{\beta}{\beta-1}} \tag{3.5}$$

where it is assumed that the factor, f, representing the BLR geometry is 1. ξ is the ratio of the luminosity of the accretion disc to the luminosity of the disc at 5100 Å ($L_{\rm Disc}/L_{5100}$) and has a value between 4.0 and 7.5 (Wang et al., 1999). Using Equations 3.4 and 3.5, the Eddington limit can be drawn on a plot of $M_{\rm BH}$ against $v_{\rm FWHM}({\rm H}\beta)$ (Figure 3.4). Any objects lying to the left of the line are suspected super-Eddington accretors and any lying to the right of are thought to be sub-Eddington accretors.

Wang (2003) also discusses the possibility that this Eddington limit relation could be altered if the Eddington limit is relaxed. The Eddington limit could be relaxed if the slim accretion disc is magnetic, resulting in photon bubble instabilities (Gammie, 1998). In essence, when the BH is accreting at super-Eddington rates, the photons trapped in low density regions within the disc, may be liberated by the magnetic field lines of the disc. Thus, relaxing the limit on the Eddington luminosity and consequently altering the limit relation. Wang (2003) cites Begelman (2001; 2002) as having worked on this problem. Begelman (2001) reports that the maximum luminosity in this situation is $L_{\rm max} \approx 300 M_{\rm BH,6}^{1/5} L_{\rm Edd}$. This maximum luminosity is known as the Begelman limit. Following the same procedure for the Eddington limit relation, a Begelman limit relation between $M_{\rm BH}$ and $v_{\rm FWHM}({\rm H}\beta)$ can be calculated. However, the Begelman limit relation is rather large (see Figure 3.4) and would not lead to any super-Eddington candidates

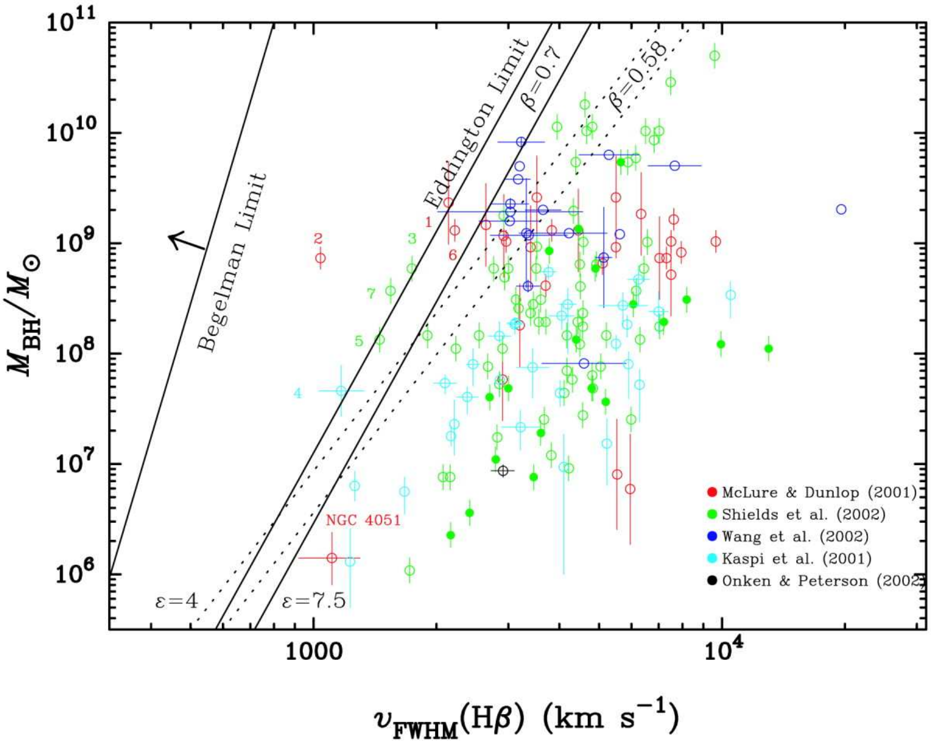

FIGURE 3.4: Plot of $v_{\rm FWHM}({\rm H}\beta)$ against $M_{\rm BH}$ for 164 AGN tested by Wang (2003). Figure taken from Wang (2003). The seven numbered targets are suggested high accretion rate objects and are discussed by Wang (2003). Six of the seven numbered sources form the sample analysed in this thesis. The significance of the differing values of β and ξ are discussed in the text, along with a brief discussion of the Begelman limit.

from current observations. For this thesis, it is assumed that the Eddington limit relation is correct. Although, it is likely that some objects reported below may be undergoing a hybrid of both the photon trapping process and photon bubble instability process in their accretion discs.

Having determined the Eddington limit relation in Equation 3.4, Wang goes on to test this relation for 164 AGN. The 164 objects are consolidated from smaller samples compiled by other authors, where $M_{\rm BH}$ had been estimated. $M_{\rm BH}$ was estimated from either reverberation mapping (Wandel et al., 1999; Kaspi et al., 2000b), the ${\rm M}_R - M_{\rm BH}$ relation (Kormendy and Richstone, 1995; Ho, 1999; McLure and Dunlop, 2001), where ${\rm M}_R$ is the absolute R-band magnitude of the host galaxy, or the $M_{\rm BH}-\sigma_*$ relation (Ferrarese and Merritt, 2000; Gebhardt et al., 2000a; Tremaine et al., 2002).

Figure 3.4 shows a plot of $M_{\rm BH}$ against $v_{\rm FWHM}({\rm H}\beta)$ for the 164 objects taken from Wang (2003). The seven numbered objects close to or above the Eddington limit line are listed in Table 3.1, along with their $v_{\rm FWHM}({\rm H}\beta)$ and estimated $M_{\rm BH}$ values. These seven objects are thought to be accreting at super-Eddington rates. Of these, six form the sample analysed in this thesis (Section 3.2.2). However, before individually discussing these six targets, it should again be noted that the Eddington limit relation is sensitive to ξ and in particular β. As shown in Figure 3.4, differences in the values of β $(0.58-0.7)$ and ξ $(4-7.5)$ can have a large effect on the Eddington limit relation.

If $\beta\sim 0.59$ as reported by Bentz et al. (2008), the number of super-Eddington candidates is dramatically increased, particularly at larger $v_{\rm FWHM}({\rm H}\beta)$ values. This suggests that a higher fraction of high-mass BHs might be accreting at super-Eddington rates, which is thought not to be the case.

The seven targets listed in Table 3.1 are narrow line objects and the empirical reverberation relation (Equation 3.3) is calibrated for broad line objects (Kaspi et al., 2000b). The question is whether this relation can be extended to include narrow line objects. For instance, broad line objects, both active and non-active, follow the same $M_{\rm BH}-\sigma_*$ relation (Nelson, 2000; Gebhardt et al., 2000b; Ferrarese et al., 2001; Wandel, 2002; Boroson, 2003; Shields et al., 2003). However, it is suggested that narrow line objects, e.g., NLS1s, do not follow the same trend as this broad line relation. NLS1s are shown to lie below the broad line relation, implying smaller BH masses (Mathur et al., 2001; Bian and Zhao, 2004; Grupe and Mathur, 2004a; Botte et al., 2004). The extreme variability seen within the X-ray spectra of NLS1s also suggests that they contain smaller BH (Pounds et al., 1995). Clearly, there are obvious observational differences between NLS1s and broad line AGN that have been well catalogued (Section 1.1.5). However, whether this apparent dichotomy is real or not is a matter of debate. Much work has been done to try and resolve this dichotomy and show that NLS1s can be classed as an extension to broad line AGN. In fact, work by Wang and Lu (2001) and Wandel (2002; 2004), who looked at the relation between $M_{\rm BH}$ and the bulge luminosity, $L_{\rm Bulge}$, shows that there is no clear difference between NLS1s and broad line objects in terms of the $M_{\rm BH} - \sigma_*$ relation. Marconi et al. (2008) discuss the effects of radiation pressure, specifically that it is not normally taken into account when calculating single epoch virial BH masses. Single epoch virial masses are mass estimates where a measured feature, e.g., the Hβ line width, from one observation is used to determine $M_{\rm BH}$ using a previously calibrated relation, e.g., $R_{\rm BLR}$ from the empirical reverberation relation, assuming the feature emitting region is virialised by the gravitational potential of the BH, e.g., $M_{\rm BH} \approx v_{\rm FWHM}({\rm H}\beta)^2 \, R_{\rm BLR}/G$. Marconi et al. (2008) find that when radiation pressure is taken into account, NLS1s move onto the $M_{\rm BH} - \sigma_*$ relation for broad line AGN. Decarli et al. (2008a; 2008b) discuss the effects that the BLR geometry can have on the $M_{\rm BH} - \sigma_*$ relation. The authors suggest that if the BLR is disc-like rather than isotropic, then the viewing angle can account for the discrepancies seen between NLS1s and broad line AGN in the $M_{\rm BH} - \sigma_*$ relation. However, this is difficult to prove and would require that NLS1s be viewed edge on, which would be in conflict with the current unification paradigm (Section 1.1.4).

Some authors have commented on the accuracy of the techniques used to determine $M_{\rm BH}$, as discussed here. Obviously, beyond the local universe (even within it in some circumstances) it is impossible to measure the velocity dispersion of individual AGN host galaxy bulge stars and it can be difficult to measure AGN host galaxy bulge luminosities due to the intrinsic nature of AGN. Instead of long duration direct stellar velocity dispersion measurements, using stellar absorption features, e.g., Mg *b* $\lambda 5180$ Å and the Ca II triplet $\sim \lambda 8600$ Å, it is common practice to use the velocity dispersion of the gas within the NLR. The origin of the [O III] line is thought to be from within the NLR and its width is thus used as a surrogate to estimate the stellar velocity dispersion, $\sigma_* = \mathrm{FWHM}\,([\mathrm{O\,III}])/2.35$, particularly in distant objects such as AGN (e.g., Nelson and Whittle, 1996; Jiménez-Benito et al., 2000; Bian and Zhao, 2004; Grupe and Mathur, 2004a; Botte et al., 2004). Botte et al. (2005) performed stellar velocity dispersion calculations of eight NLS1s using the Ca II triplet instead of the [O III] line width. They find that [O III] typically overestimates the stellar velocity dispersion values. Consequently, using Ca II measurements show that NLS1s follow the broad line AGN $M_{\mathrm{BH}} - \sigma_*$ relation. Also, work by Watson et al. (2007) on virial measurements of M_{BH} using the second moment of the $\mathrm{H}\beta$ line (the line dispersion; $\sigma_{\mathrm{H}_\beta}$) suggests $\sigma_{\mathrm{H}_\beta}$ is a better indicator of M_{BH} than $v_{\mathrm{FWHM}}(\mathrm{H}\beta)$. The authors find that the BH masses for broad line and narrow line objects are brought closer but still remain distinct. However, Watson et al. (2007) comment that they are unable to differentiate as to whether NLS1s lie under the broad line $M_{\mathrm{BH}} - \sigma_*$ relation with their masses growing via high rate accretion or whether NLS1s do follow the same $M_{\mathrm{BH}} - \sigma_*$ relation as broad line objects and therefore preferentially reside in less massive, and therefore less luminous galaxies. The use of the second moment of the line width, σ_{Line}, instead of the FWHM of the line, to estimate the virial M_{BH} has also been suggested by Peterson et al. (2004) and Collin et al. (2006). Other markers such as Mg II and C IV (for $z > 2$ objects) have, in addition to $\mathrm{H}\beta$, been used in the determination of virial masses for BHs. However, the accuracy of the C IV marker has been questioned. Shen et al. (2008) state that C IV lines tend to be, relative to the $\mathrm{H}\beta$ and Mg II lines, blueshifted and asymmetric (Gaskell, 1982; Tytler and Fan, 1992). They also state that more blueshifted objects have wider FWHM measurements (Richards et al., 2002). These characteristics could produce incorrect virial

$M_{\rm BH}$ measurements. Shen et al. (2008) produce evidence of inconsistencies between C IV and Mg II $M_{\rm BH}$ masses using SDSS data. The authors show that at low z, C IV underestimates $M_{\rm BH}$ relative to the Mg II values (the Mg II $M_{\rm BH}$ values are consistent with the Hβ values from the same sample) while at high z, C IV overestimates $M_{\rm BH}$ relative to the Mg II values. Shen et al. (2008) suggest that this inconsistency could be a result of the C IV line being modified by disc winds. However, Shen et al. (2008) conclude that all markers, on average, produce similar $M_{\rm BH}$ masses, though there may be large differences for individual objects.

As discussed, there is evidence for and against NLS1s following the same $M_{\rm BH} - \sigma_*$ relation as broad line AGN. Currently, there is no definitive way of confirming either scenario in NLS1s. The most reliable way to determine $M_{\rm BH}$ of NLS1s would be through stellar kinematics in the vicinity of the SMBH (cf. monitoring the orbits of S2 type stars around Sagittarius A* within the centre of the Galaxy; Gillessen et al., 2009, and references therein). Clearly this is all but impossible for the majority of cases. However, there are a handful of NLS1s that have accurate stellar velocity dispersion measurements. NGC 4051 is one of these sources and has a measured stellar velocity dispersion, $\sigma_* = 88 \pm 13$ km s^{-1} (Nelson and Whittle, 1995), implying $M_{\rm BH} = 5.5^{+2.7}_{-1.9} \times 10^6 {\rm M}_\odot$ (Gebhardt et al., 2000a). Reverberation mapping measurements produce smaller $M_{\rm BH}$ estimates for NGC 4051 of $M_{\rm BH} \approx 1.5 \times 10^6 {\rm M}_\odot$ (Gebhardt et al., 2000b; Denney et al., 2009). The reverberation mapping determined values of $M_{\rm BH}$ for NGC 4051 and its measured stellar velocity dispersion place it below the trend of other narrow and broad line AGN in the $M_{\rm BH} - \sigma_*$ relation using surrogate stellar velocity dispersion measurements (Gebhardt et al., 2000b; Botte et al., 2005). The positions of other sources with directly measured σ_* values do appear to follow the $M_{\rm BH} - \sigma_*$ relationship determined with surrogate σ_* measurements (Gebhardt et al., 2000b). So, it maybe that NGC 4051 is a strange case.

However, Botte et al. (2005) show that NLS1s with directly measured σ_* values have a tighter grouping in terms of σ_* in the $M_{\rm BH} - \sigma_*$ relation, whilst occupying the lower σ_* value region. This means that NLS1s cover a large range of BH masses, implying that NLS1s could be shown to follow any $M_{\rm BH} - \sigma_*$ relation. The calculated BH masses and narrow line widths of NGC 4051 would imply, from the current model of NLS1s, that NGC 4051 is accreting at a high rate. The position of NGC 4051 in the limit relation, from Wang (2003), is marked on Figure 3.4. According to the limit relation, NGC 4051 is accreting at rate lower than the Eddington limit. Which scenario is correct is unknown and NGC 4051 is only one case. Without stellar velocity dispersion measurements of many more objects, specifically NLS1s, it is not possible to determine to whether NGC 4051 is a special case or not.

Although it is not as direct as stellar kinematics, reverberation mapping can be used as a good indicator of $M_{\rm BH}$. However, this technique requires a lot of telescope time to achieve the desired accuracy and is therefore impractical for monitoring variations in a large sample of sources. This means that single epoch virial measurements must be used to estimate $M_{\rm BH}$ in a large number of targets, the accuracy of which are still a matter of debate. Therefore, in the absence of a definitive answer as to the true $M_{\rm BH} - \sigma_*$ for narrow line objects, for the purposes of this sample selection, it is a reasonable step to extend the empirical reverberation mapping relation down to narrow line objects. This allows the use of the Eddington limit relation calculated using the single epoch measurement of $v_{\rm FWHM}({\rm H}\beta)$.

3.2.2 Targets

Although there are seven sources listed in Table 3.1, only six were observable with *XMM-Newton*. These six sources make up the sample (Table 3.2) reported in this thesis. All

Table 3.1: List of Candidate Super-Eddington AGN

	NAME	$v_{\rm FWHM}(\mathrm{H}\beta)$ [km s^{-1}]	$\log(M_{\rm BH}/\,\mathrm{M}_\odot)$ $\mathrm{M}_R - M_{\rm BH}$	$\sigma - M_{\rm BH}$	Rev.[a]	Ref.
1...	PG 0157+001	2140	9.19	⋯	8.18	1
2...	QSO B0204+292	1040	8.69	⋯	7.13	1
3...	PG 1001+054	1740	⋯	8.77	7.65	2
4...	PG 1351+640	1170	⋯	⋯	7.66	3
5...	PG 1440+356	1450	⋯	8.12	7.33	2
6...	Q2247+140	2220	8.94	⋯	8.07	1
7...	MS 2254.9−3712	1545	⋯	8.17	7.04	2

This table is taken from Wang (2003). [a]$M_{\rm BH}$ estimated using reverberation mapping. References.–(1) McLure and Dunlop (2001); (2) Shields et al. (2003); (3) Kaspi et al. (2000b). The numbers in the first column refer to the numbers in Figure 3.4.

sources have narrow ($v_{\rm FWHM}(\mathrm{H}\beta) \lesssim 2200$ km s^{-1}) optical emission lines and are radio quiet. A brief introduction discussing the previously observed properties of these six sources follows.

PG 0157+001

PG 0157+001 (Mrk 1014; $z = 0.163$) is a radio quiet, luminous ($\mathrm{M}_B = -23.9$), infrared loud quasar ($L_{\rm FIR} > 10^{12}\mathrm{L}_\odot$; Sanders et al., 1988; Yun et al., 2001). PG 0157+001 was observed with *XMM-Newton* in 2000 (Boller et al., 2002). The authors suggest slight variations in the light curve and determine a power-law photon-index (Section 1.2.2), $\Gamma \approx 2.2$ for the nominal power-law, revealing a soft excess. ROSAT observations detected PG 0157+001 with a $0.5-2$ keV flux of 8.8×10^{-13} erg cm^{-2} s^{-1} (Schwope et al., 2000).

QSO B0204+292

QSO B0204+292 (PG 0204+292; 3C 59) is a low redshift ($z = 0.109$) quasar with an absolute R-band magnitude, $\mathrm{M}_R \sim -23.36$ mag (McLure and Dunlop, 2001) and a

Table 3.2: List of Objects Observable With *XMM-Newton*

Object	R.A. (J2000)	Dec (J2000)	redshift	Galactic $N_{\rm H}$ $[10^{20}\,{\rm cm}^{-2}]$
PG 0157+001	$01:59:50.21$	$+00:23:40.62$	0.1630	2.32
QSO B0204+292	$02:07:02.20$	$+29:30:46.00$	0.1096	5.34
PG 1001+054	$10:04:20.14$	$+05:13:00.50$	0.1605	2.39
PG 1351+640	$13:53:15.81$	$+63:45:45.41$	0.0882	2.16
PG 1440+356	$14:42:07.46$	$+35:26:22.92$	0.0791	1.03
MS 2254.9−3712	$22:57:38.90$	$-36:56:07.00$	0.0390	12.0

R.A., Dec and redshift obtained from NED-NASA/IPAC Extragalactic Database. Galactic $N_{\rm H}$ calculated using the FTOOL *nh*.

bolometric luminosity, $L_{\rm bol} \sim 10^{45}$ erg s^{-1} (Woo and Urry, 2002). Optical spectroscopy reveals a double peaked Hα line with a very broad base (full width zero intensity; FWZI = $26\,900$ km s^{-1}; Eracleous and Halpern, 1994), similar to the broad based Hα line found in PDS 456 (FWZI $\gtrsim 30\,000$ km s^{-1}; Simpson et al., 1999). QSO B0204+292 exhibits a narrow Hβ emission line (Table 3.1) along with narrow [O III] emission ($v_{\rm FWHM} \sim 220$ km s^{-1}; Bonning et al., 2005).

Although bright in X-rays, QSO B0204+292 has not been well studied at X-ray wavelengths. A previous X-ray observation of QSO B0204+292 with ROSAT gave a $0.5-2$ keV flux of $\sim 2.57 \times 10^{-12}$ erg cm^{-2} s^{-1} (Schwope et al., 2000). The majority of the literature on QSO B0204+292 refers to its radio properties, as it was mistakenly identified as radio loud when it was first discovered, due to the poor angular resolution of the observations at the time. Higher angular resolution MERLIN observations of the QSO B0204+292 region (Meurs and Unger, 1991) revealed that there are three discrete sources. Two are radio loud background objects and the third, QSO B0204+292, is a small compact, radio quiet ($S_{1415} \sim 26$ mJy) object.

PG 1001+054

PG $1001+054$ ($z = 0.1605$) is another optically bright ($\mathrm{m}_V = 16.38$) radio quiet quasar and was observed with *XMM-Newton* in 2003 (Schartel et al., 2005). Due to the poor counting statistics, the authors were unable to constrain the fit parameters with confidence. However, Schartel et al. (2005) suggest the presence of an ionised WA with parameters $N_\mathrm{h} = 19.2^{+11.9}_{-7.3} \times 10^{22}$ cm^{-2}, $\xi = 542^{+97}_{-147}$ erg cm s^{-1} and $\Gamma = 1.97^{+0.17}_{-0.14}$. PG 1001+054 has an extreme optical to X-ray flux ratio[4], $\alpha_\mathrm{o,x} \lesssim -2.5$ (Wang et al., 1996; Laor et al., 1997; Brandt et al., 2000). In addition, its UV spectrum shows C IV and Lyα absorption, leading to the classification of PG 1001+054 as a BAL (Brandt et al., 2000; Wills et al., 2000; Wang et al., 2000).

PG 1351+640

PG 1351+640 is one of the few known mini-BALQSOs at low redshifts ($z = 0.088$). It has reasonably broad C IV absorption ($\sim 900 - 3000$ km s^{-1}) as well as moderate Lyα, N V and Si IV absorption. Zheng et al. (2001) fit these absorption features with a five component velocity model. PG $1351+640$ was observed by ROSAT twice within the space of a year; the observed average $0.1-2$ keV flux was 8.36×10^{-13} erg s^{-1} cm^{-2}, varying between 7.2 and 10.1×10^{-13} erg s^{-1} cm^{-2} (Rush and Malkan, 1996). The authors fit the soft-band data with a very soft power-law ($\Gamma = 2.65^{+0.10}_{-0.11}$) and Galactic absorption. This is consistent with the optical to X-ray flux ratio, $\alpha_{o,x}$, of 1.9, derived by Tananbaum et al. (1986). Even though PG $1351+640$ is a radio quiet quasar, it has an unresolved radio source at its nucleus (Gower and Hutchings, 1984; Ulvestad

[4]The optical to X-ray flux ratio, $\alpha_\mathrm{o,x}$, is defined as

$$\alpha_\mathrm{o,x} = \log\left[\frac{f_\nu\,(2\,\mathrm{keV})}{f_\nu\,(2500\,\text{Å})}\right] \div \log\left[\frac{\nu\,(2\,\mathrm{keV})}{\nu\,(2500\,\text{Å})}\right]$$

et al., 2005). This radio source could be varying in size, suggesting it is either young or very confined (Neff and Hutchings, 1992; Hutchings and Neff, 1992).

PG 1440+356

PG 1440+356 (Mrk 478; $z = 0.0791$) is a classic example of an NLS1 and is one of the brightest in the extreme-ultraviolet (EUV; ~ 0.1 keV; Marshall et al., 1995). It has also been observed in the UV, but its spectrum does not show any intrinsic absorption features from C IV or Lyα (Crenshaw et al., 1999). PG 1440+356 has also been well studied in X-rays, with observations acquired with Bepposax (Vaughan et al., 1999), ASCA (Reeves and Turner, 2000), ROSAT (Wang et al., 1996), *Chandra* (Marshall et al., 2003) and *XMM-Newton* (Porquet et al., 2004). The observation with the *Chandra* Low Energy Transmission Grating (LETG) spectrometer remarkably, like the UV observations, showed no evidence of intrinsic absorption (Marshall et al., 2003). Porquet et al. (2004) fit the earliest *XMM-Newton* data of PG 1440+356 with a double power-law model, with $\Gamma_{\rm Soft} = 3.12^{+0.07}_{-0.06}$ and $\Gamma_{\rm Hard} = 2.45 \pm 0.13$, reporting that the soft spectrum is similar in shape to the observed ROSAT spectrum with $\Gamma = 3.43$ (Wang et al., 1996).

Zoghbi et al. (2008) analysed the four *XMM-Newton* observations of PG 1440+356 taken over a two year period. From the background corrected light curves, Zoghbi et al. (2008) suggest that PG 1440+356 is in a high flux state in the first observation and changes into a low flux state over the remaining 3 observations. Zoghbi et al. (2008) model the multi-epoch spectra in two ways. The first model is a reflection dominated model with the illuminating source hidden from view. The specific model that the authors use is a *reflion* component (Section 3.4) relativistically blurred by the XSPEC model *kdblur*. The results of this particular model fit cited by Zoghbi et al. (2008) are shown in Table 3.3. The second fit is a partial covering model. The authors show that allowing the parameters of the covering model to vary only serves to increase the error values. The reported column density, iron abundance and covering fraction values, kept constant between observations, are $2.7^{+2.9}_{-1.1} \times 10^{-23}$ cm^{-2}, $0.2^{+0.7}_{-0.2} \times$ solar and 0.54 ± 0.03, respectively. Also, the power-law photon-index and BB temperature determined for this model were $\Gamma = 2.66 \pm 0.02$ and kT $= 112 \pm 20$ eV, respectively. Zoghbi et al. (2008) conclude that the reflection dominated model describes the data better as it is more physically motivated. They argue that it must be the intrinsic source that varies and not the clouds covering the intrinsic source. They come to this conclusion from three points. Firstly, the spectral shape of PG 1440+356 does not vary over the four epochs. Secondly, the partial covering parameters do not change between epochs. Finally, the only thing to change is the flux during the four epochs. Thus, from a causality point of view, Zoghbi et al. (2008) argue that it is implausible for the covering fraction to remain the same over the 4 epochs if the intrinsic source is varying. They instead believe that changes in the ionisation of the reflecting material can cause the changes seen between each of the epochs.

MS 2254.9 − 3712

MS 2254.9 − 3712 was first detected at X-ray wavelengths by the Einstein Observatory Medium Sensitivity Survey (Gioia et al., 1990) and was subsequently classified as an AGN by Stocke et al. (1991). MS 2254.9 − 3712 is a low redshift ($z = 0.039$), soft X-ray bright AGN. It has also been detected by the EUV Explorer (Fruscione, 1996) and was included in the ROSAT sample of soft X-ray selected sources by Grupe et al. (1998). The observed $0.2 - 2$ keV ROSAT flux was 1.1×10^{-11} erg cm^{-2} s^{-1}. A relatively short (~ 26 ks) ASCA observation[5], taken at a similar time to that of the ROSAT data, observed a flux ~ 5 times lower. The ASCA observation also showed evidence that

[5]Observational data and information taken from the Tartarus database: http://tartarus.gsfc.nasa.gov/products/76036000/76036000_gsfc.html

Table 3.3: Zoghbi et al. (2008) *reflion* Model Fit to the PN Data of PG 1440+356

	Observation ID			
	0005010101	0005010201	0005010301	0107660201
$\Gamma_{\rm ref}$	2.35 ± 0.02	$2.47^{+0.02}_{-0.04}$	2.29 ± 0.01	2.43 ± 0.02
$\xi_{\rm ref}$	971^{+70}_{-143}	1168^{+194}_{-104}	746^{+100}_{-76}	1000^{+65}_{-208}
Fe^{a}	0.36 ± 0.03			
Inc^{a}	34 ± 2			
$R^{a}_{\rm in}$	$1.47^{+0.08}_{-0.02}$			
$R^{b}_{\rm out}$	400			
$\Gamma^{b}_{\rm emm}$	6			
χ^2/d.o.f.	1816/1754			

Parameter values, reported by Zoghbi et al. (2008), for the ionised reflection model fitted concurrently to the PN data sets from the four observations of PG 1440+356. The parameters [units] were the *reflion* incident power-law photon-index, $\Gamma_{\rm ref}$, the *reflion* ionisation, $\xi_{\rm ref}$ [erg cm s^{-1}], iron abundance, Fe [$\times$Solar], inclination, Inc [degrees], *kdblur* inner radius, $R_{\rm in}$ [$r_{\rm g}$], *kdblur* outer radius, $R_{\rm out}$ [$r_{\rm g}$], and the power-law dependence of the emissivity, $\Gamma_{\rm emm}$. The *po* photon-index was tied to the $\Gamma_{\rm ref}$ parameter for each observation. a indicates the parameter was allowed to vary but was tied between the four observations. b indicates the parameter was frozen to this value for all observations. χ^2/d.o.f. reports the final fit statistics for this model fit.

the source varied in flux by a factor of 4 in about 10 ks, almost reaching the observed flux from the ROSAT observation. Grupe et al. (2001) and Bian and Zhao (2003a) also report that the ROSAT data shows variations on similar time scales. This variation points towards a high-accretion rate as suggested by Wang (2003).

3.3 Observations and Data Reduction

XMM-Newton observations of the six targets listed in Table 3.2 took place between the 3rd of March 2002 and the 1st of May 2005. The data sets for PG 0157+001, PG 1001+054 and PG 1440+356 were public at the time of analysis and can be obtained from the XMM Science Archive (XSA) website[6]. The remaining three data sets, PG 1351+

[6]http://xmm.esac.esa.int/external/xmm_data_acc/xsa/index.shtml

Table 3.4: *XMM-Newton* Observation Details

Object	Observation ID	Rev[a]	Mode-Filter[b]		
			MOS1	MOS2	PN
PG 0157+001	0101640201	117	LW-m	LW-m	FF-m
QSO B0204+292	0205390201	850	LW-m	LW-m	LW-m
PG 1001+054	0150610101	623	FF-t	FF-t	FF-t
PG 1351+640	0205390301	831	FF-m	FF-m	FF-m
PG 1440+356	0005010101	561	SW-m	SW-m	SW-m
PG 1440+356	0005010201	562	SW-m	SW-m	SW-m
PG 1440+356	0005010301	564	SW-m	SW-m	SW-m
PG 1440+356	0107660201	373	LW-m	LW-m	LW-m
MS 2254.9−3712	0205390101	988	SW-m	SW-m	SW-m

Information on the *XMM-Newton* observations of the six candidate targets. [a] Revolution number. [b] FF-Full frame, LW-Large window and SW-Small window; m-Medium filter and t-Thin filter.

640, QSO B0204 + 292 and MS 2254.9 − 3712, were proprietary observations at the time of analysis and were granted via an AO-3 proposal. Information on the *XMM-Newton* observations including observation identification numbers (OBS ID), camera modes, filters and revolution numbers, can be found in Table 3.4.

3.3.1 Reduction

Both the EPIC and the RGS data sets were reduced in the standard way using the tasks distributed as part of the Science Analysis Software (SAS), version 8.0.0.

Filtering of the event lists took place as described in Section 1.3.1. For the EPIC cameras, high-energy background flaring events were screened for and only event patterns of $0-4$ and $0-12$ were used for the PN and MOS cameras, respectively. Finally a flag value of zero was placed upon the selection of events. The final good time interval (GTI) exposure times can be found in Table 3.5. For the RGS cameras, only high-energy background flaring events were screened for. The GTI values for the RGS spectra can

Table 3.5: *XMM-Newton* Observation GTI Values

Object	Observation	GTI Time [s]				
	ID	MOS1	MOS2	PN	RGS1	RGS2
PG 0157+001	0101640201	6763	6466	4659	14390	14004
QSO B0204+292	0205390201	62434	63934	53992	65523	65475
PG 1001+054	0150610101	11507	11527	9028	13622	13622
PG 1351+640	0205390301	49766	49737	43414	50349	50335
PG 1440+356	0005010101	24269	24263	16043	25954	25925
PG 1440+356	0005010201	8346	8443	6450	13920	13920
PG 1440+356	0005010301	25318	25319	18179	26245	26245
PG 1440+356	0107660201	23094	23492	8307	26472	25819
MS 2254.9−3712	0205390101	38562	38186	38196	65555	65534

GTI Time indicates the exposure time of the observation after filtering for high-background flaring events.

also be found in Table 3.5.

3.4 Spectral Analysis

EPIC background-subtracted spectra, response matrix files (RMF) and ancillary files (ARF) were created for each source in every observation by XMMSELECT, using the filtered event lists and extraction regions, which were selected as described in Section 1.3.1. The MOS spectra were then combined using the FTOOL *mathpha* to increase the counting statistics. The FTOOL *grppha* was then used to produce spectra with data bins that contained a minimum of twenty counts, which allowed the use of Chi-squared statistics within the X-ray spectral fitting package XSPEC. All the EPIC spectra were assessed for the presence of pile-up using EPATPLOT. Only the observation of PG 1440+356 with OBS ID 0107660201 was found to be suffering from pile-up. To rectify this for the 0107660201 observation, annuli were used in the creation of the spectra instead of circular regions, to exclude the inner 10 and 5 arc seconds from the PN and MOS extraction regions, respectively.

The RGS spectra and RMF files created by RGSPROC for each source were used during analysis. These spectra were, unlike the EPIC spectra, binned by channel to obtain the best possible resolution to maximise the likelihood of detecting any line features that may have been present. This binning was done separately for each target when it was thought that useful analysis could be performed on that target. The bandpass of the two RGS detectors is, to first order, between 5 and 37 Å and each contains 3400 channels. The resolution is therefore ~ 10 mÅ per channel. The final resolution of the RGS spectra to be analysed will be stated during the discussion of each target's spectrum, as varying amounts of binning was performed. Initial inspection of the RGS data sets confirmed that all but one (PG $1001+054$) were detected, to some level, by the RGS instruments. During the analysis of the RGS spectra within XSPEC, C-statistics were used instead of Chi-squared statistics as the data bins do not contain a Gaussian distribution of counts. This means the 'goodness of fit' can not be calculated whilst modelling the RGS data.

All spectral analysis was performed with XSPEC (Arnaud, 1996), version 11.3.2ag, unless otherwise stated. In addition to the standard models supplied within XSPEC, two non-standard models were used during the analysis of some target spectra. These models are the photoionisation modelling code XSTAR v2.1kn3 (Bautista and Kallman, 2001) and the *reflion* model, used to simulate the reflection from an illuminated constant density atmosphere (Ross and Fabian, 2005; Ross et al., 1999).

The XSTAR code is used to calculate the physical conditions of photoionised gases. The program calculates the absorption and emission spectra of a spherical shell of gas surrounding a central source emitting ionising radiation (the central engine in the case of AGN) at a given radius using the physical properties of the gas, e.g., density, chemical abundances and turbulent velocity. Along with the physical properties of the gas, the user supplies the shape (a power-law with $\Gamma = 2.0$) and the strength (luminosity, L) of the incident continuum. XSTAR splits the gas into sub-shells, then calculates the ionisation balance and thermal equilibrium in each sub-shell as the incident radiation is propagated through the entire shell. The result is a grid of synthetic models that represent the emission spectra and absorption features from the gas for a range of column densities ($N_{\rm h}$) and ionisations (ξ; Section 3.1.1), which can then be used within XSPEC. During this analysis, the range of values used for the column densities and ionisations were $N_{\rm h} = 10^{19}$ to 10^{24} cm^{-2} and $\log \xi = -2$ to 4, respectively. A turbulent velocity of 100 km s^{-1} was also included. The turbulent velocity acts to broaden both emission and absorption line widths within the synthetic spectra. This increases the opacity of the absorption lines. Normally, the equivalent width (EW) of a line will saturate as the line's opacity increases, thus limiting the line's EW. However, increasing the turbulent velocity will reduce the likelihood that the line will become optically thick at its core, allowing larger equivalent widths to be seen within the spectra. During modelling in XSPEC, redshift is a free parameter for the XSTAR components, allowing the determination of inflow or outflow velocities, where present.

The *reflion* model (Ross and Fabian, 2005; Ross et al., 1999) is used to calculate the emergent spectrum (between 1 eV and 1 MeV) of the reflection from a constant density, optically-thick medium (e.g., an accretion disc) that has been illuminated by a power-law continuum source. The power-law has a high-energy cutoff and this is set to 300 keV. The *reflion* model uses this incident power-law as a starting point to calculate temperature and ionisation structures for the reflecting medium that are consistent with the local radiation field. Various fully-ionised and important partially-ionised species are included in the calculations. The free parameters for this model are the iron abundance, the incident power-law photon-index and the ionisation state of the medium.

Analysis of the EPIC background-subtracted spectra began in the standard way. An initial Galactic absorbed power-law model was used to fit the hard-band ($2 - 10$ keV; observed) of each target. The model component *tbabs* with Wilms abundances set (Wilms et al., 2000) was used to simulate Galactic absorption. The FTOOL nh, which uses data taken from Dickey and Lockman (1990), was used to calculate the Galactic absorbing column, N_{H}, along the line of sight to each of the targets. The values of N_{H} that were used during modelling are shown in Table 3.2. In addition to the absorbed power-law, a Gaussian component was added to each model to determine the presence or absence of an iron line often found in AGN (e.g., Fe Kα emission; Section 1.2.2). This Gaussian component was only kept if its addition was statistically significant at the 99% level, i.e., the change in Chi-squared statistics, $\Delta\chi^2 \geqslant 11.345$, for the change of 3 degrees of freedom (d.o.f.) relating to the Gaussian component (energy, line width and normalisation). The same principle is used throughout the remainder of the modelling; new components are only accepted at the 99% level, i.e., for a change of 1 d.o.f., $\Delta\chi^2 \geqslant 6.635$. It should be noted that the use of the likelihood ratio test (LRT) and related F-Test[7] to determine the significance of an emission or absorption line is refuted by Protassov et al. (2002). The authors state that for these tests to hold true, the two models in question (e.g., with or without an emission line) should be nested and that the null parameter values of the additional components (e.g., normalisation of the emission line) must not be on the boundary of the available values for the parameters of the additional components in question. Thus, if an emission line is added to recreate the previous (nested) model, the emission line normalisation (cf. flux) would have to be set to zero (the normalisation's null value). This value lies at the limit of the normalisation parameter values, since an emission line cannot have a negative normalisation value. In this scenario, there is no reference dis-

[7]The LRT and related F-Test are significance tests that, in these circumstances, are used to justify the inclusion or exclusion of a model component, i.e., testing which model is more likely to represent the data.

tribution to look up, i.e., the test statistic is un-calibrated, even in the asymptotic limit (Protassov et al., 2002). Therefore, the LRT and the F-Test do not hold for emission or absorption lines. As an alternative, Protassov et al. (2002) suggest a mathematically simpler, more applicable technique in an adapted form of Bayesian posterior predictive probability (ppp) model checking (see Protassov et al., 2002, for more details). Hurkett et al. (2008, and references therein) used the Bayesian ppp technique, along with two other techniques, to analyse 40 gamma ray bursts (GRB) observed at early times (<few ks post-trigger in the rest frame of the burst) with the X-ray telescope (XRT) aboard the gamma ray observatory, *Swift*. The other two techniques used by the authors were firstly Monte Carlo testing for peaks in data after matched filter smoothing (Rutledge and Sako, 2003) and secondly Bayes factors. Hurkett et al. (2008) found that the three techniques gave similar results in terms of detection limits, i.e., the dependence of line detection with respect to energy for all three techniques were the same at energies > 1 keV. In addition, Hurkett et al. (2008) note that a large number (10^4) of spectral simulations are required to calibrate the respective statistical distributions, especially for the ppp and 'matched filter' techniques, suggesting that these techniques are both time consuming and computationally demanding. Park et al. (2008) developed new, more efficient expectation/maximisation (EM) algorithms and Markov chain Monte Carlo (MCMC) methods to search for narrow lines in X-ray spectra using Bayesian ppp statistics. The authors note that even with the increased efficiency, computational demands are still very large.

From a purely statistical point of view, Vaughan and Uttley (2008) performed a literature search to look at the evidence for narrow, relativistically shifted emission and absorption lines observed in the X-ray spectra of AGN (Section 3.1.1). They found that there was a correlation between the detected line strength (equivalent width; EW) and the uncertainty in the line detection (σ_{EW}; see Figure 1 of Vaughan and Uttley, 2008).

The authors highlight the fact that only the most significant detections are reported and false detections are never reported, resulting in a possible publication bias, meaning that some of the reported line detections could be false. If true this would imply that the number of high-velocity outflows is lower than previously thought. However, Tombesi et al. (2010a) refute this claim, citing publication bias due to the lack of uniform analysis of all the data sets included in the work by Vaughan and Uttley. Tombesi et al. have re-analysed all of the data sets to search for evidence of narrow line absorption features. The authors find a high number of weak features. These new features are faint, which implies there are more AGN with high-velocity outflows than previously thought. However, Tombesi et al. do report that they too find a correlation between EW and $\sigma_{\rm EW}$, though claim this is due to detection problems. The 'significance' of the detected lines in the work by Vaughan and Uttley (2008), determined using the LRT and related F-Test, are at a minimum of $2-3\sigma$. This means that even though the LRT and related F-Test are not statistically reliable for these features, they appear to be detections nonetheless, in particular for those sources with narrow EW lines and large $\Delta\chi^2$ values (see Vaughan and Uttley, 2008, for more details), e.g., PG 1211+143 (Pounds et al., 2003a) and NGC 4151 (Nandra et al., 2007). This would suggest that $\Delta\chi^2$ statistics, the LRT and related F-Test are still a reasonable indicator of the significance of any line detections. When combined with the complexity of the models used in the following analysis and the computational demands required to perform Bayesian ppp or Monte Carlo testing, it is not unreasonable to use $\Delta\chi^2$ statistics to test the significance of line detections.

The presence of emission or absorption features at both high- and low-energies can make the parameterisation of the power-law photon-index complex. Thus, when comparing the results obtained here with results published elsewhere, the power-law photon-index, Γ (Section 1.2.2), shall be the value of Γ obtained in the final best fit model for each source.

A summary of the initial hard-band fit results to all the sources except PG 1440+356 can be found in Table 3.6. The exclusion of PG 1440+356 from Table 3.6 is due to the variation of the photon-index between the four observations of PG 1440+356. The hard-band fit results of PG 1440+356 can be found in Section 3.4.5. Fitting the hard-band of PG 1001+054 was made difficult by the low counting statistics, a consequence of the short exposure time. Due to the low number of bins, there were a number of possible models that could represent the hard-band of PG 1001+054, which in turn lead to a varied range of photon-indices. The parameter values recorded for PG 1001+054 in Table 3.6 are those that represented the most physically motivated model, which will be discussed further in Section 3.4.3. Errors within the analysis presented here are quoted at the 90% confidence level, i.e., $\Delta\chi^2 = 2.706$ for one parameter of interest.

Of the six sources within this sample only three, QSO B0204 + 292, PG 1351 + 640 and MS 2254.9 − 3712, statistically required the addition of a Gaussian emission component, consistent with iron emission, to their hard-band model fits. Information on these features can be found in Table 3.6. Further information on the initial fit results and spectral plots of the data and models can be found in the discussion of each source's broad-band ($0.3-10$ keV; observed) spectral fits.

After modelling the standard hard-band features of each source, the same band was visually inspected for the presence of any absorption features as described in Section 3.1.1. Where absorption features were thought to be present, Gaussian absorption components were added to the hard-band model and then fitted. However, no additional absorption lines were statistically required at the 99% confidence level. To be thorough, the Gaussian components were added again but with their intrinsic line widths frozen to 10 eV (the approximate spectral resolution of the EPIC cameras at 6.4 keV). Once again, none

Table 3.6: Initial $2-10$ keV Model Fit Results

Target	Γ	$E_{\rm obs}$ keV	$\sigma_{\rm obs}$ eV	$\Delta\chi^2/$ Δd.o.f.	$\chi^2/$ d.o.f.
PG 0157+001	$2.02^{+0.16}_{-0.15}$	$\cdots$	$\cdots$	$\cdots$	$66.1/50$
QSO B0204+292	$1.53^{+0.01}_{-0.02}$	$5.74^{+0.03}_{-0.04}$	67^{+92}_{-67}	$37.8/3$	$1495.2/1479$
PG 1001+054[a]	2	$\cdots$	$\cdots$	$\cdots$	$2.8/7$
PG 1351+640	$1.89^{+0.07}_{-0.07}$	$5.98^{+0.13}_{-0.15}$	242^{+196}_{-124}	$16.0/3$	$258.4/257$
PG 1440+356	$\cdots$	$\cdots$	$\cdots$	$\cdots$	$\cdots$
MS 2254.9−3712	$1.82^{+0.04}_{-0.04}$	$6.19^{+0.06}_{-0.06}$	118^{+83}_{-57}	$29.4/3$	$592.1/626$

Initial $2-10$ keV (observed) best fit model parameters of the six *XMM-Newton* targets. Γ is the power-law photon-index, $E_{\rm obs}$ and $\sigma_{\rm obs}$ are the observed energy and intrinsic width of the observed Gaussian emission line, respectively. $\Delta\chi^2/\Delta$d.o.f. is the change in χ^2 statistics and degrees of freedom due to the addition of the Gaussian emission line and χ^2/d.o.f. is the final χ^2 statistics and degrees of freedom for the best fit model. a – Due to the low number of counting statistics in the hard-band for PG 1001+054, it was not possible to constrain any fit parameters with a reasonable amount of certainty (Section 3.4.3). Therefore, the results of a power-law fit with $\Gamma = 2$ to PG 1001+054 is stated above.

of the additional Gaussian absorption components were statistically required. It should be noted that most of these suspect features were at best, tentative (Figures 3.6, 3.10, 3.22, 3.30, 3.40 and 3.57). Thus, the absorption features previously found in the X-ray spectra of sources with high-ionisation, high-velocity outflows, such as those found in PDS 456 (Figure 3.1) and PG 1211+143 (Figure 3.2), were not obvious and likely absent. However, before confirming the absence of high-ionisation, high-velocity outflows, the broad-band ($0.3-10$ keV; observed) spectra of the objects need to be modelled.

To begin modelling the broad-band spectra for each source, the hard-band fits for each source were extrapolated down to 0.3 keV and inspected. Figure 3.5 shows the ratio plots (data relative to model; data/model) of the model fits to the data of the hard-band fits extended down to 0.3 keV. PG 1440+356 is not shown in Figure 3.5 on account of there being multiple observations of that target. The extended hard-band ratio plots (data/model) of the four PG 1440+356 observations are shown in Figure 3.41. Also,

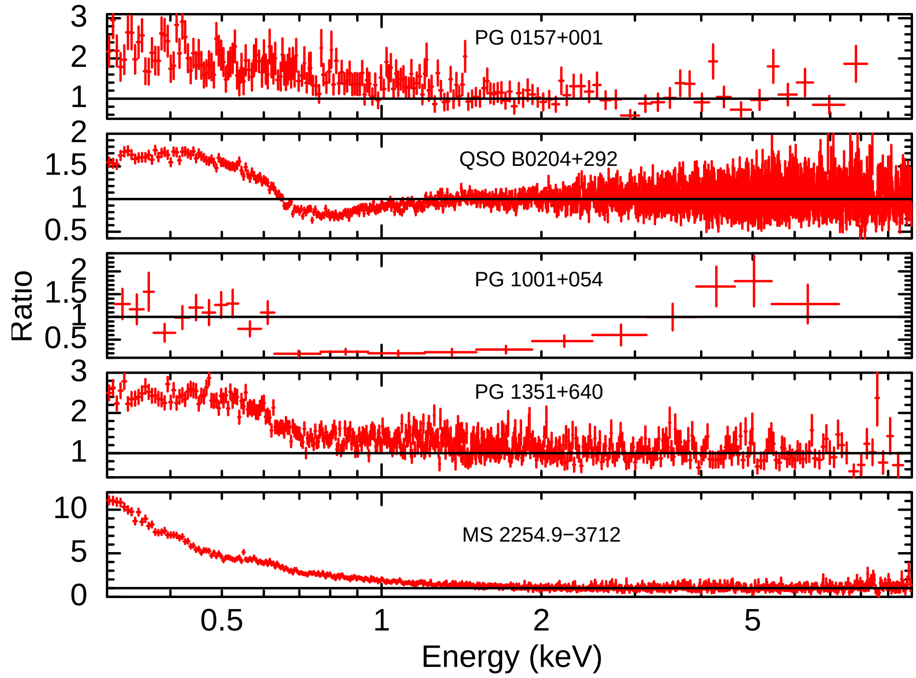

FIGURE 3.5: Ratio plots (data/model) of the initial hard-band ($2-10$ keV; observed) absorbed power-law fits to the EPIC data extended down to 0.3 keV. Only the PN data is shown for clarity. The plots are labelled with the relevant target name. The ratio plot for PG 1001+054 shows the residuals resulting from a power-law-index frozen at $\Gamma = 2$, as reported in Table 3.6. QSO B0204+292, PG 1351+640 and MS 2254.9−3712 statically required the inclusion of a Gaussian emission component. PG 1440+356 is not shown here due to the variation in Γ between the four observations and is instead shown in Figure 3.41.

the ratio plot (data/model) of PG 1001 + 054 shows the extended model fit between 2 and 10 keV with the photon-index frozen at a value of 2. Immediately, it can be seen that all of the sources shown in Figure 3.5 have varying amounts of soft excess (SE; Section 1.2.2) and/or absorption at lower energies. The remainder of the spectral fitting will be discussed on an individual basis for each source.

3.4.1 PG 0157+001

EPIC Data

Although the exposure time for the observation of PG 0157+001 was relatively short (~ 6 ks), a power-law photon-index, $\Gamma = 2.02^{+0.16}_{-0.15}$ was calculated from the $2-10$ keV fit. There was no evidence of an iron emission line when visually inspected (Figure 3.6) and the inclusion of a Gaussian emission component during the hard-band fit was not required at the 99% confidence level. The presence of absorption lines were not visually apparent and were not required at the 99% confidence level.

As with all of the sources, Figure 3.5 shows the presence of a SE in the spectrum of PG 0157+001. It is normal practice, as a first pass, to parameterise any SE using blackbody (BB) spectral components. However, this is not a very physical concept as it is very unlikely that the SE is a result of pure thermal emission from the accretion disc, as discussed in Section 1.2.2.

Including a single BB component to the broad-band fit modelled the lower energies well with χ^2/d.o.f. $= 278/296$ (Figure 3.7). The resulting BB temperature was kT $=$ 81^{+12}_{-13} eV, with $\Gamma = 2.19 \pm 0.06$ for the nominal power-law (*po*). This value of Γ is consistent with the model dependent value, $\Gamma \simeq 2.2$, determined by Boller et al. (2002).

In addition to the power-law plus BB model, a broken power-law model was fitted to the data. This broken power-law model also resulted in a good fit with χ^2/d.o.f. $=$ $276/296$. The resulting parameter values were the power-law break energy, $E_{\rm B}$ $=$ $1.04^{+0.16}_{-0.35}$ keV, the power-law index below $E_{\rm B}$, $\Gamma_1 = 2.64^{+0.14}_{-0.06}$ and the power-law index above E$_B$, $\Gamma_2 = 2.16^{+0.10}_{-0.07}$.

Figure 3.5 suggests that the SE is not smooth. If this is the case, there may be absorption or emission present that is not discernible in this observation. Fitting more

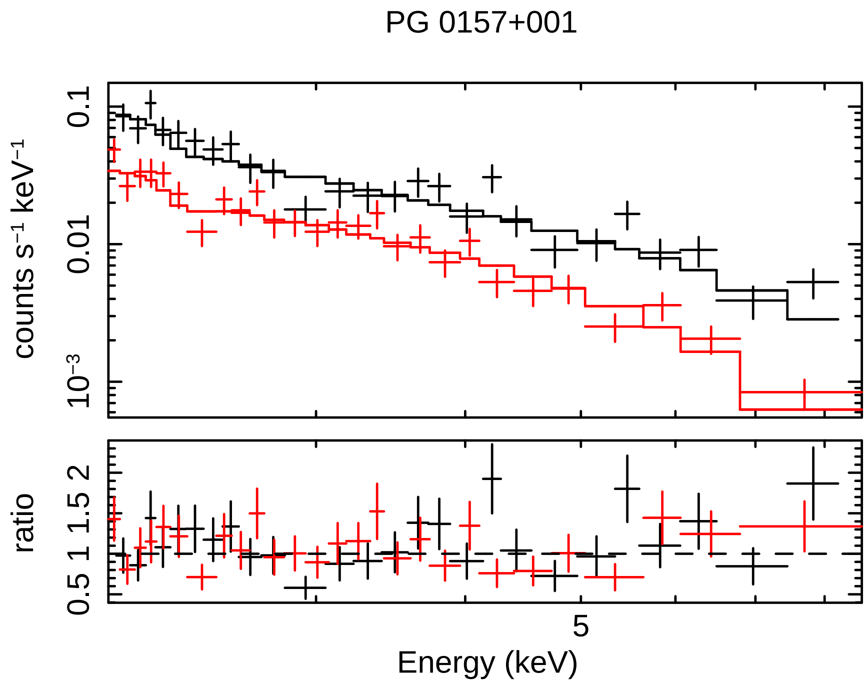

FIGURE 3.6: Initial hard-band ($2-10$ keV; observed) absorbed power-law fit to PG $0157+001$. Top: data points and model fit line. Bottom: ratio of data points to model fit line. Black: PN data. Red: MOS data.

complex models to these data sets would result in over-fitting. Therefore, it would be instructive to perform a longer observation of PG $0157+001$ to attempt to determine the true nature of its observed SE. For the purpose of this analysis, the best fit model is *tbabs*$\times$(BB+*po*), to allow comparison to the other sources analysed here. The observed broad-band ($0.3-10$ keV), unabsorbed fluxes for the PN and MOS data sets were $2.65^{+0.08}_{-0.07}\times10^{-12}$ erg s^{-1} cm^{-2} and $3.11^{+0.10}_{-0.09}\times10^{-12}$ erg s^{-1} cm^{-2}, respectively. The PN and MOS observed $0.5-2$ keV, unabsorbed fluxes are $1.10\pm0.03\times10^{-12}$ erg s^{-1} cm^{-2} and $1.24\pm0.04\times10^{-12}$ erg s^{-1} cm^{-2}, respectively. These values are roughly consistent, but are not within errors, with the ROSAT $0.5-2$ keV flux of 8.8×10^{-13} erg s^{-1} cm^{-2} reported by Schwope et al. (2000).

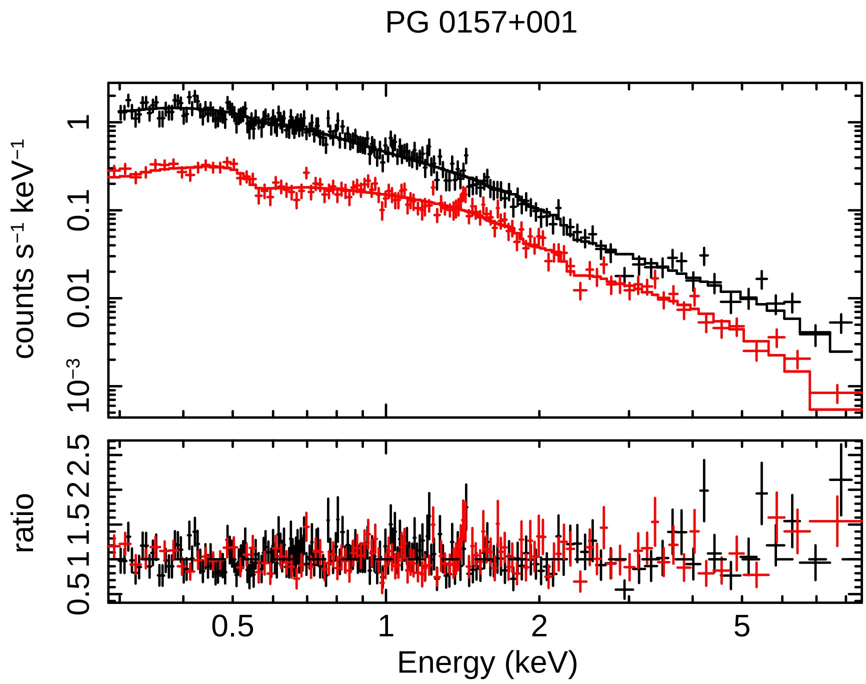

FIGURE 3.7: Best fit broad-band ($0.3 - 10$ keV; observed) model, *tbabs*×(BB+*po*), for PG 0157+001. Top: data points and model fit line. Bottom: ratio of data points to model fit line. Black: PN data. Red: MOS data.

RGS data

PG 0157+001 was barely detected by the RGS detectors. The count rates, determined by XSPEC, for PG 0157+001 in the RGS1 and RGS2 detectors were 0.039 ± 0.005 counts s^{-1} and 0.035 ± 0.004 counts s^{-1}, respectively. The data sets are quite noisy and various binning widths were tested before attempting any kind of modelling. Figure 3.8 shows both the RGS1 and RGS2 data for PG $0157 + 001$ grouped with 10 (black), 20 (red) and 40 (green) channels per bin. Even with 40 channels per bin the data sets are still extremely noisy and performing anything other than a continuum fit to the data would be futile. With that in mind, a simple Galactic absorbed power-law was fitted to the RGS data to place minimum constraints on the flux of PG 0157+001 for comparison with the EPIC fluxes. As the data were binned by channel rather than by number of counts per

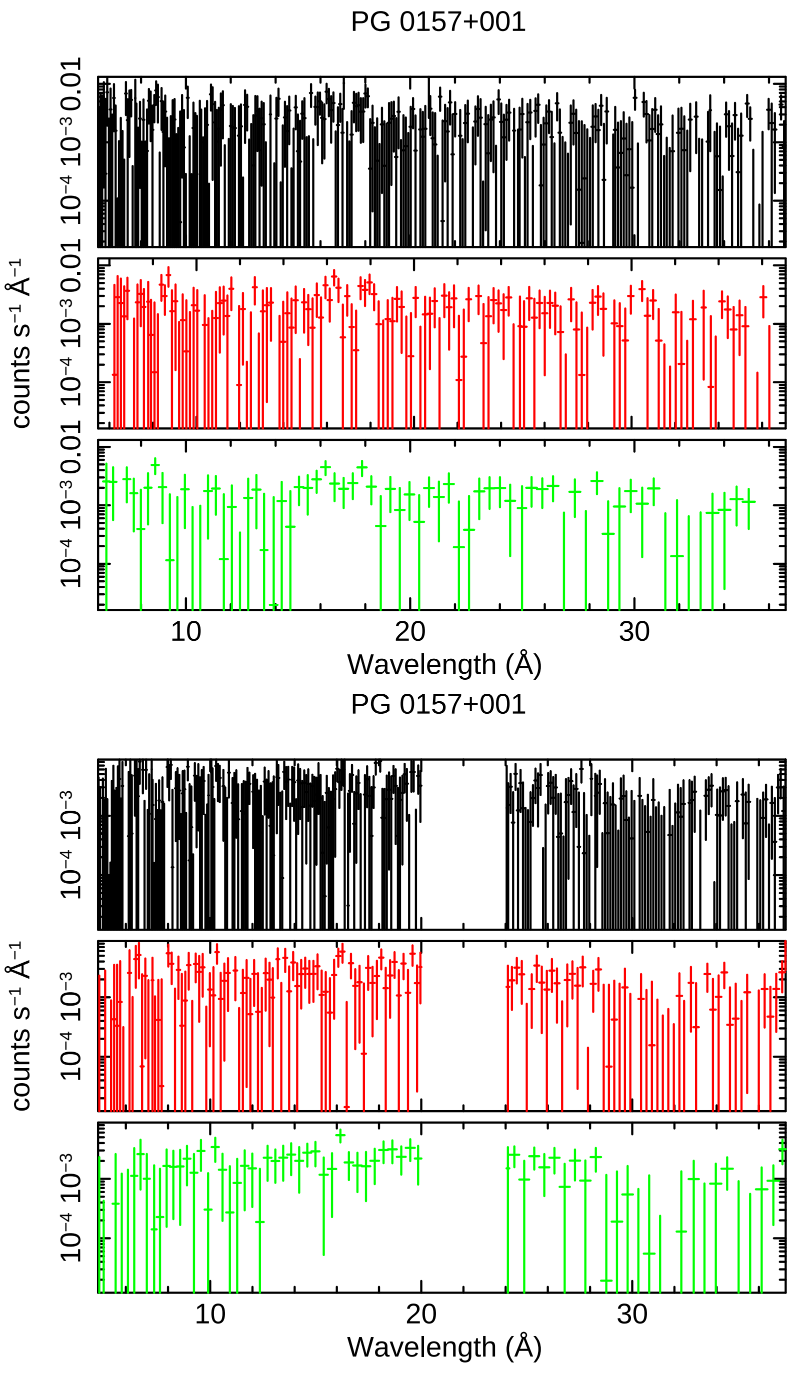

FIGURE 3.8: Binned ($6-37$ Å; observed) RGS1 (top) and RGS2 (bottom) data for PG $0157+001$. Black, red and green points show the data sets binned into groups of 10, 20 and 40 channels, respectively.

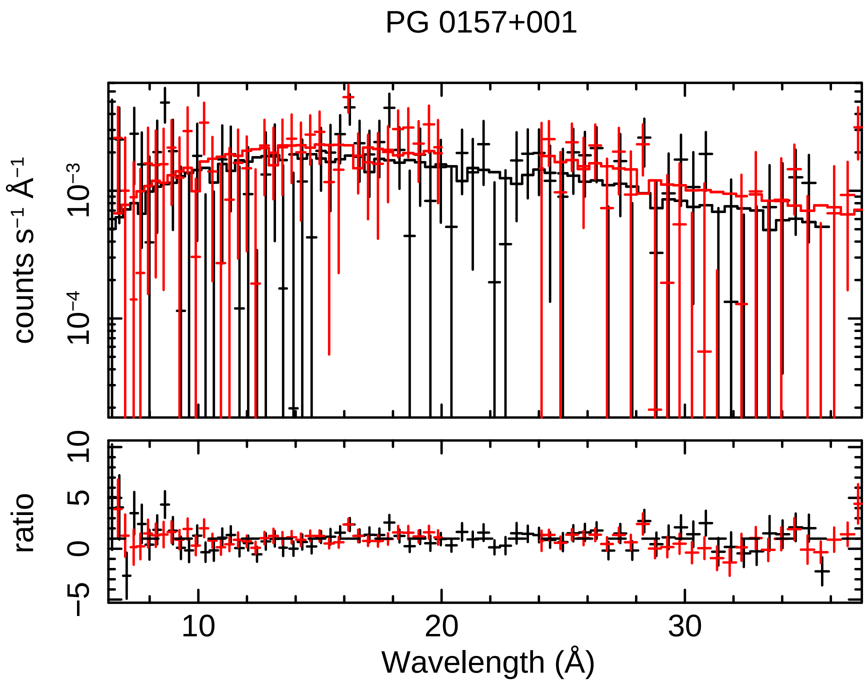

FIGURE 3.9: Continuum model fit, *tbabs*×(*po*), to the RGS data (6 – 37 Å; observed) of PG 0157+001. Top: data points and model fit line. Bottom: ratio of data points to model fit line. Black: RGS1 data. Red: RGS2 data.

bin, Chi-squared statistics are not valid and thus C-statistics (S) were used whilst fitting the RGS data for PG 0157+001 in XSPEC. The RGS data sets were fitted between 6 and 37 Å. The absorbed power-law fit returned $\Gamma = 2.40^{+0.02}_{-0.02}$ with $S = 117.4$ for 131 d.o.f. (Figure 3.9). The resulting observed $0.35 - 2$ keV, unabsorbed fluxes for the RGS1 and RGS2 spectra were $1.15^{+0.16}_{-0.21} \times 10^{-12}$ erg cm^{-2} s^{-1} and $1.30^{+0.17}_{-0.24} \times 10^{-12}$ erg cm^{-2} s^{-1}, respectively. Unfortunately, these fluxes are much lower than those values determined for the same energy range in the PN and MOS spectra, $1.55 \pm 0.04 \times 10^{-12}$ erg cm^{-2} s^{-1} and $1.77 \pm 0.05 \times 10^{-12}$ erg cm^{-2} s^{-1}, respectively. However, this is likely due to the quality and binning of the RGS data.

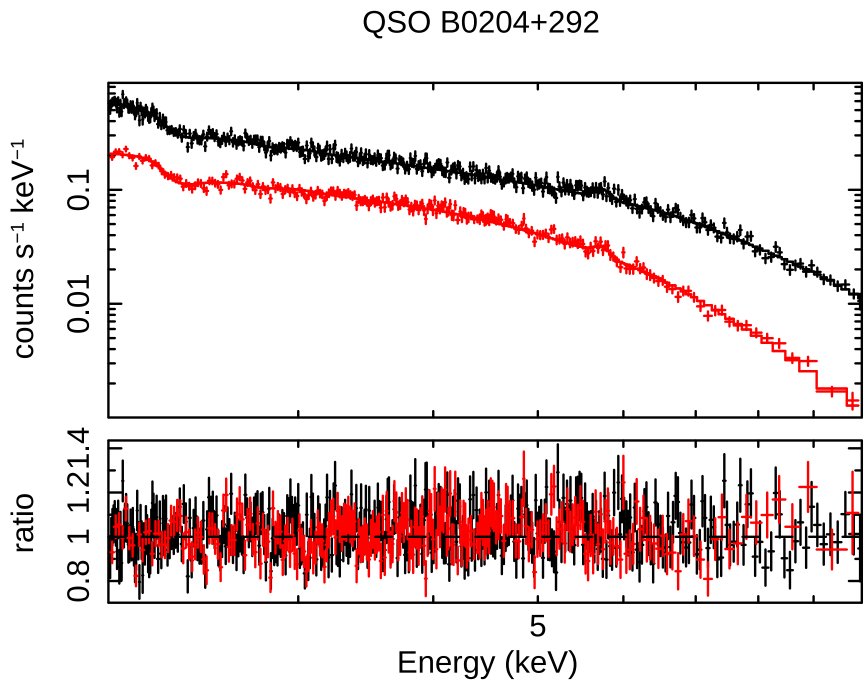

FIGURE 3.10: Initial hard-band (2 – 10 keV; observed) absorbed power-law fit to QSO B0204 + 292. Top: data points and model fit line. Bottom: ratio of data points to model fit line. Black: PN data. Red: MOS data. The data have been re-binned within XSPEC for viewing purposes only, with a minimum significance of 10σ and a maximum number of 10 data points per bin.

3.4.2 QSO B0204+292

EPIC Data

The hard-band fit to QSO B0204+292 resulted in a photon-index, $\Gamma = 1.53^{+0.01}_{-0.02}$. The addition of a narrow, $\sigma = 67^{+92}_{-67}$ eV, Gaussian emission line, at $5.74^{+0.03}_{-0.04}$ keV was required at the 99% confidence level ($\Delta\chi^2/\Delta$d.o.f. $= 37.8/3$). This is consistent with neutral Fe Kα (6.4 keV) line emission at the redshift, $z = 0.1096$, of QSO B0204+292. As with PG 0157+001, QSO B0204+292 did not show any evidence of absorption at high energies (Figure 3.10).

QSO B0204 + 292 has the most interesting ratio plot (data/model) relative to the extrapolated power-law fit (Figure 3.5). QSO B0204+292 shows both a SE and a large amount of absorption below 2 keV. This is similar to the residuals seen in the extrapolated hard-band fit to PG 1211+143 (Figure 3.2; Pounds et al., 2003a).

The inclusion of an XSTAR absorption component with absorbing column, $N_{\rm h} = 1.15 \pm 0.01 \times 10^{22}$ cm^{-2}, and ionisation[8], $\log(\xi) = 1.55 \pm 0.02$ to the extrapolated hard-band fit reduces the residuals below 2 keV. However, they are still prominent and residuals start to appear above 8 keV (Figure 3.11). The power-law photon-index increases to $\Gamma = 1.85 \pm 0.01$, though this model is a bad fit with χ^2/d.o.f. $= 3052.4/1938$. The addition of a second XSTAR absorption component ($N_{\rm h,1} = 1.03^{+0.28}_{-0.95} \times 10^{23}$ cm^{-2}, $\log(\xi_1) = 3.01^{+0.01}_{-0.04}$ and $N_{\rm h,2} = 7.20^{+0.27}_{-0.41} \times 10^{21}$ cm^{-2}, $\log(\xi_2) = 1.30 \pm 0.02$) does once again reduce, though not completely, the residuals below 2 keV (Figure 3.12). Also, the residuals above 8 keV are still prominent, with apparent excess emission around $\sim$ 6 keV that is not being modelled by the Gaussian component at $\sim$ 5.7 keV. It is still a poor fit with χ^2/d.o.f. $= 2566.1/1936$. Clearly, from Figures 3.5 and 3.12, there is a SE present and the current absorbed power-law model does not adequately model the lower energies. Including BB components to represent the SE leads to two BB components being present in the model. The inclusion of the first component produces $\Delta\chi^2/\Delta$d.o.f. $= 368.3/2$ and a further change of $\Delta\chi^2/\Delta$d.o.f. $= 116.6/2$ is produced with the addition of the second BB component. This removes the residuals at higher energies and gives a reasonable fit to the lower energies (Figure 3.13). This model fit does harden the photon-index, $\Gamma = 1.62 \pm 0.02$, back to a value similar to the initial hard-band model fit ($\Gamma \approx 1.53$; Table 3.6). Figure 3.13 also shows the ratio plot (data/model) for the best model fit to the QSO B0204+292 data between 0.3 and 2 keV. This plot clearly shows that the residuals are far from constant. There is possible absorption seen around $\sim$ 0.45 keV in the MOS data. However, the PN data at this energy shows an

[8] The units of ξ are erg cm s^{-1}.

excess compared to the model. This residual feature and other residuals are less than 10% deviation from the model and are unable to be modelled with any significance. However, inspection of the RGS data for QSO B0204 + 292 will assist in identifying any possible real features seen in the soft-band of the EPIC data. The best fit model for QSO B0204+292 is, therefore, *tbabs*$\times$XSTAR$_1\times$XSTAR$_2\times$(BB$_1$+BB$_2$+*ga*$_{\rm obs}$+*po*) with final fit statistics of $\chi^2/\mathrm{d.o.f.} = 2073.8/1932$. The parameter values were kT$_1 = 94^{+1}_{-2}$ eV, kT$_2 = 264^{+9}_{-15}$ eV, $\Gamma = 1.62 \pm 0.02$, $N_{\rm h,1} = 3.27^{+0.69}_{-0.74} \times 10^{21}$ cm^{-2}, $\log(\xi_1) = 2.30^{+0.08}_{-0.16}$, $N_{\rm h,2} = 3.96^{+0.29}_{-0.07} \times 10^{21}$ cm^{-2}, $\log(\xi_2) = 0.66 \pm 0.03$, $E_{\rm obs} = 5.75^{+0.04}_{-0.03}$ keV and $\sigma_{\rm obs} = 70^{+66}_{-48}$ eV. Figure 3.14 shows the contour plots of the confidence regions for the temperatures of the two BB components, the parameters of the first XSTAR component and the parameters of the second XSTAR component. The contours represent $\Delta\chi^2$ values of 2.3 (black), 4.61 (red) and 9.21 (green), approximately equivalent to 68%, 90% and 99% confidence regions for 2 degrees of freedom, respectively. The crosses in each of the contour plots mark the best fit values for those particular parameters. From Figure 3.14 it can be seen that the BB temperatures and XSTAR model parameters are well constrained. Allowing the redshift parameters to vary, both together and individually, was not significant at the 99% level and therefore no outflow velocity could be determined.

As a check, a partial covering model was fitted to the EPIC data of QSO B0204+292. A simple partially covered power-law model, *tbabs*$\times$*pcfabs*$\times$(*ga*$_{\rm obs}$+*po*), fits the hard-band data well ($\chi^2/\mathrm{d.o.f.} = 1484.8/1477$). The inclusion of the partial covering component is significant at the 99% level compared to the hard-band model fit recorded in Table 3.6. However, after further modelling, a final partial covering model of *tbabs*$\times$*pcfabs*$\times$XSTAR$\times$XSTAR$\times$(BB$_1$+BB$_2$+*ga*$_{\rm obs}$+*po*) is required to fit the broad-band data ($\chi^2/\mathrm{d.o.f.} = 2072.1/1930$). This model is virtually identical to the best fit model

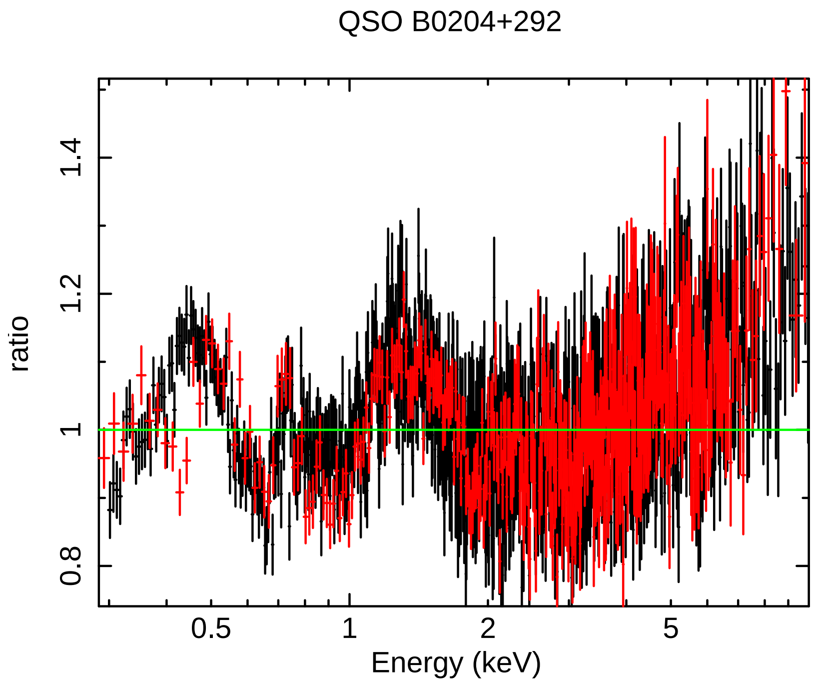

FIGURE 3.11: Ratio plot (data/model) of the initial broad-band ($0.3-10$ keV; observed) model fit, *tbabs*×XSTAR(*po+ga*$_{\rm obs}$), to the QSO B0204+292 EPIC data. Black: PN data. Red: MOS data. The data have been re-binned within XSPEC for viewing purposes only, with a minimum significance of 10σ and a maximum number of 10 data points per bin.

and the change in χ^2 statistics between them is not significant at the 99% level. Thus, the inclusion of a partial covering component is not required.

The observed broad-band ($0.3-10$ keV), unabsorbed fluxes for the best fit model to the PN and MOS data sets were $2.01^{+0.09}_{-0.12} \times 10^{-11}$ erg s^{-1} cm^{-2} and $2.17^{+0.10}_{-0.13} \times 10^{-11}$ erg s^{-1} cm^{-2}, respectively. Also, the observed $0.5-2$ keV, unabsorbed fluxes for the PN and MOS data sets were $6.94^{+0.53}_{-0.37} \times 10^{-12}$ erg s^{-1} cm^{-2} and $7.36^{+0.49}_{-0.40} \times 10^{-12}$ erg s^{-1} cm^{-2}, respectively. These values are $\sim 2-3$ times the ROSAT values ($\sim 2.57 \times 10^{-12}$ erg cm^{-2} s^{-1}) reported by Schwope et al. (2000). However, the ROSAT data were modelled with a power-law model with the photon-index set at 2, which did not fit the data fully.

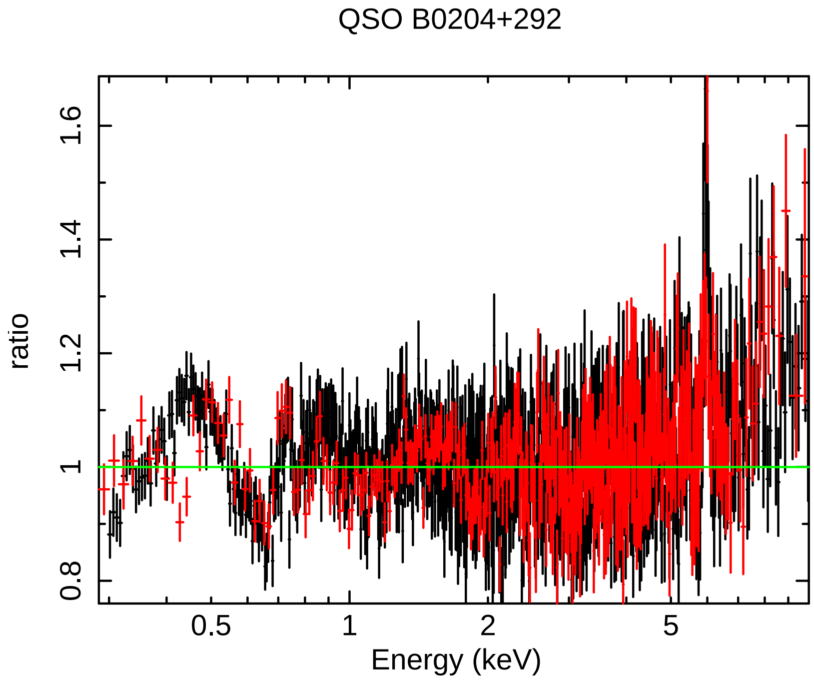

FIGURE 3.12: Ratio plot (data/model) of the second broad-band ($0.3-10$ keV) model fit, *tbabs*$\times$XSTAR$_1\times$XSTAR$_2\times$(*po*+*ga*$_{\mathrm{obs}}$), to the QSO B0204+292 EPIC data. Black: PN data. Red: MOS data. The data have been re-binned within XSPEC for viewing purposes only, with a minimum significance of 10σ and a maximum number of 10 data points per bin.

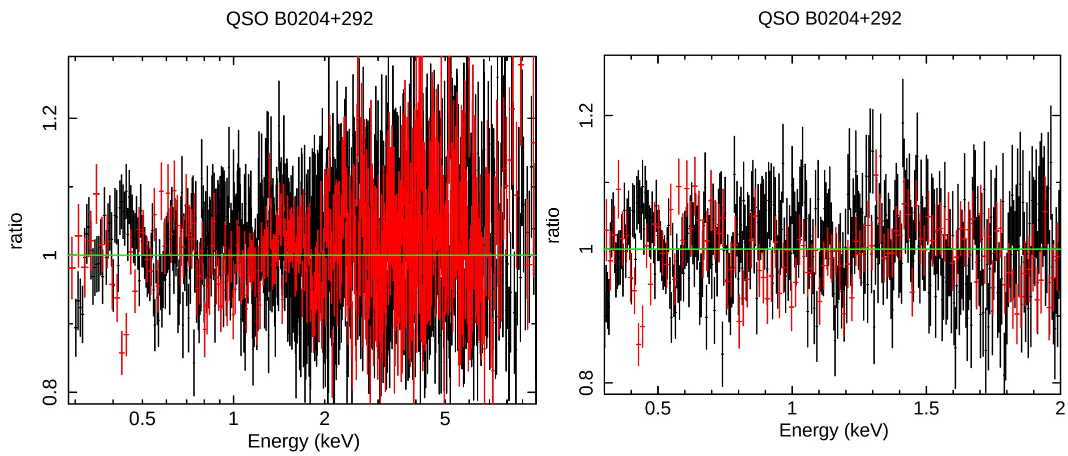

FIGURE 3.13: Ratio plots (data/model) of the broad-band ($0.3-10$ keV) best model fit, *tbabs*$\times$XSTAR$_1\times$XSTAR$_2\times$(BB$_1$+BB$_2$+*ga*$_{\mathrm{em}}$+*po*+*ga*$_{\mathrm{obs}}$), to the QSO B0204 + 292 EPIC data. Left: $0.3-10$ keV. Right: $0.3-2$ keV using a linear energy scale. Black: PN data. Red: MOS data. The data have been re-binned within XSPEC for viewing purposes only, with a minimum significance of 10σ and a maximum number of 10 data points per bin.

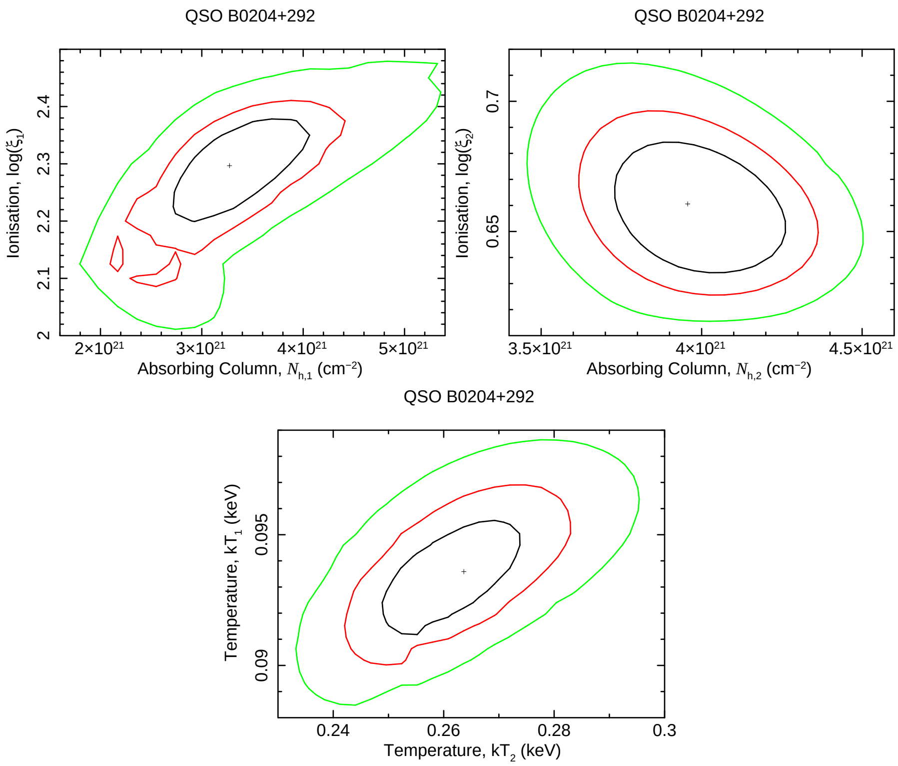

FIGURE 3.14: Confidence region contours determined for the parameters of the XSTAR and BB components from the best fit model to the EPIC data of QSO B0204+292. Top left: ionisation and column density for the first XSTAR component. Top right: ionisation and column density for the second XSTAR component. Bottom: temperatures from the two BB components. The crosses mark the best fit parameter values. The contours coloured black, red and green represent $\Delta\chi^2$ values of 2.3, 4.61 and 9.21, respectively, equivalent to approximate confidence regions, for 2 degrees of freedom, of $\sim 68\%$, 90% and 99%, respectively.

RGS Data

QSO B0204+292 was detected by the RGS detectors. The count rates for QSO B0204+292 in the RGS1 and RGS2 data sets, determined by XSPEC, were 0.082 ± 0.002 counts s^{-1} and 0.091 ± 0.002 counts s^{-1}, respectively. The data sets are quite noisy and various binning widths were tested before settling on a final value. Figure 3.15 shows both the RGS1 and RGS2 data grouped with 5 (black), 10 (red) and 20 (green) channels per bin. The binning is quite heavy, even at 10 channels per bin, and is required due to the quality

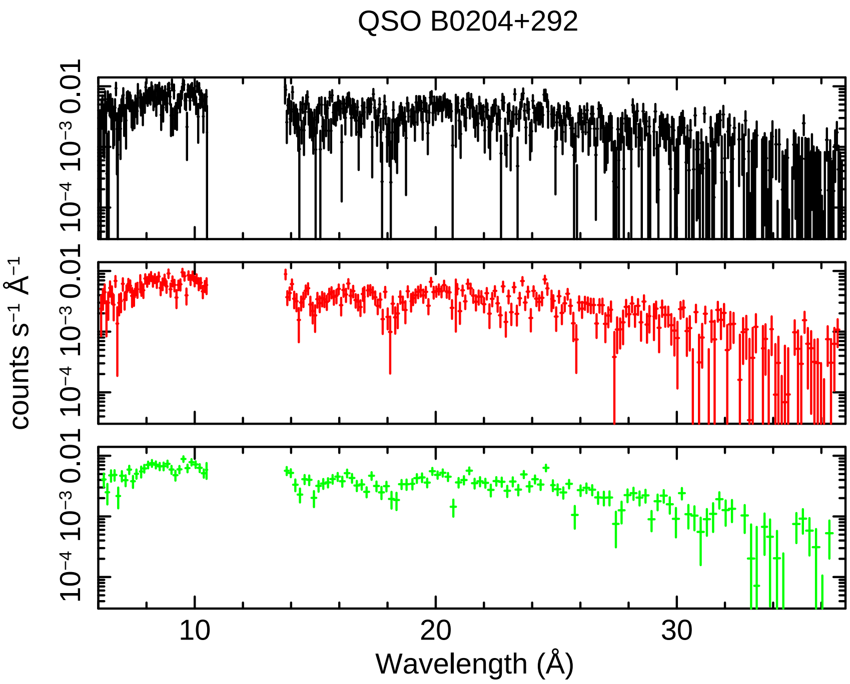

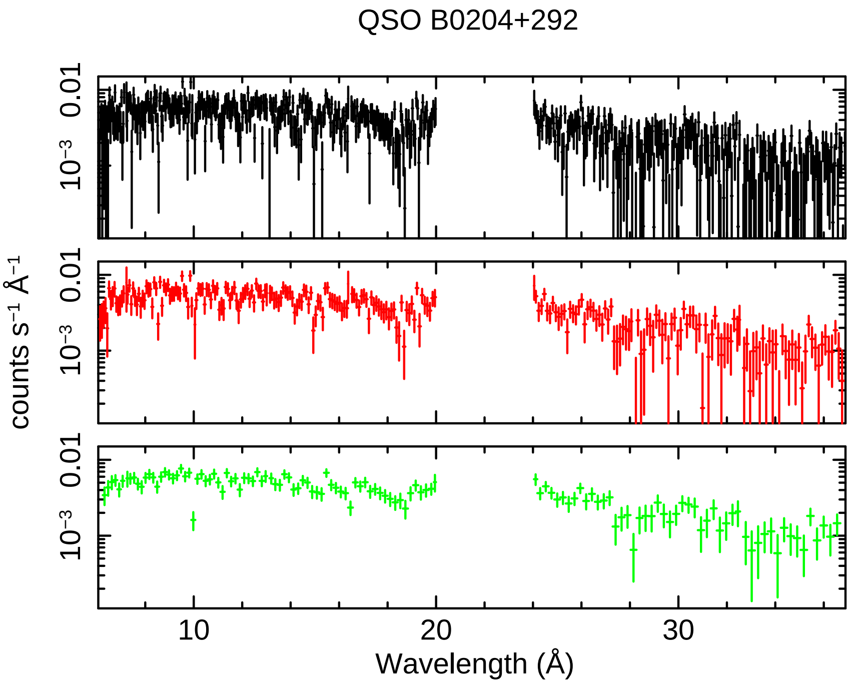

FIGURE 3.15: Binned ($6-37$ Å; observed) RGS1 (top) and RGS2 (bottom) data for QSO B0204+292. Black, red and green points show the data sets binned into groups of 5, 10 and 20 channels, respectively.

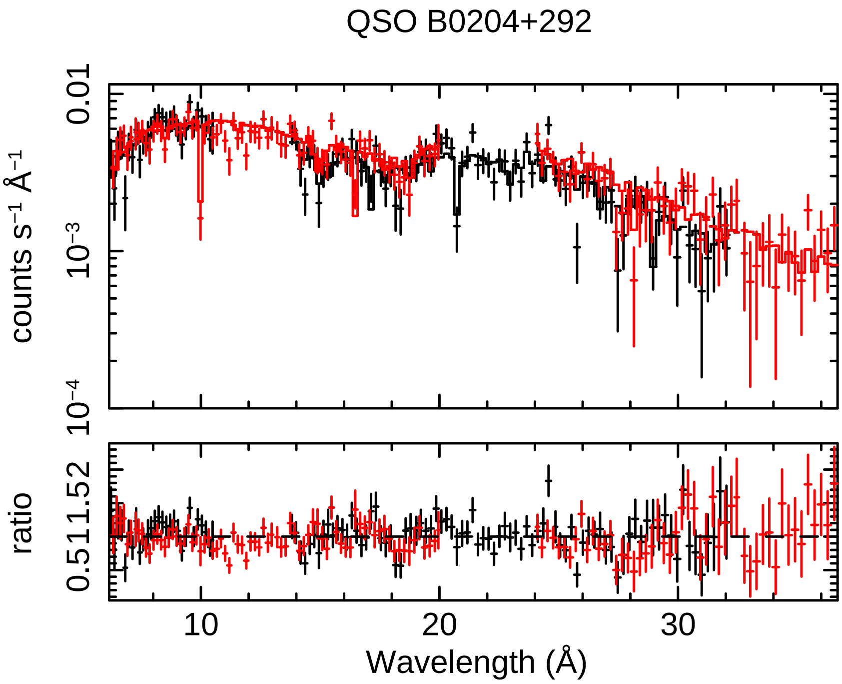

FIGURE 3.16: QSO B0204 + 292 EPIC best fit model folded through RGS response plotted over the RGS data (6 – 37 Å; observed). Top: data points and model fit line. Bottom: ratio of data points to model fit line. Black: RGS1 data. Red: RGS2 data.

of the data. A final value of 20 channels per bin was chosen. This binning corresponds to an approximate bin width of ~ 0.18 Å. Unfortunately, this is approximately three times the RGS resolution of ~ 60 mÅ. Therefore, the data will be under-sampled with respect to the RGS resolution, so any particularly narrow features will be binned out of the data. However, it is unlikely, due to the signal-to-noise of the data, that such features would be evident. To test this a visual inspection of the RGS data was made whilst choosing which binning to use, with the final decision of the binning being based on what, if any, features were visible and how noisy the data was. The RGS1 and RGS2 data sets were fitted between 6 and 32.5 Å and 6 and 37 Å, respectively. As the data were binned by channel rather than by number of counts per bin, Chi-squared statistics are not valid and thus C-statistics (S) were used whilst fitting the RGS data for QSO B0204+292 in XSPEC.

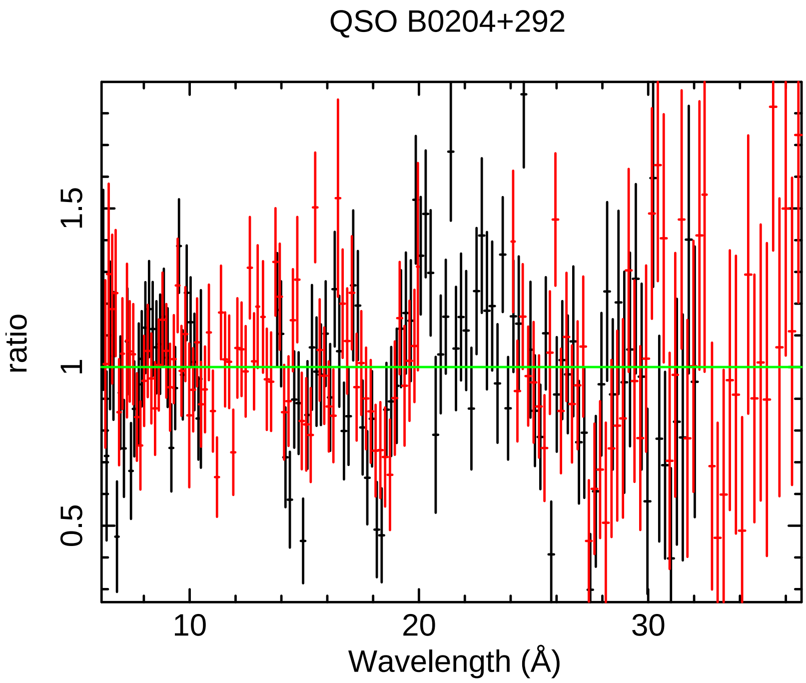

FIGURE 3.17: Ratio plot (data/model) of the model fit, *tbabs*×(BB$_1$+BB$_2$), to the RGS data ($6-37$ Å; observed) of QSO B0204+292. Black: RGS1 data. Red: RGS2 data.

An initial inspection of the RGS data for QSO B0204+292 was made by over-plotting the EPIC best fit model. This was done to search the RGS data for any predicted features from the EPIC model. Figure 3.16 shows the EPIC best fit model folded through the RGS response plotted over the RGS data. It is clear that all that predicted features from the EPIC best model fit are present in the RGS data.

Modelling of the RGS data for QSO B0204$+$292 began with a Galactic absorbed power-law fit. This gave a very poor fit (S/d.o.f. $= 1262.3/233$) as was to be expected from the best fit to the EPIC data. Adding a BB component with kT $= 85 \pm 4$ eV improved the fit (S/d.o.f. $= 654.3/231$). However, this returned a photon-index of $\Gamma = 0.74^{+0.11}_{-0.12}$, resulting in a negatively sloped power-law. A second BB was included to replace the power-law. The latest model, *tbabs*×(BB$_1$+BB$_2$), returned parameter values of kT$_1$ $= 91 \pm 30$ eV and kT$_2$ $= 535^{+35}_{-30}$ eV, with fit statistics of S/d.o.f. $=$

$635.4/231$. This model clearly leaves broad absorption residuals at ~ 18 Å and possible absorption around ~ 28 Å (Figure 3.17). The absorption at ~ 18 Å is likely to be the UTA, while the absorption at ~ 28 Å is possibly due to N VII, both at the redshift of QSO B0204+292 ($z = 0.1096$). An XSTAR component was included to model the apparent absorption. This model improved the fit statistics to S/d.o.f. $= 534.8/229$, though it still left residuals around ~ 18 and 28 Å. Thus, a second XSTAR component was added. This returned the best fit to the RGS data of QSO B0204$+$292 so far, with fit statistics of S/d.o.f. $= 506.7/227$. Figure 3.18 shows the ratio plot (data/model) of the latest model fit, *tbabs*×XSTAR×XSTAR×(BB$_1$+BB$_2$), to the RGS data of QSO B0204$+$292. This model fit removes the broad absorption at ~ 18 Å though appears to leave a narrower absorption feature at the same wavelength. A Gaussian absorption line with energy $E_{\mathrm{abs}} = 678^{+3}_{-4}$ eV ($18.29^{+0.11}_{-0.08}$ Å) and an intrinsic width of $\sigma_{abs} = 4^{+163}_{-2}$ eV ($0.12^{+4.41}_{-0.04}$ Å) was added to try and model this narrow feature at ~ 18 Å. Although the absorption line did appear to reduce the residuals (Figure 3.19), it was not significant at the 99% level ($\Delta S/\Delta$d.o.f $= 10.0/3$). Also, the errors determined for the line width are quite large and do not appear to be well constrained. Figure 3.20 shows the contour plot of the confidence regions for the absorption line's energy and intrinsic width. The contours represent ΔS values of 2.3 (black), 4.61 (red) and 9.21 (green), approximately equivalent to 68%, 90% and 99% confidence regions for 2 degrees of freedom, respectively. The crosses in the contour plots mark the best fit values for those particular parameters. As the Gaussian line is not significant at the 99% level, the best fit model to the RGS data of QSO B0204$+$292 is *tbabs*×XSTAR×XSTAR×(BB$_1$+BB$_2$), with parameter values of kT$_1$ $= 108^{+5}_{-4}$ eV, kT$_2$ $= 433^{+25}_{-16}$ eV, $N_{\mathrm{h},1} = 5.91^{+4.76}_{-3.54} \times 10^{21}$ cm^{-2}, $\log(\xi_1) = 2.56^{+0.18}_{-0.19}$, $N_{\mathrm{h},2} = 3.49^{+0.27}_{-0.68} \times 10^{21}$ cm^{-2} and $\log(\xi_2) = 0.75^{+0.01}_{-0.05}$, with fit statistics of S/d.o.f. $= 506.7/227$. Figure 3.21 shows the contour plots of the confidence regions for the temperatures of the two BB components, the parameters of the first XSTAR component and the parameters of the second XSTAR component. The contours are equivalent to those shown in Figure 3.14. From Figure 3.21, it can be seen that the first XSTAR component parameters are not well constrained, unlike the BB temperatures and the XSTAR_2 model parameters, which appear well constrained. The best fit parameter values for the XSTAR components in the best fit model to the RGS data of QSO B0204 + 292 are consistent with those values obtained for the EPIC data of QSO B0204+292. Allowing the redshift parameters to vary, both together and individually, was not significant at the 99% level and therefore no outflow velocity could be determined.

The observed $0.35-2.0$ keV, unabsorbed fluxes for the RGS1 and RGS2 data sets were $8.17^{+1.13}_{-0.61} \times 10^{-12}$ erg s^{-1} cm^{-2} and $8.23^{+1.24}_{-1.11} \times 10^{-12}$ erg s^{-1} cm^{-2}, respectively. These fluxes are consistent, within errors, with the observed $0.35-2.0$ keV, unabsorbed flux for the PN data ($1.00^{+0.06}_{-0.10} \times 10^{-11}$ erg s^{-1} cm^{-2}). Also, the RGS fluxes are similar, though not within errors, to the observed $0.35-2.0$ keV, unabsorbed flux for the MOS data ($1.06^{+0.07}_{-0.10} \times 10^{-11}$ erg s^{-1} cm^{-2}).

The possible absorption feature seen in the MOS data of QSO B0204 + 292 at ~ 0.45 keV (~ 31 Å) appears to be absent in the RGS spectra of QSO B0204+292 (Figure 3.18). However, it is possible that the feature seen in the MOS spectrum is real but has been resolved out by the RGS detectors due to its broad nature. Although a longer look at QSO B0204 + 292 with the RGS detectors would be instructive to resolve the narrow features seen within its spectra, and possibly determine an outflow velocity for the absorbing material. However, looking for broad absorption features may prove futile.

Both the EPIC and RGS data for QSO B0204+292 show evidence for the presence of a WA along the line of sight towards the centre of QSO B0204+292. The absorbing

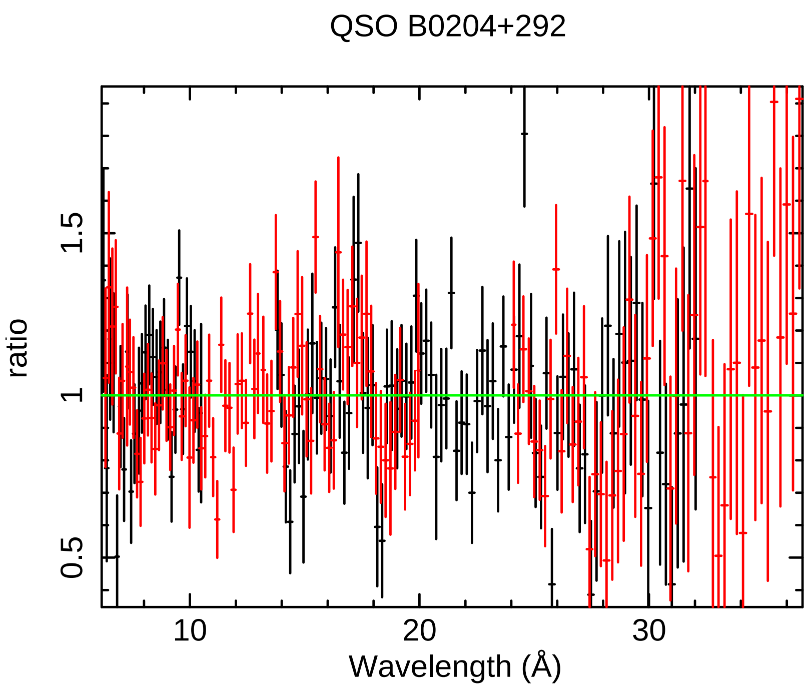

FIGURE 3.18: Ratio plot (data/model) of the double absorbed model fit, *tbabs*×XSTAR×XSTAR×(BB_1+BB_2), to the RGS data ($6-37$ Å; observed) of QSO B0204+292. Black: RGS1 data. Red: RGS2 data.

column values determined are similar in each case ($\simeq 3\times10^{21}$ cm^{-2}) and typical of WAs (Section 3.1.1). There are two ionisations returned by the model fits, again consistent with those typically found in WA. A simultaneous model fit to the EPIC and RGS data sets was performed to confirm this. The EPIC model, *tbabs*×XSTAR×XSTAR× (BB_1 + BB_2 + *po* + ga_{obs}), was used and the RGS data used was grouped by a minimum of 20 counts per bin to allow the use of χ^2 statistics. The resulting fit statistics were χ^2/d.o.f. $= 2635.8/2434$. The parameter values determined for this joint fit were $N_{\rm h,1} = 3.50^{1.81}_{-0.71}\times 10^{21}$ cm^{-2}, $\log(\xi_1) = 2.35^{+0.11}_{-0.10}$, $N_{\rm h,2} = 4.03^{+0.18}_{-0.14}\times10^{21}$ cm^{-2}, $\log(\xi_2) = 0.68^{+0.02}_{-0.03}$, $kT_1 = 96\pm2$ eV, $kT_2 = 270^{+9}_{-14}$ eV, $\Gamma = 1.62\pm0.01$, $E_{\rm obs} = 5.75^{+0.04}_{-0.03}$ keV and $\sigma_{\rm obs} = 70^{+66}_{-48}$ eV. The XSTAR component parameter values are consistent, within errors, with the XSTAR parameter values from the individual data set modelling. As the absorbing columns are similar for the two ionisations it is likely that the absorbing material is

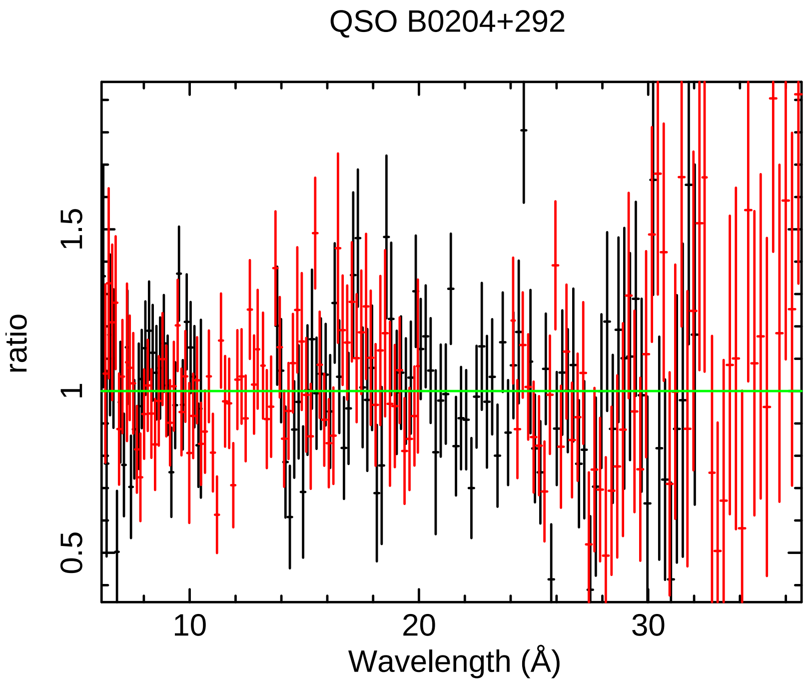

FIGURE 3.19: Ratio plot (data/model) of the double absorbed model fit (including an extra Gaussian absorption component), *tbabs*×XSTAR×XSTAR×(BB$_1$+BB$_2$+*ga*$_{\rm abs}$), to the RGS data ($6-37$ Å; observed) of QSO B0204$+$292. Black: RGS1 data. Red: RGS2 data.

multi-phased and therefore has an ionisation gradient rather than there being two distinct ionisation regions.

Bregman and Lloyd-Davies (2007) analysed the RGS data of QSO B0204$+$292 as part of a sample of 25 bright AGN, which the authors searched to look for evidence of O VII X-ray absorption from million degree gas in the Milky Way halo and the Local Group medium. QSO B0204$+$292 had the worst signal-to-noise of the sample but the authors claim a detection of O VII absorption at $\lambda = 21.603$ Å, with a width of $2\sigma = 0.08$ mÅ (EW $= 60.9 \pm 19.2$ mÅ). QSO B0204+292 lies $\sim 9°$ (~ 130 kpc) from M33. Due to the large uncertainty on the EW of the line detection the authors are unable to determine whether a hot gas halo surrounds M33. Bregman and Lloyd-Davies (2007) appear to use unbinned data (required for their analysis) and when the same feature

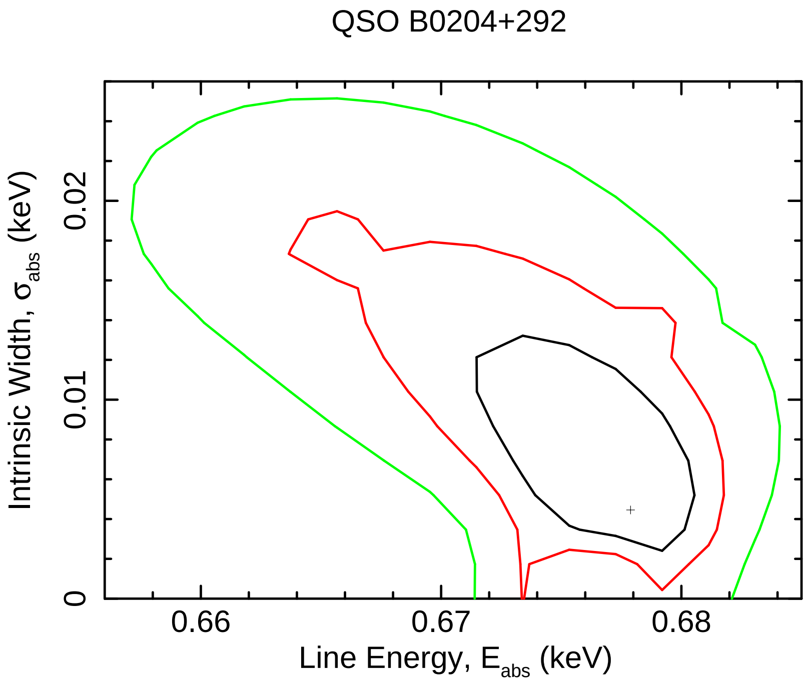

FIGURE 3.20: Confidence region contours determined for the parameters of the Gaussian absorption line tested with the best fit model to the RGS data of QSO B0204 + 292. The cross marks the best fit parameter values. The contours coloured black, red and green represent $\Delta\chi^2$ values of 2.3, 4.61 and 9.21, respectively, equivalent to approximate confidence regions, for 2 degrees of freedom, of $\sim 68\%$, 90% and 99%, respectively.

is searched for in the binned data sets analysed here it is not found. The FWHM (~ 0.06 mÅ) of the detected O VII line is smaller than the width of one bin in the current data set. This feature, if present, will not affect the results of the RGS modelling done here as the feature is thought to be at $z = 0$ and is not prominent in this data set. As stated previously, a longer observation of QSO B0204 + 292 with *XMM-Newton* would be instructive.

3.4.3 PG 1001+054

EPIC Data

Due to the low number of bins in the hard-band of both the PN and MOS spectra, the initial power-law fits were tentative at best. An initial Galactic absorbed power-law

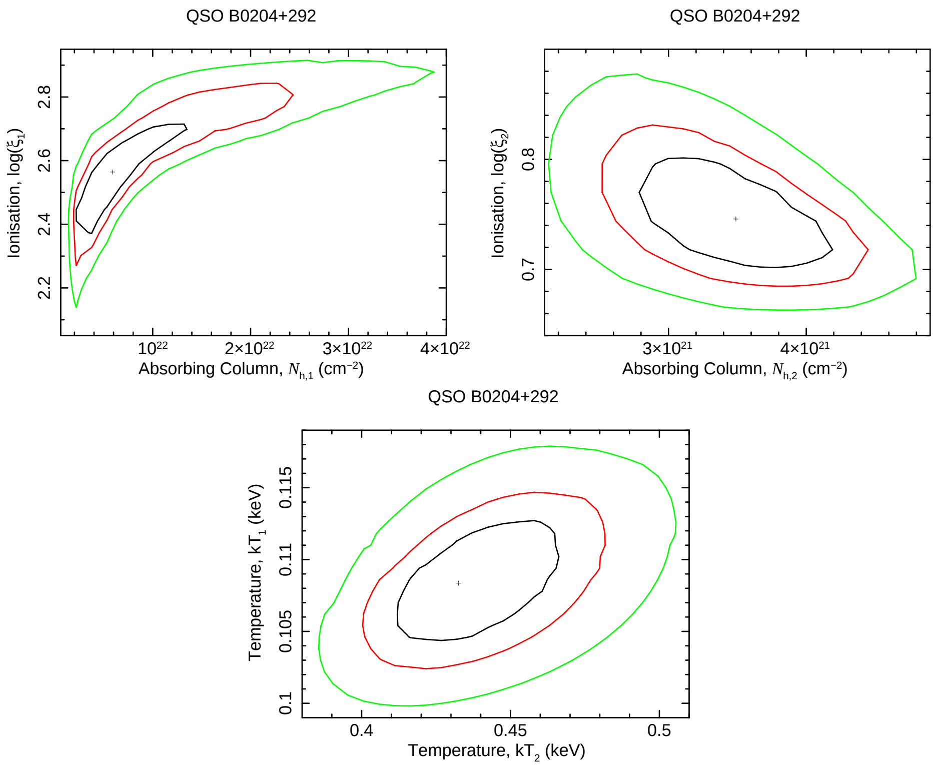

FIGURE 3.21: Confidence region contours determined for the parameters of the XSTAR and BB components from the best fit model to the EPIC data of QSO B0204+292. Top left: ionisation and column density for the first XSTAR component. Top right: ionisation and column density for the second XSTAR component. Bottom: temperatures from the two BB components. The crosses mark the best fit parameter values. The contours coloured black, red and green represent ΔS values of 2.3, 4.61 and 9.21, respectively, equivalent to approximate confidence regions, for 2 degrees of freedom, of $\sim 68\%$, 90% and 99%, respectively.

fit to the hard-band resulted in a photon-index of $\Gamma = 0.71^{+0.53}_{-0.54}$, with fit statistics of χ^2/d.o.f. $= 5.0/6$. However, this left a relatively large residual feature around 5 keV (Figure 3.22). A Gaussian emission line component was added in an attempt to model this feature. This new model led to fit statistics of χ^2/d.o.f. $= 1.2/3$, with $\Gamma = 2.33$, $E_{\rm obs} = 4.77^{+0.63}_{-3.54}$ keV and $\sigma_{\rm obs} = 1.18^{+4.57}_{-1.18}$ keV. As seen from the errors on $E_{\rm obs}$ and $\sigma_{\rm obs}$, and the fit statistics, this model is clearly over-fitting the data; the errors on Γ could not be constrained. However, this model seems to result in a preferred photon-index, though the physical origins of the Gaussian emission line is unclear. At the redshift of

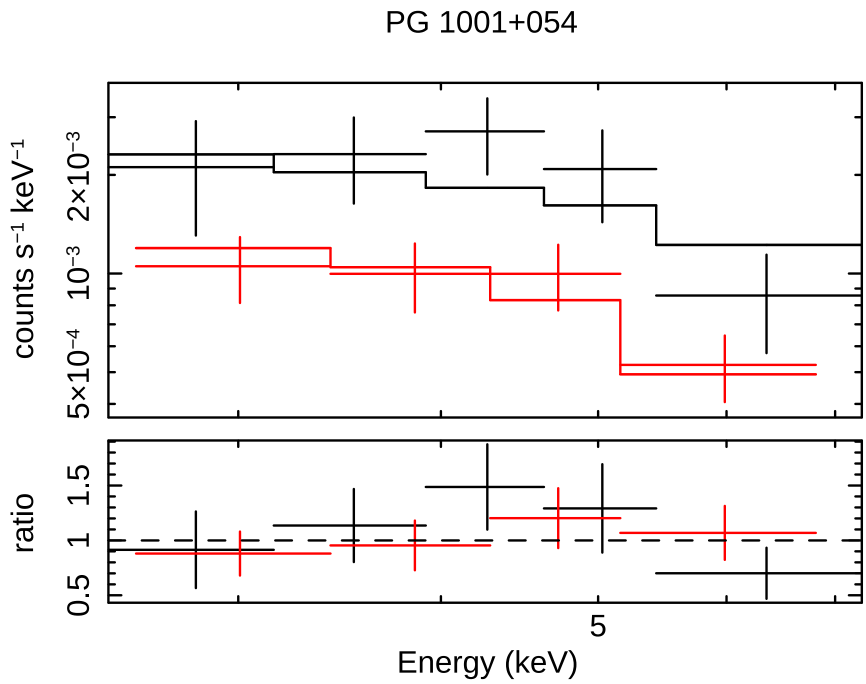

FIGURE 3.22: Initial hard-band ($2-10$ keV; observed) absorbed power-law fit to PG $1001+054$. Top: data points and model fit line. Bottom: ratio of data points to the model fit line. Black: PN data. Red: MOS data.

PG $1001+054$ ($z = 0.1605$), an iron emission line (e.g., Fe Kα) should be observed at ~ 5.5 keV. This energy is much greater than the energy of the included Gaussian emission line. In addition, the Gaussian emission line is extremely broad, which most likely indicates that the residuals left by the initial power-law fit are of a continuum origin.

As a way of gauging the previous model fit, a Galactic absorbed power-law model was fitted to the data with the photon-index frozen at $\Gamma = 2$, typical of AGN (Nandra and Pounds, 1994). The fit statistics for this model were χ^2/d.o.f. $= 2.8/7$ and are reported in Table 3.6. The fit reveals the same residuals between 4 and 7 keV, and apparent absorption below 4 keV (Figure 3.23). This fit clearly shows that the hard-band of PG $1001+054$ is more complex than a simple power-law. However, due to the lack of counts in the hard-band no parameters can be determined with any reasonable accuracy. Therefore, a longer observation of PG $1001+054$ with *XMM-Newton* would be

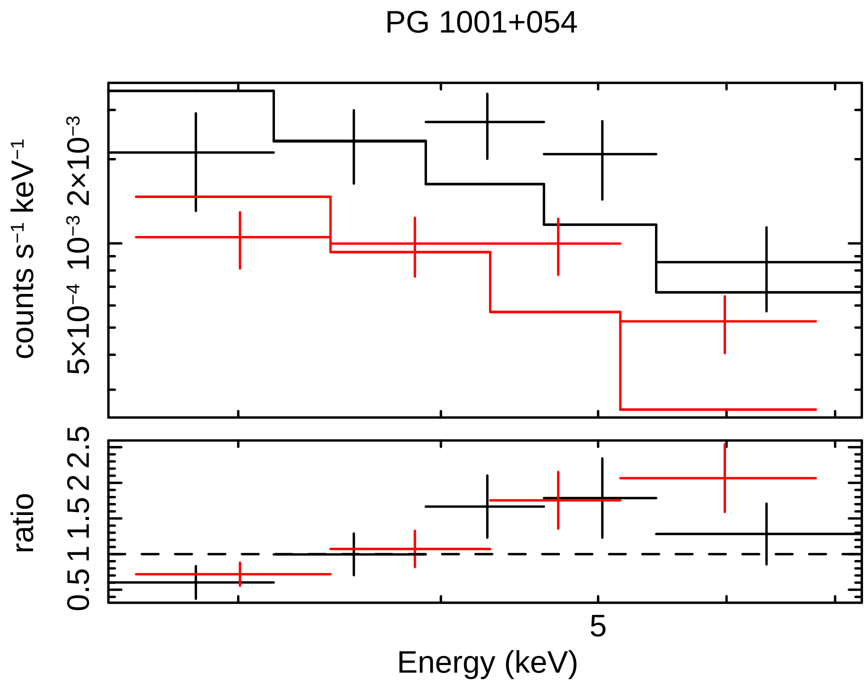

FIGURE 3.23: Second hard-band ($2-10$ keV; observed) absorbed power-law fit to PG $1001+054$. The photon-index, Γ, is frozen at 2. Top: data points and model fit line. Bottom: ratio of data points to the model fit line. Black: PN data. Red: MOS data.

instructive.

The above models were applied to PG $1001+054$ once again but for the energy range $1.0-10$ keV. However, this did not improve the model fits, since the increase in the number of data bins was small. Also, it is likely that any features, such as continuum absorption, present within PG $1001+054$ will manifest themselves below 2 keV. With this in mind and in the interest of having a typical photon-index, the hard-band model containing the Gaussian emission around ~ 4.7 keV will be used to begin modelling of the broad-band data EPIC for PG $1001+054$. The inclusion of the Gaussian emission component in the final best fit model will be decided during the broad-band modelling. Obviously, due to the low number of bins, the presence of absorption features at high energies cannot be determined.

Extending the hard-band best fit model to 0.3 keV reveals absorption between ~ 0.6 and 2 keV (Figures 3.5 and 3.24). The lower boundary of this absorption occurs at the jump in opacity due to O VII. Also, the data at low energies does not look smooth, suggesting further narrow absorption below 0.6 keV. Figure 3.24 shows the hard-band model extended down to 0.3 keV for both the PN (black) and MOS (red) data. In an attempt to model the absorption between ~ 0.6 and 2 keV, the XSPEC model *absori* was included in the broad-band model. The *absori* component mimics an ionised absorber along the line of sight to the continuum source and was used instead of an XSTAR component due to the complexity of the XSTAR models and the quality of the data. The inclusion of the *absori* component resulted in fit statistics of $\chi^2/\text{d.o.f.} = 31/30$. Under the assumption that the continuum source (the *po* seen at high-energies) is ionising the absorbing material, the photon-index parameter of the *absori* component was tied to the power-law photon-index, which had a value of $\Gamma = 2.57^{+0.27}_{-0.25}$. The ionisation ($\xi$) and absorbing column ($N_{\rm h}$) were $426.5^{+387.4}_{-161.9}$ erg cm s^{-1} and $6.2^{+4.2}_{-2.6} \times 10^{22}$ cm^{-2}, respectively.

The photon-index, $\Gamma \approx 2.6$, for the above model is moderately high and the fit leaves some residuals around ~ 0.5 keV. A BB component was added to model these residuals. Even though the inclusion of the BB component (kT $= 121^{+50}_{-30}$ eV) over-fitted the data ($\chi^2/\text{d.o.f.} = 25.2/28$) and was not statistically required ($\Delta\chi^2/\Delta\text{d.o.f.} = 4.8/2$), this latest model appears to have reduced the residuals around ~ 0.5 keV. Its inclusion has also reduced Γ to $1.68^{+0.89}_{-0.59}$. However, the absorbing material parameters have dramatically changed to $\xi = 18.9^{+39.5}_{-12.1}$ erg cm s^{-1} and $N_{\rm h} = 3.39 \pm 1.97 \times 10^{22}$ cm^{-2}. The removal of the Gaussian component whilst the BB component is still present does not affect the absorber's parameters significantly nor the fit statistics, but the resulting Γ value is quite hard at ~ 1.1.

As stated earlier, the hard-band continuum is likely to be more complex than a simple

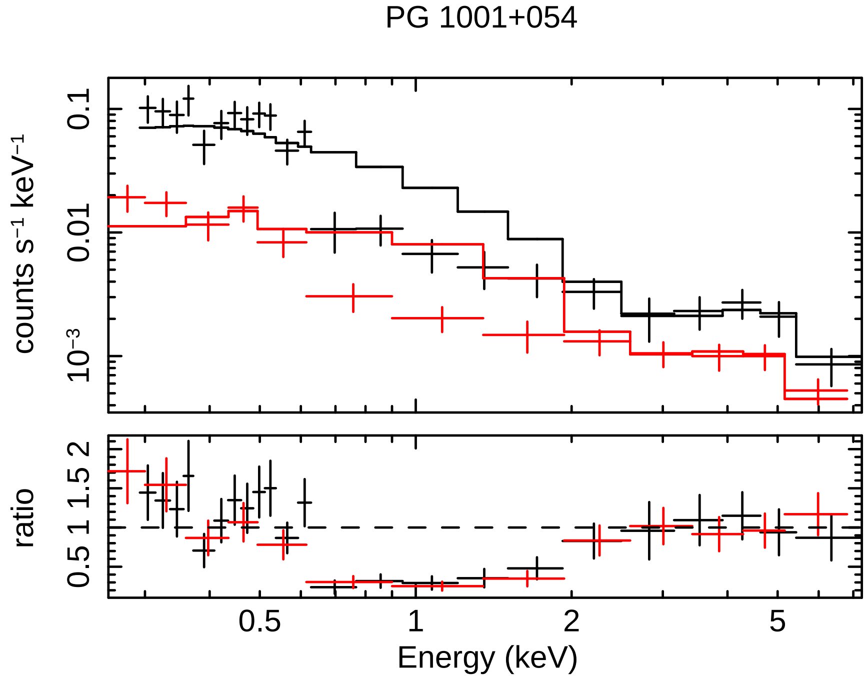

FIGURE 3.24: Initial hard-band ($2-10$ keV; observed) absorbed power-law fit (containing broad Gaussian emission around ~ 4.5 keV) to PG $1001+054$ extended down to 0.3 keV. Top: data points and model fit line. Bottom: ratio of data points to the model fit line. Black: PN data. Red: MOS data.

power-law and the inclusion of an absorbing column will certainly affect the continuum model. If both the BB and Gaussian components are removed, the resulting parameter values are $\Gamma = 2.02^{+0.13}_{-0.12}$, $\xi = 289.5^{+106.6}_{-71.5}$ erg cm s^{-1} and $N_{\rm h} = 17.5^{+7.1}_{-4.9} \times 10^{22}$ cm^{-2}, with fit statistics of χ^2/d.o.f. $= 47.4/31$. The latest model, *tbabs*$\times$*absori*$\times$(*po*), is the same as the model used by Schartel et al. (2005). The parameter values for this model determined in this analysis are consistent with the parameter values presented by Schartel et al. (2005) of $\Gamma = 1.97^{+0.17}_{-0.14}$, $\xi = 542^{+97}_{-147}$ erg cm s^{-1} and $N_{\rm h} = 19.2^{+11.9}_{-7.3} \times 10^{22}$ cm^{-2}. However, this model fit leaves rather large residuals around $\sim 0.5-1.5$ keV (Figure 3.25). As a final check the *absori* component was replaced with an XSTAR component, and the following model, *tbabs*$\times$XSTAR$\times$(*po*), was applied to the broad-band EPIC data for PG $1001+054$. The resulting parameter values were $\Gamma = 2.48^{+0.16}_{-0.20}$,

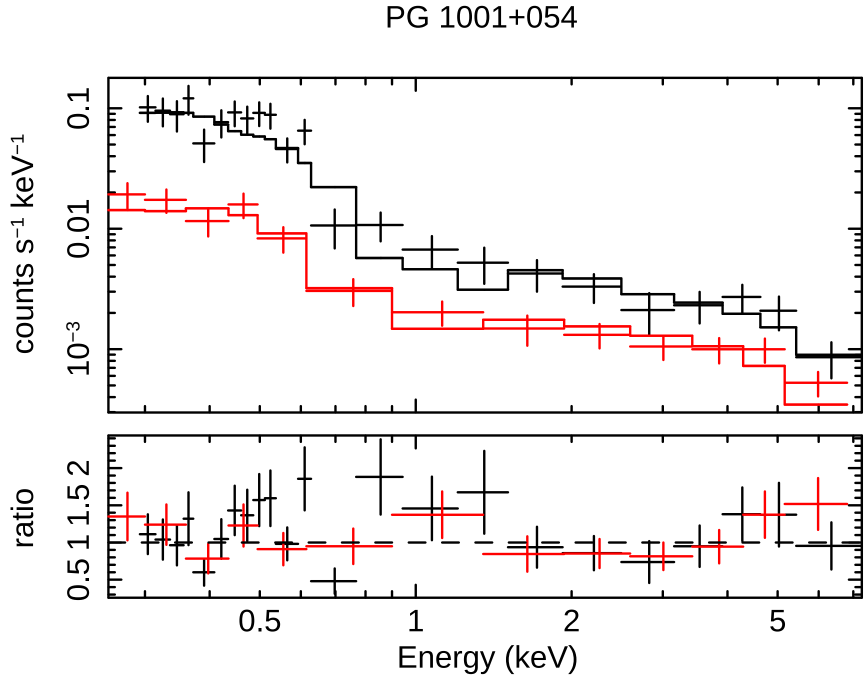

FIGURE 3.25: Broad-band ($0.3-10$ keV; observed) intrinsic absorbed power-law fit, *tbabs*×*absori*×(*po*), to the PG 1001+054 EPIC data. Top: data points and model fit line. Bottom: ratio of data points to model fit line. Black: PN data. Red: MOS data.

$\log(\xi) = 2.05^{+0.13}_{-0.12}$ and $N_{\rm h} = 21.0^{+4.56}_{-4.04} \times 10^{22}$ cm^{-2}, with fit statistics of χ^2/d.o.f. $= 32.8/29$ (Figure 3.26). This latest model statistically fits the data best, though returns a softer photon-index ($\Gamma \approx 2.5$) than the model containing the *absori* component. The absorbing columns and ionisations returned by both models are similar, $N_{\rm h} \sim 2 \times 10^{23}$ cm^{-2} and $\log(\xi) \sim 2$, respectively. The residuals from the XSTAR model fit, shown in Figure 3.26, appear reduced but similar when compared to the residuals from the *absori* model shown in Figure 3.25. However, both sets of residuals are still quite large. In light of the newest model, the best fit model for the EPIC data of PG $1001+054$ is *tbabs*×XSTAR×(*po*), with the parameters and fit statistics mentioned earlier. Figure 3.27 shows a contour plot of the confidence regions for the parameters, N and $\log(\xi)$, of the XSTAR model component. The contours represent $\Delta\chi^2$ values of 2.3 (black), 4.61 (red) and 9.21 (green), approximately equivalent to 68%, 90% and 99% confidence regions

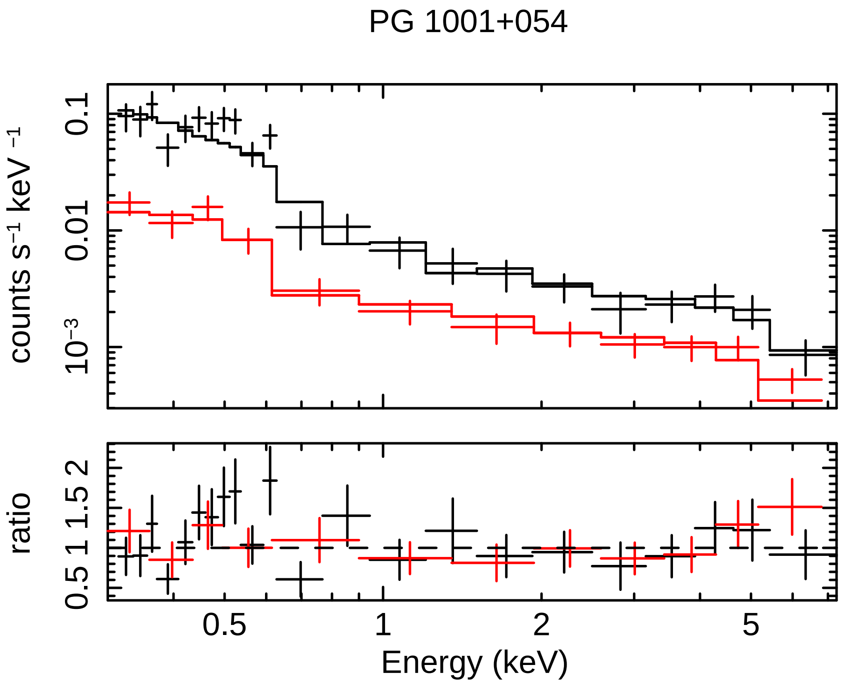

FIGURE 3.26: Broad-band ($0.3-10$ keV; observed) intrinsic absorbed power-law fit, containing an XSTAR component, *tbabs*×XSTAR×(*po*), to the PG $1001+054$ EPIC data. Top: data points and model fit line. Bottom: ratio of data points to model fit line. Black: PN data. Red: MOS data.

for 2 degrees of freedom, respectively. The cross marks the best fit values for the two parameters. From Figure 3.27 it can be seen that the ionisation and absorbing column of the XSTAR component are well constrained. In addition, allowing the redshift parameter to vary was not significant at the 99% level and therefore no outflow velocity could be determined.

Although the intrinsically absorbed power-law model is the best fit model so far, two final sets of models were fitted to the EPIC data of PG $1001+054$ to test alternative physical scenarios. The first set of models include a partial covering component, *pcfabs*. The model *tbabs*×(BB+*po*) was fitted to the EPIC data. This resulted in a reasonable fit (χ^2/d.o.f. $= 35.5/29$) and left residuals both at high- and low-energies (Figure 3.28). Once again an XSTAR component was added, though it was not significant at the 99%

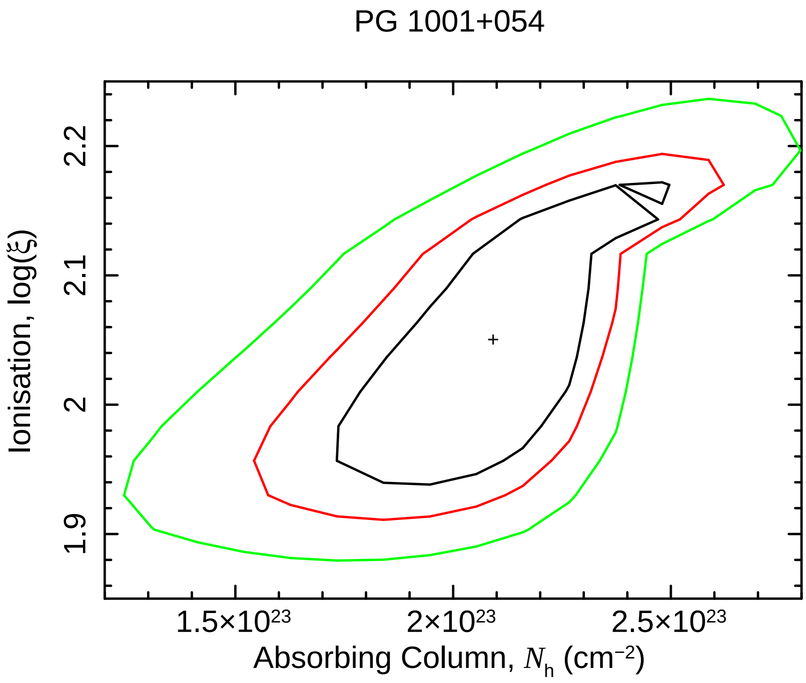

FIGURE 3.27: Confidence region contours determined for the XSTAR component parameters, $\log(\xi)$ and N_h, used in best fit model, *tbabs*×XSTAR×(*po*), for the EPIC data of PG 1001+054. The cross marks the best fit parameter values. The three contours coloured black, red and green represent $\Delta\chi^2$ values of 2.3, 4.61 and 9.21, respectively. These $\Delta\chi^2$ values represent approximate confidence regions, for 2 degrees of freedom, of $\sim 68\%$, 90% and 99%, respectively.

level ($\Delta\chi^2/\Delta$d.o.f. $= 6.8/2$).

The second set of models include a *reflion* component (Section 3.4; Ross and Fabian, 2005; Ross et al., 1999), which is used to represent the reflection from an ionised medium. The XSPEC model *kdblur* was used to relativistically blur the *reflion* component, assuming that the reflection occurs close to the SMBH and is undergoing gravitational effects. Within the *kdblur* model, the outer radius, R_out, was frozen to $400\ r_\mathrm{g}$ and the power-law dependence of the emissivity was frozen to a value of 3. The first model used, *tbabs*×(*kdblur*×*reflion*), returned a bad fit with fit statistics of χ^2/d.o.f. $= 144.7/27$; large residuals were left above 2 keV. Thus, an XSTAR component was added, *tbabs*× XSTAR ×(*kdblur*×*reflion*). This model appeared to fit the data well (Figure 3.29) but

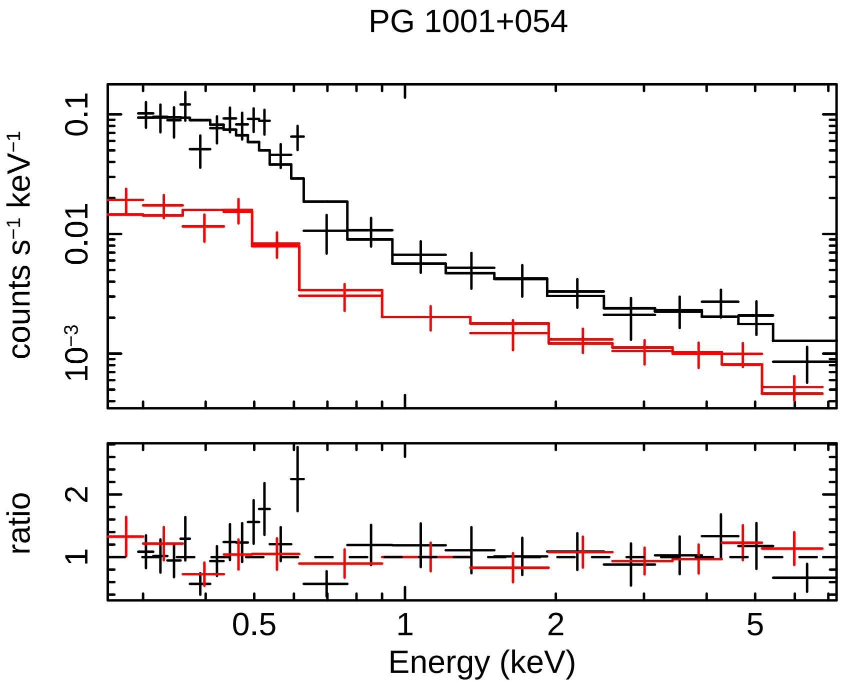

FIGURE 3.28: Broad-band ($0.3 - 10$ keV; observed) partial covered power-law model fit, *tbabs*×*pcfabs*×(*po*), to the PG 1001+054 EPIC data. Top: data points and model fit line. Bottom: ratio of data points to model fit line. Black: PN data. Red: MOS data.

over-fitted the data ($\chi^2/\text{d.o.f.} = 20.3/25$).

With the latest model, *tbabs*×XSTAR×(*kdblur*×*reflion*), over-fitting the data and the partial covering model returning a worse fit, the best fit model for PG $1001 + 054$ is therefore still the intrinsically absorbed power-law model, *tbabs*×XSTAR×(*po*), with the parameter values and fit statistics given earlier.

The resulting observed broad-band ($0.3 - 10$ keV), unabsorbed fluxes for the best fit model were $7.93^{+2.11}_{-1.84} \times 10^{-13}$ erg cm^{-2} s^{-1} and $9.08^{+2.55}_{-2.26} \times 10^{-13}$ erg cm^{-2} s^{-1}, for the PN and MOS data sets, respectively.

Even though the signal-to-noise of the current data sets of PG 1001+054 is poor, the spectra appear to be more complex than the current modelling suggests. More detailed analysis of the X-ray spectra of PG 1001+054 can only be performed with higher quality

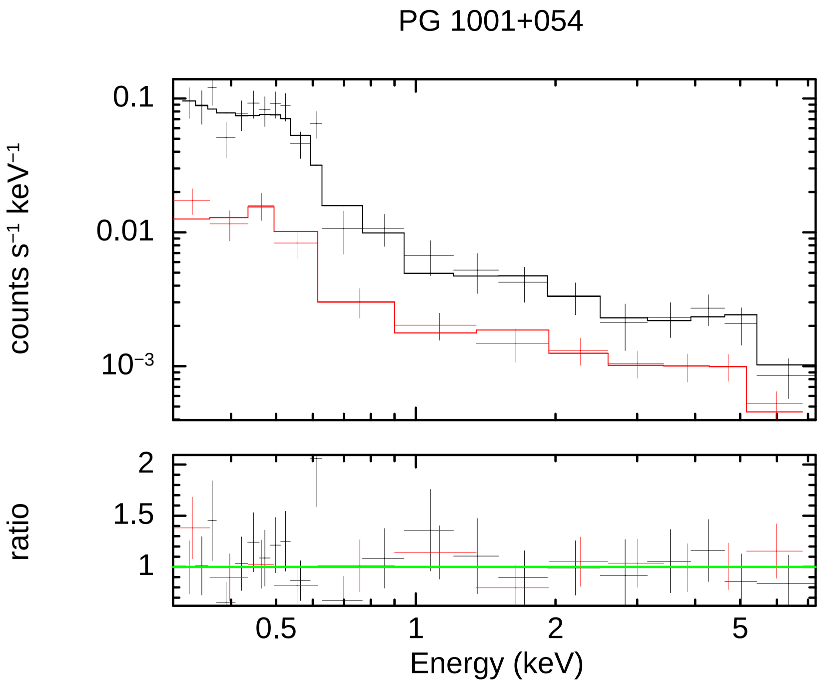

FIGURE 3.29: Intrinsically absorbed, relativistically blurred, ionised reflection model fit, *tbabs*×XSTAR×(*kdblur*×*reflion*), to the broad-band $(0.3-10$ keV; observed) EPIC data of PG 1001+054. Top: data points and model fit line. Bottom: ratio of data points to model fit line. Black: PN data. Red: MOS data.

data. Therefore, as stated earlier, a longer observation of PG $1001+054$ with *XMM-Newton* would be instructive.

RGS Data

Unfortunately, PG $1001+054$ was not detected by the RGS instruments with any significance. Therefore, no analysis of the RGS data for PG $1001+054$ will be performed.

3.4.4 PG 1351+640

EPIC Data

The hard-band fit to the EPIC spectra of PG $1351+640$ resulted in a photon-index, $\Gamma = 1.89{\pm}0.07$ and required the presence of a Gaussian emission line at $E_{\rm obs} = 5.98^{+0.13}_{-0.15}$ keV

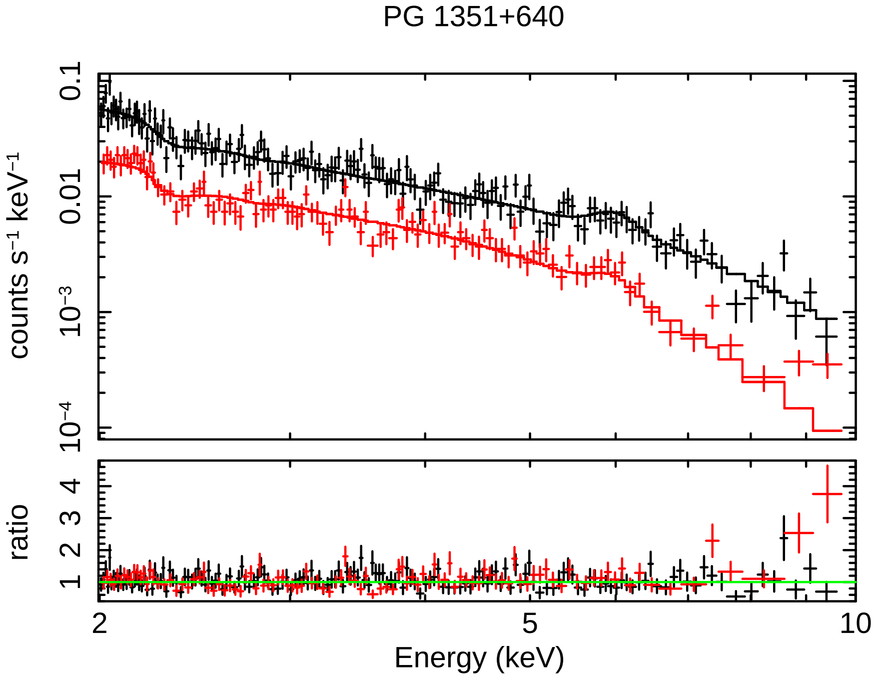

FIGURE 3.30: Initial hard-band (2 – 10 keV; observed) absorbed power-law fit to PG 1351 + 640. Top: data points and model fit line. Bottom: ratio of data points to model fit line. Black: PN data. Red: MOS data.

with an intrinsic width of $\sigma_{\rm obs} = 243^{+195}_{-124}$ eV ($\Delta\chi^2/\Delta$d.o.f. $= 16.0/3$). This feature, within errors, is consistent with Fe Kα emission at the redshift of PG 1351 + 640 ($z = 0.0882$). The hard-band of PG 1351 + 640 (Figure 3.30) was also inspected for absorption features; none were obvious. An attempt was made to model the feature around ~ 7.9 keV in the PN data (Figure 3.30). However, a Gaussian absorption line component was unable to fit this feature with any significance. The final fit statistics for the hard-band fit, *tbabs*×(*ga*$_{\rm obs}$+*po*), were χ^2/d.o.f. $= 258.4/257$.

Figure 3.5 shows a SE that starts around ~ 0.6 keV and looks like a step function in the ratio plot (data/model) of the hard-band fit to the PN data for PG 1351 + 640 extended down to 0.3 keV. This step is indicative of the jump in opacity of O VII around 0.6 – 0.7 keV. Having extended the initial hard-band fit down to 0.3 keV for both the PN and MOS data sets, the broad-band fitting began with the addition of a BB component to the hard-band model in an attempt to model the apparent SE. The energy and intrinsic width of the Gaussian emission component were frozen to the values obtained from the hard-band fit until the final broad-band model was fitted. The inclusion of the BB component with a temperature, kT $= 80 \pm 3$ eV, altered the photon-index slightly to $\Gamma = 2.02 \pm 0.03$ and returned moderate fit statistics of χ^2/d.o.f. $= 830.9/688$. This model leaves clear residuals between 0.5 and 1.2 keV (Figure 3.31), partially in absorption around ~ 0.65 keV. This absorption feature is consistent with UTA absorption at the redshift of PG 1351+640 ($z = 0.0882$). The residuals shown in Figure 3.31 imply that there are more complex features present, which are most likely absorption features. With this in mind, the BB component was removed and an XSTAR component included to see if the presence of an absorbing column could model the apparent features. The inclusion of the XSTAR component resulted in a particularly soft photon-index, $\Gamma = 2.40^{+0.02}_{-0.01}$, an absorbing column, $N_{\rm h} = 7.58^{+0.68}_{-0.65} \times 10^{21}$ cm^{-2}, ionisation, $\log(\xi) = 1.61^{+0.06}_{-0.09}$, and fit statistics of χ^2/d.o.f. $= 871.6/688$. This obviously gives a worse fit than the inclusion of the BB component and the softer Γ leads to large residuals at higher energies (Figure 3.32). This suggests there is a SE present that is being absorbed. Therefore, the BB was re-introduced with the XSTAR component still present.

The latest model, *tbabs*×XSTAR×(BB+*po*+*ga*$_{\rm obs}$), gave a much better fit, χ^2/d.o.f. $=$ $760.0/686$ ($\Delta\chi^2$/d.o.f. $= 111.6/2$). The model parameters were kT $= 100^{+5}_{-3}$ eV, $\Gamma = 2.16^{+0.03}_{-0.04}$, $N_{\rm h} = 1.67^{+0.25}_{-0.27} \times 10^{21}$ cm^{-2} and $\log(\xi) = 0.73^{+0.12}_{-0.07}$. Even though this model gives a much better fit, there are still some broad residuals around ~ 1.2 keV (Figure 3.33). A second BB component was added. This removed the residuals left over from the previous model (Figure 3.34) and the inclusion of the second BB was significant with $\Delta\chi^2/\Delta$d.o.f. $= 60.1/2$. Therefore, the best fit model (χ^2/d.o.f. $= 699.9/684$) for PG 1351+640 is *tbabs*×XSTAR×($\rm BB_1$+$\rm BB_2$+*po*+*ga*$_{\rm obs}$). The model parameters were

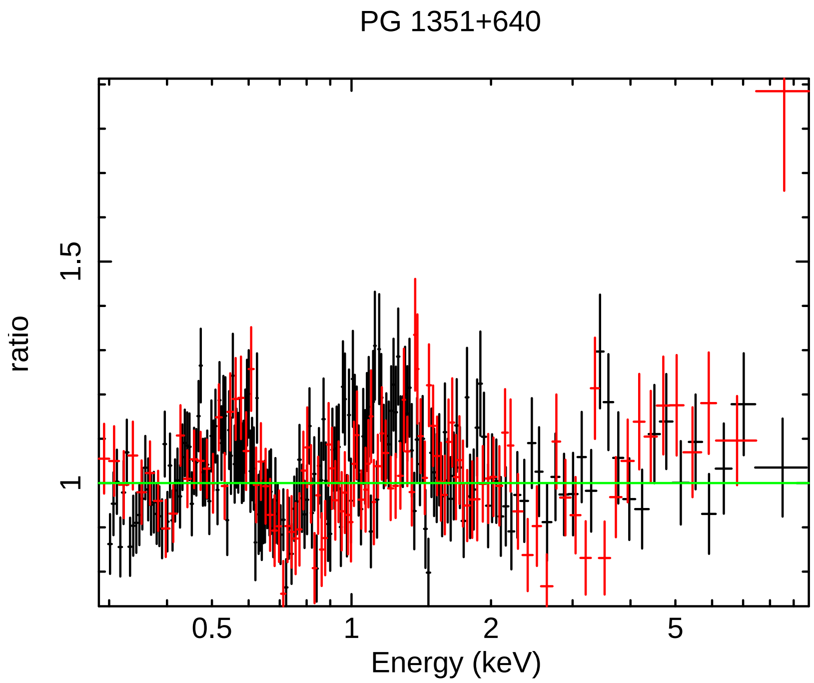

FIGURE 3.31: Ratio plot (data/model) of the first broad-band ($0.3 - 10$ keV; observed) model fit, *tbabs*×(BB+*po*), to the PG 1351+640 EPIC data. The data points have been re-binned within XSPEC for viewing purposes only, to a significance of 10σ and a maximum number of 10 data points per bin. Black: PN data. Red: MOS data.

kT$_1$ $= 94^{+5}_{-4}$ eV, kT$_2$ $= 236^{+32}_{-19}$ eV, $\Gamma = 1.89^{+0.10}_{-0.12}$, $N_{\rm h} = 2.82^{+0.66}_{-0.51} \times 10^{21}$ cm^{-2} and $\log(\xi) = 0.67^{+0.11}_{-0.05}$. Figure 3.35 shows the confidence region contour plots for the XSTAR parameter values $N_{\rm h}$ and ξ. The contours represent $\Delta\chi^2$ values of 2.3 (black), 4.61 (red) and 9.21 (green), approximately equivalent to 68%, 90% and 99% confidence regions for 2 degrees of freedom, respectively. The cross in Figure 3.35 marks the best fit values for $N_{\rm h}$ and $\log(\xi)$. The $N_{\rm h}$ and $\log(\xi)$ values appear to be well constrained. The best fit model fit statistics were $\chi^2/\text{d.o.f.} = 699.9/684$.

The redshift parameter for the XSTAR component was thawed and the data re-fitted in an attempt to determine an outflow speed for the absorbing column. However, this was found to not be significant at the 99% level ($\Delta\chi^2/\text{d.o.f.} = 1.8/1$) and was thus rejected.

One final model, a partial covering model, was fitted to the data of PG 1351$+$640 to

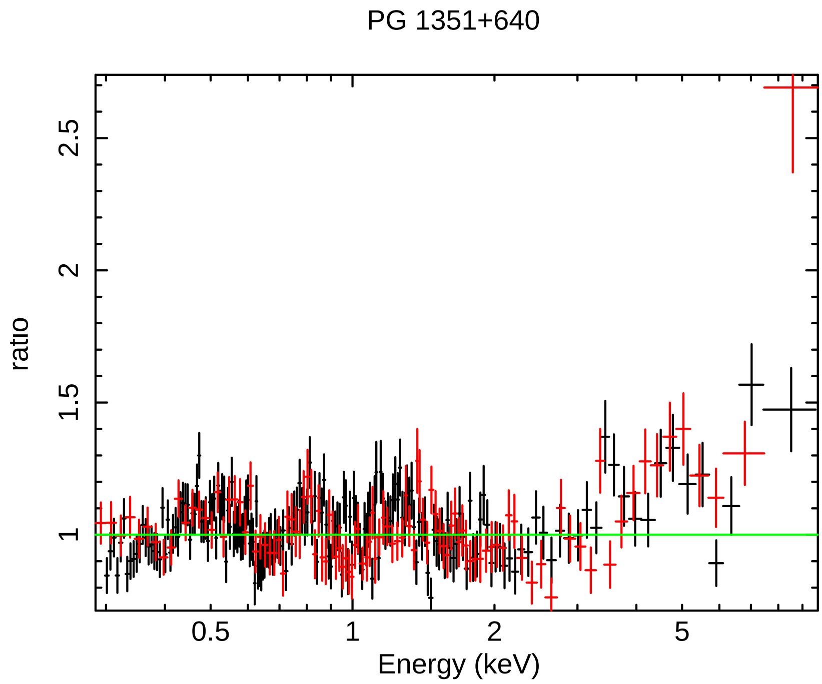

FIGURE 3.32: Ratio plot (data/model) of the second broad-band ($0.3-10$ keV; observed) model fit, *tbabs*×XSTAR×(*po*), to the PG $1351+640$ EPIC data. The data points have been re-binned within XSPEC for viewing purposes only, to a significance of 10σ and a maximum number of 10 data points per bin. Black: PN data. Red: MOS data.

see if such a complex absorber as the XSTAR component was truly required or whether something simpler would suffice. The first model used was *tbabs*×*pcfabs*×($ga_{\rm obs}$+*po*). This resulted in a poor fit, $\chi^2/\text{d.o.f.} = 1061.5/688$. A BB component was included, which proved significant and returned fit statistics of $\chi^2/\text{d.o.f.} = 799.1/686$. This model still left absorption around ~ 0.7 keV. An XSTAR component was added, *tbabs*×*pcfabs*× XSTAR×(ga_{rmobs}+*po*), which returned fit statistics of $\chi^2/\text{d.o.f.} = 757.4/684$. This model has worse fit statistics compared to the best fit model and the way in which the modelling progressed, it is clear that the partial covering component, *pcfabs*, is not required but the XSTAR component is.

The observed broad-band ($0.3-10$ keV), unabsorbed fluxes for the best fit model, *tbabs*×XSTAR×(BB_1+BB_2+*po*+$ga_{\rm obs}$), to PG 1351+640 were calculated to be $1.99^{+0.05}_{-0.10}\times$

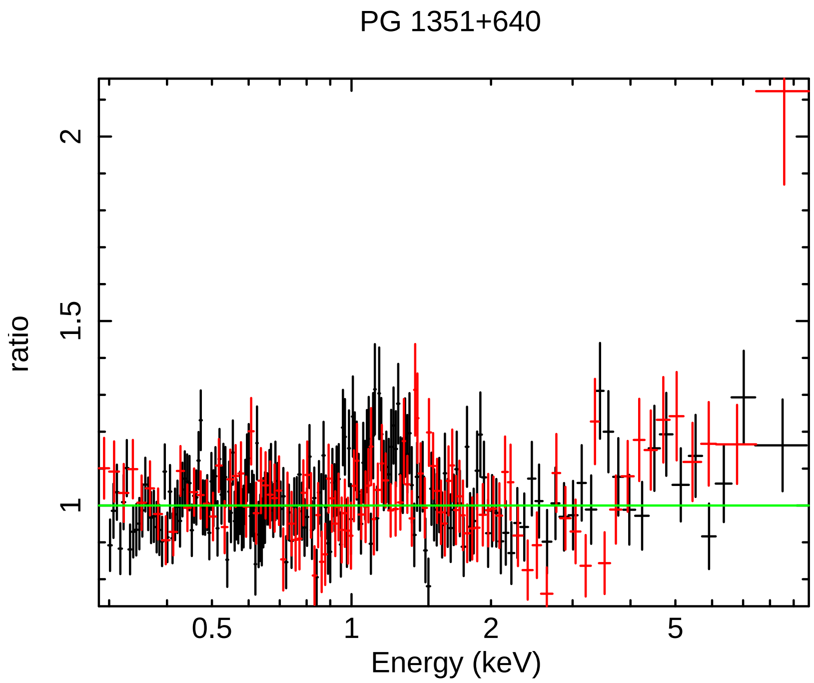

FIGURE 3.33: Ratio plot (data/model) of the third broad-band ($0.3-10$ keV; observed) model fit to PG $1351+640$. The model shown here is *tbabs*×XSTAR×(BB+*po*+*ga*$_{\rm obs}$). There are clear residuals around 1.2 keV. The data points have been re-binned within XSPEC for viewing purposes only, to a significance of 10σ and a maximum number of 10 data points per bin. Black: PN data. Red: MOS data.

10^{-12} erg cm^{-2} s^{-1} and $2.14^{+0.14}_{-0.03} \times 10^{-12}$ erg cm^{-2} s^{-1} for the PN and MOS data, respectively.

RGS Data

PG 1351+640 was detected by the RGS detectors. However, the count rates for PG 1351+640 in the RGS1 and RGS2 data sets were, 0.022 ± 0.001 counts s^{-1} and 0.019 ± 0.001 counts s^{-1}, respectively. The data sets are quite noisy and various binning widths were tested before settling on the final value. Figure 3.36 shows both the RGS1 and RGS2 data grouped with 10 (black), 20 (red) and 40 (green) channels per bin. The binning is quite heavy, even at 10 channels per bin, and is required due to the quality of the data. A final value of 40 channels per bin was chosen. This binning corresponds to an

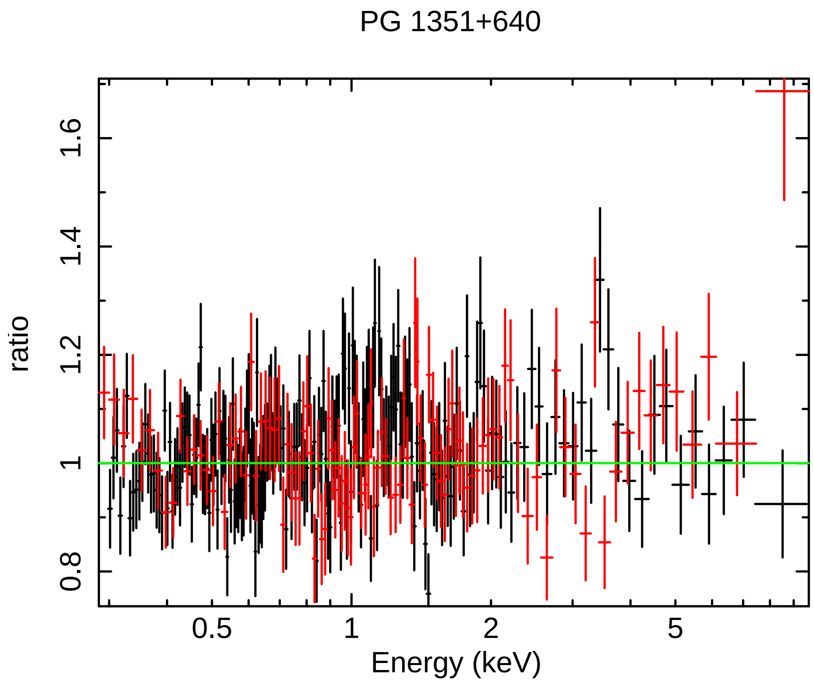

FIGURE 3.34: Ratio plot (data/model) of the best model fit to PG $1351+640$. The best fit model is *tbabs*×XSTAR×(BB$_1$+BB$_2$+*po*+*ga*$_{\rm obs}$). The data points have been re-binned within XSPEC for viewing purposes only, to a significance of 10σ and a maximum number of 10 data points per bin. Black: PN data. Red: MOS data.

approximate bin width of ~ 0.40 Å. Unfortunately, this is approximately six times the RGS resolution of ~ 60 mÅ. Therefore, the data will be under-sampled with respect to the RGS resolution, so any particularly narrow features will be binned out of the data. However, it is unlikely, due to the signal-to-noise of the data, that such features would be evident. At best, a continuum fit can be made to the RGS data sets of PG $1351+640$ for comparison to the EPIC best fit continuum parameters. The RGS data sets were fitted between 6 and 37 Å. As the data were binned by channel rather than by number of counts per bin, Chi-squared statistics are not valid and thus C-statistics (S) were used whilst fitting the RGS data for PG $1351+640$ in XSPEC.

An initial inspection of the RGS data for PG $1351+640$ was made by over-plotting the EPIC best fit model. This was done to search the RGS data for any predicted features

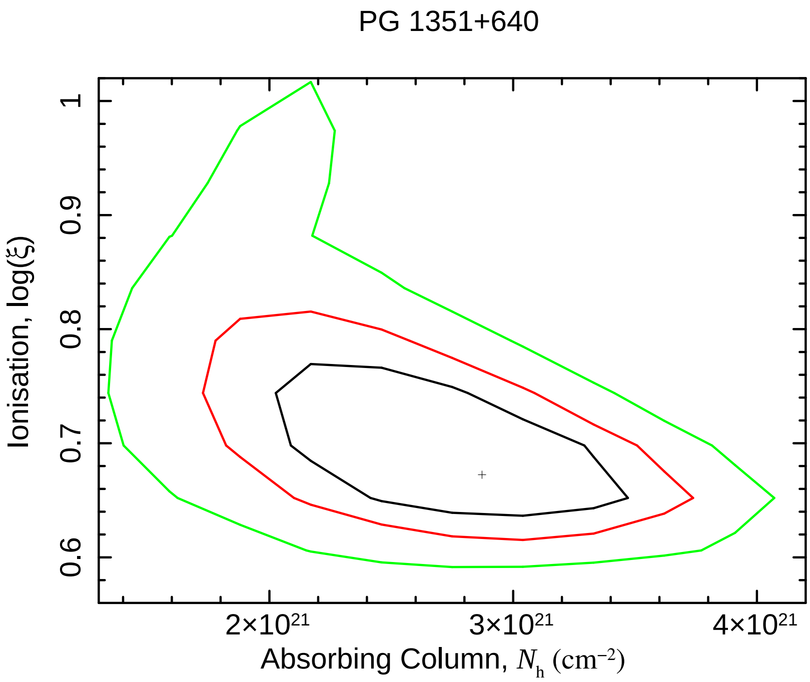

FIGURE 3.35: Confidence region contours determined for the XSTAR component parameters, $\log(\xi)$ and $N_{\rm h}$, used in best fit model for the EPIC data of PG 1351+640. The cross marks the best fit parameter values. The three contours coloured black, red and green represent $\Delta\chi^2$ values of 2.3, 4.61 and 9.21, respectively. These $\Delta\chi^2$ values represent approximate confidence regions, for 2 degrees of freedom, of $\sim 68\%$, 90% and 99%, respectively.

from the EPIC model. Figure 3.37 shows the EPIC best fit model folded through the RGS response plotted over the RGS data. It is clear that all predicted features from the EPIC best fit model are present in the RGS data.

Modelling began by fitting a Galactic absorbed power-law to the data sets. This first model resulted in a photon-index of $\Gamma = 2.33 \pm 0.17$ and fit statistics of S/d.o.f. $= 155.9/123$. The addition of a BB component, kT $= 91^{+14}_{-15}$ eV, appeared significant with $\Delta S/\Delta$d.o.f. $= 16.4/2$, and resulted in a photon-index of $\Gamma = 1.26^{+0.51}_{-0.60}$ and fit statistics of S/d.o.f. $= 139.5/121$. Finally, an XSTAR component ($N_{\rm h} \approx 5 \times 10^{21}$ cm^{-2}, $\log(\xi) \approx 0.56$; errors could not be constrained) was added to the model. This was not significant at the 99% confidence level ($\Delta S/\Delta$d.o.f. $= 6.9/2$). It should be noted that in

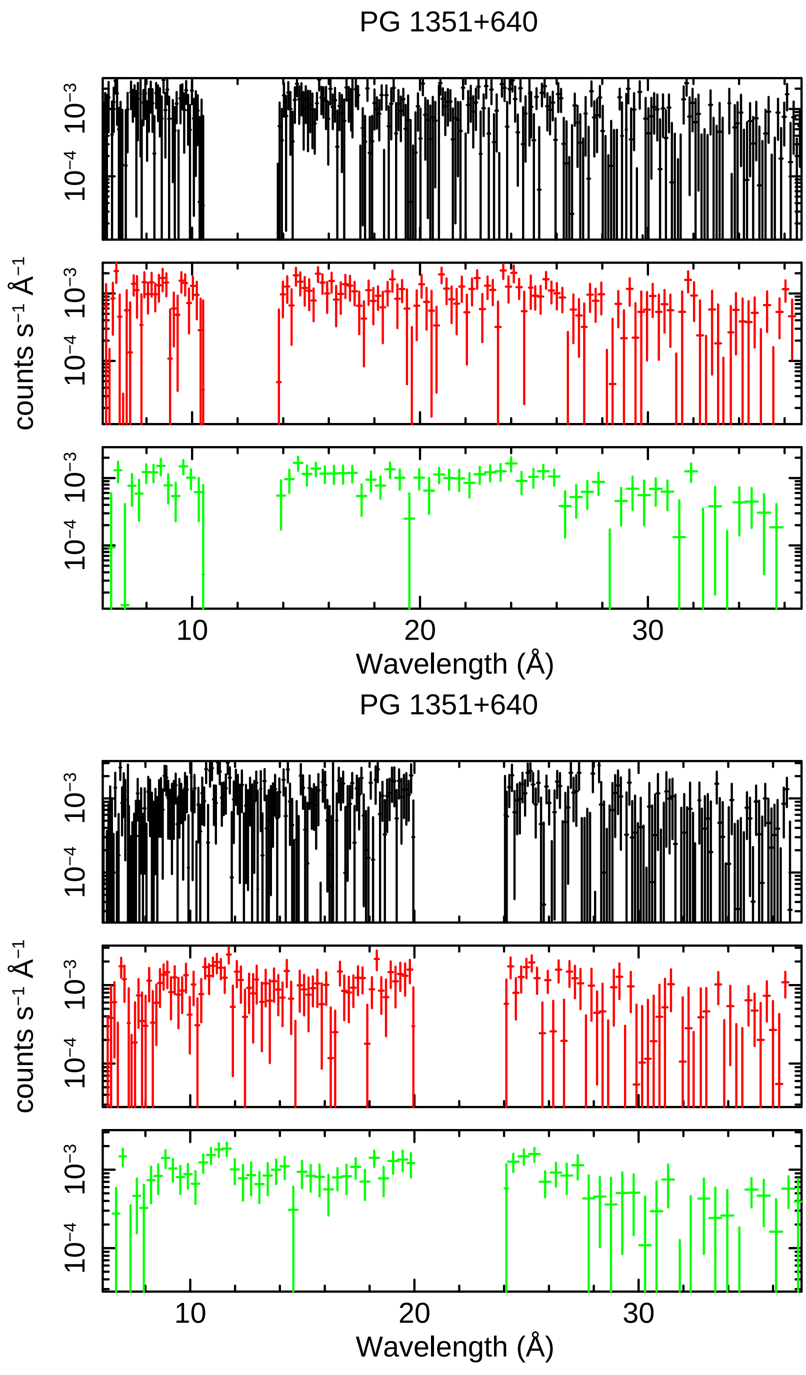

FIGURE 3.36: Binned ($6-37$ Å; observed) RGS1 (top) and RGS2 (bottom) data for PG 1351+640. Black, red and green points show the data sets binned into groups of 10, 20 and 40 channels, respectively.

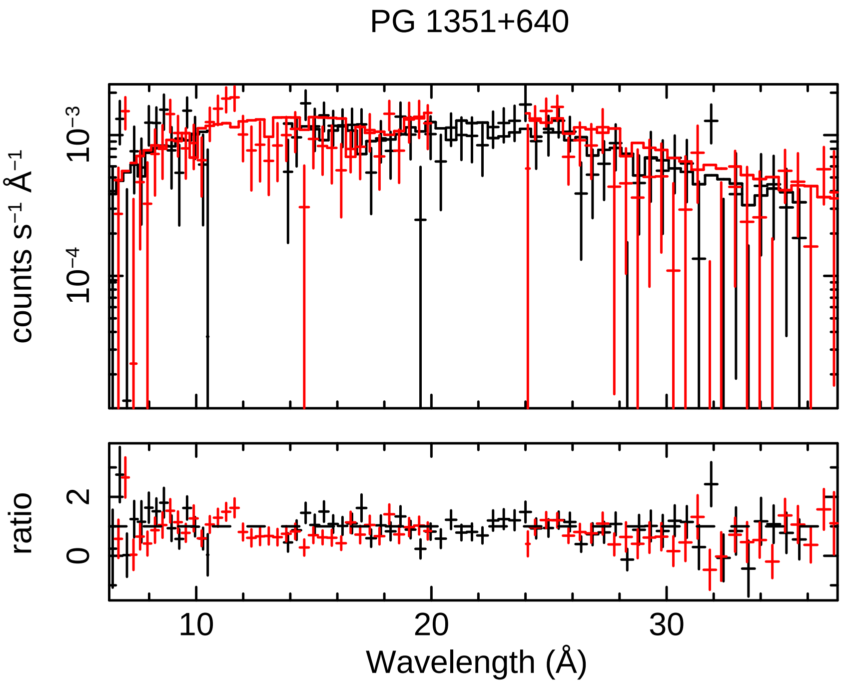

FIGURE 3.37: PG $1351+640$ EPIC best fit model folded through the RGS response plotted over the RGS data ($6-37$ Å; observed). Top: data points and model fit line. Bottom: ratio of data points to model fit line. Black: RGS1 data. Red: RGS2 data.

this particular case, re-arranging the order in which the model components were added can change whether that component is significant or not; though the final fit statistics were found to be almost identical.

The power-law in the *tbabs*×(BB+*po*) model was replaced with a second BB component. The resulting parameter values were kT$_1 = 96 \pm 10$ eV and kT$_2 = 411^{+105}_{-66}$ eV with $S/$d.o.f. $= 137.0/121$. Once again, an XSTAR component was added, but it was found not to be significant with $\Delta S/\Delta$d.o.f. $= 4.6/2$. However, the parameter values obtained during this fit, kT$_1 = 90^{+16}_{-13}$ eV, kT$_2 = 285^{+97}_{-50}$ eV, $N_{\rm h} \approx 4.6 \times 10^{21}$ cm^{-2} and $\log(\xi) \approx 0.57$ (the errors on $N_{\rm h}$ and $\log(\xi)$ could not be constrained) are consistent with those reported here for the EPIC data of PG $1351+640$.

The poor quality of the RGS data sets for PG $1351+640$, made distinguishing be-

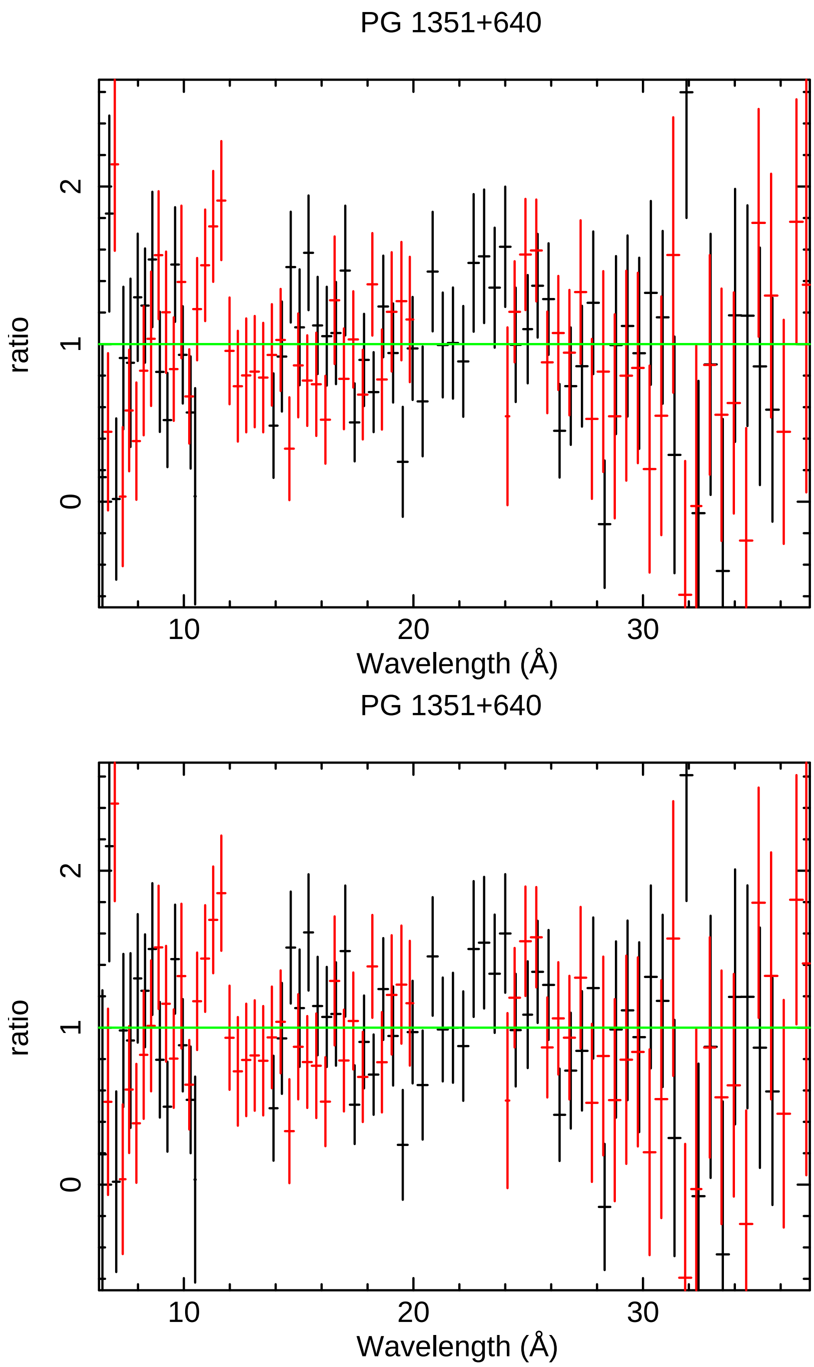

FIGURE 3.38: Ratio plots (data/model) of the two model fits to the RGS data ($6-37$ Å; observed) of PG $1351+640$, which do not contain an XSTAR component. Top: Model - *tbabs*$\times$(BB+*po*). Bottom: Model - *tbabs*$\times$(BB$_1$+BB$_2$). Black: RGS1 data. Red: RGS2 data.

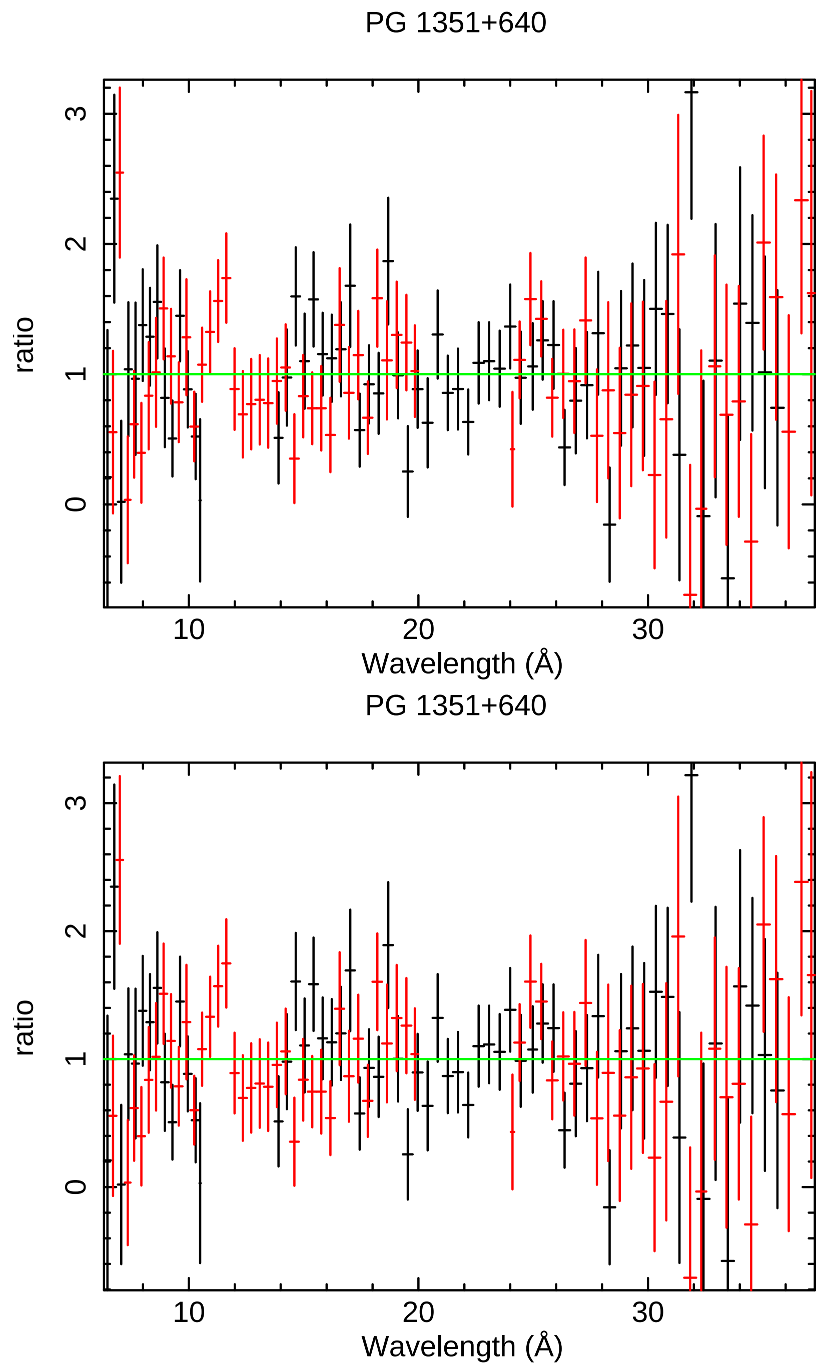

FIGURE 3.39: Ratio plots (data/model) of two model fits to the RGS data ($6-37$ Å; observed) of PG 1351+640, which contain the non-significant XSTAR model components. Top: Model - *tbabs*×XSTAR×(BB+*po*). Bottom: Model - *tbabs*×XSTAR×(BB_1+BB_2). Black: RGS1 data. Red: RGS2 data.

tween the two models suggested to fit the data best impossible. Further modelling would be redundant. For both models, *tbabs*×(BB+*po*) and *tbabs*×(BB_1+BB_2), the fit residuals are practically identical (Figure 3.38) and the addition of the XSTAR component is not significant, though the residuals around 21 Å are reduced (Figure 3.39). Also, both models only parameterise the data and are not true physical representations of the processes occurring within the source. Therefore, to simply compare fluxes with the EPIC PG 1351+640 data, the former of the two contending models, *tbabs*×(BB+*po*), will be called the best-fit model. The resulting observed $0.35-2$ keV, unabsorbed fluxes for PG 1351+640 in the RGS1 and RGS2 detectors are, $9.70^{+0.36}_{-0.90} \times 10^{-13}$ erg cm^{-2} s^{-1} and $8.31^{+0.61}_{-0.85} \times 10^{-13}$ erg cm^{-2} s^{-1}, respectively. These fluxes are consistent with the EPIC PN and MOS observed 0.35–2.0, unabsorbed fluxes of $8.63^{+0.92}_{-0.85} \times 10^{-13}$ erg cm^{-2} s^{-1} and $1.96^{+0.24}_{-0.40} \times 10^{-12}$ erg cm^{-2} s^{-1}, respectively.

3.4.5 PG 1440+356

EPIC Data

PG 1440+356 was observed on four separate occasions with *XMM-Newton*. The observation dates were the 23$^{\rm rd}$ of December 2001 and the 1$^{\rm st}$, 4$^{\rm th}$ and 7$^{\rm th}$ of January 2003. The respective observation identification numbers (OBS ID) were 0107660201, 0005010101, 0005010201, 0005010301. As mentioned in Section 3.4, the 0107660201 observation was affected by pile-up in both the PN and MOS detectors. To combat this, the spectra for this observation were extracted using an annulus to exclude the central 10 and 5 arc seconds from the PN and MOS source extraction regions, respectively. It should be noted by doing this, the effect of pile-up is reduced but at the cost of losing counts, which may lead to improper flux values for this observation.

As with the previous targets, an absorbed power-law fit was made to each individual

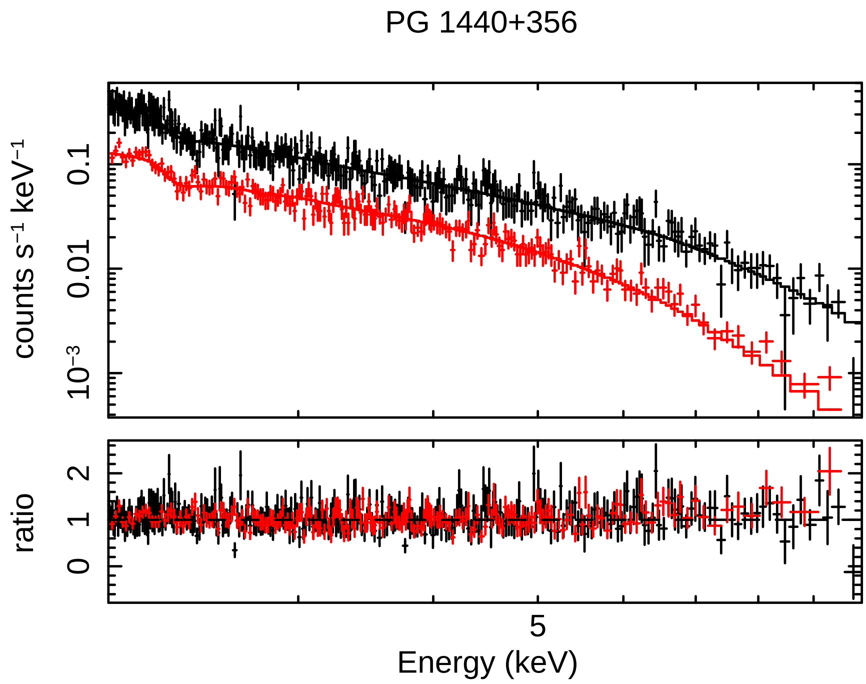

FIGURE 3.40: Initial hard-band ($2-10$ keV; observed) absorbed power-law model fit to the 0005010101 observation of PG $1440+356$. A slight up-turn in the residuals can be seen above 5 keV, suggesting that a more complex model is required. Top: data points and model fit line. Bottom: ratio of data points to model fit line. Black: PN data. Red: MOS data

data set of PG $1440+356$ between $2-10$ keV. It was noticed during this modelling that the absorbed power-law model was not fitting the data above 5 keV particularly well; there appears to be a slight excess above 5 keV (Figure 3.40). With this in mind, the absorbed power-law was only fitted between 2 and 5 keV as this part of the spectrum is assumed to be unaffected by features such as the complex iron line region and the onset of the SE. In each case, the power-law photon-index for the $2-5$ keV fit, Γ_{2-5}, was slightly softer that the initial Γ_{2-10} values. The results of the absorbed power-law fits are shown in Table 3.7. The new $2-5$ keV fits were extended to 10 keV and the resulting χ^2 values from this extension were also recorded in Table 3.7. Figure 3.41 shows the simultaneous PN and MOS $2-5$ keV absorbed power-law model fits extended across the entire broad-band ($0.3-10$ keV; observed). It can be clearly seen that all

Table 3.7: Initial Hard-band Model Fits to PG 1440+356

OBS ID	Γ_{2-10} χ^2/d.o.f.	Γ_{2-5} χ^2_a/d.o.f.	χ^2_b/d.o.f.	Γ_{2-5} PN	MOS
0005010101	$2.14^{+0.05}_{-0.05}$ $427.2/493$	$2.24^{+0.07}_{-0.06}$ $325.4/377$	$444.9/493$	$2.23^{+0.11}_{-0.11}$	$2.26^{+0.08}_{-0.08}$
0005010201	$2.17^{+0.09}_{-0.08}$ $172.0/190$	$2.32^{+0.12}_{-0.12}$ $123.1/151$	$182.0/190$	$2.31^{+0.20}_{-0.19}$	$2.34^{+0.15}_{-0.15}$
0005010301	$2.07^{+0.06}_{-0.06}$ $302.0/336$	$2.27^{+0.09}_{-0.09}$ $226.9/260$	$335.4/336$	$2.17^{+0.15}_{-0.14}$	$2.33^{+0.11}_{-0.11}$
0107660201	$2.12^{+0.08}_{-0.08}$ $235.7/216$	$2.27^{+0.10}_{-0.10}$ $185.0/169$	$246.9/216$	$2.36^{+0.23}_{-0.23}$	$2.26^{+0.12}_{-0.12}$

Initial hard-band, absorbed power-law fits to PG 1440+356. Γ_{2-10} and Γ_{2-5} represent the resultant photon-indices from joint fits to the PN and MOS spectra for PG 1440+356 between $2-10$ keV and $2-5$ keV, respectively. χ^2_a/d.o.f. and χ^2_b/d.o.f., are the χ^2/d.o.f. values for the $2-5$ keV absorbed model fit and for the $2-5$ keV absorbed model fit extended up to 10 keV, respectively. Columns headed PN and MOS represent the photon-indices returned from individual absorbed power-law fits between $2-5$ keV to the PN and MOS spectra, respectively.

observations have a SE, as well as excess residuals at energies greater than 5 keV. Fitting an absorbed power-law model to only the PN data sets between $2-5$ keV does have an effect on the Γ_{2-5} values (Table 3.7) and the slopes of the ratio plots (Figure 3.42). In this case the residuals for each observation are almost identical and the slope of the SE appears the same. However, when the same model is fitted independently to the MOS data (Figure 3.43), the SE residuals do not appear to be the same as in the PN only case. Obviously, the simultaneous PN and MOS fit results are an approximate average of the two individual fits.

Fitting the MOS and PN data simultaneously for the individual observations continued by comparing the $2-10$ keV hard-band with various models that could represent the excess features above 5 keV. Three different models were tested. The first was a partially covered absorbed power-law model, *tbabs*$\times$*pcfabs*$\times$(*po*). The second model, *tbabs*$\times$(*pexrav*) incorporates a component, *pexrav*, that mimics reflection from a neutral

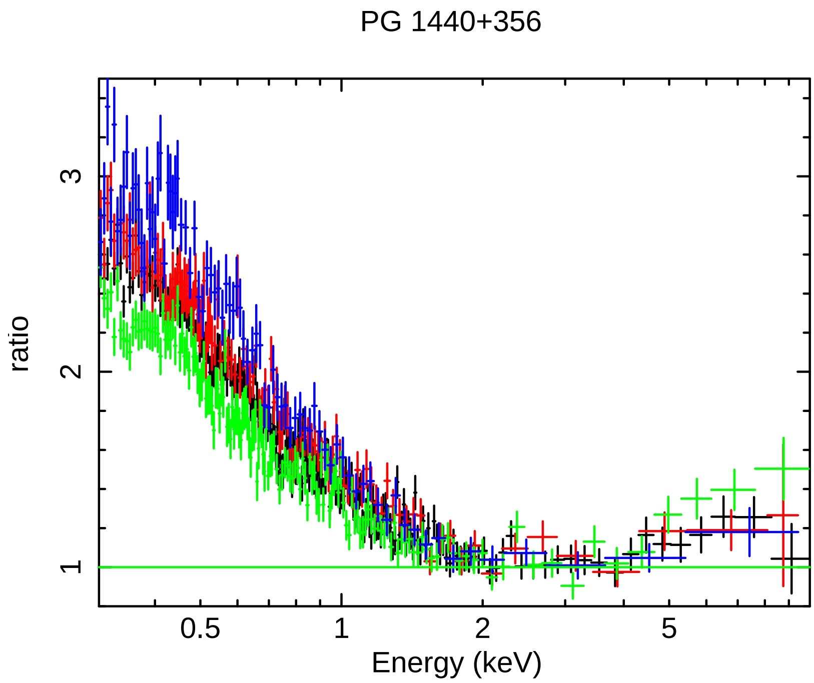

FIGURE 3.41: Ratio plot (data/model) of the joint (PN and MOS) absorbed power-law fit between $2-5$ keV to all four *XMM-Newton* EPIC observations of PG $1440+356$, extended across $0.3-10$ keV (observed). There is a clear SE and curvature above 5 keV in all observations. The feature around ~ 2.2 keV is a result of the binning and is not believed to be a real feature. For clarity, only the PN data is shown for each observation. The data has been re-binned in XSPEC to a minimum significance of 15σ and a maximum number of 15 data points per bin. Black: 0005010101. Red: 0005010201. Green: 0005010301. Blue: 0107660201.

medium (Magdziarz and Zdziarski, 1995). The last model, *tbabs*$\times$(*pexriv*) is similar to the second model except that the component *pexriv* (Magdziarz and Zdziarski, 1995) mimics reflection from an ionised medium. In both the *pexrav* and *pexriv* cases, inclination and cut-off energy were frozen at 30 degrees and 100 keV, respectively. Table 3.8 presents the results for the hard-band fits with these three models. Figures 3.44, 3.45 and 3.46 show the *pcfabs*, *pexrav* and *pexriv* model fits, respectively, to the hard-band of the 0005010101 observation of PG $1440+356$. It can be seen from Table 3.8 that the three models give comparable fits to each of the observations and appear to over-fit the data in each case. As the models are not nested it is improper to use the F-Test to compare the

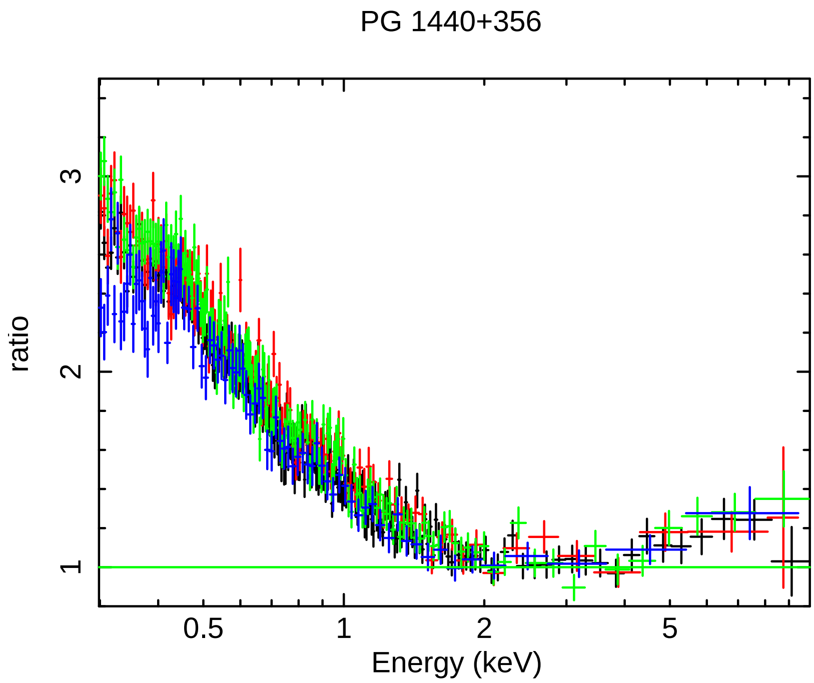

FIGURE 3.42: Ratio plot (data/model) of the absorbed power-law fit between $2-5$ keV to all four *XMM-Newton* PN observations of PG 1440+356, extended across $0.3-10$ keV (observed). Once again, there is clear SE and curvature above 5 keV. However, the SE in each case appears almost identical. The feature around ~ 2.2 keV is a result of the binning and is not believed to be a real feature. The data has been re-binned in XSPEC to a minimum significance of 15σ and a maximum number of 15 data points per bin. Black: 0005010101. Red: 0005010201. Green: 0005010301. Blue: 0107660201.

results directly, which makes determining the best-fit model difficult. The uncertainties returned for the ionisation parameter values in the *pexriv* model suggest that this model is inappropriate for the hard-band data. The *pcfabs* returns the lowest χ^2 value for each observation for 1 less d.o.f., although this is only significant at the 99% level for one observation (0005010101). Therefore, the hard-band for each observation can be modelled by either the *pcfabs* or *pexrav* models. Obviously the broad-band modelling will determine which model components will be used to describe the hard-band. It should also be noted that the returned values of Γ were all consistent with one another within errors.

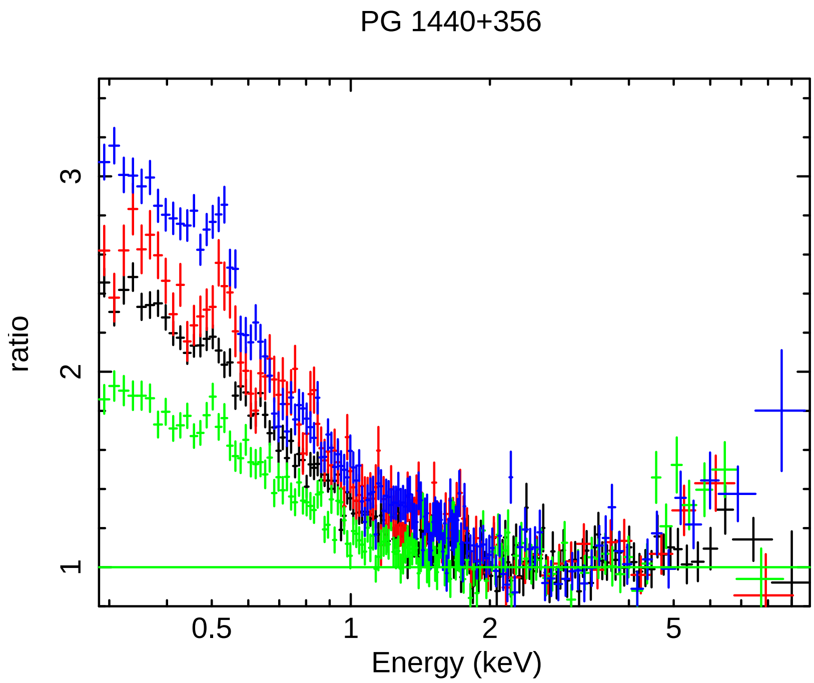

FIGURE 3.43: Ratio plot (data/model) of the absorbed power-law fit between $2-5$ keV to all four *XMM-Newton* MOS observations of PG 1440+356, extended across $0.3-10$ keV (observed). Once again, there is a clear SE and curvature above 5 keV in all observations. However, unlike the PN ratio plots, the SE does not appear to be identical. The feature around ~ 0.5 keV is likely a result of the response matrix and is not believed to be a real feature. The data has been re-binned in XSPEC to a minimum significance of 10σ and a maximum number of 10 data points per bin. Black: 0005010101. Red: 0005010201. Green: 0005010301. Blue: 0107660201.

Broad-band fitting was performed in the usual manner using the three hard-band models previously described as starting points. BB components were added as required in each case and only kept if significant at the 99% level. In addition, standard absorbed power-law models plus BB components were fitted to the data. The broad-band model fit results for the four observations are reported in Table 3.9. Each observation's broad-band modelling results will be discussed on an individual basis. On occasion, where appropriate, a broken power-law version of the hard-band model was fitted to the data. The results of these extra fits are given for the relevant observations.

Table 3.8: Additional $2-10$ keV Model Fits to PG 1440+356

OBS ID	*pcfabs* Γ	$N_{\rm h}$	cf	χ^2/d.o.f.
0005010101	$2.31^{+0.10}_{-0.11}$	$80.6^{+83.4}_{-32.0}$	$0.43^{+0.34}_{-0.14}$	$409.4/491$
0005010201	$2.32^{+0.18}_{-0.13}$	$110.4^{+148.7}_{-63.2}$	$0.53^{+0.29}_{-0.28}$	$164.5/188$
0005010301	$2.59^{+0.19}_{-0.17}$	$47.6^{+14.8}_{-10.0}$	$0.61^{+0.08}_{-0.10}$	$260.7/334$
0107660201	$2.30^{+0.17}_{-0.13}$	$116.4^{+127.3}_{-67.0}$	$0.61^{+0.24}_{-0.24}$	$222.5/214$
	pexrav Γ	R		χ^2/d.o.f.
0005010101	$2.33^{+0.17}_{-0.14}$	$2.00^{+1.81}_{-1.21}$		$421.1/492$
0005010201	$2.29^{+0.26}_{-0.23}$	$0.81^{+2.46}_{-0.63}$		$172.0/189$
0005010301	$2.79^{+0.26}_{-0.24}$	$9.40^{+6.30}_{-3.96}$		$264.7/335$
0107660201	$2.48^{+0.31}_{-0.25}$	$3.67^{+4.46}_{-2.47}$		$228.9/215$
	pexriv Γ	R	ξ	χ^2/d.o.f.
0005010101	$2.38^{+0.16}_{-0.15}$	$2.11^{+1.59}_{-1.24}$	$28.6^{+35.1}_{-27.5}$	$417.4/491$
0005010201	$2.39^{+0.51}_{-0.17}$	$2.03^{+6.74}_{-1.26}$	$0.0001^{+135}_{-0.0001}$	$166.5/188$
0005010301	$2.78^{+0.27}_{-0.23}$	$8.26^{+5.76}_{-3.38}$	$0.008^{+2.92}_{-0.008}$	$263.6/334$
0107660201	$2.51^{+0.33}_{-0.25}$	$3.52^{+4.21}_{-2.30}$	$44.7^{+1541.0}_{-44.7}$	$227.3/214$

The results from the extra hard-band ($2-10$ keV; observed) modelling to the four observations of PG 1440+356. The models used were – *pcfabs*: *tbabs*×*pcfabs*×(*po*); *pexrav*: *tbabs*×(*pexrav*); and *tbabs*×(*pexriv*). The model parameters [units] for each model were – *pcfabs*: photon-index, Γ, column density, $N_{\rm h}$ [$\times 10^{22}$ cm^{-2}] and covering fraction, cf; *pexrav*: incident photon-index, Γ and reflection, R; and *pexriv*: incident photon-index, Γ, reflection, R, and ionisation, ξ [erg cm s^{-1}].

0005010101

From Table 3.9 it is clear that only one BB component is required to model the SE for this observation. All models appear to over-fit the data. The best fit model (χ^2/d.o.f. $=$ $839.0/947$) for the 0005010101 observation is *tbabs*×(BB+*pexriv*) with parameter values of kT $= 88 \pm 1$ eV, $\Gamma = 2.69 \pm 0.04$, $R = 5.07^{+1.03}_{-0.94}$, and $\xi = 74.0^{+58.5}_{-65.8}$ erg cm s^{-1} (Figure 3.47). It should be noted that the *pcfabs* and *pexrav* also gave reasonable fits of χ^2/d.o.f. $= 849.8/947$ and χ^2/d.o.f. $= 850.6/948$, respectively. All three types of

Table 3.9: Broad-band Model Fits to PG 1440+356

Model	Observation ID			
	0005010101	0005010201	0005010301	0107660201
pcfabs				
kT_1	84^{-3}_{-3}	87^{+6}_{-7}	84^{+4}_{-4}	83^{+3}_{-3}
kT_2	$\cdots$	$\cdots$	$\cdots$	203^{+17}_{+23}
Γ	$2.63^{+0.04}_{-0.03}$	$2.80^{+0.06}_{-0.06}$	$2.59^{+0.04}_{-0.03}$	$2.29^{+0.18}_{-0.14}$
$N_{\rm h}$	$28.3^{+8.5}_{-6.8}$	$30.5^{+17.2}_{-11.3}$	$42.5^{+10.0}_{+8.8}$	$104.6^{+118.3}_{-61.3}$
cf	$0.51^{+0.04}_{-0.05}$	$0.59^{+0.07}_{-0.08}$	$0.61^{+0.04}_{-0.05}$	$0.57^{+0.26}_{-0.22}$
χ^2/d.o.f.	$849.9/947$	$564.7/607$	$684.8/782$	$633.6/590$
pexrav				
kT_1	82^{+2}_{-6}	116^{+23}_{-16}	85^{+6}_{-6}	85^{+3}_{-3}
kT_2	$\cdots$	$\cdots$	$\cdots$	217^{+34}_{-24}
Γ	$2.73^{+0.02}_{-0.06}$	$2.98^{+0.03}_{-0.08}$	$2.74^{+0.05}_{-0.05}$	$2.45^{+0.20}_{-0.25}$
R	$7.15^{+0.92}_{-0.80}$	$5.08^{+0.53}_{-0.80}$	$8.60^{+1.69}_{-1.49}$	$3.71^{+3.00}_{-2.4}$
χ^2/d.o.f.	$850.6/948$	$581.8/608$	$678.0/783$	$638.7/591$
pexriv				
kT_1	88^{+6}_{-5}	97^{+22}_{-12}	84^{+6}_{-6}	86^{+4}_{-4}
kT_2	$\cdots$	$\cdots$	$\cdots$	222^{+36}_{-28}
Γ	$2.69^{+0.04}_{-0.04}$	$2.91^{+0.06}_{-0.06}$	$2.73^{+0.05}_{-0.05}$	$2.44^{+0.25}_{-0.23}$
R	$5.07^{+1.03}_{-0.94}$	$8.32^{+2.09}_{-1.77}$	$7.72^{+1.46}_{-1.36}$	$2.89^{+3.42}_{-1.79}$
ξ	$74.0^{+58.5}_{-65.8}$	$0.0003^{+5.2401}_{-0.0003}$	$0.004^{+3.075}_{-0.004}$	$80.7^{+132.5}_{-80.7}$
χ^2/d.o.f.	$839.0/947$	$554.3/607$	$676.8/782$	$635.2/590$

The results from the broad-band ($0.3-10$ keV; observed) modelling of the four observations of PG $1440+356$. The models used were – *pcfabs*: *tbabs*×*pcfabs*×(BB_1+*po*); *pexrav*: *tbabs*×(BB_1+*pexrav*); and *tbabs*×(BB_1+*pexriv*). The model parameters [units] for each model were – *pcfabs*: BB temperature, kT_1 [eV], photon-index, Γ, column density, $N_{\rm h}$ [$\times10^{22}$ cm^{-2}] and covering fraction, cf; *pexrav*: BB temperature, kT_1 [eV], incident photon-index, Γ and reflection, R; and *pexriv*: BB temperature, kT_1 [eV], incident photon-index, Γ, reflection, R, and ionisation, ξ [erg cm s^{-1}]. In the case of the 0107660201 observation a second BB component, BB_2, was included, with parameter kT_2 [eV].

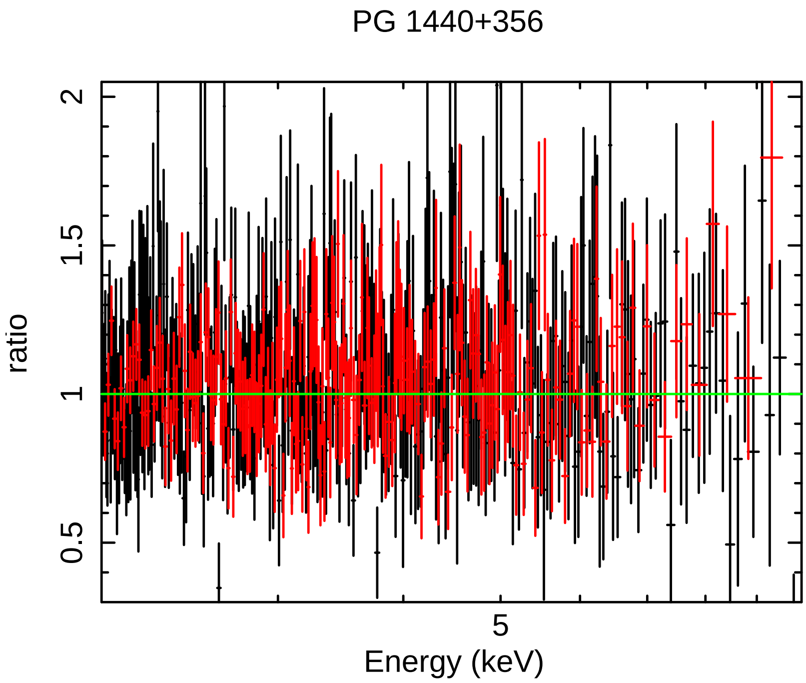

FIGURE 3.44: Ratio plot (data/model) of the additional hard-band (2 – 10 keV; observed) partial covering, *pcfabs*, model fit to the 0005010101 observation of PG 1440+356. Top: data points and model fit line. Bottom: ratio of data points to model fit line. Black: PN data. Red: MOS data.

model return similar photon-indices, $\Gamma \simeq 2.7$.

0005010201

It is clear from Table 3.9 that only one BB component is required to model the SE in this observation and that in all cases the models over-fit the data. The model *tbabs*×(BB+ *pexriv*) returns the lowest fit statistics with $\chi^2/\text{d.o.f.} = 554.3/607$ and parameter values of kT $= 97^{+22}_{-12}$ eV, $\Gamma = 2.91 \pm 0.06$, $R = 8.32^{+2.09}_{-1.77}$, and $\xi = 0.0003^{+5.24}_{-0.0003}$ erg cm s^{-1}. However, as with the 0005010101 observation, the fit statistics for the *pcfabs* and *pexrav* are close to that of the better fitting model, $\chi^2/\text{d.o.f.} = 564.7/607$ and $\chi^2/\text{d.o.f.} = 581.8/608$, respectively. In fact, in the case of the *pcfabs* and *pexrav* model fits, the broken power-law versions return better fit statistics than the BB versions, $\chi^2/\text{d.o.f.} =$

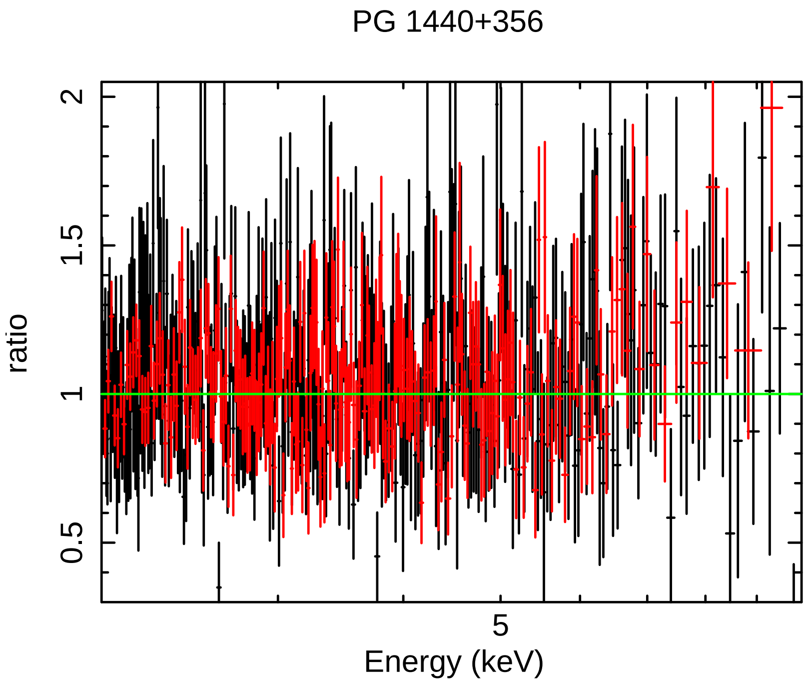

FIGURE 3.45: Ratio plot (data/model) of the additional hard-band (2 – 10 keV; observed) *pexrav* model fit to the 0005010101 observation of PG 1440+356. Top: data points and model fit line. Bottom: ratio of data points to model fit line. Black: PN data. Red: MOS data.

$559.7/607$ and χ^2/d.o.f. $= 558.2/608$, respectively. The parameter values for these two broken power-law fits are $\Gamma_1 = 2.96^{+0.04}_{-0.02}$, $E_{\rm B} = 1.89^{+0.28}_{-0.70}$ keV, $\Gamma_2 = 2.37^{+0.42}_{-0.25}$, $N_{\rm h} = 98.1^{+108.3}_{-49.0}$ cm^{-2} and $cf = 0.54^{+0.28}_{-0.24}$ for the *pcfabs* model and $\Gamma_1 = 2.97^{+0.02}_{-0.02}$, $E_{\rm B} = 2.16^{+0.68}_{-1.03}$ keV, $\Gamma_2 = 2.66^{+0.29}_{-0.33}$ and $R = 5.49^{+4.51}_{-3.41}$ for the *pexrav* model. All of the fits give reasonable results, with rather soft photon-indices. The low ionisation value and its large errors within the *pexriv* model makes it difficult to claim that this particular model best fits the data. The value of ξ almost suggests that the medium is neutral, although the fit statistics for the *pexrav* model with the BB component are much worse. Removing the *pexriv* models from the scenario means that the best fit model for the 0005010201 observation of PG 1440+356 is the broken power-law version of the *pexrav* model, *tbabs*$\times$(*bexrav*), with the parameter values and fits statistics previously

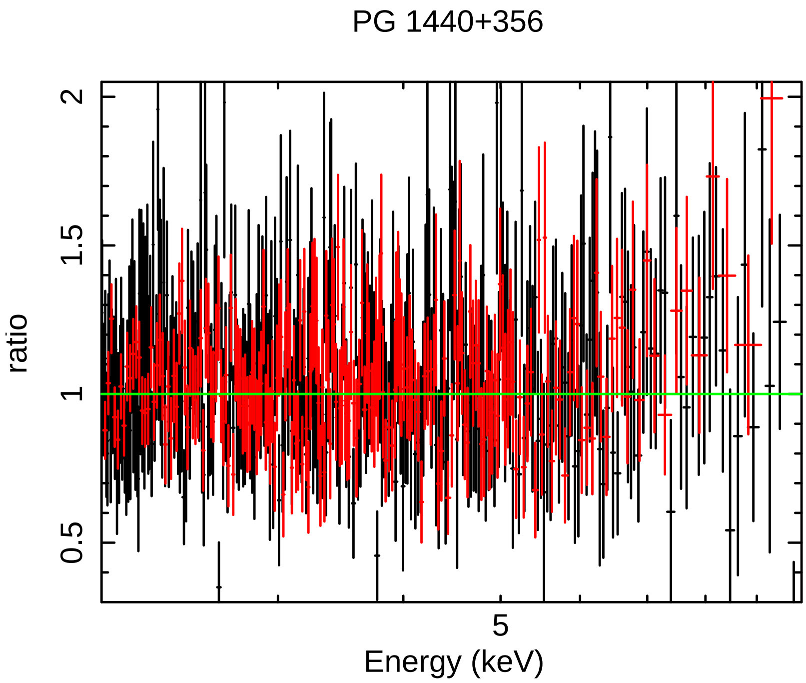

FIGURE 3.46: Ratio plot (data/model) of the additional hard-band ($2-10$ keV; observed) *pexriv* model fit to the 0005010101 observation of PG 1440+356. Top: data points and model fit line. Bottom: ratio of data points to model fit line. Black: PN data. Red: MOS data.

mentioned. The best fit model is shown in Figure 3.48. It should be noted that, as previously mentioned, both versions of the *pcfabs* model give similar results.

0005010301

During modelling of the hard-band ($2-10$ keV; observed) of the 0005010301 observation with a standard Galactic absorbed power-law model, residuals in emission were seen around ~ 6.2 keV. It was found that the inclusion of a narrow $\sigma = 10$ eV (frozen) Gaussian emission line with energy, $E_{\rm obs} = 6.28 \pm 0.05$ keV, reduced these residuals and improved the fit statistics to $\chi^2/\text{d.o.f.} = 290.02/334$ ($\Delta\chi^2/\Delta\text{d.o.f.} = 12.0/2$). However, using the other three models gave better fits (Table 3.8), with the *pcfabs* model being the preferred choice for the hard-band of this observation.

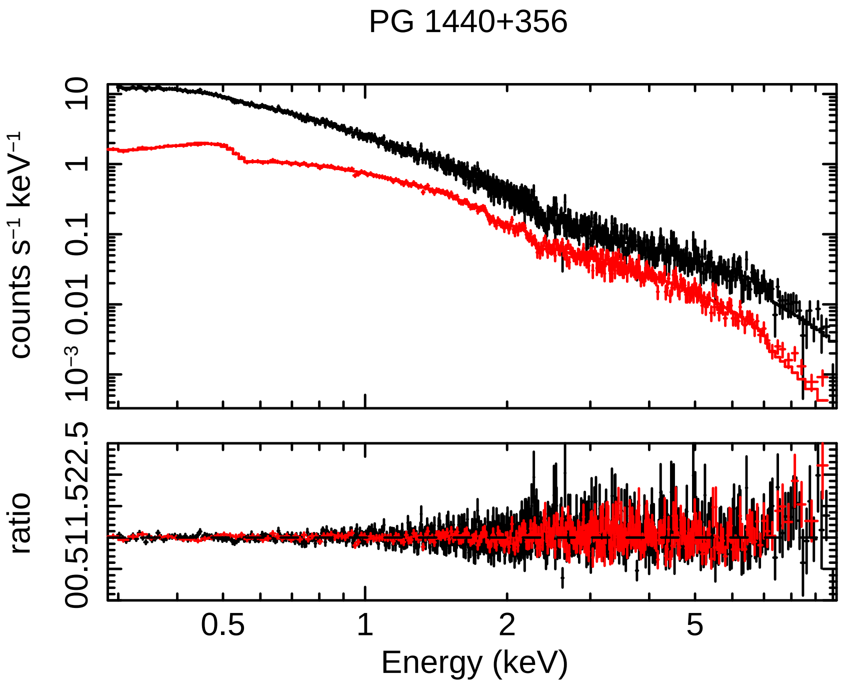

FIGURE 3.47: Best fit model, *tbabs*×(BB+*pexriv*), to the broad-band ($0.3-10$ keV; observed) of the 0005010101 observation of PG 1440+356. Top: data points and model fit line. Bottom: ratio of data points to model fit line. Black: PN data. Red: MOS data.

Once again the broad-band requires only one BB component and all models statistically over-fit the data. Also, all models return similar fit statistics and consistent photon-indices (Table 3.9). As with the 0005010201 observation, the *pexriv* model returns the lowest χ^2 value (χ^2/d.o.f. $= 676.8/782$) and a low ionisation value, $\xi = 0.004^{+3.075}_{-0.004}$ erg cm s^{-1}, also with large errors. Again, this suggests that the medium is neutral. It should be noted that the broken power-law versions of all the models, *pcfabs*, *pexrav* and *pexriv*, result in similar fit statistics as the other BB fits, χ^2/d.o.f. $=$ $678.5/782$, χ^2/d.o.f. $= 681.7/783$ and χ^2/d.o.f. $= 679.6/782$, respectively. The value of the ionisation in the BB version of the *pexriv* model and its errors suggest that it is incorrect. Thus, the best fit model for the 0005010301 observation is chosen to be the BB version of the *pexrav* model, *tbabs*×(BB+*pexrav*), with model parameters $\Gamma =$ 2.74 ± 0.05, $R = 8.60^{+1.69}_{-1.49}$ and kT $= 85^{+6}_{-5}$ eV and fit statistics of χ^2/d.o.f. $= 678.0/783$

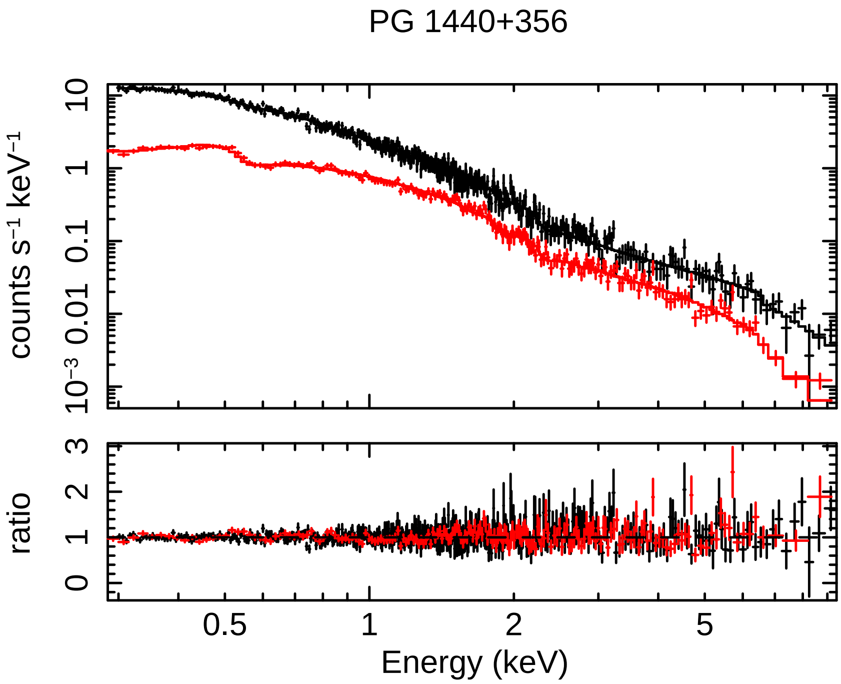

FIGURE 3.48: Best fit model, *tbabs*$\times$(*bexrav*), to the broad-band ($0.3 - 10$ keV; observed) of the 0005010201 observation of PG 1440+356. Top: data points and model fit line. Bottom: ratio of data points to model fit line. Black: PN data. Red: MOS data.

(Figure 3.50).

0107660201

Unlike the other three observations, the earliest observation, 0107660201, requires the inclusion of two BB components in all models to describe the SE present in the EPIC spectra. It appears to be in a high flux state as mentioned in Section 3.4 and the observation suffered from pile-up. Again, unlike the other observations, the models do not over-fit the data and none of the broken power-law versions of the hard-band models fit the data better than the BB versions. All three types of model fitting return similar fit statistics (Table 3.9). The returned photon-indices, $\Gamma \simeq 2.4$, are consistent with one another, so too are the BB temperature values of $\mathrm{kT}_1 \simeq 85$ eV and $\mathrm{kT}_2 \simeq 210$ eV. Once again this makes the conclusion of a best-fit model difficult. The best fit model for

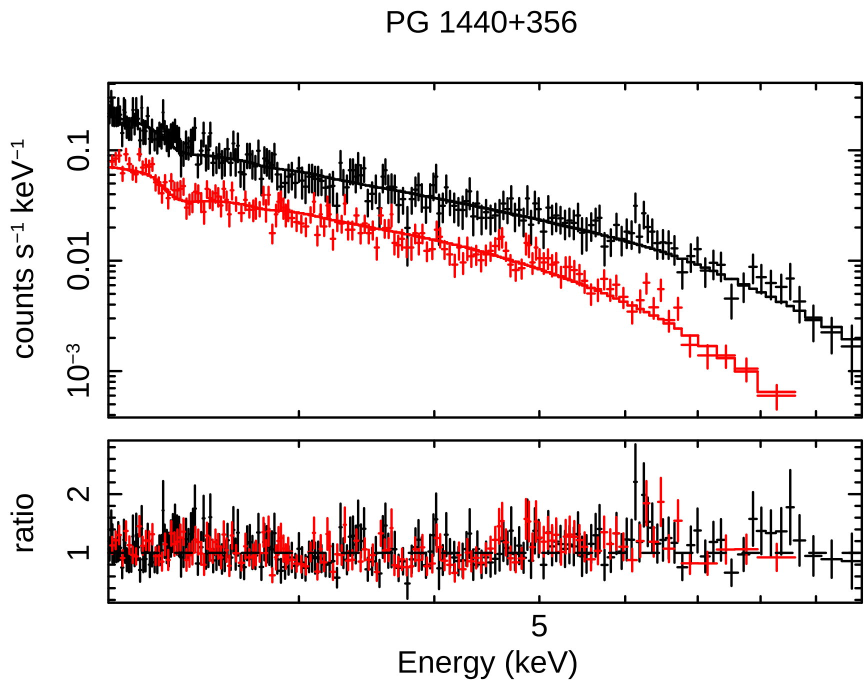

FIGURE 3.49: Initial hard-band (2 – 10 keV; observed) absorbed power-law fit to the 0005010301 observation of PG 1440+356. Note the residuals left at $\sim$ 6.2 keV. Top: data points and model fit line. Bottom: ratio of data points to model fit line. Black: PN data. Red: MOS data.

the 0107660201 observation is chosen to be, *tbabs*$\times$(BB_1+BB_2+*pexrav*), with parameter values of $kT_1 = 85 \pm 3$ eV, $kT_2 = 217^{+34}_{-24}$ eV, $\Gamma = 2.45^{+20}_{-25}$ and $R = 3.71^{+3.00}_{-2.40}$ with fit statistics of $\chi^2/\mathrm{d.o.f.} = 638.7/591$ (Figure 3.51).

Joint Fits

As discussed in Section 3.2.2, Zoghbi et al. (2008) have previously analysed the PN data from the four observations of PG 1440+356. To be thorough in this analysis, similar analysis of the PN data was performed. A relativistically blurred, ionised reflection model was fitted concurrently to the four PN data sets. The model *reflion* (Section 3.4; Ross and Fabian, 2005; Ross et al., 1999) was used to simulate reflection from an ionised medium. The XSPEC model *kdblur* was used to relativistically blur the *reflion* component assum-

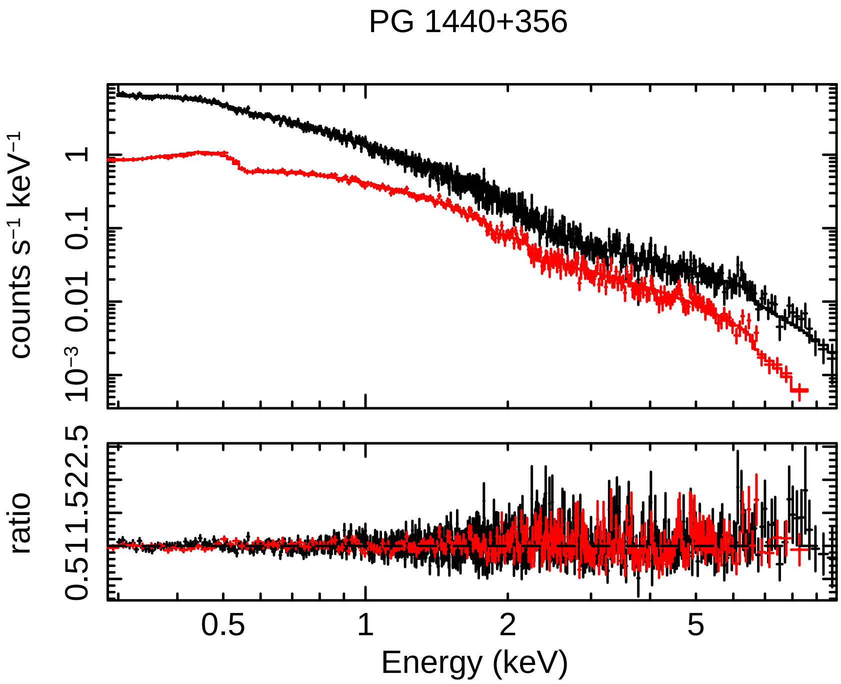

FIGURE 3.50: Best fit model, *tbabs*×(BB+*pexrav*), to the broad-band ($0.3-10$ keV; observed) of the 0005010301 observation of PG 1440+356. Top: data points and model fit line. Bottom: ratio of data points to model fit line. Black: PN data. Red: MOS data.

ing that the reflection occurs close to the SMBH and is undergoing gravitational effects. The final model used to fit the PN data was *tbabs*×(*po*+[*kdblur*×*reflion*]). During fitting, the photon-indices for the power-law and *reflion* components were tied but allowed to vary between each observation. Also, the ionisation, ξ, from the *reflion* component was allowed to vary between all observations. The iron abundance in the *reflion* component was allowed to vary but was tied between all four observations. Within the *kdblur* model, the outer radius, $R_{\rm out}$, was frozen to 400 gravitational radii ($r_{\rm g} = GM_{\rm BH}/c^2$) and the power-law dependence of the emissivity was frozen to a value of 6. Finally, the inner radius of the blurring, $R_{\rm in}$, and the inclination of the reflector, Inc, were allowed to vary but were tied between all observations. The results of this joint fit are shown in Table 3.10. Figure 3.52 shows the data with the model line and the ratio (data/model) plot for this joint fit.

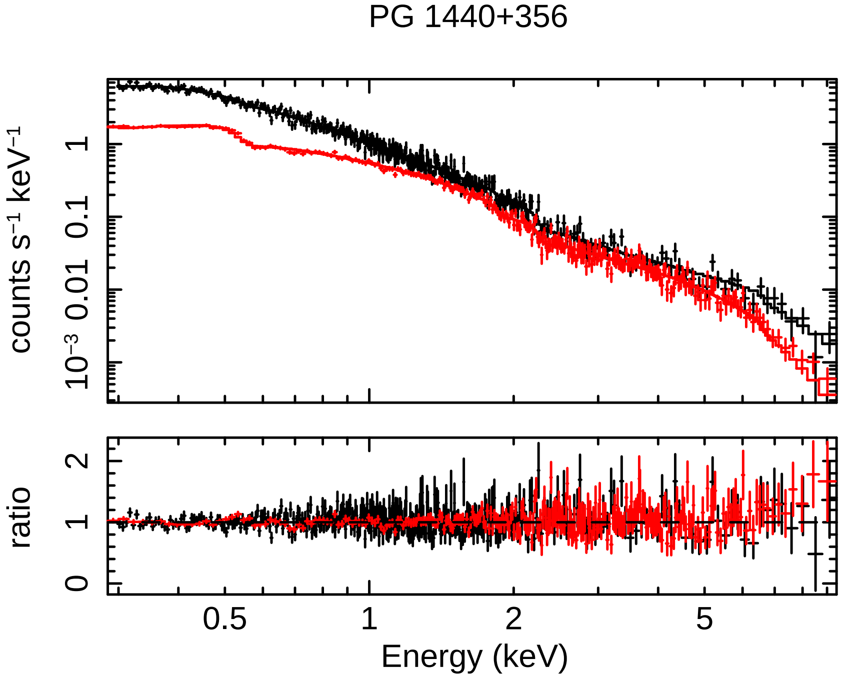

FIGURE 3.51: Best fit model, *tbabs*×(BB$_1$+BB$_2$+*pexrav*), to the broad-band ($0.3-10$ keV; observed) of the 0107660201 observation of PG $1440+356$. Top: data points and model fit line. Bottom: ratio of data points to model fit line. Black: PN data. Red: MOS data.

RGS Data

PG 1440+356 was clearly detected by the RGS detectors in each observation. The count rates, determined by XSPEC, were between 0.2 and 0.3 counts s^{-1}. The RGS data for PG $1440+356$ was modelled between 8 and 37Å. A binning of 10 channels per bin was chosen. This binning results in a bin width of ~ 90 mÅ. This is moderate binning and is approximately 1.5 times the resolution of the RGS detectors (~ 60 mÅ), which means that the data will be slightly under-sampled. Each observation was modelled in one of two ways: the first by a power-law, *tbabs*×(*po*), with $\Gamma \approx 3$ and the second with two BB components, *tbabs*×(BB$_1$+BB$_2$), with temperatures of ≈ 80 eV and ≈ 230 eV, respectively. These fits did not leave any significant residuals and the data appeared featureless; no broad or narrow features were evident, which is similar to the results

Table 3.10: Joint *reflion* Model Fit to the PN Data of PG 1440+356

	Observation ID			
	0005010101	0005010201	0005010301	0107660201
$\Gamma_{\rm ref}$	$2.31^{+0.03}_{-0.03}$	$2.38^{+0.04}_{-0.03}$	$2.20^{+0.03}_{-0.01}$	$2.37^{+0.09}_{-0.02}$
$\xi_{\rm ref}$	1833^{+234}_{-194}	2753^{+500}_{-475}	1182^{+132}_{-112}	2699^{+579}_{-558}
Fe^a	$0.41^{+0.04}_{-0.03}$			
Inc^a	$35.0^{+1.54}_{-1.39}$			
$R^a_{\rm in}$	$1.62^{+0.12}_{-0.09}$			
$R^b_{\rm out}$	400			
$\Gamma^b_{\rm emm}$	6			
χ^2/d.o.f.	$2036.5/1888$			

Parameter values returned for the ionised reflection model fitted concurrently to the PN data sets from the four observations of PG $1440+356$. The model used was *tbabs*×*kdblur*×(*reflion*+*po*). The parameters [units] were the *reflion* incident power-law photon-index, $\Gamma_{\rm ref}$, the *reflion* ionisation, $\xi_{\rm ref}$ [erg cm s^{-1}], iron abundance, Fe [×Solar], inclination, Inc [degrees], *kdblur* inner radius, $R_{\rm in}$ [$r_{\rm g}$], *kdblur* outer radius, $R_{\rm out}$ [$r_{\rm g}$], and the power-law dependence of the emissivity, $\Gamma_{\rm emm}$. The *po* photon-index was tied to the $\Gamma_{\rm ref}$ parameter for each observation. a indicates the parameter was allowed to vary but was tied between the four observations. b indicates the parameter was frozen to this value for all observations. χ^2/d.o.f. reports the final fit statistics for this model fit.

of the *Chandra* LETG observation reported by Marshall et al. (2003). Figures 3.53, 3.54, 3.55 and 3.56 show the ratio plots (data/model) for the two model fits to the RGS data of the 0005010101, 0005010201, 0005010301 and 0107660201 observations of PG 1440+356, respectively. As the data were binned by channel rather than by number of counts per bin, Chi-squared statistics are not valid and thus C-statistics (S) were used whilst fitting the RGS data for PG 1440+356 in XSPEC. The specific count rates, model parameter values, fit statistics and model flux values are reported in Table 3.11.

Overview

Although the best-fit models to each observation of the EPIC data of PG 1440+356 are not all the same, similar results are determined for all model fits (Table 3.9). This indi-

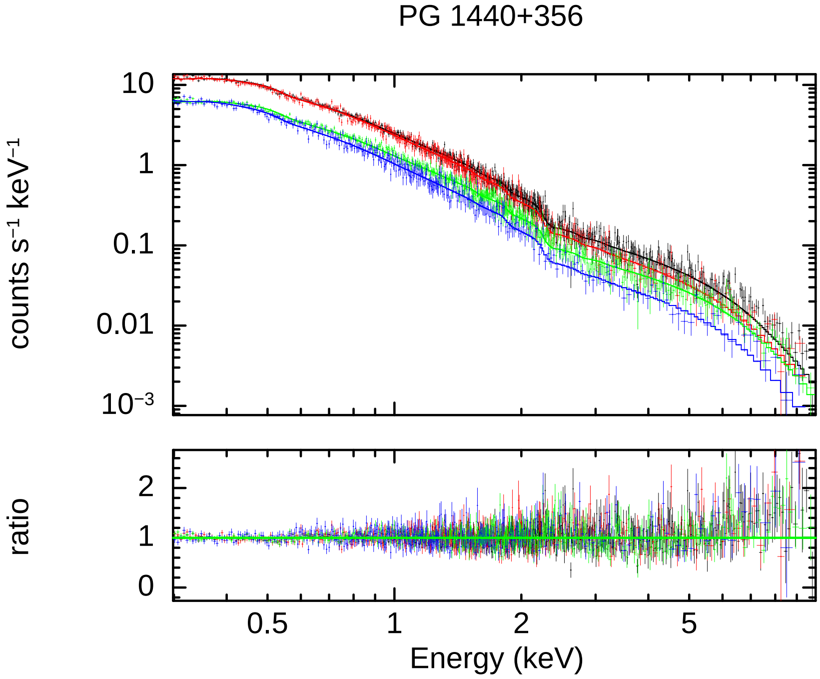

FIGURE 3.52: Joint model fit, *tbabs*×(*po*+[*kdblur*×*reflion*]), to the broad-band ($0.3-10$ keV; observed) of the PN observations of PG $1440+356$. Top: data points and model fit line. Bottom: ratio of data points to model fit line. Black: 0005010101. Red: 0005010201. Green: 0005010301. Blue: 0107660201.

cates that the true nature of the SE and the excess emission above ~ 5 keV seen in the X-ray spectra of PG 1440+356 is unclear. At a basic level the model fits to the EPIC data fall into two categories, partial covering absorption and reflection from a neutral/ionised medium. It is difficult to distinguish between the various scenarios with the resolution and collecting areas of the current X-ray detectors available. The question of whether it is absorption or reflection is a question that has been asked about other sources, e.g., 1H $0419-577$ (Pounds et al., 2004a; Pounds et al., 2004b; Fabian et al., 2005) and 1H 0707−495 (Tanaka et al., 2004; Fabian et al., 2004; Fabian et al., 2009). However, in the cases of 1H 0419−577 and 1H 0707−495, a sudden drop in flux above 7 keV is seen in their *XMM-Newton* EPIC spectra. To model this feature with either a partial covering absorber or reflection from an ionised medium, generally a greater than solar iron abun-

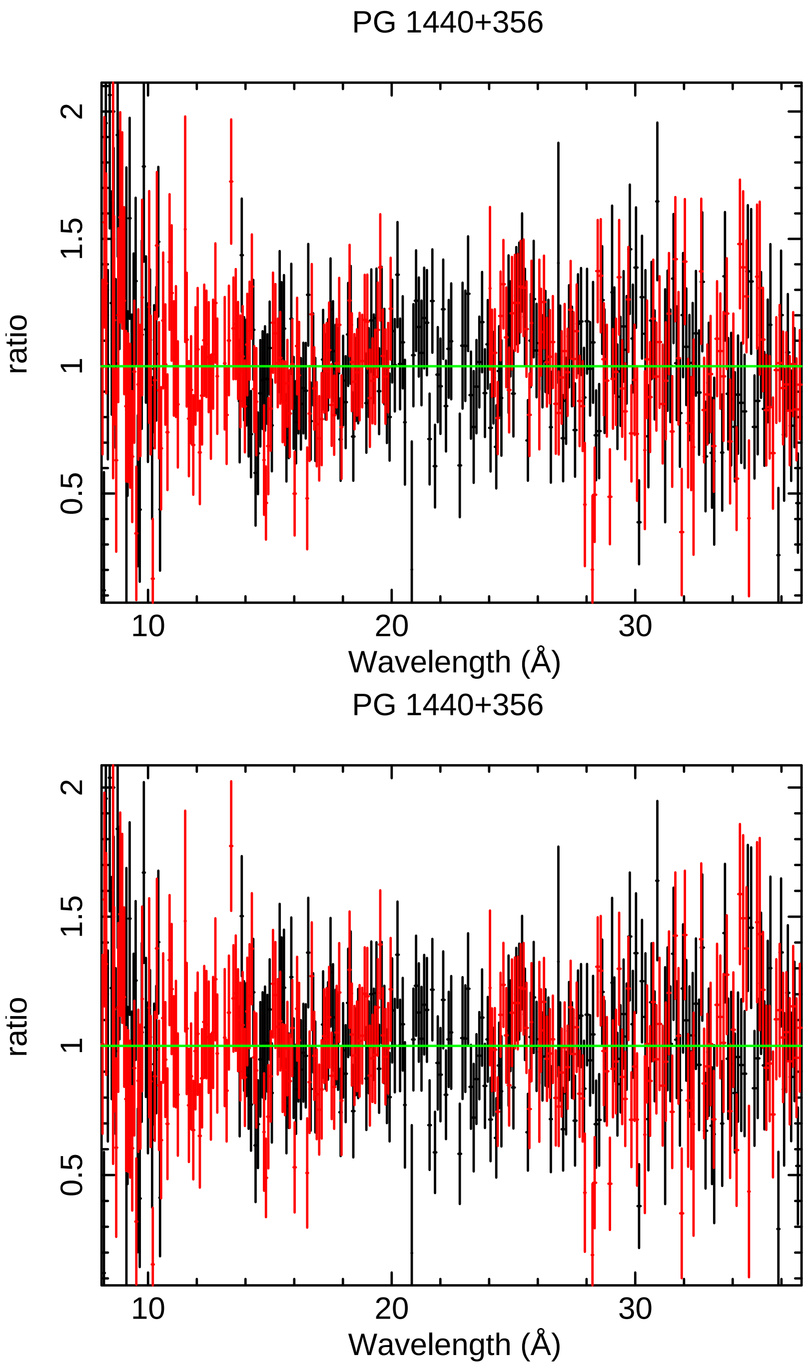

FIGURE 3.53: Ratio plots (data/model) of the two model fits to the RGS data ($8-37$ Å; observed) from the 0005010101 observation of PG 1440+356. Top: Model - *tbabs*$\times$(*po*). Bottom: Model - *tbabs*$\times$(BB_1+BB_2). Black: RGS1 data. Red: RGS2 data.

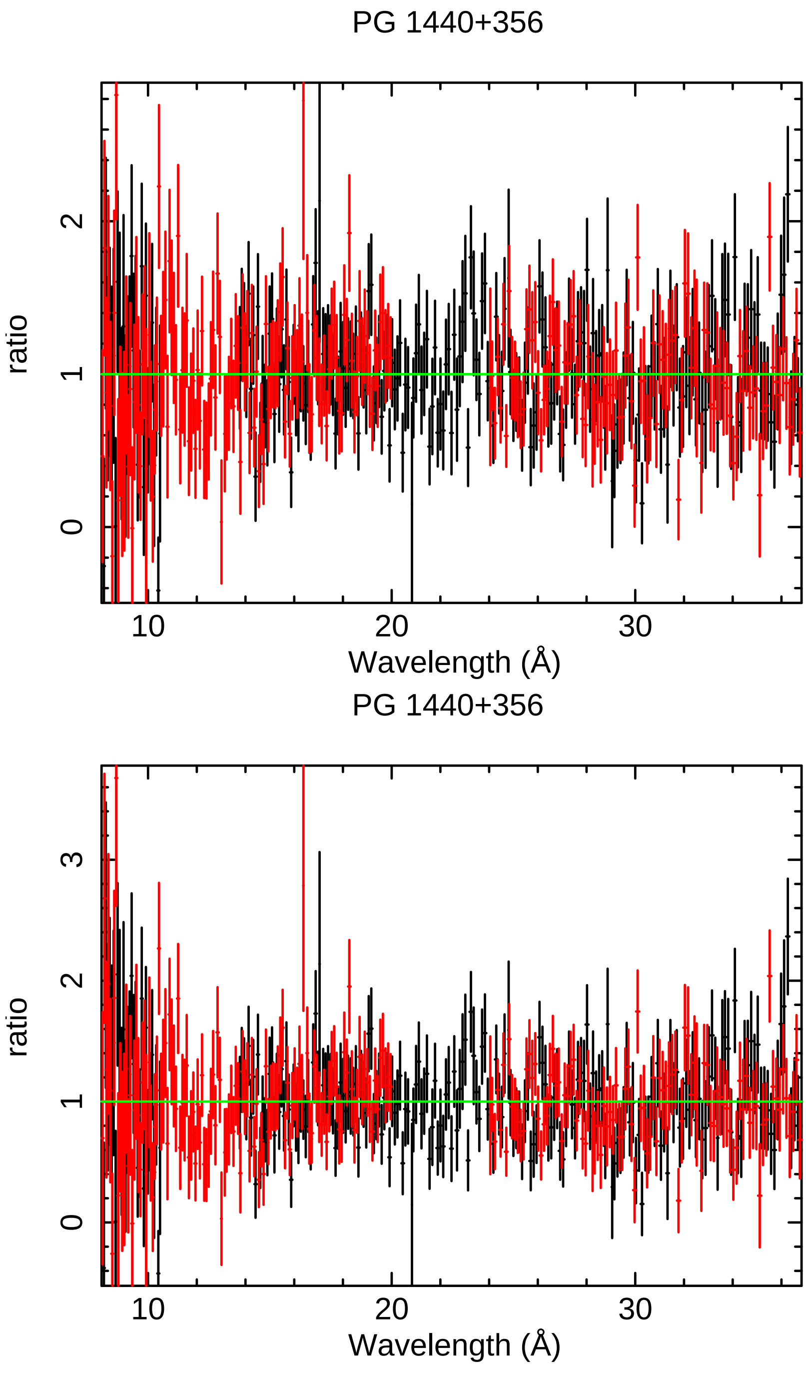

FIGURE 3.54: Ratio plots (data/model) of the two model fits to the RGS data (8 – 37 Å; observed) from the 0005010201 observation of PG 1440+356. Top: Model - *tbabs*×(*po*). Bottom: Model - *tbabs*×(BB_1+BB_2). Black: RGS1 data. Red: RGS2 data.

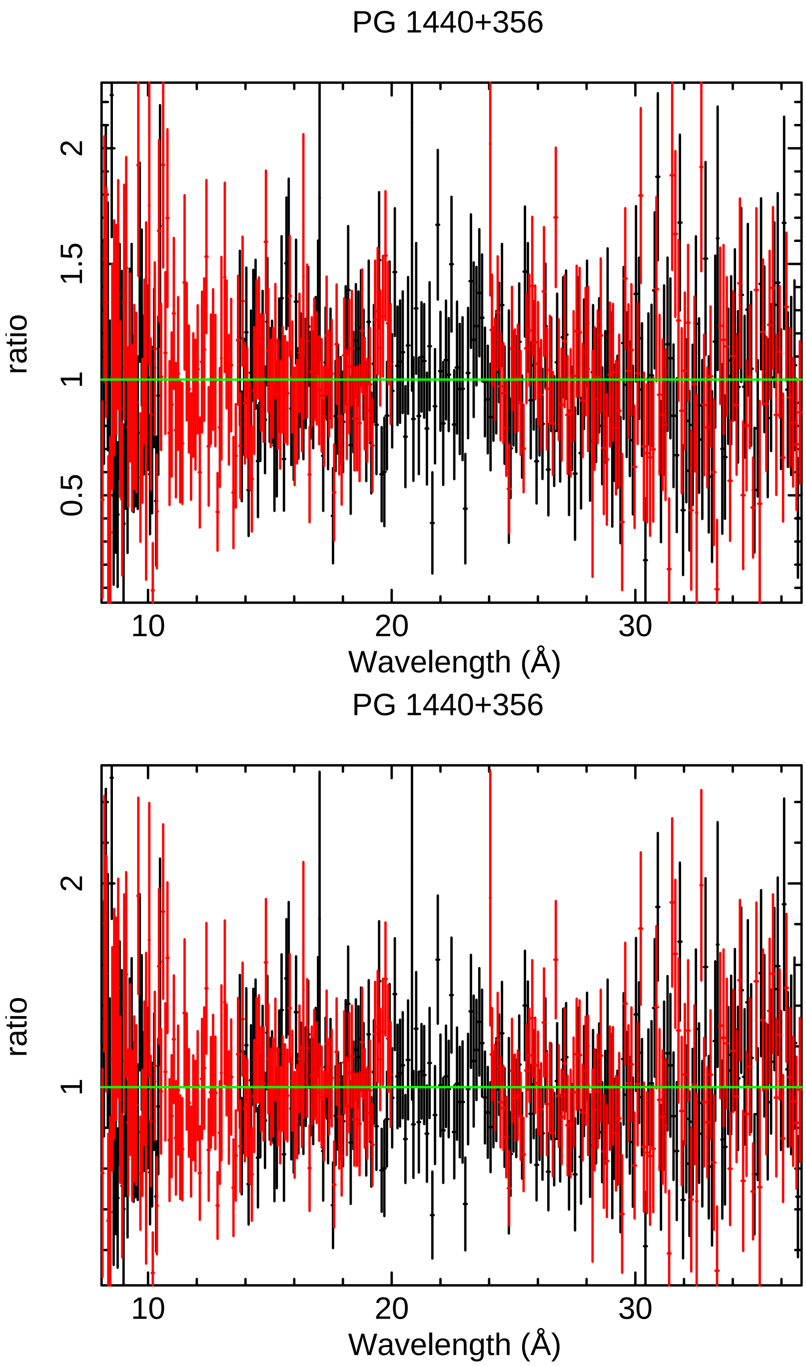

FIGURE 3.55: Ratio plots (data/model) of the two model fits to the RGS data (8 – 37 Å; observed) from the 0005010301 observation of PG 1440+356. Top: Model - *tbabs*×(*po*). Bottom: Model - *tbabs*×(BB$_1$+BB$_2$). Black: RGS1 data. Red: RGS2 data.

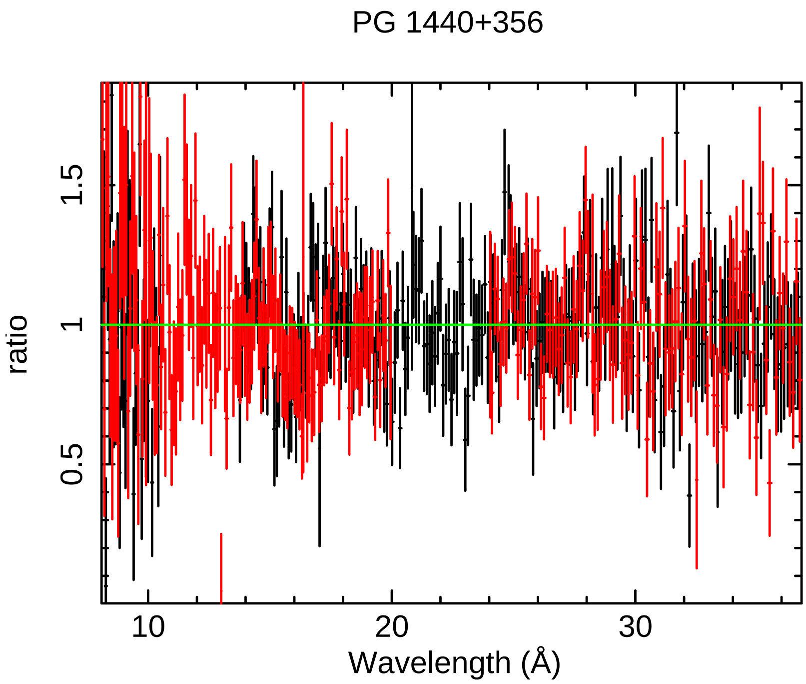

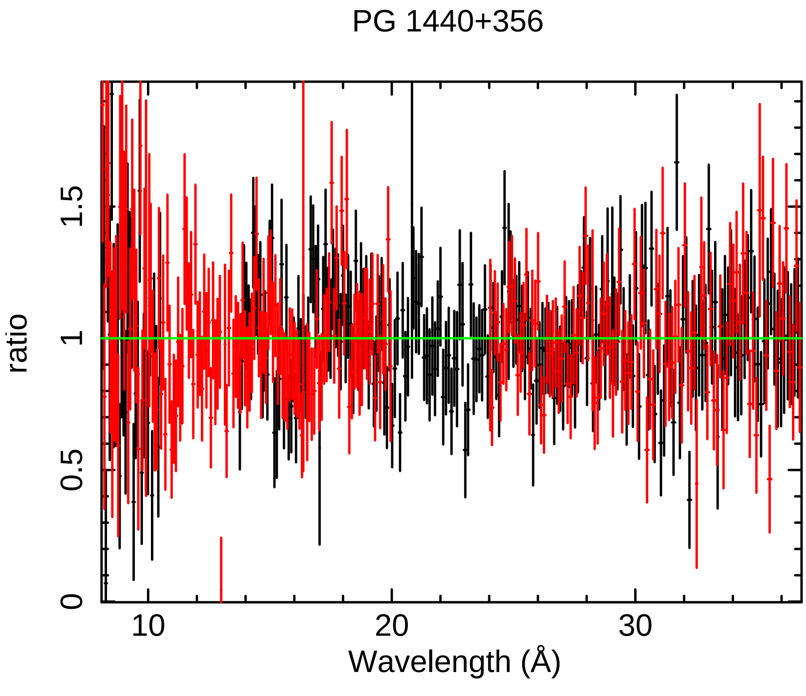

FIGURE 3.56: Ratio plots (data/model) of the two model fits to the RGS data (8 – 37 Å; observed) from the 0107660201 observation of PG 1440+356. Top: Model - *tbabs*×(*po*). Bottom: Model - *tbabs*×(BB_1+BB_2). Black: RGS1 data. Red: RGS2 data.

Table 3.11: Model Fit Results to the RGS Data of PG 1440+356

	Observation ID			
	0005010101	0005010201	0005010301	0107660201
Count Rate (counts s^{-1})	0.247 ± 0.004	0.260 ± 0.006	0.146 ± 0.003	0.295 ± 0.004
Model 1				
Γ	2.99 ± 0.05	3.08 ± 0.07	2.90 ± 0.06	3.08 ± 0.04
S/d.o.f.	$474.4/416$	$491.5/452$	$446.5/452$	$449.4/452$
$F_{\rm RGS1}$	7.95 ± 0.20	7.19 ± 0.26	4.19 ± 0.14	8.66 ± 0.19
$F_{\rm RGS2}$	7.75 ± 0.19	7.05 ± 0.25	4.16 ± 0.13	8.53 ± 0.19
Model 2				
kT$_1$ (eV)	89 ± 4	74^{+8}_{-7}	84^{+7}_{-6}	78 ± 4
kT$_1$ (eV)	260^{+25}_{-19}	204^{+22}_{-15}	237^{+25}_{-18}	232^{+14}_{-12}
S/d.o.f.	$463.0/414$	$499.8/450$	$453.4/450$	$451.8/450$
$F_{\rm RGS1}$	7.99 ± 0.21	$7.16^{+0.28}_{-0.27}$	4.17 ± 0.14	8.75 ± 0.20
$F_{\rm RGS2}$	$7.69^{+0.69}_{-0.48}$	7.00 ± 0.26	4.19 ± 0.13	8.56 ± 0.20

Count rates, parameter values and fluxes for the model fits to the RGS data ($8-37$ Å; observed). The count rates were determined by XSPEC. Model 1 - *tbabs*$\times$(*po*). Model 2 - *tbabs*$\times$(BB$_1$+BB$_2$). $F_{\rm RGS1}$ and $F_{\rm RGS2}$ indicate the observed, $0.35-1.5\,{\rm keV}$, unabsorbed flux values for each model measured in the RGS1 and RGS2 cameras, respectively. $F_{\rm RGS1}$ and $F_{\rm RGS2}$ are measured in 10^{-12} erg cm^{-2} s^{-1}.

dance is required, $\sim 3.8\times$solar for 1H 0419$-$577 (reflection model; Fabian et al., 2005) and $\sim 3-30\times$solar (partial covering model; Tanaka et al., 2004) and $\sim 30\times$solar (reflection model; Fabian et al., 2009) for 1H 0707$-$495. The iron abundance calculated during the joint PN *reflion* modelling is less than solar ($0.41^{+0.03}_{-0.04}\times$solar). Also, the sudden drop in flux above 7 keV is not seen in the EPIC spectra of PG 1440$+$356. One thing that may distinguish between the two scenarios would be the presence of Fe L shell emission in a source's X-ray spectra. If the iron abundance is high and assuming a reflection dominated scenario, as suggested for 1H 0707$-$495 by Fabian et al. (2009), Fe L emission should be present,. There is no obvious Fe sc l emission in the EPIC spectra of PG 1440+356. In addition, there are no obvious features, narrow or broad, seen in the

RGS data of PG 1440+356.

As described in Section 3.2.2, Zoghbi et al. (2008) prefer the reflection dominated model as the spectral shape of PG 1440+356 and absorbing column (for the partial covering model) do not vary between observations. As the only thing that does vary is the flux, the authors argue that if the intrinsic source varies then it is implausible for the covering fraction to remain the same in all observations. The partial covering absorber model results (*pcfabs*; Table 3.9) from this work return similar covering fractions for each observation, $cf \sim 0.55$. Although the absorbing column, N_{h}, appears to vary by a factor of $\sim 2-3$ between the first and last observation, this variation is not extreme and is consistent, within errors, with the absorbing component remaining constant between each of the observations of PG 1440+356. For the high flux state observation, 0107660201, the photon-index in the *pcfabs* model is harder than the other observations, a likely consequence of the additional BB component. However, the harder photon-index could suggest a slight change in spectral shape. The inclusion of a second BB component for this observation is in disagreement with Zoghbi et al. (2008) and could be a result of the slightly different extraction regions used as this observation suffered from pile-up. Zoghbi et al. (2008) use a circular extraction region for both source and background spectra with radii of 35 arc seconds with 'the central region excluded' from the source region. However, the radii used in this analysis were 50 arc seconds for both source and background regions with the central 10 and 5 arc seconds excluded from the source regions of the PN and MOS data, respectively. However, the joint PN *reflion* model fit results from this analysis (Table 3.10) are consistent with the results calculated by Zoghbi et al. (2008) (Table 3.3). So, it is difficult to state whether there is a true discrepancy between the results presented here and by Zoghbi et al. (2008) for that particular observation.

In conclusion, the EPIC data for the four PG 1440+356 observations can be modelled in a number of ways, with partial covering and reflection models fitting the data well. The low ionisation in some of the individual ionised reflection models (*pexriv*) does not rule out the presence of an ionised medium. The joint PN ionised reflection model fit does model the data well, but the lack of any obvious indicators such as low flux above 7 keV and Fe L emission, still leaves the option of a partial covering absorber. The causality arguments used by Zoghbi et al. (2008) to discredit the presence of a partial covering absorber could be refuted if it is assumed that the absorbing material is varying on short time scales. For example, if the the absorbing material is clumpy and the parameters of all the clumps are identical or at least similar then when the clumpy material passes back into the line of sight, the absorbing material parameters will be the same. Unfortunately, current X-ray observatories are limited by their resolution and collecting areas, meaning the areas where the absorption or reflection takes place cannot be resolved. Hopefully, future missions will help in this matter and the debate of absorption versus reflection can be answered.

3.4.6 MS 2254.9 − 3712

EPIC Data

The initial hard-band ($2-10$ keV; observed) power-law fit returned a photon-index, $\Gamma = 1.82 \pm 0.04$, and required the inclusion of a broad, $\sigma_{\rm obs} = 118^{+83}_{-57}$ eV, Gaussian emission line with an observed energy, $E_{\rm obs} = 6.19 \pm 0.06$ keV. This is consistent with iron emission at the redshift of MS 2254.9 − 3712 ($z = 0.039$).

Figure 3.57 shows the initial hard-band model fit to the MS 2254.9 − 3712 data. The ratio plot (data/model) in Figure 3.57 shows residuals both in emission and absorption around ~ 8.6 keV in the PN data. These features were unable to be modelled with any significance. Further investigation suggests that the residuals are instead a consequence of the background correction of the source spectra; the feature coincides with the fluorescence lines of Ni K, Cu K and Zn K, which are found in the PN detector background spectra. Figure 3.58 shows the PN source (red; not background corrected) and background (black; grouped by 5 channels per bin) spectra for MS 2254.9$-$3712. It is possible, due to the location of the background region and its size, that not enough background counts were sampled, resulting in incorrect background subtraction. MS 2254.9 $-$ 3712 was observed in 'small window' mode and a background region of radius 36 arc seconds was selected on the same chip as the source region, which also had a radius of 36 arc seconds. This meant that there was little separation between the two extraction regions, which could have led to some source counts being included in the background spectra. It should be noted that due to the number of counts below 8 keV, the selection of this particular background region will only affect energies above 8 keV. Therefore, the residuals seen around ~ 8.6 keV are likely not to be real.

Extending the initial hard-band fit down to 0.3 keV, MS 2254.9$-$3712 shows a large excess above the model fit at lower energies, rising to over 10 times that of the model fit (Figure 3.5). As with the previous targets, modelling of the SE began with the inclusion of a BB component to the model. The addition of a BB component did not fit the data well (χ^2/d.o.f. $= 2223.3/1085$), leaving large residuals at low energies. The inclusion of a second BB component reduced the fit statistics to χ^2/d.o.f. $= 1265.7/1083$. However, there were still large residuals at low energies. The use of a third BB component produces the first reasonable fit. The resulting fit statistics were χ^2/d.o.f. $= 1132.4/1081$. Although this latest model gives a reasonable fit it still leaves emission residuals around ~ 0.55 keV (Figure 3.59). Due to the width of these residuals, a Gaussian emission line was included in the model to fit this feature, rather than a BB component. The Gaussian component had an energy of $E_{\rm em} = 0.56^{+0.01}_{-0.03}$ keV and width of

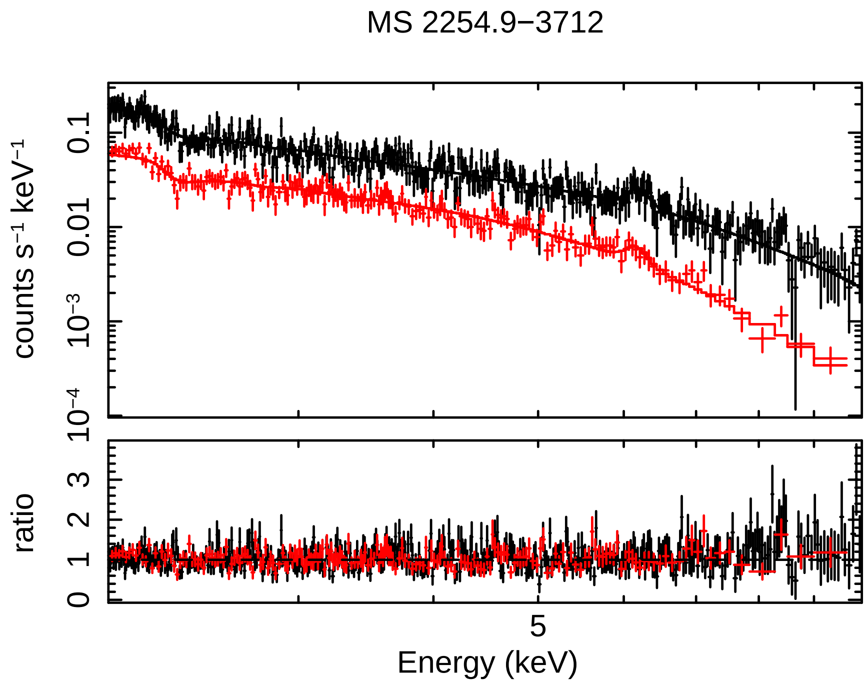

FIGURE 3.57: Initial hard-band (2 – 10 keV; observed) absorbed power-law fit to MS 2254.9 – 3712. Top: data points and model fit line. Bottom: ratio of data points to model fit line. Black: PN data. Red: MOS data.

$\sigma_{\rm em} = 56^{+11}_{-12}$ eV. Its inclusion was significant, with $\Delta\chi^2/\Delta$d.o.f. $= 119.4/3$. This Gaussian emission could represent blended emission lines from the O VII triplet at the redshift of MS 2254.9−3712 ($z = 0.039$). If blended emission lines are present, then their widths will have been increased due to the response of the EPIC detectors. The final best fit model for MS 2254.9 – 3712 was, therefore, *tbabs*×(*ga*$_{\rm em}$+BB$_1$+BB$_2$+BB$_3$+*po*+*ga*$_{\rm obs}$). The ratio plot (data/model) of the best fit model is shown in Figure 3.59. The final fit statistics were χ^2/d.o.f. $= 1013.9/1079$, with the following parameter values, $\Gamma = 1.72^{+0.03}_{-0.02}$, kT$_1$ $= 250^{+11}_{-15}$ eV, kT$_2$ $= 117^{+26}_{-6}$ eV, kT$_3$ $= 34^{+2}_{-1}$ eV, $E_{\rm em} = 0.56^{+0.01}_{-0.03}$ keV, $\sigma_{\rm em} = 56^{+11}_{-12}$ eV, $E_{\rm obs} = 6.19 \pm 0.06$ keV and $\sigma_{\rm obs} = 118^{+83}_{-57}$ eV.

The observed broad-band (0.3 – 10 keV), unabsorbed flux values for MS 2254.9 – 3712 were $1.17^{+0.01}_{-0.02} \times 10^{-11}$ erg cm^{-2} s^{-1} and $1.16^{+0.02}_{-0.03} \times 10^{-11}$ erg cm^{-2} s^{-1}, for the PN and MOS detectors, respectively.

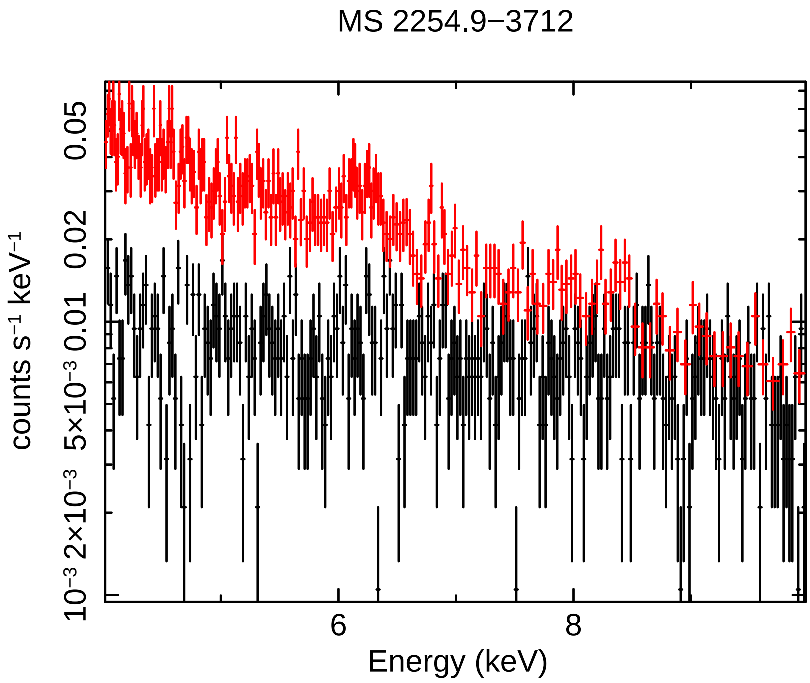

FIGURE 3.58: MS 2254.9 − 3712 EPIC PN source (red; not background corrected) and background (black; grouped by 5 channels per bin) spectra, shown between $4 - 10$ keV (observed). The feature seen at ~ 8.6 keV in Figure 3.57 is not seen in the uncorrected PN source spectrum and occurs when the background spectrum has more counts than the source spectrum.

RGS Data

MS 2254.9 − 3712 was detected by the RGS detectors. However, like the other targets, the detected count rates were low; 0.07 ± 0.002 counts s^{-1} and 0.08 ± 0.002 counts s^{-1}, for RGS1 and RGS2, respectively. Figure 3.60 shows both the RGS1 and RGS2 data grouped with 10 (black), 15 (red) and 20 (green) channels per bin. Once again, the binning is heavy, and a value of 20 channels per bin was chosen. This binning corresponds to a width of ~ 0.2Å per bin, approximately 3 times the resolution of the RGS detectors ($\sim$ 60 mÅ). Therefore, the data will be under-sampled with respect to the RGS resolution, so any particularly narrow features will be binned out of the data. However, it is unlikely, due to the signal-to-noise of the data, that such features would be evident.

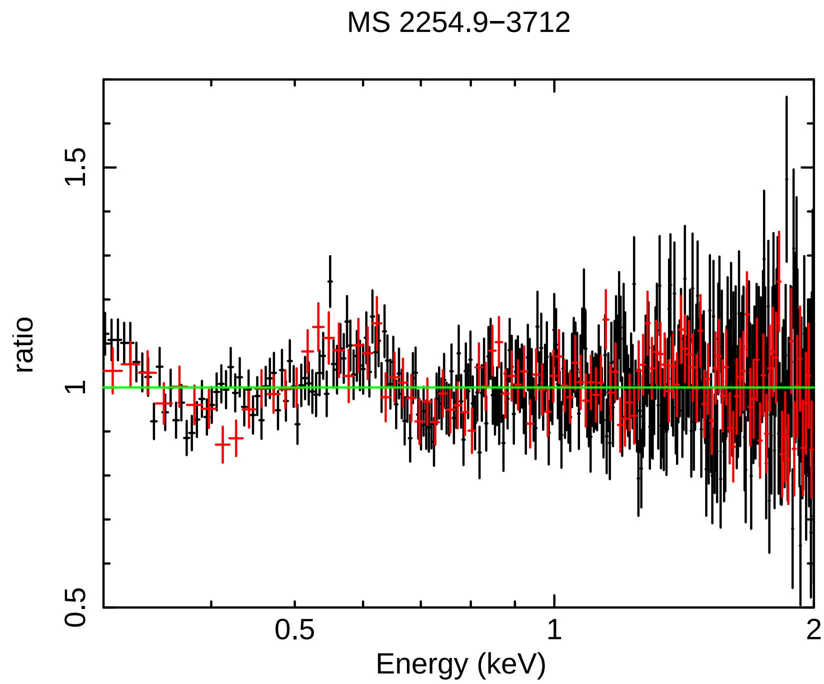

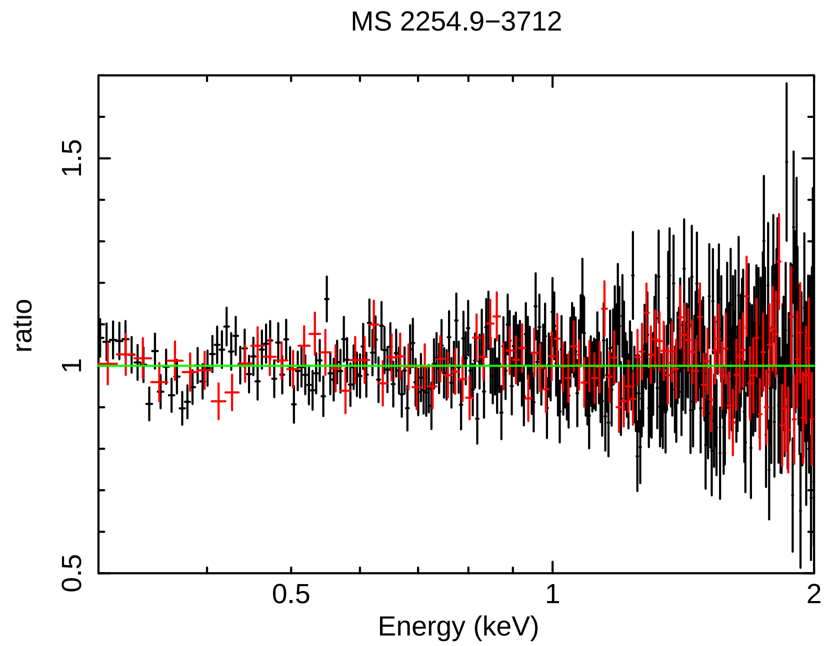

FIGURE 3.59: Ratio plots (data/model) of the final two broad-band ($0.3-10$ keV; observed) model fits to MS 2254.9$-$3712. Top: *tbabs*$\times$(BB$_1$+BB$_2$+BB$_3$+*po*+*ga*$_{\rm obs}$). Bottom: *tbabs*$\times$(*ga*$_{\rm em}$+BB$_1$+BB$_2$+BB$_3$+*po*+*ga*$_{\rm obs}$). Only $0.3-2$ keV are shown for clarity. Black: PN data. Red: MOS data.

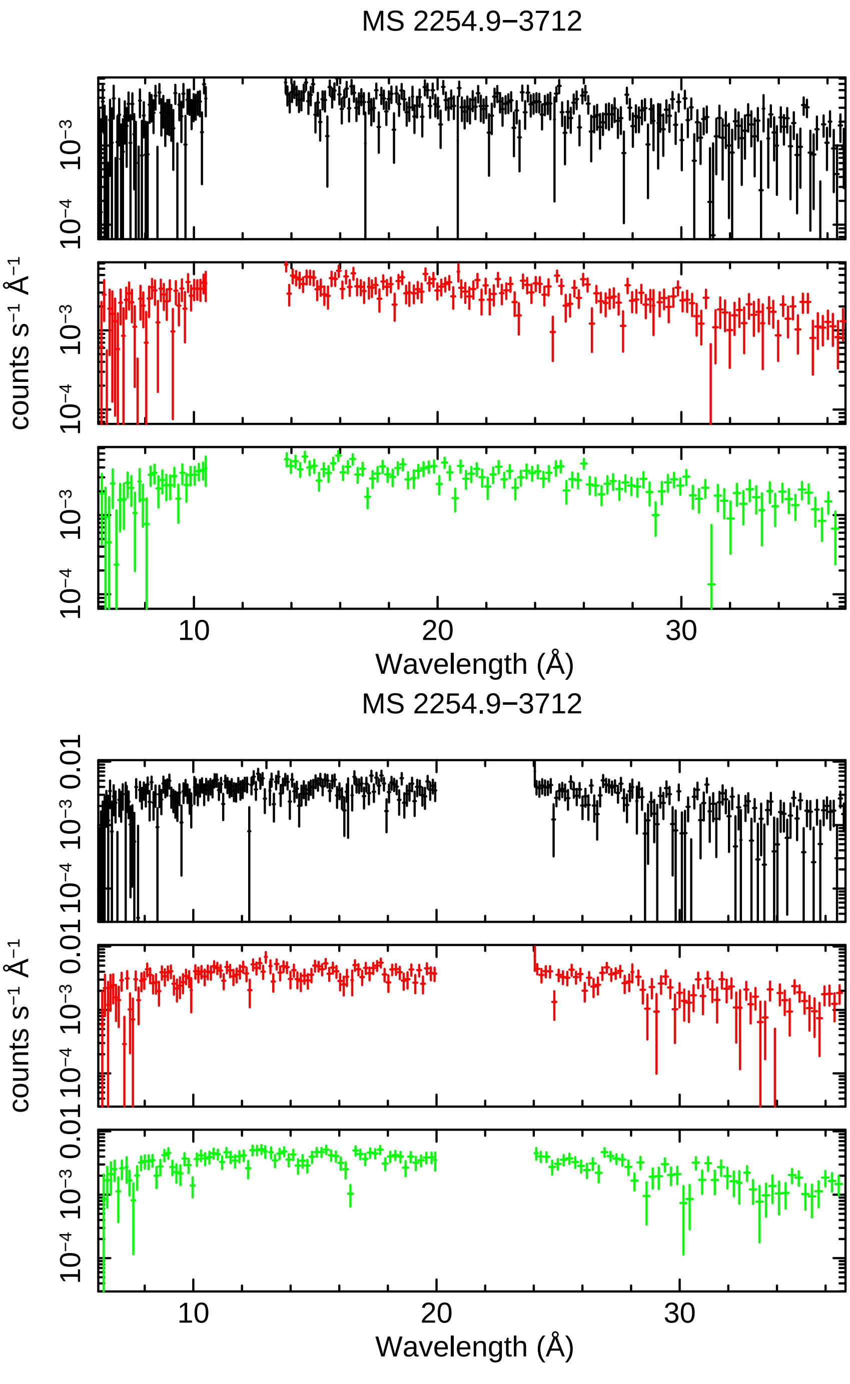

FIGURE 3.60: Binned (6 – 37 Å; observed) RGS1 (top) and RGS2 (bottom) data for MS 2254.9 − 3712. Black, red and green points show the data sets binned into groups of 10, 15 and 20 channels, respectively.

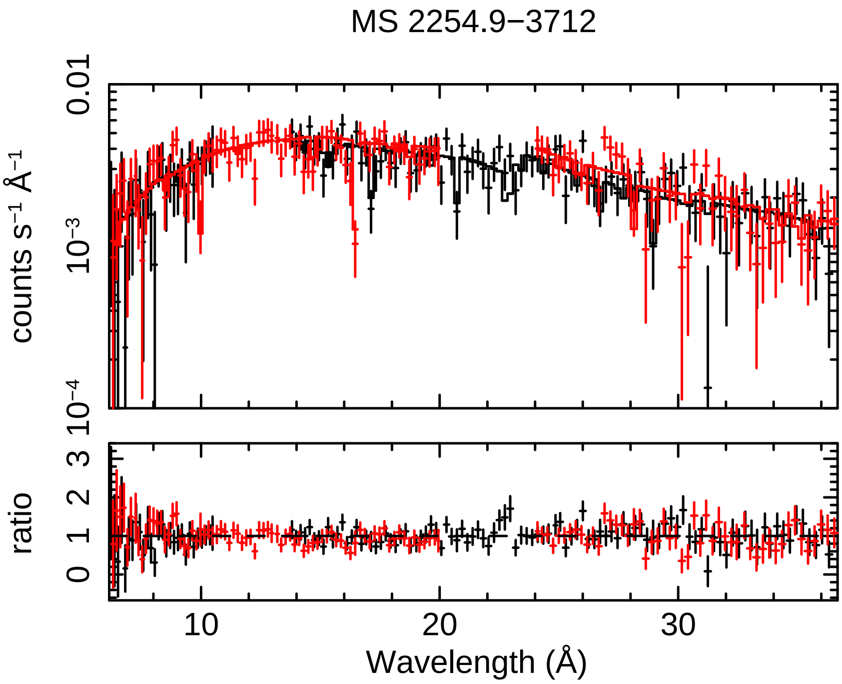

FIGURE 3.61: MS 2254.9 − 3712 EPIC best fit model folded through the RGS response plotted over the RGS data (6 − 37 Å; observed). Top: data points and model fit line. Bottom: ratio of data points to model fit line. Black: RGS1 data. Red: RGS2 data.

The RGS data sets were fitted between 6 Å and 37 Å. As the data were binned by channel rather than number of counts per bin, Chi-squared statistics are not valid and thus C-statistics (S) were used whilst fitting the RGS data for MS 2254.9 − 3712 in XSPEC.

An initial inspection of the RGS data for MS 2254.9–3712 was made by over-plotting the EPIC best fit model. This was to search the RGS data for any predicted features from the EPIC model. Figure 3.61 shows the EPIC best fit model folded through the RGS response plotted over the RGS data. It is clear that all predicted features from the EPIC best model fit are present in the RGS data.

To begin modelling, the best fit model for the EPIC data across the RGS bandpass, *tbabs*×(*ga*$_{\rm em}$+BB$_1$+BB$_2$+BB$_3$+*po*), was used to fit the RGS data. This gave a reasonable fit with $S/\mathrm{d.o.f.} = 212.5/231$, although errors could not be constrained for all model parameters and the resulting power-law photon-index was negative. This model was rejected and modelling began again. Only BB components were used to model the continuum. As for the EPIC data, three BB components were required to model the RGS data continuum. The fit statistics for this model, *tbabs*×(BB_1+BB_2+BB_3), were S/d.o.f. $= 221.1/245$ and the parameter values were $kT_1 = 343^{+60}_{-48}$ eV, $kT_2 = 109^{+10}_{-9}$ eV and $kT_3 = 39 \pm 8$ eV. This model left prominent emission residuals around $\sim$ 22Å (Figure 3.62). This coincides with the O VII triplet emission at the redshift of MS 2254.9−3712 ($z = 0.039$). The residuals seen in Figure 3.62 could not be modelled with a 99% significance ($\Delta S/\Delta$d.o.f. $= 10.5/3$) using a Gaussian emission line ($E_{\rm em} = 0.55 \pm 0.01$ keV, $\sigma_{em} = 5^{+3}_{-2}$ eV). The energy of this line is consistent with the energy of the emission line used in modelling the EPIC data. However, its width is much narrower, which is most likely a result of the broader response of the EPIC cameras. Instead, an XSTAR additive model representing the emergent emission spectrum from an ionised medium was used. The inclusion of this XSTAR component with an absorbing column of $N_{\rm h} \simeq 2.3 \times 10^{19}$ cm^{-2} and an ionisation of $\log(\xi) \simeq 0.9$ does remove the residuals seen in Figure 3.62. Its inclusion also appears significant at the 99% level, with $\Delta S/\Delta$d.o.f. $= 14.3/3$. However, the errors for the absorbing column and ionisation parameters were unable to be constrained and a confidence region contour plot (Figure 3.63) does not show correlation to any particular region or value.

Clearly, there is something more complex than continuum emission present within the RGS data for MS 2254.9−3712. There appears to be emission corresponding to the O VII triplet and there is tentative evidence that the continuum emission is being modified by absorption. A longer observation of MS 2254.9−3712 with *XMM-Newton* would be instructive. Due to the lack of constraint on the XSTAR component, the best fit model for the RGS data of MS 2254.9−3712 is *tbabs*×(BB_1+BB_2+BB_3) with the parameter values

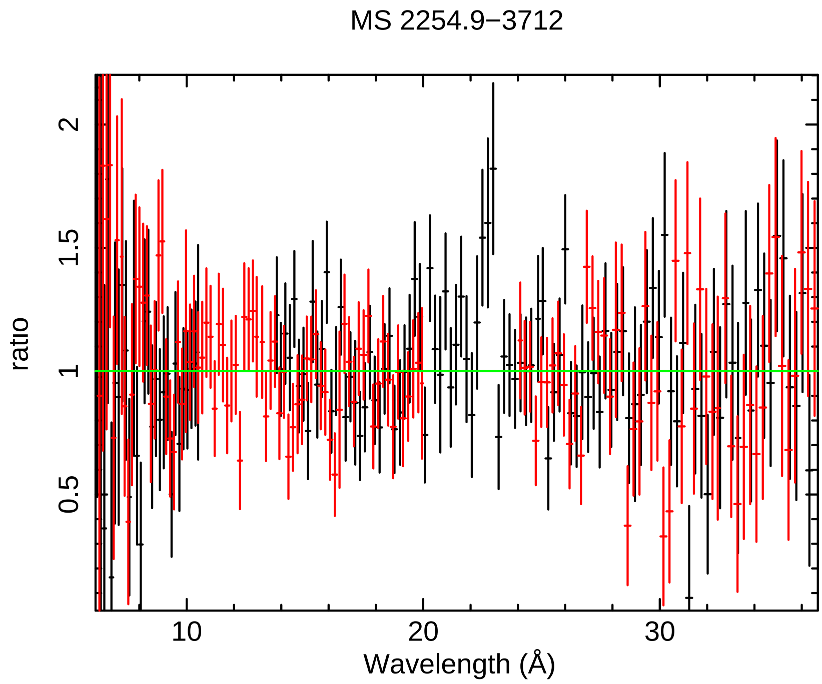

FIGURE 3.62: Ratio plot (data/model) of the best fit model, *tbabs*×(BB$_1$+BB$_2$+BB$_3$), to the RGS data ($6-37$ Å; observed) of MS 2254.9$-$3712.

and fit statistics stated previously. Two of the BB component temperatures (the lowest and the middle temperatures) are consistent with the equivalent components in the EPIC data. The exclusion of a power-law, for the reasons previously stated, in the RGS model fits may be why the highest temperature BB components are inconsistent between the EPIC and RGS best fit models.

The observed $0.35-2$ keV, unabsorbed flux values for this best fit model were $5.55 \pm 0.25 \times 10^{-12}$ erg cm^{-2} s^{-1} and $5.41 \pm 0.25 \times 10^{-12}$ erg cm^{-2} s^{-1} for the RGS1 and RGS2 detectors, respectively. The observed $0.35-2$ keV, unabsorbed RGS fluxes are consistent with each other and are consistent with the unabsorbed flux values of the EPIC data in the same energy range, $5.50^{+0.44}_{-0.52} \times 10^{-12}$ erg cm^{-2} s^{-1} and $5.55^{+0.08}_{-0.12} \times 10^{-12}$ erg cm^{-2} s^{-1}, for the PN and MOS data, respectively.

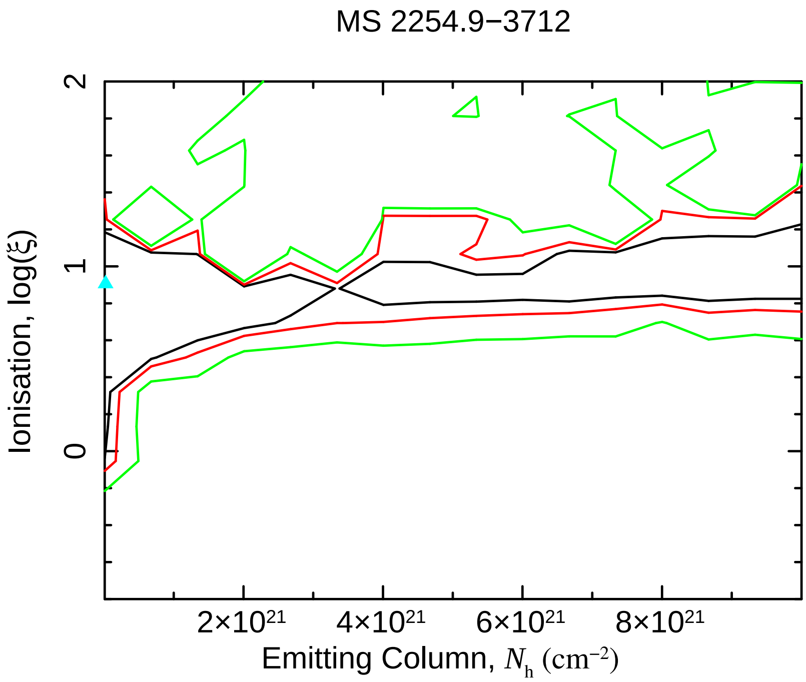

FIGURE 3.63: Confidence region contours determined for the parameters of the XSTAR emitting component used to attempt to model the excess seen at ~ 22 Å in the RGS data of MS 2254.9 − 3712. The light blue, filled triangle seen at $N_{\rm h} \sim 10^{19}$ cm^{-2} and $\log(\xi) \sim 0.9$ marks the best fit parameter values. The contours coloured black, red and green represent ΔS values of 2.3, 4.61 and 9.21, respectively, equivalent to approximate confidence regions, for 2 degrees of freedom, of $\sim 68\%$, 90% and 99%, respectively. Clearly, the best fit parameter values for the XSTAR emitting component are not well constrained.

3.5 Discussion

The concept behind this chapter was to look for evidence of high-ionisation, high-velocity X-ray outflows in the *XMM-Newton* spectra of a sample of six narrow line type 1 AGN. The six targets under analysis were chosen on account of their position on the limit relation plot (Figure 3.4) determined by Wang (2003). The limit relation (Section 3.2.1) uses an object's $\mathrm{H}\beta$ emission line width along with its estimated BH mass to determine whether that object is accreting at or above the Eddington limit. The six targets analysed here lie above or close to this limit relation, suggesting that the six targets are high-accretion rate objects and may therefore harbour high-ionisation, high-velocity X-ray outflows.

Evidence of high-ionisation, high-velocity outflows has been found in a number of targets, for example, PDS 456 (Reeves et al., 2002; Reeves et al., 2003; Reeves et al., 2009), PG 1211$+$143 (Pounds et al., 2003a; Pounds and Page, 2006; Pounds and Reeves, 2009), APM 08279$+$5255 (a BAL; Chartas et al., 2002; Hasinger et al., 2002; Chartas et al., 2009), PG 0844+349 (Pounds et al., 2003b), PG 1115+080 (a mini-BAL; Chartas et al., 2003), IRAS 13197$-$1627 (Dadina and Cappi, 2004), RXJ0136.9$-$3510 (Ghosh et al., 2004), Mrk 509 (Dadina et al., 2005), MR 2251$-$178 (Gibson et al., 2005), IC 4329a (Markowitz et al., 2006), MCG$-$5-23-16 (Braito et al., 2007) and Ark 564 (Papadakis et al., 2007). In particular, PDS 456 (Reeves et al., 2003; Reeves et al., 2009) exhibits blueshifted ($\sim 0.2c$) highly-ionised iron (Fe XXVI) absorption in the high-energy band of its *XMM-Newton* EPIC (Figure 3.1) and *Suzaku* X-ray spectra. The *XMM-Newton* EPIC spectra of the six targets analysed here, were searched for evidence of these features. Spectral fitting of the six targets did not show any evidence of highly-ionised iron absorption, indicative of the extreme outflow seen in PDS 456. The best fit models to the X-ray spectra of the six targets analysed in this thesis (Table 3.12) are varied in their complexity and composition.

With no high-ionisation, high-velocity X-ray outflows detected in the *XMM-Newton* EPIC spectra of the sample of six targets analysed in this work, limits can be placed on the non-detection of the X-ray absorption features. To calculate these limits a Gaussian absorption line was added to the best fit model for each observation of each target. The energy, $E_{\rm L}$, and intrinsic width, $\sigma_{\rm L}$, of the Gaussian line were fixed during fitting. The intrinsic width was frozen at 0.15 keV and the energy was fixed at two separate energies $E_{\rm L,1}$ and $E_{\rm L,2}$. $E_{\rm L,1}$ and $E_{\rm L,2}$ were fixed at the redshifted (observed) energies of the 1s–

Table 3.12: Best Fit Models to *XMM-Newton* EPIC data

Target Model	χ^2 d.o.f.	Γ	kT$_1$ [eV]	kT$_2$ [eV]	kT$_3$ [eV]	$N_{\rm h,1}$ $\times 10^{21}$[cm^{-2}]	$\log(\xi_1)$	$N_{\rm h,2}$ $\times 10^{21}$[cm^{-2}]	$\log(\xi_2)$	$E_{\rm obs}$ [keV]	$\sigma_{\rm obs}$ [eV]	$E_{\rm em}$ [keV]	$\sigma_{\rm em}$ [eV]	R^e
PG 0157+001 BB$_1$+*po*	278 296	2.19 ± 0.06	81^{+12}_{-13}											
QSO B0204+292 XSTAR$_1$ $\times$XSTAR$_2$ $\times$ (BB$_1$+BB$_2$+*po*+*ga*$_{\rm obs}$)	2074 1932	1.62 ± 0.02	94^{+1}_{-2}	264^{+9}_{-15}		$3.27^{+0.69}_{-0.74}$	$2.30^{+0.08}_{-0.16}$	$3.96^{+0.29}_{-0.07}$	0.66 ± 0.03	$5.75^{+0.04}_{-0.03}$	70^{+66}_{-48}			
PG 1001+054 XSTAR$_1$ $\times$(*po*)	33 29	$2.48^{+0.16}_{-0.20}$				210^{+46}_{-40}	$2.05^{+0.13}_{-0.12}$							
PG 1351+640 XSTAR$_1$ $\times$(BB$_1$+ BB$_2$+*po*+*ga*$_{\rm obs}$)	700 684	$1.89^{+0.10}_{-0.12}$	94^{+5}_{-4}	236^{+32}_{-19}		$2.82^{+0.66}_{-0.51}$	$0.67^{+0.11}_{-0.05}$		$5.98^{+0.13}_{-0.15}$	243^{+195}_{-124}				
PG 1440+356^a BB$_1$+*pexriv*^{f}	839 947	2.69 ± 0.04	88 ± 1	$\xi=74.0^{+58.5}_{-65.8}$										$5.1^{+1.0}_{-0.9}$
PG 1440+356^b *bexrav*^{g}	558 608	$\Gamma_1=2.97\pm0.02$		$E_{\rm B}=2.16^{+0.68}_{-1.03}$		$\Gamma_2=2.66^{+0.29}_{-0.33}$								$5.5^{+4.5}_{-3.4}$
PG 1440+356^c BB$_1$+*pexrav*	678 783	2.74 ± 0.05	85^{+6}_{-6}											$8.6^{+1.7}_{-1.5}$
PG 1440+356^d BB$_1$+BB$_2$+*pexrav*	639 591	$2.45^{0.20}_{-0.25}$	85 ± 3	217^{+34}_{-24}										$3.7^{+3.0}_{-2.4}$
MS 2254.9−3712 *ga*$_{\rm em}$+BB$_1$+BB$_2$+ BB$_3$+*po*+*ga*$_{\rm obs}$	1014 1079	$1.72^{+0.03}_{-0.02}$	34^{+2}_{-1}	117^{+26}_{-6}	250^{+11}_{-15}					6.19 ± 0.06	118^{+83}_{-57}	$0.56^{+0.01}_{-0.03}$	56^{+11}_{-12}	

Best fit models and corresponding parameter values for the six candidate high-accretion rate AGN. a - OBS ID 0005010101. b - OBS ID 0005010201. c - OBS ID 0005010301. d - OBS ID 0107660201. e - R represents the reflection component coefficient. f - the ionisation parameter, ξ, from the ionised reflection model, *pexriv*, is measured in erg cm s^{-1}. g - the parameters for the broken power-law neutral reflection model, *bexrav*, are Γ_1, the power-law photon-index for energies below the break energy, $E_{\rm B}$, and Γ_2, the power-law photon-index for energies above $E_{\rm B}$. $E_{\rm B}$ is measured in keV.

2p Fe XXV line (rest energy 6.7 keV; intrinsic) and the same Fe XXV line blueshifted[9] by $v = 0.3c$ in the rest frame of the target, respectively. During modelling the normalisation of the Gaussian absorption line was allowed to vary. The STEPPAR command was then used to calculate the 90% error ($\Delta\chi^2 = 2.706$) on the absorption line's normalisation. The EW of the Gaussian absorption line was then calculated at the 90% error level of the normalisation. The EW values at the two energies are reported in Table 3.13 for each target. For comparison, the EW of the strongest absorption lines detected in the X-ray spectra of PDS 456 and PG 1211 + 143 are 133 ± 39 eV (Reeves et al., 2009) and 210 ± 35 eV (Pounds and Page, 2006), respectively. Using the lower limit on the EWs for PDS 456 and PG 1211 + 143 it can be seen from Table 3.13 that both lines could have been detected at the two energies, $E_{\mathrm{L},1}$ and $E_{\mathrm{L},2}$, in the spectra of QSO B0204 + 292, MS 2254.9−3712 and the 0005010101 and 0005010301 observations of PG 1440+356. Both the PDS 456 and the PG 1211+143 lines could be detected at $E_{\mathrm{L},1}$ but not at $E_{\mathrm{L},2}$ in PG 0157+001 and the 0005010201 observation of PG 1440+356. In the case of PG 1351+640, the PG 1211+143 line could be detected at both energies but the PDS 456 line would not be. For the 0107660201 observation of PG 1440+356, the PG 1211 + 143 line could be detected at $E_{\mathrm{L},1}$ but not at $E_{\mathrm{L},2}$, with the PDS 456 line not likely to be detected at either energy. Finally, in the case of PG 1001 + 054, neither line would be detected at either energy due to the poor quality of the data. With the exception of PG 1001 + 054, it is likely that if a high-ionisation, high-velocity outflow with properties and observed characteristics similar to those found in PDS 456 and PG 1211 + 143 were present in the targets analysed here, the outflow would have been detected in the EPIC spectra of all targets.

One feature common in all six source spectra was the presence of a SE. This feature

[9] In the intrinsic frame of a source, the energy of a relativistically blueshifted line, E_{o}, is related to the rest energy of the line, E_{r}, by $\frac{E_{\mathrm{o}}}{E_{\mathrm{r}}} = \left(\frac{1+\beta}{1-\beta}\right)^{1/2}$ where $\beta = v/c$ and v is the blueshifted velocity.

Table 3.13: Observed Equivalent Width Detection Limits

Object	$E_{\mathrm{L},1}$ [keV]	EW_1 [eV]	$E_{\mathrm{L},2}$ [keV]	EW_2 [eV]
PG 0157+001	5.76	86.4	6.97	233.1
QSO B0204+292	6.03	15.8	8.23	17.6
PG 1001+054	5.77	295.6	7.87	2E+5
PG 1351+640	6.15	111.8	8.39	124.1
PG 1440+356^a	6.20	80.9	8.46	80.0
PG 1440+356^b	6.20	71.6	8.46	204.6
PG 1440+356^c	6.20	22.9	8.46	77.3
PG 1440+356^d	6.20	120.6	8.46	255.8
MS 2254.9−3712	6.44	67.0	8.79	88.1

Calculated EW detection limits for a Gaussian absorption line inserted into the best fit models for each target, measured at the 90% error level of the Gaussian absorption line's normalisation. The Gaussian absorption line's intrinsic width was frozen at 0.15 keV and its energy frozen at two different energies, $E_{\mathrm{L},1}$ and $E_{\mathrm{L},2}$, where the EW was measured in each case. $E_{\mathrm{L},1}$ is the energy of the Fe XXV line (6.7) at the observed redshift of the target. $E_{\mathrm{L},2}$ is the energy of the Fe XXV line (6.7) blueshifted in the rest frame of the target by $v = 0.3c$, then redshifted into the observed frame. a, b, c and d indicate the 0005010101, 0005010201, 0005010301 and 0107660201 observations of PG 1440+356, respectively.

can be seen in Figures 3.5 and 3.41. In each instance the SE can be represented by one or more BB components. In some cases the SE has been modified by absorption (PG 1351+640 and QSO B0204+292) or by excess line emission (MS 2254.9–3712). The temperatures obtained for the BB components were in the range kT $\approx 40-260$ eV. As discussed in Section 1.2.2, the model components often used to describe a SE, e.g., BB or comptonised thermal emission from the accretion disc, have very similar temperatures, almost always around $100-200$ eV (Gierliński and Done, 2004; Crummy et al., 2006; Sobolewska and Done, 2007). Not all of the temperatures reported in Table 3.12 lie within this temperature range.

The nature of the SE is unclear. There are two physical models suggested that could explain its origin; reflection emission from the inner accretion disc (Crummy et al.,

2006) or atomic absorption from a relativistically blurred, moderately-ionised medium (Gierliński and Done, 2004; Gierliński and Done, 2006; Sobolewska and Done, 2007). The current data sets do not have a high enough resolution to discern which of these is the dominant process. However, in both cases, the SE is likely to be produced close to the central source ($\sim$ few$\times r_{\rm g}$). Therefore, as X-ray telescopes become more powerful in terms of resolution and collecting power, more detailed analysis of the inner regions of AGN can be performed.

In addition to the SE, three of the targets show evidence of intrinsic absorption in the form of a WA; QSO B0204+292, PG 1001+054 and PG 1351+640. The detection of the WA, with an absorbing column, $N_{\rm h} = 21.0^{+4.56}_{-4.04} \times 10^{22}$ cm^{-2} and ionisation, $\log(\xi) = 2.05^{+0.13}_{-0.12}$, in the EPIC spectra of PG 1001+054 is tentative. Since the data were of such low quality (29 d.o.f.) and the fact that no RGS data were available, an outflow velocity could not be calculated. Thus, a longer look at PG 1001+054 would be instructive to determine a more complete picture of the possible WA in PG 1001+054.

Zheng et al. (2001) classified PG 1351+640 as a mini-BAL and suggested that the weak X-ray flux seen by Tananbaum et al. (1986) with the Einstein Observatory is intrinsic to the continuum source within PG 1351+640. Their conclusion is drawn from the extrapolation of the steep UV continuum to X-ray wavelengths and the calculated column density of the UV absorber ($\sim 10^{21}$ cm^{-2}); such a UV absorbing column should not have much affect on the opacity at 1 keV. The *XMM-Newton* data analysed here shows evidence of an absorbing medium with a similar column density, which does have an effect on the X-ray continuum. The WA detected in PG 1351+640 has a moderate column density ($N_{\rm h} = 2.82^{+0.66}_{-0.51} \times 10^{21}$ cm^{-2}) and a low ionisation (almost neutral, $\log\xi = 0.67^{+0.11}_{-0.05}$), which is consistent with WAs found in other PG quasars (Porquet et al., 2004; Ashton et al., 2004) and other AGN in general (e.g., Blustin et al., 2005).

An outflow velocity for the XSTAR component used to model the WA was unable to be tied down at the 99% level and so no mass loss rate could be calculated. Also, the mass of the absorber could not be calculated with any certainty due to its low ionisation compared to the ionising luminosity. Assuming a spherical radial outflow, the mass of an absorber can be calculated using the following equation

$$M_{\rm abs} = 4\pi r^2 N_{\rm h} m_{\rm p} C_{\rm g} \qquad [\rm g] \tag{3.6}$$

where r is the distance of the absorbing material from the ionising source, $N_{\rm h}$ is the column density of the absorbing material, $m_{\rm p}$ is the mass of a proton and $C_{\rm g}$ is the global covering factor of the absorber. Assuming a homogeneous spherical outflow ($C_{\rm g} = 1$), the density $n(r)$ of the absorber varies inversely with r^2. Therefore, the ionisation parameter ($\xi = L_{\rm ion}/n(r)r^2$) is mainly independent of radial position along the outflow. Therefore, the column density down to the base of the outflow, $R_{\rm wind}$, can be estimated as

$$N_{\rm h} = \int_{R_{\rm wind}}^{\infty} n(r)dr = \int_{R_{\rm wind}}^{\infty} \left(L_{\rm ion}/\xi r^2\right) dr = L_{\rm ion}/\xi R_{\rm wind} \tag{3.7}$$

where $L_{\rm ion}$ is the luminosity of the ionising source. Assuming a power-law spectrum with a photon-index, $\Gamma = 2$, integrated over 1 and 1000 Rydbergs, $L_{\rm ion} = 10^{44}$ erg s^{-1} for the XSTAR component (Section 3.4). Using the values of $N_{\rm h}$ and $\log(\xi)$ determined for PG 1351+640 and assuming a global covering fraction, $C_{\rm g} = 1$, $R_{\rm wind} = 7.58 \times 10^{21}$ cm $\sim 1 \times 10^9\, r_{\rm g}$. This would place the base of the WA well into the host galaxy at $\sim 2.5 \times 10^3$ kpc from the central source. This cannot be correct and this fact is confirmed by the mass estimate for the WA. Substituting $R_{\rm wind}$ into Equation 3.6 for r results in an unbelievable mass contained within the absorber, $M_{\rm abs} = 3.4 \times 10^{42}$ g $\sim 1.7 \times 10^9\,{\rm M}_\odot$. Clearly this mass is not correct. Reducing $C_{\rm g}$ does not alter these values enough to give a reasonable mass. The ionisation level for this particular ionising luminosity would automatically place the absorbing material at a large distance from the ionising source.

This, in combination with the lack of an outflow velocity, means that describing the location and general properties of the WA is not possible in this case. A WA is clearly present but the above calculations imply that the WA does not take the form of a spherical radial outflow.

The target QSO B0204+292 presents the most interesting intrinsic absorption (Figure 3.5) of the sources with a WA present. QSO B0204+292 shows evidence in its EPIC spectra of two moderate absorbing columns ($N_{\rm h,1} = 3.27^{+0.69}_{-0.74} \times 10^{21}$ cm^{-2} and $N_{\rm h,2} = 3.96^{+0.29}_{-0.07} \times 10^{21}$ cm^{-2}), with a moderate- ($\log(\xi_1) = 2.30^{+0.08}_{-0.16}$) and low- ($\log(\xi_2) = 0.66 \pm 0.03$) ionisation, respectively. The RGS spectra for QSO B0204+292 are in agreement with the EPIC results (Section 3.4.2). However, the RGS spectra also show evidence for additional narrow absorption in the region of the UTA at the redshift of QSO B0204+292 ($z = 0.1096$; Figure 3.18) that could not be modelled by the two XSTAR components present in the best fit model for QSO B0204+292. Unfortunately, the inclusion of a Gaussian absorption line was not significant at the 99% level and the errors on the line parameters were not well constrained (Figure 3.20). In addition, no outflow velocities could be determined at the 99% confidence level. No mass loss rates or WA mass estimates can be made. The intrinsic absorption within QSO B0204+292 is clearly complex. Whether the absorption is by clumpy material orbiting in another less dense absorbing material or whether it is a multi-phased medium is impossible to discern. The additional narrow absorption present could be a result of an over abundance of Fe M shell ions, though other elements should be evident. More likely, a third ionisation component may be present, suggesting a multi-phased medium.

If a spherical radial outflow, with a global covering factor, $C_{\rm g}$, of 1, as used for PG 1351+640, is assumed for the WAs in QSO B0204+292 and PG 1001+054, an estimate on the location and mass of the WA can be made. In the case of PG 1001+054,

$R_{\rm wind} = 4.24 \times 10^{18}$ cm ~ 1.4 pc and $M_{\rm abs} = 7.95 \times 10^{34}$ g $\sim 40\,{\rm M}_{\odot}$, respectively. This would place the base of the WA at or close to the putative torus surrounding the central engine. For the lower ionisation component in QSO B0204+292, $R_{\rm wind} = 5.52 \times 10^{21}$ cm ~ 1.8 kpc and $M_{\rm abs} = 2.54 \times 10^{39}$ g $\sim 1 \times 10^{6}\,{\rm M}_{\odot}$, respectively. The higher ionisation component results in $R_{\rm wind} = 1.53 \times 10^{20}$ cm $\sim$ 50 pc and $M_{\rm abs} = 1.61 \times 10^{36}$ g $\sim 805\,{\rm M}_{\odot}$, respectively. There is a large separation between the calculated bases of the two WA winds. The base of the low-ionisation component places the absorber firmly within the host galaxy. This, combined with the large calculated absorber mass, suggests that the outflow is not a spherical radial outflow. It is likely that the two components in QSO B0204$+$292 are part of the same outflow and that the simplified calculations used above are not appropriate.

The EPIC data for PG 0157$+$001, PG 1440$+$356 and MS 2254.9$-$3712 show no evidence of a WA imprinted on the SE in their X-ray spectra. In the case of PG 0157+001, the observation was short ($\sim$ 6 ks). Although the PN data shown in Figure 3.5 is a little noisy, the growth of the residuals (the SE) above the extended hard-band power-law model fit is not completely smooth. It is possible that there are emission or absorption features within the PN data for PG 0157$+$001 that would become obvious with a longer look at this target with *XMM-Newton*. The RGS data for PG 0157$+$001 is noisy and only a continuum model fit was possible. Therefore, the presence of any features in the soft-band of the EPIC spectra could not be confirmed or denied.

PG 1440$+$356 showed no evidence of intrinsic absorption in its EPIC spectra, which was confirmed by its featureless RGS spectra. The EPIC spectra were modelled well with either a partial covering absorber model or by a model simulating relativistically blurred reflection from an ionised medium. As discussed in Section 3.4.5, the exact nature of the SE in PG 1440$+$356 is not obvious. However, it is likely that the SE is a hybrid of both models as both scenarios require extreme parameters, such as large absorbing columns or large iron abundances, respectively. The acquisition of higher quality data will begin to answer this question.

The apparent SE in the PN data of MS 2254.9−3712 (Figure 3.5) is ~ 5 and ~ 10 times that of the extended hard-band power-law fit at energies of 0.5 and 0.3 keV, respectively. The best fit model to the EPIC data for MS 2254.9 − 3712 requires three BB components and the inclusion of a Gaussian emission line at an observed energy of $E_{\rm em} = 0.56^{+0.01}_{-0.03}$ keV ($\lambda 22.1$) with an intrinsic width of $\sigma_{\rm em} = 56^{+11}_{-12}$ eV. This is consistent with the O VII triplet at the redshift of MS 2254.9−3712 ($z = 0.039$). The analysis of the RGS1 data for MS 2254.9−3712 shows an excess above the continuum model fit at $\sim$ 22 Å (Figure 3.62). Attempts to model this feature were not successful at the 99% level, although the inclusion of an XSTAR emission component, with column density, $N_{\rm h} \simeq 2.3 \times 10^{19}$ cm^{-2}, and ionisation, $\log(\xi) \simeq 0.9$, did appear to remove the residuals. Unfortunately, the O VII triplet at this redshift falls on the dead CCD chip in the RGS2 detector array and thus the residuals cannot be confirmed with the current *XMM-Newton* data. However, the excess emission seen in the EPIC cameras and the RGS1 camera, suggests that it is highly likely that the residuals are real and that there is O VII emission present. The origin of the O VII triplet emission is unclear. However, since no corresponding absorption is detected, the line emitting region is likely not to be along the line of sight. Interestingly, MS 2254.9−3712 appears to show variability in its soft-band ($0.5-2$ keV) of the order of a factor of two over a time period of $2-3$ ks (Figure 3.64). This is consistent with the variation seen in the ASCA observation of this target, as discussed in Section 3.2.2. Such variability is typical of NLS1s (Leighly, 1999*a*; Leighly, 1999*b*; Pounds and Vaughan, 2000) and would suggest a compactness size of several $r_{\rm g}$ for the X-ray emitting region. A longer obser-

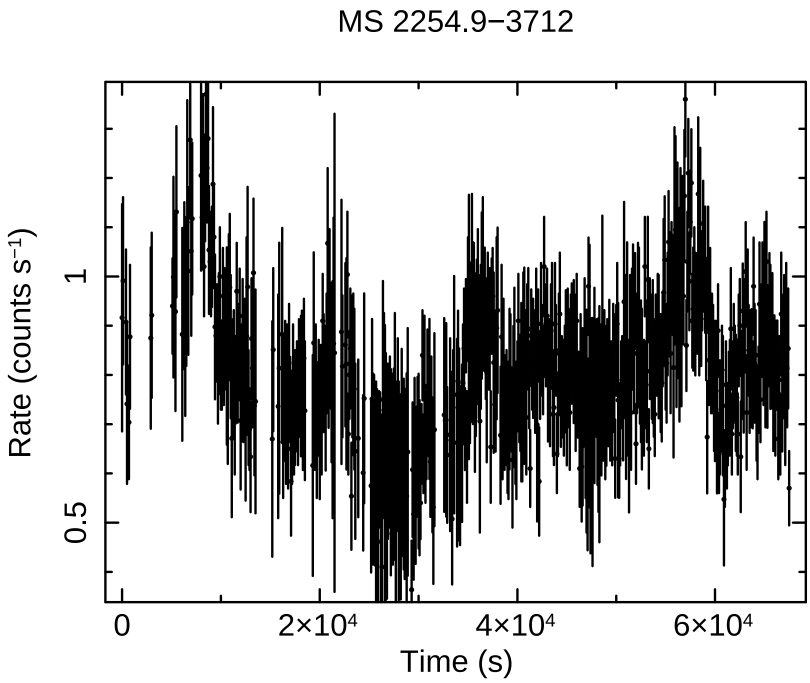

FIGURE 3.64: EPIC PN light curve showing the variability of MS 2254.9 − 3712 in the observed $0.5-2$ keV energy range. A standard bin size of 100 s was used.

vation of MS 2254.9 − 3712 with *XMM-Newton* would be instructive in determining the properties of the suspected O VII emission and any associated variability.

The presence of WAs and the possible detection of O VII triplet emission show evidence of ionised material in four of the six systems observed. It is possible, depending on the nature of the SE, that this number could be revised to include all six sources. However, none of the sources provide evidence for a high-ionisation, high-velocity outflow similar to that detected in PDS 456. The non-detection of high-ionisation, high-velocity outflows in the sample of the six narrow line objects analysed in this thesis questions the hypothesis that all high-accretion rate AGN will harbour such outflows. These findings suggest that the type of outflow found in PDS 456 are not common. However, the detection of a high-ionisation, high-velocity outflow depends on the limits of the data. Evidence of an outflow could be present in the data presented in this chapter but may be deemed non-significant, cf. the publication bias suggested by Vaughan and Uttley (2008, see Section 3.4). In addition, there could be a high-ionisation, high-velocity outflow present but it may be fully-ionised, thus making the outflow transparent in X-rays. Although if this were the case, there should be evidence of such an outflow in other wavebands as it recombines.

At the other extreme, it is possible that no outflows were present at the time of the observations of the six targets analysed here. Maybe the outflows stalled, stopped or just slowed down and started to recombine, leaving a WA or a neutral absorber present. However, it could also be the case that no high-ionisation, high-velocity outflow has even started or is even likely to start. Perhaps a trigger is needed, such as a galaxy interaction or a star forming event, or assuming that all outflows occur at some point throughout the lifetime of AGN, it could be that an evolutionary process has not yet occurred. This would lead to the question of what process in the AGN's evolution could spark a high-ionisation, high-velocity outflow. It is possible that such outflows are short lived, recurring phenomena, such that minor events can trigger them. For example, PDS 456 exhibits large variability in its X-ray spectra, which suggests that the lower-ionisation absorbing component is varying (Reeves et al., 2009). This variation could affect the properties of the high-ionisation component of the outflow or it could indicate a recurring process that may be causing the extreme X-ray outflow seen in PDS 456.

If high-ionisation, high-velocity outflows are extreme versions of WAs or BALs, then the right conditions may not have been met in the current sample. The lack of detection of these outflows could be due to orientation effects (e.g., Elvis, 2000), although one would expect some correlation with viewing angle in this case. If the presence of a high-ionisation, high-velocity outflow was solely based on orientation then one might expect some evidence of an extreme outflow in the X-ray spectra of PG $1001+054$ (a BAL) and PG 1351+640 (a mini-BAL). One other suggestion is that magnetic collimation (if present) in the ejection phase of the outflow may not have been tight enough to accelerate it to the required speeds. The presence or absence of a high-ionisation, high-velocity outflow could be a result of the morphology of the central engine or even just the shape of the accretion disc. Without more detailed data, these questions will remain unanswered.

There are more direct factors to investigate due to the absence of high-ionisation, high-velocity outflows. For example, are the assumptions made when selecting the sample correct? Are the sources truly super-Eddington? Can the empirical-reverberation relationship be extended down to include narrow line objects? PDS 456 ($v_{\rm FWHM} \approx$ 3500 km s^{-1}, $M_{\rm BH} \approx 2 \times 10^9$ M$_\odot$) lies to the right of the limit relation when the parameter values $\xi = 4$ and $\beta = 0.7$ (Section 3.2.1) are used, as shown in Figure 3.4, but lies to the left of the limit relation when the parameter values $\xi = 7.5$ and $\beta = 0.58$ are used instead. However, for both sets of parameter values in the limit relation, PG 1211+143 ($v_{\rm FWHM} \approx 1832$ km s^{-1}, $M_{\rm BH} \approx 4 \times 10^7$ M$_\odot$) always lies to the right of the limit relation, suggesting it is accreting at a sub-Eddington rate. Therefore, although the limit relation could suggest candidate super-Eddington accretion rate objects, it is clear that high $\dot{M}$ cannot be the only observable marker of a high-ionisation, high-velocity X-ray outflow. The question of the observable properties of an AGN that indicate the presence of such an outflow can only be answered with more detailed observations and monitoring in more wavebands of the sample targets. It is likely that other properties such as bolometric luminosity, accretion efficiency or simply just the age of the system may also be factors in whether a high-ionisation, high-velocity outflow is present in an AGN. Only with a larger sample of candidates, along with an uniform analysis of the data, will it be possible to see any possible correlation between high-ionisation, high-velocity outflows and their host galaxy's observable properties.

3.6 Conclusions

A sample of six narrow line AGN suspected of accreting at or above the Eddington limit were observed with *XMM-Newton* to search for the presence of any high-ionisation, high-velocity outflows. Unfortunately, no such evidence was found down to the detection limits given in Table 3.13. However, all of the sources display a SE, with half of them displaying evidence of a WA and one target displaying excess emission around the O VII triplet. The non-detection of any high-ionisation, high-velocity outflows does not mean that they do not exist but does suggest that such outflows may not be present in all high $\dot{M}$ objects all of the time. A uniform analysis of X-ray data from a larger sample of narrow line AGN over a range of redshifts (e.g., Tombesi et al., 2010a) is required to attempt to constrain the required environmental parameters for the presence of high-ionisation, high-velocity outflows.

Chapter 4

Identifying the AGN Population of Super Soft X-ray Sources

4.1 Introduction

The *XMM-Newton* observatory has kept a keen eye on the X-ray sky since its launch in 1999. The majority of the observations have been made while pointing at specific targets. However, full advantage has been made of the impressive observing capabilities of *XMM-Newton* (Section 1.3), as shown by the *XMM-Newton* Slew Survey EPIC Source catalogue (XMMSL1; Saxton et al., 2008). XMMSL1 contains $9{,}240$ sources, with a detection minimum likelihood value (DET_ML; Section 4.2.1) > 10, that were detected by *XMM-Newton* whilst slewing between targeted observations (Read et al., 2006; Saxton et al., 2008). In addition to XMMSL1, *XMM-Newton* is compiling a huge amount of data from pointed observations, resulting in the detection of a large number of serendipitous sources ($\sim 50-100$ per observation, depending upon the exposure time; Watson et al., 2001). The *XMM-Newton* Survey Science Centre (SSC) has contributed to the science analysis software (SAS) and to the processing of all *XMM-Newton* data sets for the archive. The SSC also spent a large amount of time collating these sources into catalogues, which contain the observed X-ray properties of each source and initial cross-correlation results with other catalogues that cover the entire electromagnetic

(EM) spectrum. The first version of this catalogue (1.0.1) was publicly released on the 7$^{\rm th}$ of April 2003 with an updated version (1.1.0) following on the 16$^{\rm th}$ of December 2004 (*XMM-Newton* Survey Science Centre, 2003). The first *XMM-Newton* Serendipitous EPIC Source Catalogue (1XMM) contains a total of $56{,}711$ sources, of which $28{,}279$ sources are unique, with a detection summary flag (SUMM_FLAG; Section 4.2.1) > 0 and a detection minimum likelihood value (DET_ML) > 8. The source information in 1XMM was collected from 585 pointed observations acquired between the 1$^{\rm st}$ of March 2000 and the 5$^{\rm th}$ of May 2002. These observations cover a total of ~ 90 square degrees, of which ~ 50 square degrees were unique. All data sets were publicly available by the 31$^{\rm st}$ of January 2003. The median flux of the data in the catalogue in the $0.2-10$ keV band is $\sim 3\times10^{-14}$ erg s^{-1} cm^{-2} (*XMM-Newton* Survey Science Centre, 2003). 1XMM has been superseded by the second *XMM-Newton* Serendipitous EPIC Source Catalogue (2XMM[1]; Watson et al., 2008; Watson et al., 2009). The 2XMM catalogue is discussed in more detail in Section 4.4.

Large serendipitous catalogues like 1XMM and 2XMM are extremely useful as they are a repository for all types of sources, both known and unknown. These catalogues allow various forms of research to be performed, e.g., the statistical analysis of certain groups of objects. In addition, they allow rare classes of object to be found and subsequently studied. This is the concept behind this chapter, which focuses on searching 1XMM and 2XMM for a particular group of objects that reside in an extreme region of parameter space; super soft X-ray sources (SSXs), specifically the AGN population of SSXs. AGN classified as SSXs are extreme objects that are likely to be accreting at a high rate ($\dot{m} = \dot{M}/\dot{M}_{\rm Edd} \sim 1$, e.g., NLS1s; Section 1.1.5). The results of the analysis of these objects could contribute towards the understanding of accretion at near-Eddington

[1]At the time of writing, the Incremental Second *XMM-Newton* Serendipitous EPIC Source Catalogue (2XMMi) had been released on the 20$^{\rm th}$ of August 2008 (http://xmmssc-www.star.le.ac.uk/Catalogue/2XMMi/).

rates. As a pilot study, a blind search of 1XMM was carried out to find the global and AGN populations of SSXs by performing a cut in the first EPIC PN (EPN) hardness ratio value (HR1; Section 4.2). Although the AGN population of SSXs is the primary objective of this search, other (interesting) SSXs will also be discussed.

4.1.1 Super Soft X-ray Sources

A SSXs is described as having an observed $0.2-2$ keV spectrum softer than that of a 100 eV blackbody (BB) in the same observed bandpass. The searches of 1XMM and 2XMM will yield both Galactic and extragalactic sources. It is likely that a number of the SSXs from within our Galaxy and local galaxies will be known super soft sources (SSS). SSS are typically stellar in nature and display very soft X-ray emission dominating below 0.5 keV, which can be characterised by an effective BB emission temperature, $kT_{\rm eff} \lesssim 100-175$ eV, and luminosities greater than $\sim 10^{35}$ erg s^{-1} (Di Stefano and Kong, 2003). Thus, SSS will form a subset of the selected SSXs. However, *XMM-Newton* is sufficiently sensitive that other fainter types of sources contributing to the general population of SSXs will be detected, i.e., AGN.

The archetypal SSS CAL 83 and CAL 87 were first discovered with the *Einstein* observatory by Long et al. (1981). Both sources are white dwarfs (WDs) and have effective temperatures, $kT_{\rm eff} \lesssim 84$ eV (Greiner, 2000). Since then, further studies of SSS with later generations of X-ray observatories have been performed, particularly with *ROSAT* (Singh et al., 1995; Greiner, 1996; Dotani et al., 2000; Greiner, 2000). Not all SSS have optical counterparts associated with them. Of the sources that do, the optical properties suggest a binary nature. However, not all SSS have been classified. The commonly accepted explanation for the majority of the unclassified SSS is that they are close-binary super soft (CBSS) X-ray sources. CBSS X-ray emission can be explained by the quasisteady burning of matter accreting at or above the Eddington limit onto the surface of a WD (van den Heuvel et al., 1992; Hachisu et al., 1996). Other types of objects associated with SSS are non-interacting hot WDs, magnetic cataclysmic variables (CVs; polars in particular), recurrent novae, nova, symbiotic binary systems and planetary nebulae (PN).

4.1.2 Overview

This chapter begins with a pilot study of SSXs within 1XMM to determine the number of AGN that meet the criteria for a SSXs. The study starts by searching 1XMM for SSXs and performing cross-correlation of the SSXs sample with other catalogues at different wavelengths. Imaging data from SuperCOSMOS (SC; Hambly et al., 2001) and the Isaac Newton Telescope Wide Field Survey (INT-WFS; McMahon et al., 2001) are also used to identify possible candidate counterparts. Following this, optical spectra of a small number of SSXs, mainly with unclassified optical candidate counterparts, taken with the Intermediate dispersion Spectrograph and Imaging System (ISIS) on the William Herschel Telescope (WHT), were analysed in an attempt to classify the candidate counterparts and in turn the SSXs. The latter sections of this chapter discuss work based on the search for candidate SSXs within 2XMM using the same criteria as the 1XMM search. The 2XMM candidate SSXs were visually inspected and a clean 2XMM SSXs list produced. These 2XMM SSXs were then cross-correlated with the 1XMM SSXs list and other catalogues at different wavelengths. The known and candidate AGN populations of SSXs from 2XMM are identified. Finally, the findings of this work and their implications are discussed.

4.2 1XMM SSXs Sample

1XMM is ideal for searching for SSXs as the detectors aboard *XMM-Newton* are an order of magnitude more sensitive to a 100 eV BB spectrum than the *ROSAT* Position Sensitive Proportional Counter (PSPC; Truemper, 1982), which is due to the large throughput of *XMM-Newton*. The limiting flux of the *ROSAT* All Sky Survey in the $0.1-2.4$ keV band is $\sim 5\times10^{-13}$ erg s^{-1} cm^{-2} (Voges et al., 1999), while the median flux of the data in 1XMM in the $0.2-2$ keV band is $\sim 2.5\times10^{-14}$ erg s^{-1} cm^{-2} (*XMM-Newton* Survey Science Centre, 2003). The superior sensitivity of *XMM-Newton* should result in the detection of fainter SSXs, both Galactic and extragalactic, along with SSXs at higher redshifts. In addition to the desired AGN population of SSXs, fainter sources and sources without optical counterparts are of interest too. For example, interesting non-AGN X-ray sources include isolated neutron stars (INS), e.g., RX J0720.4$-$3125 (Paerels et al., 2001; Hohle et al., 2009, and references therein). Figure 4.1 shows the EPN $0.2-10$ keV spectrum of the INS RX J0720.4$-$3125 from the November 2002 *XMM-Newton* observation. RX J0720.4$-$3125 has very little emission above 2 keV and matches the criteria for SSXs.

4.2.1 Sample Selection

In order to investigate SSXs with *XMM-Newton*, a simple list of criteria were drawn up and applied to 1XMM. The first and main stage of filtering was the selection of sources based on their first EPN hardness ratio, HR1. HR1 is defined as

$$\mathrm{HR1} = \frac{C2 - C1}{C2 + C1} \tag{4.1}$$

where $C1$ and $C2$ are the number of counts from 1XMM band 1 (b1; $0.2-0.5$ keV) and 1XMM band 2 (b2; $0.5-2$ keV), respectively. Sources were selected if the HR1 value,

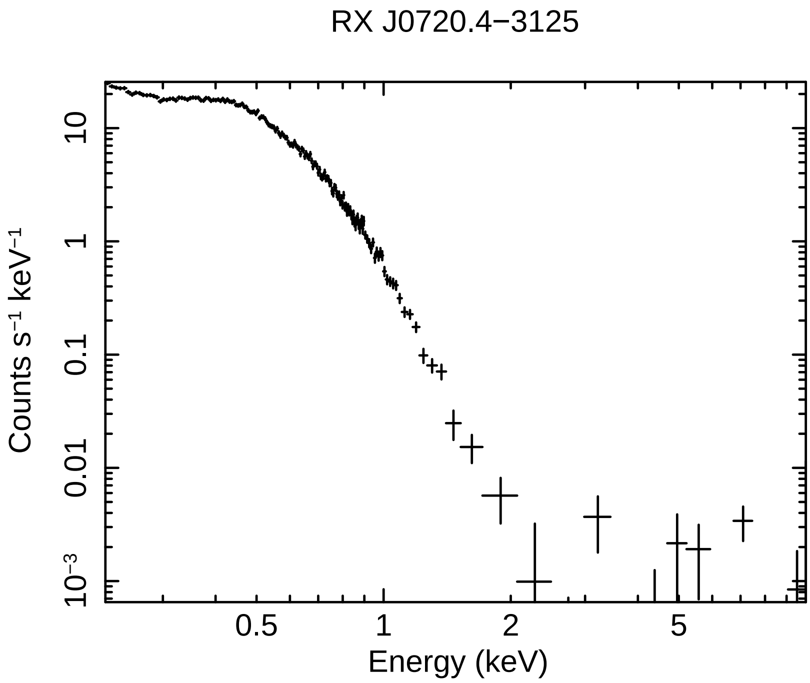

FIGURE 4.1: EPIC PN spectrum ($0.2-10$ keV; observed) of the INS RX J0720.4-3125, observed by *XMM-Newton* in November 2002 (observation identification 0156960201). Data were obtained from the *XMM-Newton* Science Archive (XSA; http://xmm.esac.esa.int/xsa/index.shtml) and were reduced as described in Section 1.3.1 using SAS version 7.1.0.

with the addition of a value two times its error, was below zero, i.e.,

$$\text{Criteria} \equiv \text{HR1} + (2 \times \sigma_{\text{HR1}}) < 0 \qquad (4.2)$$

where σ_{HR1} is the error on HR1, determined from the errors quoted for $C1$ and $C2$. The errors on $C1$ and $C2$ were calculated using Poisson statistics and are supplied in 1XMM.

The second stage of filtering selected only sources with an EPN total DET_ML value (calculated using the DET_ML values from all of the 1XMM bands) > 8, which corresponds to a $> 3\sigma$ detection[2]. The next stage was to remove sources with a SUMM_FLAG[3]

[2]To obtain a $> 3\sigma$ detection, the actual DET_ML value used was 19 due to the incorrect calculation of the DET_ML values within 1XMM

[3]The SUMM_FLAG parameter, which has a value of $0-4$, is used as a quick way of determining the reliability of a source and is set by the SAS task EMLDETECT during source detection. A SUMM_FLAG value of 4 is given to a source that is likely to be a good detection and a value of $2-3$ means that there

< 2, corresponding to those sources where there was a problem with the detection of that source, i.e., the source is most likely spurious. The 95 sources that remained after this stage of filtering were candidate SSXs.

The sample number was reduced further, to a total of 86 sources, by removing duplicate detections determined from the 1XMM unique source number (UNIQUE_SRCNUM), which is associated with sources assumed to be the same source. The remaining 86 sources were then visually inspected. 1XMM b1 and b2 images were used to verify whether the source was real. There are no definitive rules when performing a visual inspection of sources. However, some obvious spurious sources were easily detected, such as bright individual pixels, bright columns (detector noise) emanating from the centre line of the detector, sources lacking any visibly grouped counts and optically loaded sources.

Optical loading is the term used to describe the detection of events on the CCD that are not caused by X-ray photons. These false X-ray events are produced by a large number of optical photons from an optically bright source. This occurs because the optical photons penetrate the aluminium filters in front of the detectors and are incorrectly registered by the CCD, which in turn affects the registered energy scale. For each optically generated photo-electron that is registered, the energy scale shifts[4] by ~ 3.6 eV. This means that bright optical sources could be registered as false X-ray sources with an apparent soft excess. If this effect is not visually inspected for, optically loaded sources could falsely match the selection criteria for SSXs. The aluminium filters do a very good job at masking out optical photons but at the expense of soft X-ray photons. There are three aluminium filters for each of the EPIC cameras named THICK, MEDIUM and

could be a problem with the source detection and the source maybe spurious. A value of $0 - 1$ means that there was a problem with the detection of that source and it is most likely spurious.

[4]http://xmm.esac.esa.int/docs/documents/XMM-SOC-CAL-TN-0051

Table 4.1: Super Soft X-ray Sources Selected from the 1*XMM-Newton* EPIC Source Catalogue

IAUNAME 1XMM	R.A. [Degrees]	Dec [Degrees]	POSITION ERROR [arc seconds]	EPN HR1	EPN DET ML	SUMM FLAG	GTI [S]	EPN RATE b1 [cts s^{-1}]	EPN RATE b2 [cts s^{-1}]	EPN TOTAL COUNTS [cts]
J004755.3−251907	11.980362	−25.318573	0.9	−0.96±0.06	74.6	4	35385	0.00353±0.00045	0.00012±0.00006	85±11
J005413.0−373308	13.554085	−37.552271	0.5	−0.38±0.09	191.1	4	30510	0.00743±0.00075	0.00064±0.00337	138±13
J005511.0−373855	13.795697	−37.648687	0.1	−0.64±0.04	887.2	3	30510	0.02517±0.00151	0.00077±0.00555	461±25
J005520.2−374018	13.834018	−37.671617	1.2	−1.00±0.24	26.5	4	30510	0.00146±0.00027	0.00017±0.00005	36±8
J005555.6−274633	13.981609	−27.775819	0.4	−1.00±0.02	274.7	4	360	0.61829±0.07768	0.00509±0.00046	73±9
J010459.3−062846	16.246947	−6.479483	0.5	−0.29±0.12	170.9	4	20000	0.00545±0.00072	0.00071±0.00297	148±13
J012323.9−583834	20.849441	−58.642887	0.5	−0.26±0.10	132.4	4	28978	0.00733±0.00086	0.00077±0.00430	151±15
J013304.7+302107	23.269714	30.352023	1.2	−1.00±0.28	26.8	4	9264	0.00283±0.00055	0.00039±0.00010	24±5
J013409.9+303221	23.541450	30.539276	0.3	−0.55±0.05	616.2	2	12819	0.04670±0.00328	0.00190±0.01345	271±17
J021721.7−050630	34.340455	−5.108261	0.5	−0.29±0.10	160.3	2	40470	0.00782±0.00098	0.00080±0.00433	141±14
J022255.9−051352	35.732939	−5.230994	0.5	−0.37±0.09	187.6	4	19670	0.00642±0.00070	0.00055±0.00295	138±13
J031505.7−550942	48.773549	−55.161680	0.8	−0.47±0.15	24.2	4	6199	0.00572±0.00099	0.00070±0.00205	23±3
J031559.1−552638	48.996224	−55.443911	1.1	−0.39±0.11	67.2	4	4848	0.00879±0.00135	0.00077±0.00388	49±6
J031605.7−551539	49.023745	−55.260786	0.7	−0.35±0.15	27.0	4	1960	0.01436±0.00293	0.00187±0.00696	28±4
J033754.9+095555	54.478836	9.931901	0.9	−0.46±0.15	61.9	4	9600	0.01988±0.00391	0.00230±0.00740	60±10
J043151.9−780011	67.966135	−78.003040	0.9	−0.60±0.11	50.0	4	5598	0.01025±0.00181	0.00074±0.00259	35±5
J043328.3−780713	68.367931	−78.120372	0.5	−0.31±0.12	109.6	4	5598	0.01297±0.00186	0.00149±0.00686	67±8
J043447.9−775214	68.699601	−77.870671	1.4	−0.81±0.14	32.5	4	5598	0.00666±0.00098	0.00054±0.00071	24±3
J050803.2−684017	77.013132	−68.671504	0.9	−1.00±0.21	87.8	4	9945	0.00980±0.00123	0.00104±0.00045	75±11
J051541.5+010439[a]	78.922800	1.077603	0.1	−0.71±0.01	64409.2	4	22878	0.67634±0.00582	0.00236±0.11498	16658±131
J052214.9−701657	80.562192	−70.282378	1.7	−0.42±0.18	41.4	4	16222	0.00815±0.00137	0.00134±0.00334	64±10
J054334.2−682223[a]	85.892352	−68.373123	0.0	−0.77±0.00	178896.9	4	9749	3.98415±0.02153	0.00851±0.52078	37265±191
J060011.5−501831	90.047948	−50.308548	1.5	−0.37±0.15	24.2	4	4510	0.00616±0.00107	0.00086±0.00286	28±4
J072024.9−312551[a]	110.103793	−31.430858	0.0	−0.47±0.00	920308.4	4	38667	4.63349±0.00420	0.00694±1.66114	217330±280
J074602.6+280110	116.510669	28.019579	2.7	−1.00±0.33	19.6	4	31939	0.00147±0.00031	0.00024±0.00020	18±7
J080623.4−412231[a]	121.597527	−41.375191	0.0	−0.42±0.01	44384.5	4	8489	1.07643±0.01213	0.00765±0.43948	11578±109
J091729.5−115738	139.372877	−11.960586	1.1	−0.54±0.16	63.3	4	19530	0.00930±0.00159	0.00118±0.00281	65±13
J093854.5+355750	144.726951	35.963805	0.9	−1.00±0.17	89.0	4	16307	0.01203±0.00156	0.00100±0.00028	73±11
J094349.1+465526	145.954661	46.923974	0.8	−0.66±0.13	75.2	4	43690	0.00365±0.00050	0.00033±0.00075	81±12
J095736.8+693757	149.403235	69.632570	1.7	−0.45±0.15	22.4	4	24986	0.00217±0.00048	0.00025±0.00083	53±8
J095742.6+693732	149.427501	69.625525	2.7	−1.00±0.25	20.1	4	24986	0.00298±0.00069	0.00036±0.00033	21±8
J104416.5−012350	161.068672	−1.397255	1.4	−0.87±0.14	21.1	4	37547	0.00107±0.00022	0.00009±0.00007	35±8
J104519.5−011619	161.331266	−1.271846	0.7	−0.28±0.11	120.1	4	37547	0.00710±0.00091	0.00078±0.00399	124±14
J105838.7−765133	164.661232	−76.859278	2.0	−1.00±0.08	24.3	4	35368	0.00178±0.00036	0.00006±0.00015	28±7
J110618.9−181953	166.578630	−18.331419	1.3	−0.82±0.14	35.2	4	10640	0.00313±0.00054	0.00025±0.00031	31±5
J111711.4+180727	169.297690	18.124265	1.1	−0.52±0.17	79.3	4	15300	0.00632±0.00085	0.00087±0.00198	59±10
J111944.7+133719	169.936378	13.621823	2.4	−1.00±0.15	25.7	4	44940	0.00195±0.00036	0.00012±0.00047	33±11
J120947.9+393043	182.449710	39.511979	0.7	−0.52±0.11	70.1	4	19699	0.00568±0.00091	0.00047±0.00181	64±10
J121035.0+393123	182.645829	39.523086	0.4	−0.62±0.06	437.5	4	19699	0.01627±0.00125	0.00068±0.00381	218±16
J122741.5+011828	186.922898	1.307663	0.7	−0.44±0.14	34.4	4	10120	0.00751±0.00153	0.00083±0.00291	43±7
J123229.6+641114	188.123452	64.187153	0.1	−0.20±0.04	1370.2	4	28700	0.03751±0.00217	0.00181±0.02493	622±28
J130200.1+274657	195.500491	27.782565	0.1	−0.62±0.02	7004.8	4	22110	0.14273±0.00336	0.00171±0.03364	2116±45
J133055.0+111407	202.729346	11.235243	0.4	−0.11±0.04	2148.6	4	4648	0.26209±0.01380	0.01266±0.21142	700±27
J134624.7+581208	206.603032	58.202214	0.4	−0.19±0.08	322.0	4	28456	0.00905±0.00087	0.00078±0.00621	221±16
J140622.0+222346[a]	211.591487	22.395994	0.1	−0.26±0.02	6781.0	4	3470	0.41632±0.01210	0.00933±0.24555	2137±48
J141711.0+522542	214.295752	52.428203	0.2	−0.60±0.05	514.7	4	51188	0.01257±0.00087	0.00049±0.00316	401±26
J152130.7+074917	230.377835	7.821348	0.1	−0.37±0.02	5729.4	3	35425	0.09960±0.00238	0.00175±0.04602	2607±52
J174645.4−281548	266.689049	−28.263335	0.3	−0.90±0.14	447.1	4	12900	0.00139±0.00011	0.00011±0.00007	298±19
J204045.6−005829	310.190015	−0.974748	1.5	−0.36±0.18	31.7	4	10778	0.00503±0.00102	0.00084±0.00239	40±7
J213658.5−143818	324.243771	−14.638325	2.4	−0.75±0.18	34.9	4	28484	0.00387±0.00067	0.00044±0.00056	26±13
J213804.8−142931	324.520150	−14.491903	2.1	−0.83±0.13	25.4	4	28484	0.00189±0.00034	0.00015±0.00018	29±10
J223440.0−374259	338.666594	−37.716436	0.1	−0.11±0.01	16514.5	3	4489	0.72395±0.01333	0.01220±0.58166	5407±72

Table 4.1: Super Soft X-ray Sources Selected from the 1*XMM-Newton* EPIC Source Catalogue (*Cont.*)

IAUNAME 1XMM	R.A. [Degrees]	Dec [Degrees]	POSITION ERROR [arc seconds]	EPN HR1	EPN DET ML	SUMM FLAG	GTI [S]	EPN RATE b1 [cts s^{-1}]	EPN RATE b2 [cts s^{-1}]	EPN TOTAL COUNTS [cts]
J231439.2−424243	348.663224	-42.711855	0.2	-0.22 ± 0.05	814.9	3	33341	0.01848 ± 0.00107	0.00091 ± 0.01178	548 ± 25

List of sources in 1XMM that match the criteria for SSXs as defined in Section 4.2.1. The list is ordered by right ascension. The 'IAUNAME 1XMM' column contains, when prefixed with "1XMM", the IAUNAME source name. 'R.A.' and 'Dec' are given in decimal degrees. 'POSITION ERROR', in arc seconds, is the 1σ positional error, given as RADEC_ERR in 1XMM. 'EPN HR1' is the 1XMM first hardness ratio as defined by Equation 4.1. 'EPN DET_ML' and 'SUMM_FLAG' are the broad-band EPN DET_ML and SUMM_FLAG values, respectively, calculated by EMLDETECT during source detection. 'GTI' is the good time interval exposure time, in seconds, for the observation in which the source was detected. 'EPN RATE' gives the EPN count rates, in counts s $^{-1}$, for b1 and b2, respectively, calculated during source detection. 'EPN TOTAL COUNTS' is the total detected counts in the EPN broad-band ($0.2-12$ keV). a – target of the pointed observation.

THIN, relating to their relative thicknesses. The thicker the filter, the brighter an optical source has to be before it becomes problematic. The THICK, MEDIUM and THIN filters will safely remove optical photons from sources with V-band magnitudes of 0, 7 and 12 mags, respectively. The point spread function (PSF) of an optically loaded source detected by the EPN camera does not look like that of a true X-ray source; it is decidedly box-like.

In addition to searching for spurious sources, the location of each source with respect to the chip edges was noted. After visually inspecting each source, a final list of SSXs from 1XMM that were deemed to be real remained. This final list contained a total of 53 sources.

Table 4.1 lists the final 53 sources, along with some of their more important X-ray information, including their corrected positional coordinates, as given in 1XMM. Of the final 53 SSXs, only 5 were the target of the observation.

4.2.2 1XMM SSXs Sample Cross-Correlation

As with any survey, the aim is to determine the nature of the sources that have been selected. In this case, the process began by cross-correlating the final list of 53 SSXs from 1XMM with other survey catalogues at different wavelengths. The catalogues searched were: SIMBAD, USNO-B1.0 (Monet et al., 2003), GSC-II (McLean et al., 2000), APM (McMahon et al., 2000), 2MASS (Skrutskie et al., 2006) and SDSS DR3 (Abazajian et al., 2005). Imaging and catalogue data from SC and the INT-WFS were also used to identify possible optical counterparts to the selected SSXs. These catalogues were chosen in some instances for their all-sky coverage and others for their limiting magnitudes. Using such a large number of catalogues for cross-correlation allows for a greater chance of matching and identifying as many sources as possible.

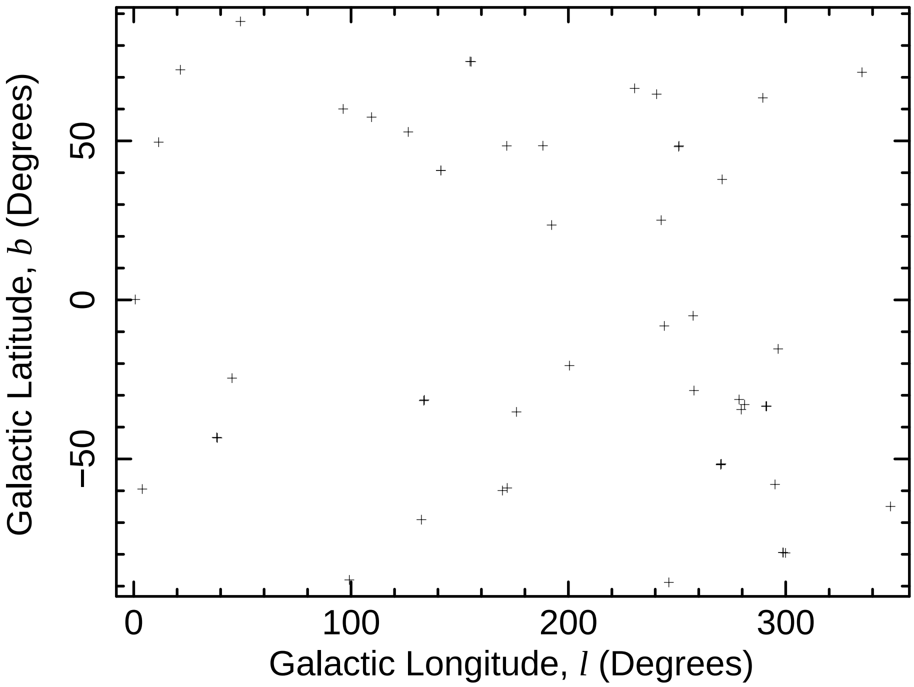

FIGURE 4.2: Galactic coordinates of the selected 53 1XMM SSXs sample.

Before cross-correlation of the SSXs to the other catalogues was performed, the Galactic coordinates of the SSXs were plotted to give an indication of their location. Figure 4.2 shows the Galactic coordinates (l, b) of the 53 selected SSXs and indicates that their positions appear randomly across the sky, i.e., they are not clustered in the Galactic plane.

A value of 10 arc seconds was chosen as the standard search radius for cross-correlation, which encompasses three times the 1XMM 1σ positional error for all sources. Table 4.2 summarises the search results, detailing the number and types, including redshift ranges, of the SIMBAD candidate counterparts returned. Tables 4.3 and 4.4 contain the full search results. Under each catalogue heading, there is a column named ‘arcsec’. The values in this column state the separation in arc seconds between the X-ray source position and the nearest candidate counterpart within 10 arc seconds for that particular catalogue. The ‘Mag’ columns under each catalogue heading contain the magnitudes

Table 4.2: 1XMM SSXs Cross-Correlation Summary

Results		Total
SIMBAD		
Type	Redshift Range	
Stars	–	3
vs	–	1
CV	–	1
PN	–	1
INS	–	1
xb	–	1
eml	$0.024-0.983$	3
Sy1	$0.098-0.141$	2
QSOs	$0.743-2.260$	4
xs	–	5
Number of SSXs with candidate counterparts including SIMBAD results		40
Number of SSXs with no candidate counterparts		13
Total		53

Summary of 1XMM SSXs cross-correlation searches. Acronyms used: vs – Variable Star; CV – cataclysmic variable; PN – Planetary Nebula; INS – Isolated Neutron Star; xb – X-ray Binary; eml – Emission Line Galaxy; Sy1 – Type 1 Seyfert Galaxy; QSO – Quasi Stellar Object; xs – X-ray source of unknown nature.

for that object taken from that catalogue, when given. Within the SDSS search results (Table 4.3), the second value in the third 'Mag' column is the spectroscopic redshift, denoted as 'z='. Under the INT-WFS heading in Table 4.4, the celestial coordinates of the nearest object, within 10 arc seconds, are given along with its magnitude. Also stated under this heading is whether there were any INT-WFS data available containing the SSXs coordinates. Finally, the SIMBAD columns include the classification, 'TYPE', and redshift, 'z', where available, for known sources. The acronyms used within the tables are given in the caption of each table.

Table 4.3: Cross-Correlation of Super Soft X-ray Sources – part I

IAUNAME	USNO		APM		GSC-II		2MASS		SDSS			
1XMM	arcsec	Mag	arcsec	Mag	arcsec	Mag	arcsec	Mag	arcsec	Mag	Mag	Mag
J004755.3−251907	-	-	-	-	-	-	-	-	-	-	-	-
J005413.0−373308	-	-	-	-	-	-	-	-	-	-	-	-
J005511.0−373855	-	-	-	-	-	-	-	-	-	-	-	-
J005520.2−374018	-	-	-	-	-	-	-	-	-	-	-	-
J005555.6−274633	0.8	8.14B 5.32R	-	-	0.8	8.32Bj -	0.8	2.98J 2.20H	-	-	-	-
J010459.3−062846	1.1	20.41B 19.30R	-	-	-	-	-	-	-	-	-	-
J012323.9−583834	1.6	- 19.61R	-	-	-	-	-	-	-	-	-	-
J013304.7+302107	-	-	6.4	22.02b 19.94r	-	-	-	-	-	-	-	-
J013409.9+303221	-	-	3.0	21.25b 20.00r	-	-	-	-	-	-	-	-
J021721.7−050630	1.3	20.26B 19.65R	-	-	-	-	-	-	-	-	-	-
J022255.9−051352	0.6	19.16B 19.12R	-	-	0.39	18.83Bj 18.38R	-	-	-	-	-	-
J031505.5−550946	-	-	-	-	-	-	-	-	-	-	-	-
J031559.1−552638	1.1	21.70B 18.49R	-	-	9.7	18.79Bj 17.65R	-	-	-	-	-	-
J031605.7−551539	1.9	21.62 18.52R	-	-	-	-	-	-	-	-	-	-
J033754.9+095555	3.4	10.19B 7.16R	3.3	11.65b 20.00r	3.4	10.41Bj -	3.5	4.59J 3.58H	-	-	-	-
J043151.9−780011	0.4	19.51 18.66R	-	-	-	-	-	-	-	-	-	-
J043328.3−780713	4.2	18.61 18.53R	-	-	4.3	18.71Bj 18.25R	-	-	-	-	-	-
J043447.9−775214	-	-	-	-	-	-	-	-	-	-	-	-
J050803.2−684017	1.2	14.29B 12.38R	-	-	0.5	- 14.40R	0.8	15.88J 14.27H	-	-	-	-
J051541.5+010439	2.3	15.23B 14.86R	3.3	16.23b 14.73r	2.1	15.92Bj 16.16R	2.0	14.22J 13.66H	-	-	-	-
J052214.9−701657	6.4	17.43B 18.81R	-	-	-	-	-	-	-	-	-	-
J054334.2−682223	0.3	16.45B 17.19R	-	-	0.6	17.19Bj 17.25R	-	-	-	-	-	-
J060011.5−501831	0.8	20.60B 20.30R	-	-	-	-	-	-	-	-	-	-
J072024.9−312551	5.6	19.88B 19.92R	-	-	-	-	-	-	-	-	-	-
J074602.6+280110	-	-	-	-	-	-	-	-	-	-	-	-
J080623.4−412231	7.4	19.92B 18.98R	-	-	8.1	17.90Bj 16.23R	8.2	15.46J 14.96H	-	-	-	-
J091729.5−115738	6.7	8.32B 6.49R	-	-	6.7	8.42Bj -	6.8	5.31J 4.87H	-	-	-	-
J093854.5+355750	-	-	-	-	-	-	-	-	4.3	25.3u 24.7i	25.8g 21.3z	24.3r -
J094349.1+465526	0.9	21.67B 19.18R	0.8	21.53b 19.92r	-	-	-	-	0.2	23.2u 19.3i	21.6g 18.9z	19.9r -
J095736.8+693757	-	-	-	-	-	-	-	-	8.1	22.8u 20.1i	22.8g 19.7z	21.2r -
J095742.6+693732	-	-	9.8	21.19b 19.96r	-	-	-	-	5.0	23.2u 20.2i	22.3g 19.7z	20.8r -
J104416.5−012350	-	-	-	-	-	-	-	-	8.1	25.9u 20.7i	22.8g 20.6z	21.6r -
J104519.5−011619	1.7	19.23B 19.02R	1.6	19.36b 19.01r	2.0	18.89Bj -	-	-	1.8	19.2u 18.9i	19.0g 18.7z	18.8r -
J105838.7−765133	-	-	-	-	-	-	-	-	-	-	-	-
J110618.9−181953	-	-	-	-	-	-	-	-	-	-	-	-
J111711.4+180727	-	-	-	-	-	-	-	-	-	-	-	-
J111944.7+133719	-	-	-	-	-	-	-	-	-	-	-	-
J120947.9+393043	1.8	20.97B 20.20R	2.2	21.16b 20.00r	-	-	-	-	2.1	21.1u 20.4i	20.8g 20.4z	20.6r -
J121035.0+393123	0.1	20.46B 19.65R	0.1	21.74b 19.17r	-	-	-	-	0.2	22.0u 19.1i	20.5g 18.8z	19.5r -
J122741.5+011828	-	-	-	-	-	-	-	-	2.0	23.6u 21.3i	22.5g 20.8z	22.1r -
J123229.6+641114	1.4	17.79B 17.45R	1.3	17.90b 17.07r	1.2	18.22Bj 17.69R	1.4	16.48J 15.61H	1.4	18.3u 17.9i	18.0g 17.8z	17.9r z=0.74
J130200.1+274657	0.4	12.98B 12.07R	0.6	13.37b 12.37r	0.8	13.03Bj 12.18R	0.1	14.23J 13.37H	0.6	16.9u 14.7i	15.4g 14.5z	14.9r -
J133055.0+111407	0.2	18.21B 17.84R	0.2	19.39 18.18r	0.3	18.12Bj 17.39R	0.1	16.41J 15.47H	0.6	19.3u 17.5i	18.5g 17.3z	17.9r -

Table 4.3: Cross-Correlation of Super Soft X-ray Sources – part I (*Cont.*)

IAUNAME	USNO		APM		GSC-II		2MASS		SDSS			
1XMM	arcsec	Mag	arcsec	Mag	arcsec	Mag	arcsec	Mag	arcsec	Mag	Mag	Mag
J134624.7+581208	1.1	19.38B 19.32R	1.4	19.57b 18.82r	-	-	-	-	1.2	20.5u 19.8i	20.0g 19.8z	20.0r -
J140622.0+222346	1.9	15.85B 14.94R	1.6	15.89b 15.15r	1.5	14.88Bj 14.62R	1.6	14.80J 14.03H	1.3	16.3u 15.7i	16.0g 15.9z	16.0r -
J141711.0+522542	1.2	21.73B 19.76R	2.8	21.90b 19.31r	-	-	-	-	1.1	24.7u 19.4i	21.6g 18.9z	20.0r -
J152130.7+074917	0.5	20.25B -	-	-	-	-	-	-	0.8	22.4u 19.5i	21.1g 19.2z	19.9r -
J174645.4−281548	-	-	-	-	-	-	2.1	15.39J 9.96H	-	-	-	-
J204045.6−005829	1.9	19.38B 19.573B	-	-	-	-	-	-	1.8	20.5u 19.8i	19.9g 19.6z	19.9r z=2.24
J213658.5−143818	-	-	-	-	-	-	-	-	-	-	-	-
J213804.8−142931	-	-	-	-	-	-	-	-	-	-	-	-
J223440.0−374259	0.9	17.56B 15.41R	-	-	0.9	16.42Bj 16.32R	1.2	15.50J 14.67H	-	-	-	-
J231439.2−424243	0.7	23.52B 19.59R	-	-	-	-	-	-	-	-	-	-

The results of the cross-correlation of the 1XMM SSXs sample with the USNO-B1.0, APM, GSC-II, 2MASS and SDSS DR3 catalogues. The offset of the optical source position from the X-ray source coordinates is given in arc seconds under the 'arcsec' headings. Optical magnitudes and wavebands are given under the 'Mag' headings. If available, SDSS redshifts are given in the third 'Mag' column under the SDSS heading and are denoted with 'z='.

Figure 4.3 shows example EPN X-ray image cutouts (2×2 arc minutes^2) of two SSXs in the 1XMM sample and two optical image cutouts (1×1 arc minutes^2), one from the INT-WFS and the other from SC, for the same regions of sky centred on the X-ray source positions. The left hand images are centred on the X-ray source 1XMM J123229.6+641114 (top left image in Figure 4.3). A candidate optical counterpart can be seen in the INT-WFS i-band image (bottom left image in Figure 4.3) and is marked by the red cross. However, in the SC B_J-band optical image (bottom right image in Figure 4.3), which is centred on 1XMM J004755.3−251907 (top right image in Figure 4.3), no optical candidate counterpart can be seen within the red 10 arc second radius circle down to a limiting magnitude of $\mathrm{B}_J = 22.5$ mag. The two X-ray sources shown in Figure 4.3 lie on chip gaps of the EPN detector. The number of SSXs in 1XMM that lie on chip edges is 17. It is possible that these sources were included in the 1XMM SSXs sample as a result

Table 4.4: Cross-Correlation of Super Soft X-ray Sources – part II

IAUNAME	SC			INT-WFS				SIMBAD		
1XMM	arcsec	Mag	Mag	Data	RA	DEC	Mag	arcsec	TYPE	z
J004755.3 − 251907	-	-	-	no	-	-	-	-	-	-
J005413.0 − 373308	-	-	-	no	-	-	-	-	-	-
J005511.0 − 373855	4.8	19.2I	-	no	-	-	-	3.0	xs	-
J005520.2 − 374018	-	-	-	no	-	-	-	-	-	-
J005555.6 − 274633	1.8	-	10.6R	no	-	-	-	0.6	vs	-
J010459.3 − 062846	1.4	21.8B	19.3R	yes	01:04:59.35	-06:28:45.6	19.7r	-	-	-
J012323.9 − 583834	1.2	22.0B	20.0R	no	-	-	-	-	-	-
J013304.7 + 302107	-	-	-	yes	01:33:04.78	+30:21:07.2	18.5V	0.6	xs	-
J013409.9 + 303221	-	-	-	yes	01:34:10.14	+30:32:21.5	21.3V	0.6	xs	-
J021721.7 − 050630	1.1	20.7B	19.0R	yes	02:17:21.7	-05:06:28.8	20.3V	6.0	QSO	0.983
J022255.9 − 051352	0.7	19.0B	18.2R	yes	02:22:55.88	-05:13:51.5	18.4r	-	-	-
J031505.5 − 550946	-	-	-	no	-	-	-	-	-	-
J031559.1 − 552638	1.2	21.6B	20.2R	no	-	-	-	1.2	eml	0.983
J031605.7 − 551539	1.7	21.4B	20.4R	no	-	-	-	1.2	eml	0.636
J033754.9 + 095555	-	-	-	no	-	-	-	3.6	star	-
J043151.9 − 780011	0.9	20.1B	18.7R	no	-	-	-	-	-	-
J043328.3 − 780713	4.6	19.0B	18.1R	no	-	-	-	-	-	-
J043447.9 − 775214	-	-	-	no	-	-	-	-	-	-
J050803.2 − 684017	3.4	15.1B	13.2R	no	-	-	-	7.2	PN	-
J051541.5 + 010439	1.5	15.5B	15.1R	no	-	-	-	1.2	cv	-
J052214.9 − 701657	4.1	21.1B	-	no	-	-	-	-	-	-
J054334.2 − 682223	0.3	19.6B	-	no	-	-	-	5.4	xb	-
J060011.5 − 501831	0.7	20.7B	19.5R	no	-	-	-	-	-	-
J072024.9 − 312551	5.5	20.4B	19.5R	no	-	-	-	1.2	star	-
J074602.6 + 280110	-	-	-	no	-	-	-	-	-	-
J080623.4 − 412231	-	-	-	no	-	-	-	5.4	INS	-
J091729.5 − 115738	2.8	16.8B	14.9R	no	-	-	-	6.6	star	-
J093854.5 + 355750	-	-	-	yes	-	-	-	-	-	-
J094349.1 + 465526	-	-	-	yes	-	-	-	-	-	-
J095736.8 + 693757	-	-	-	yes	-	-	-	6.6	xs	-
J095742.6 + 693732	-	-	-	yes	-	-	-	-	-	-
J104416.5 − 012350	-	-	-	no	-	-	-	-	-	-
J104519.5 − 011619	1.6	18.9B	18.8R	no	-	-	-	1.2	QSO	0.940
J105838.7 − 765133	-	-	-	no	-	-	-	-	-	-
J110618.9 − 181953	-	-	-	no	-	-	-	-	-	-
J111711.4 + 180727	-	-	-	yes	-	-	-	-	-	-
J111944.7 + 133719	-	-	-	no	-	-	-	-	-	-
J120947.9 + 393043	-	-	-	no	-	-	-	-	-	-
J121035.0 + 393123	-	-	-	no	-	-	-	-	-	-
J122741.5 + 011828	5.0	21.8B	20.2R	no	-	-	-	-	-	-
J123229.6 + 641114	-	-	-	yes	12:32:29.73	+64:11:15.3	17.6U	1.2	QSO	0.743
J130200.1 + 274657	-	-	-	no	-	-	-	0.6	eml	0.024
J133055.0 + 111407	-	-	-	no	-	-	-	8.4	xs	-
J134624.7 + 581208	-	-	-	yes	13:46:24.68	+58:12:09.5	19.6U	-	-	-
J140622.0 + 222346	-	-	-	yes	14:06:22.15	22:23:45.3	22.1r	1.2	Sy1	0.098
J141711.0 + 522542	-	-	-	yes	14:17:11.06	+52:25:40.9	20.3r	-	-	-
J152130.7 + 074917	-	-	-	yes	15:21:30.74	+07:49:16.9	19.9r	-	-	-
J174645.4 − 281548	4.9	-	20.9B	no	-	-	-	-	-	-
J204045.6 − 005829	1.8	20.3B	20.0R	yes	20:40:45.69	-00:58:27.5	19.4r	1.8	QSO	2.26
J213658.5 − 143818	-	-	-	yes	-	-	-	-	-	-
J213804.8 − 142931	4.7	-	19.4R	yes	-	-	-	-	-	-
J223440.0 − 374259	0.7	18.1B	16.7R	no	-	-	-	1.2	Sy1	0.141
J231439.2 − 424243	1.2	-	20.1R	no	-	-	-	-	-	-

The results of the cross-correlation of the 1XMM SSXs sample with the SC, INT-WFS and SIMBAD catalogues. The offset of the optical source position from the X-ray source position is given in arc seconds under the 'arcsec' headings, and optical magnitudes and wavebands are given under the 'Mag' headings. Acronyms used: CV – cataclysmic variable, eml – Emission Line Galaxy, INS – Isolated Neutron Star, xb – X-ray Binary, PN – Planetary Nebula, vs – Variable Star, QSO – Quasi Stellar Object, Sy1 – type 1 Seyfert Galaxy, xs – X-ray source of unknown nature.

of the incorrect calculation of their HR1 values rather than them actually being SSXs. With the exception of the 5 pointed targets in the 1XMM SSXs sample, the X-ray images in Figure 4.3 are representative of the quality (but not position) of the 1XMM SSXs.

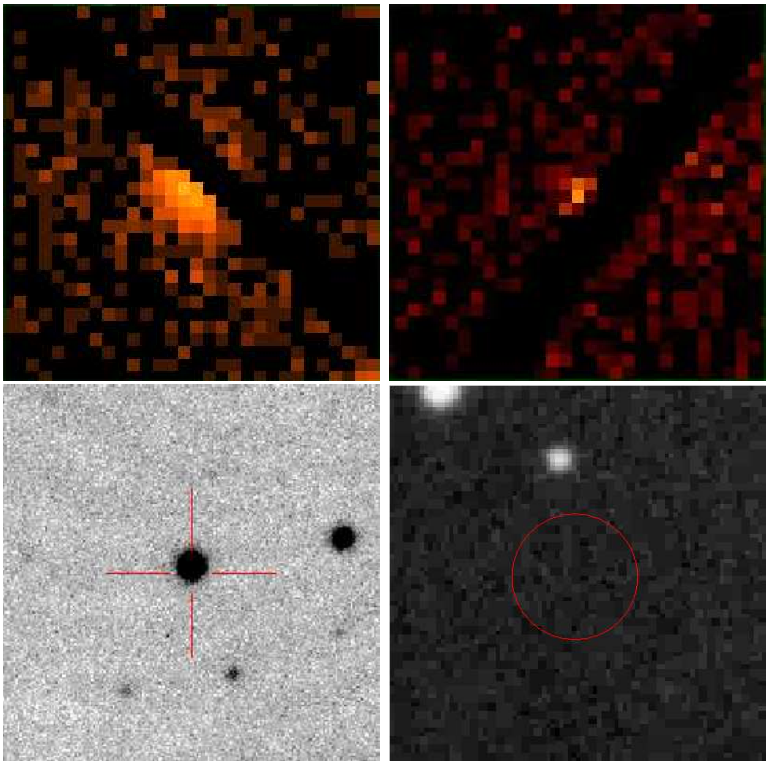

FIGURE 4.3: Top: *XMM-Newton* X-ray image cut-outs (2×2 arc minute^2) of the sources 1XMMJ123229.6+641114 (left) and 1XMMJ004755.3–251907 (right). Bottom: optical image cut-outs (1×1 arc minute^2) centred on the X-ray positions. The optical image of 1XMMJ123229.6+641114 is an INT-WFC i-band image with the red cross centred on the X-ray position. A candidate counterpart can be seen lying near the centre of the cross. The optical image for 1XMMJ004755.3−251907 is a B_J-band image from SC. The red 10 arc second radius circle is centred on the X-ray coordinates of 1XMMJ004755.3−251907. There are no optical candidates within the circle down to a limiting magnitude of $\mathrm{B}_J = 22.5$ mag.

The results of the cross-correlation (Table 4.2) show that of the 53 SSXs, 40 have a minimum of 1 candidate counterpart within a 10 arc second search radius. Of the 40 sources, 17 were previously identified sources within SIMBAD, with an additional 5 sources identified as X-ray sources of an unknown nature (xs) within SIMBAD.

The number of SSXs with unclassified candidate counterparts from the catalogue searches is therefore 23 (including the 5 xs). Of the 13 SSXs with no candidate counterparts within a 10 arc second search radius, 2 sources (1XMMJ111711.4+180727 and

1XMMJ213658.5$-$143818) have been observed as part of the INT-WFS. In the case of 1XMMJ213658.5$-$143818, there is a bright, stellar-like object at a distance of ~ 12 arc seconds from the X-ray source position in all the INT-WFS images. Also, in the case of 1XMMJ111711.4+180727, there is a faint, point-like object ~ 15 arc seconds from the X-ray source position in the g-band INT-WFS images. It should be noted that the SC imaging data covers all SSXs source positions with limiting magnitudes of $\mathrm{B}_J = 22.5$ and $\mathrm{R} = 21.5$, depending on the surveys used to produce the images.

Of the 17 SSXs that lie on chip edges, 14 have a minimum of one candidate counterpart within a 10 arc second search radius. Of the 14 with candidate counterparts, 4, 8 and 11 of the SSXs have a candidate counterpart within a distance of 1, 2 and 5 arc seconds, respectively. It is likely that the SSXs that lie on chip edges and that have a candidate counterpart are real X-ray sources, particularly those with candidate counterparts within 1 arc second. However, further investigation of the X-ray properties of these sources are required to confirm their super soft nature.

The candidate counterparts returned by the SIMBAD 10 arc second searches that had previously been classified were of both Galactic and extragalactic origin. Galactic candidate counterparts ranged from stars, CVs (type G2) and variable stars (type M0III) to PN and X-ray binaries. The spectral types of the stars matched in the SIMBAD search included K0, K2, and M0V, all of which are possible X-ray emitters (Rosner et al., 1985). Reassuringly, a previously identified INS was detected in the SSXs sample. This suggests that if other INS were present in the catalogue, the selection criteria used here would include them in this sample.

The extragalactic candidate counterparts account for approximately 40% of the previously classified candidate counterparts. Of these, there are three types of sources returned; QSOs, type 1 Seyfert galaxies (Sy1s) and emission line galaxies (eml). Interestingly, the extragalactic candidate counterparts had, on average, a smaller offset from the X-ray position coordinates than the Galactic candidate counterparts. The largest redshift for each type of extragalactic object is 2.26, 0.141 and 0.983, respectively.

To summarise, there are different types of objects, both Galactic and extragalactic, that could be possible candidate counterparts to the sample of SSXs selected from 1XMM. The true nature of these SSXs will only become apparent when a larger fraction of the currently unknown SSXs candidate counterparts have been identified.

4.3 1XMM SSXs Optical Spectra

The identification of the unknown SSXs with candidate optical counterparts became a priority. By increasing the number of classified SSXs, statistical limits can be placed on the true nature of SSXs, especially with regards to extragalactic sources. A sample list of possible candidates to observe was drawn up. These candidates were selected on their likelihood of being a real source, whether they were observable (date dependent) with the William Herschel Telescope (WHT) and whether they were within the magnitude limits of the telescope. In addition to the unclassified candidate counterparts chosen, three previously classified candidate counterparts were included, to act as a control group for the spectral analysis and to confirm their classification. The final list of the 14 candidates observed is shown in Table 4.5.

4.3.1 Observations and Data Reduction

The optical data were acquired using the Intermediate dispersion Spectrograph and Imaging System (ISIS) instrument on the WHT between the $12^{\rm th}$ and the $14^{\rm th}$ of February 2004, inclusively. A short description of the WHT and ISIS instrumentation, along with the observing set-up, can be found in Section 1.4. During the observing run, both the

Table 4.5: Candidate SSXs Observed with the WHT

IAUNAME 1XMM	R.A.	Dec	Galactic $N_{\rm H}$ [$\times 10^{20}$ cm^{-2}]
J021721.7−050630[a]	02 17 21.71	−05 06 29.7	25.80
J022255.9−051352	02 22 55.91	−05 13 51.6	2.59
J094349.1+465526	09 43 49.12	+46 55 26.3	1.22
J095742.6+693732	09 57 42.60	+69 37 31.9	3.94
J104519.5−011619	10 45 19.50	−01 16 18.6	4.10
J120947.9+393043	12 09 47.93	+39 30 43.1	1.99
J121035.1+393123	12 10 35.06	+39 31 22.6	2.00
J123229.6+641114	12 32 29.63	+64 11 13.8	1.96
J130200.1+274657[a]	13 02 00.12	+27 46 57.2	0.95
J133055.0+111407	13 30 55.04	+11 14 06.9	1.93
J134624.7+581208	13 46 24.73	+58 12 08.0	1.29
J140622.0+222346[a]	14 06 21.96	+22 23 45.6	2.10
J141711.0+522542	14 17 10.98	+52 25 41.5	1.30
J152130.7+074917	15 21 30.68	+07 49 16.9	2.99

The list of SSXs observed with the WHT. The Galactic $N_{\rm H}$ values were calculated using the FTOOL nh. a – previously classified sources.

blue (R300B grating) and red (R158R grating) arms of the ISIS instrument were used in conjunction with the 5400 dichroic slide. This gave a total wavelength coverage of $\sim$5000 Å ($\sim$3300 – 8500 Å), with a dispersion of $\sim$120 Å/mm for both arms. Throughout each evening's observing run, the standard calibration exposures, consisting of arcs, flats, biases and standards, were acquired in addition to the target exposures. The observing conditions were not favourable over this period, with a typical seeing for the first two nights of $\sim$ 2 arc seconds, peaking at $\sim$6 arc seconds during the first evening. This resulted in the loss of a large amount of source light whilst using the 1 arc second slit, which severely degraded the quality of the target spectra. The third evening was slightly better with a typical seeing of $\sim$1.2 arc seconds. However, sporadic cloud coverage reduced the amount of observing time and hindered the attempts to re-observe the previous nights' targets.

Reduction of the data was performed using the Image Reduction and Analysis Facility (IRAF; Tody, 1986) software. All of the tasks discussed in the following reduction steps can be found in the IMRED package, which is part of the larger, standard NOAO package written for IRAF.

CCD Reduction

Before any spectral information could be extracted, the data had to be reduced and characteristics due to the CCD removed. Data reduction began by combining the bias images using the task ZEROCOMBINE, which produced an average combined bias image. The task CCDPROC was then run to subtract the combined bias image from each object, standard and arc image, after rescaling the combined bias image to match the bias levels from each object, standard and arc image. The combined bias image was also subtracted from the individual flat images, which were then combined using FLATCOMBINE, resulting in an average combined flat image. The task IMARITH was used to normalise the combined flat image to a value of one. A second pass through CCDPROC was then performed, using the normalised flat image to remove the response of the CCD from each object, standard and arc image. The penultimate step in the reduction of the CCD images was to pass the images through the task BCLEAN, which is part of the Starlink package FIGARO. This removed any cosmic rays that were present in any of the images. Finally, the task FIXPIX was used to smooth out anomalous pixels that had not been removed by BCLEAN. This left object, standard and arc images that were de-biased, flattened and cleaned, ready for their spectral information to be extracted.

Spectral Extraction

Once the CCD characteristics from the data had been removed, the spectral information could then be extracted. The raw spectra from the object, standard and arc images were extracted using the task APALL. Initially, APALL determines the aperture (parallel to the dispersion axis) of the spectral extraction region. Then two background regions, adjacent to the selected aperture, are manually selected. APALL then traces the spectrum along the entire dispersion axis. At the same time, the background spectra are extracted, median combined, modelled and finally subtracted from the source spectrum. This is repeated for all object and standard images. In the case of the arc images, a spectrum is extracted from the appropriate arc image for each individual object and standard spectra. The traces used to extract the object and standard spectra are also used to extract the arc spectra.

Conversion of the dispersion axis into the more tangible wavelength scale was then required. The wavelength calibration was carried out using the spectra extracted from the arc images. By identifying the known emission lines within the various arc spectra, a relationship between pixel position and wavelength was determined. The tasks IDENTIFY and RE-IDENTIFY were used, respectively, to interactively and non-interactively identify the lines within the arc spectra using line lists and annotated images supplied by the observatory. Once the lines had been identified, the dispersion relation was modelled, resulting in a function that described the wavelength scale in terms of pixel position along the dispersion axis. For future tasks to correctly use the databases created by IDENTIFY and RE-IDENTIFY, the object and standard spectral files were associated with the correct arc. The task HEDIT was used to edit the headers of each extracted spectrum accordingly. The task DISPCOR was then used to combine the information in the databases created by the tasks IDENTIFY and RE-IDENTIFY and the individual images to create the final dispersion relation, which was written to the header of each object and standard spectrum.

The final stage of the reduction procedure was to flux calibrate the target spectra using the standard spectra and the known position of the observatory. Firstly, using the time of the observation, source position and observatory location, the task SETAIRMASS calculated the column of air that the light from the target passed through, giving an indication of the amount of absorption from the atmosphere. Following this, the standard spectra were calibrated using the task STANDARD. The expected spectral shape and fluxes of the standard stars were provided by the observatory and are taken from Oke (1990) and Turnshek et al. (1990). The task SENSFUNC was then used to interactively model the ratio between the observed and actual fluxes for each of the standard stars. The appropriate standard model created with SENSFUNC was then applied to each of the target spectra using the task CALIBRATE. This resulted in reduced wavelength and flux calibrated spectra for each arm of the ISIS instrument.

Until now, the reduction and spectral extraction have been performed separately on the data taken with the blue and red arms of the ISIS instrument. Thus, the next step was to create a combined spectrum for each target. The task SCOMBINE was used to combine the spectra taken with the two arms. These individual spectra were finally average combined, producing a single wavelength and flux calibrated spectrum for each object.

4.3.2 Spectral Analysis and Results

The final target spectra were viewed, analysed and classified using standard packages within IRAF. Due to the unfavourable observing conditions (Section 4.3.1) seven of the target spectra suffered from poor signal-to-noise and classification of these targets was not possible, since their spectra showed no apparent features. The spectra of the remaining seven targets are shown in Figures 4.4 to 4.10. The combined ISIS spectrum for each target is plotted in the top panel of Figures 4.4 to 4.10, with the lower panel showing the individual ISIS blue and red arm spectra. The spectra in Figures 4.4 to 4.10 have been re-binned from a scale of ~ 1.8 Å/pixel to a scale of ~ 10 Å/pixel. The classification and line width measurements for the seven targets in Figures 4.4 to 4.10 are shown in Table 4.6.

Two of the seven targets have speculative classifications, whereas the remaining five have good signal-to-noise and include two of the three known targets. Beginning with the two speculative classifications; 1XMM J022255.9$-$051352 and 1XMM J134624.7$+$581208 were both classified as AGN due to the emission line feature at the observed wavelengths of 5170 Å and 5059 Å, respectively. This feature is likely to be the Mg II ($\lambda 2798$) emission line based on the absence of other emission lines in their observed spectra. The resulting redshifts of these two targets are 0.848 and 0.808, respectively. Of the five targets with good signal-to-noise, four were spectroscopically identified as AGN. Two of these four targets, 1XMM J133055.0+111407 ($z = 0.077$) and 1XMM J140622.0+222346 ($z = 0.098$; a known target), had multiple features present in their spectra, whereas the two other targets, 1XMM J104519.5$-$011619 ($z = 0.941$) and 1XMM J123229.6$+$641114 ($z = 0.743$), were classified as AGN by identifying the observed emission line at 5432 Å and 4878 Å, respectively, as the Mg II emission line. The seventh target was spectroscopically identified as an emission line galaxy (1XMM J130200.1$+$274657; the second previously known target; $z = 0.024$).

From Table 4.6 it can be seen that the redshifts of the spectroscopically identified AGN span a large range ($0.077 \leqslant z \leqslant 0.939$) and are consistent with the redshifts of the previously classified optical candidate counterparts identified as AGN during the catalogue searches ($0.098 \leqslant z \leqslant 2.260$; Table 4.2). It can also be seen in Table 4.6 that all but one of the targets classified as AGN (1XMM J104519.5$-$011619; $v_{\rm FWHM} \lesssim$ 3,100 km s^{-1}) are narrow line objects ($v_{\rm FWHM} \lesssim$ 2,400 km s^{-1}). These classifications

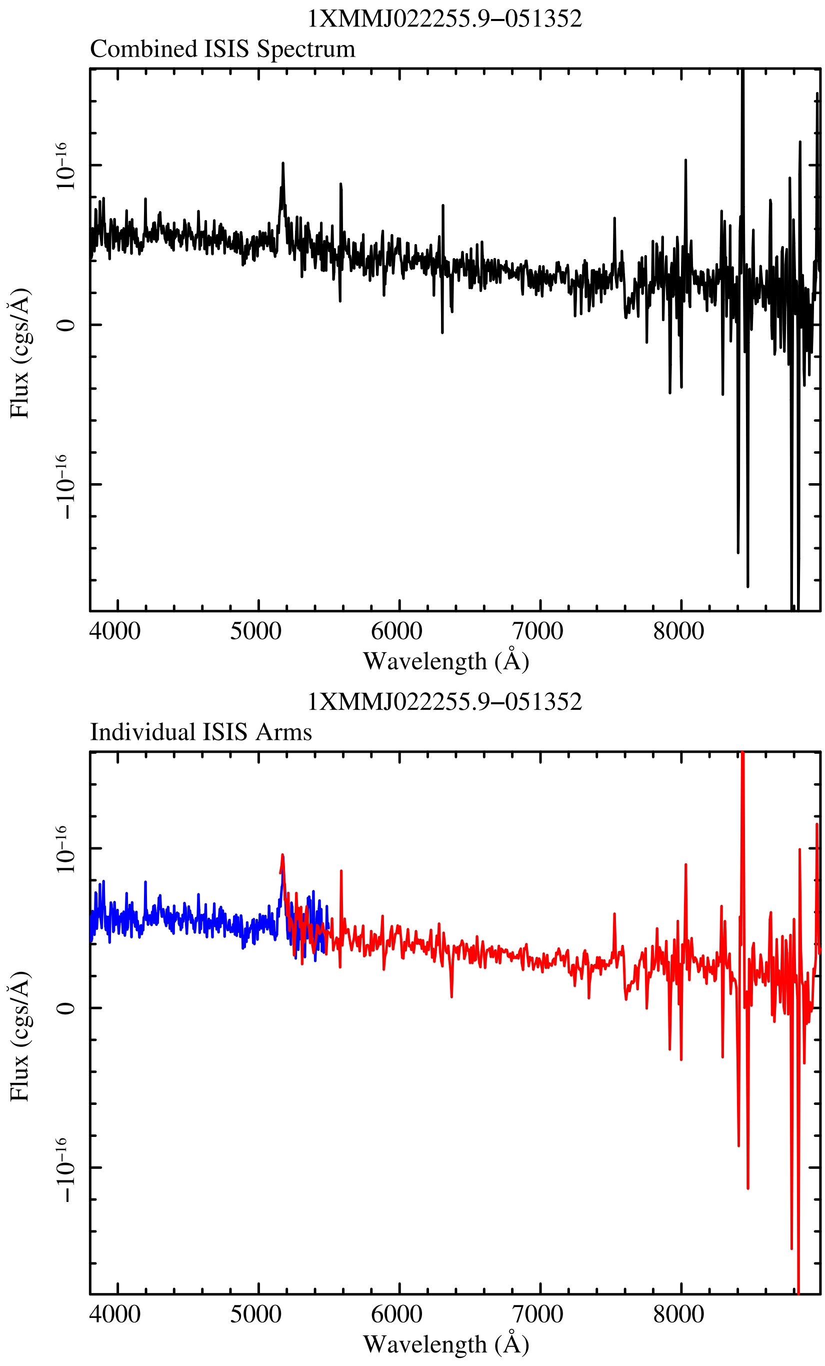

FIGURE 4.4: Flux calibrated, WHT ISIS optical spectra of 1XMM J022255.9−051352. Top: combined ISIS spectrum. Bottom: individual ISIS blue and red arm spectra. The narrow feature at ~ 8400 Å is due to a sky line that has not been properly subtracted from the source spectrum.

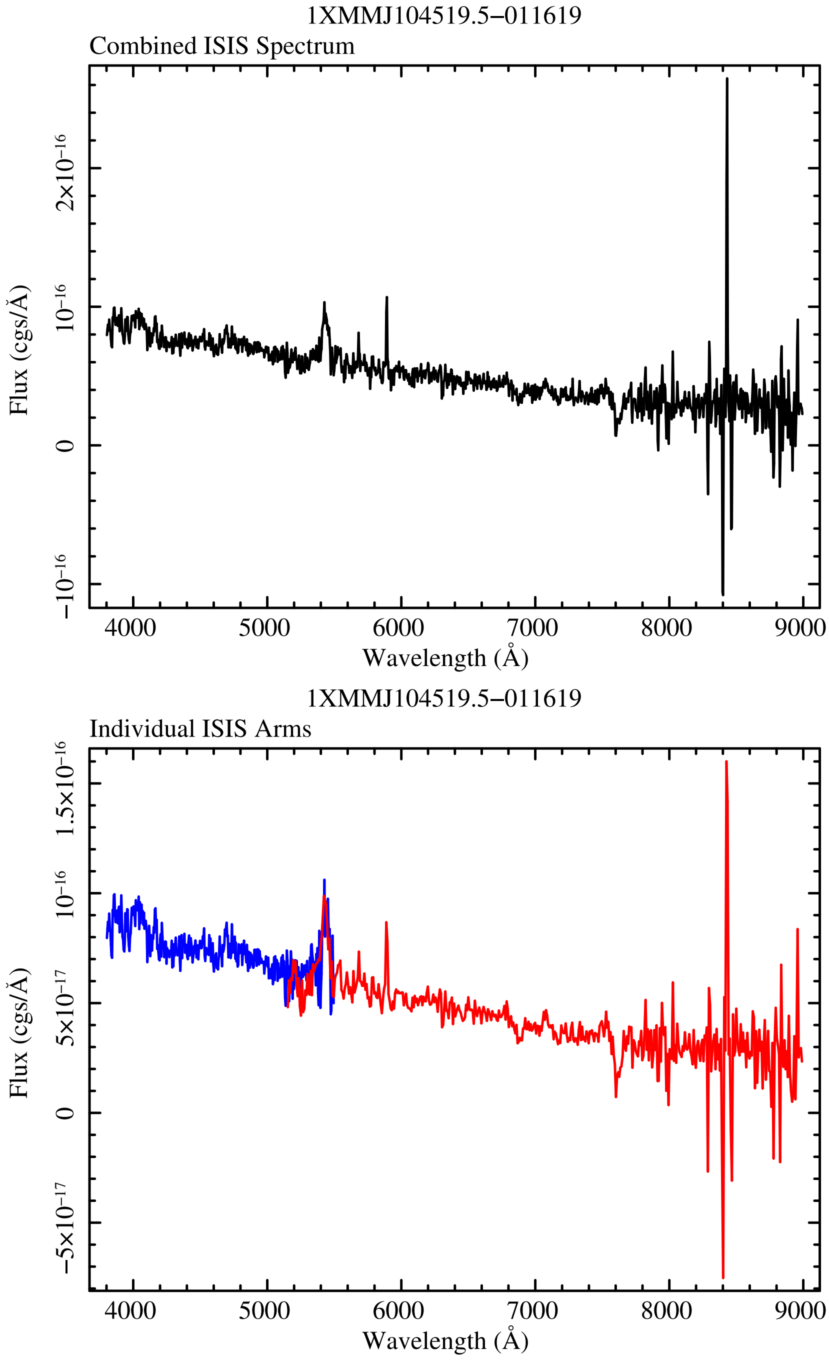

FIGURE 4.5: Flux calibrated, WHT ISIS optical spectra of 1XMM J104519.5−011619. Top: combined ISIS spectrum. Bottom: individual ISIS blue and red arm spectra. The narrow feature at ~ 8400 Å is due to a sky line that has not been properly subtracted from the source spectrum.

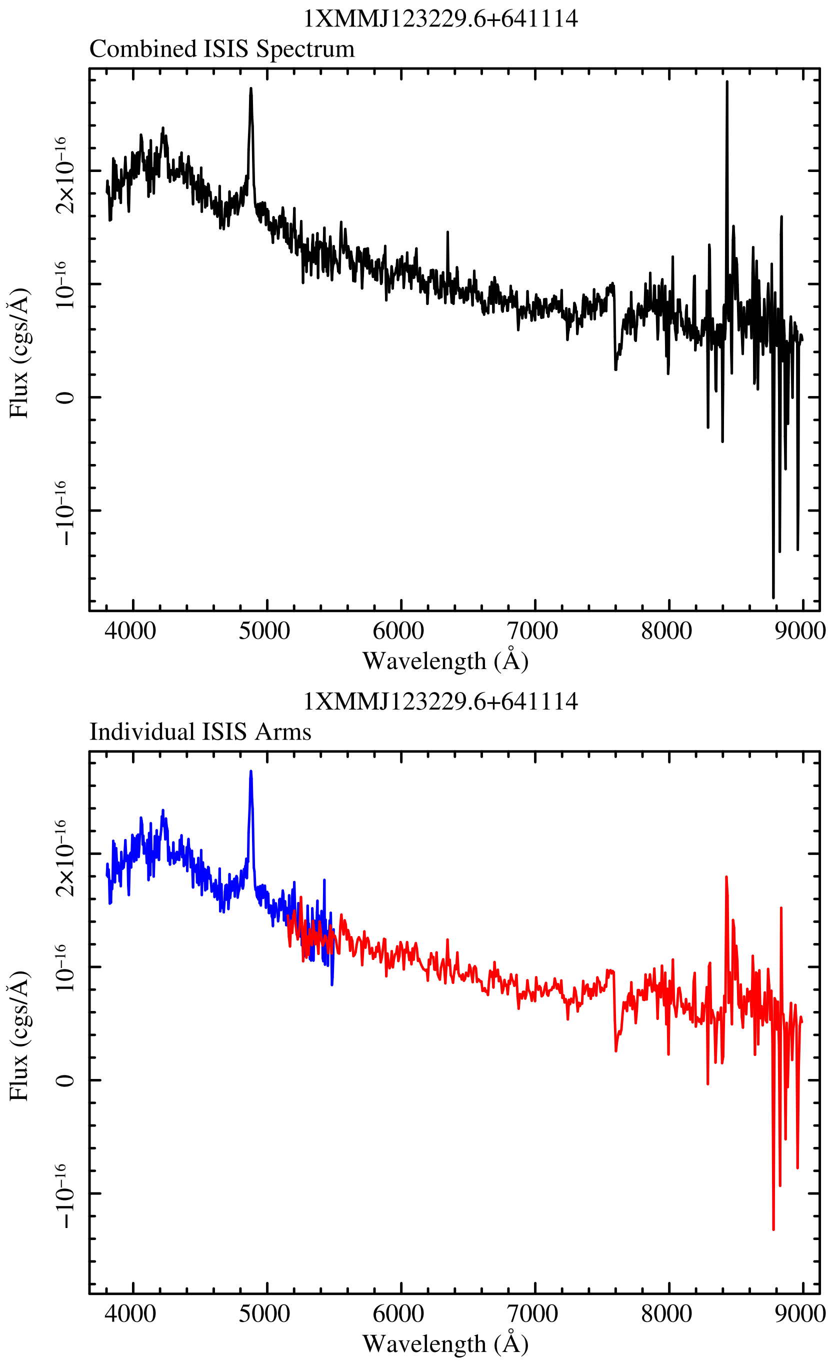

FIGURE 4.6: Flux calibrated, WHT ISIS optical spectra of 1XMM J123229.6+641114. Top: combined ISIS spectrum. Bottom: individual ISIS blue and red arm spectra. The narrow feature at ~ 8400 Å is due to a sky line that has not been properly subtracted from the source spectrum.

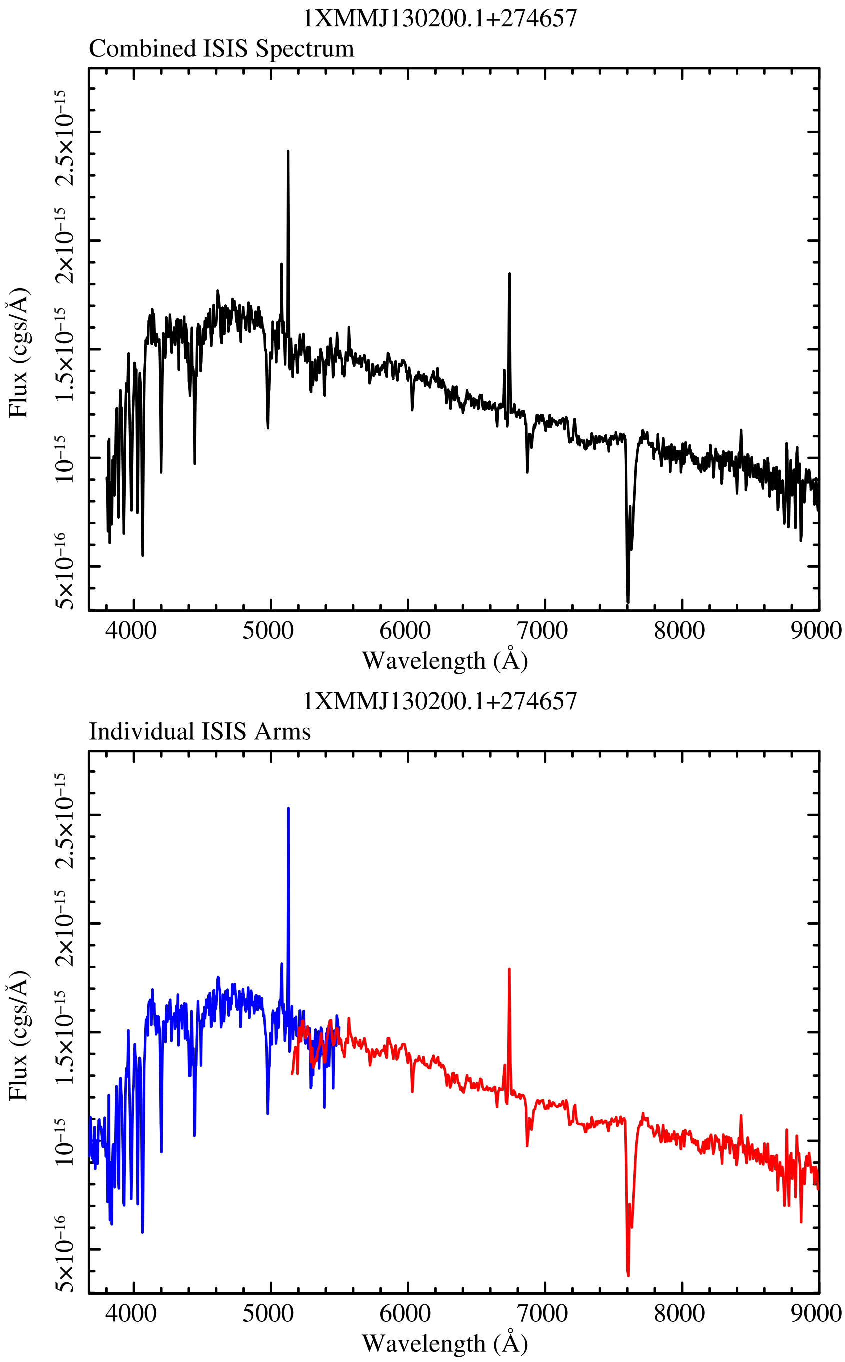

FIGURE 4.7: Flux calibrated, WHT ISIS optical spectra of 1XMM J130200.1+274657. Top: combined ISIS spectrum. Bottom: individual ISIS blue and red arm spectra.

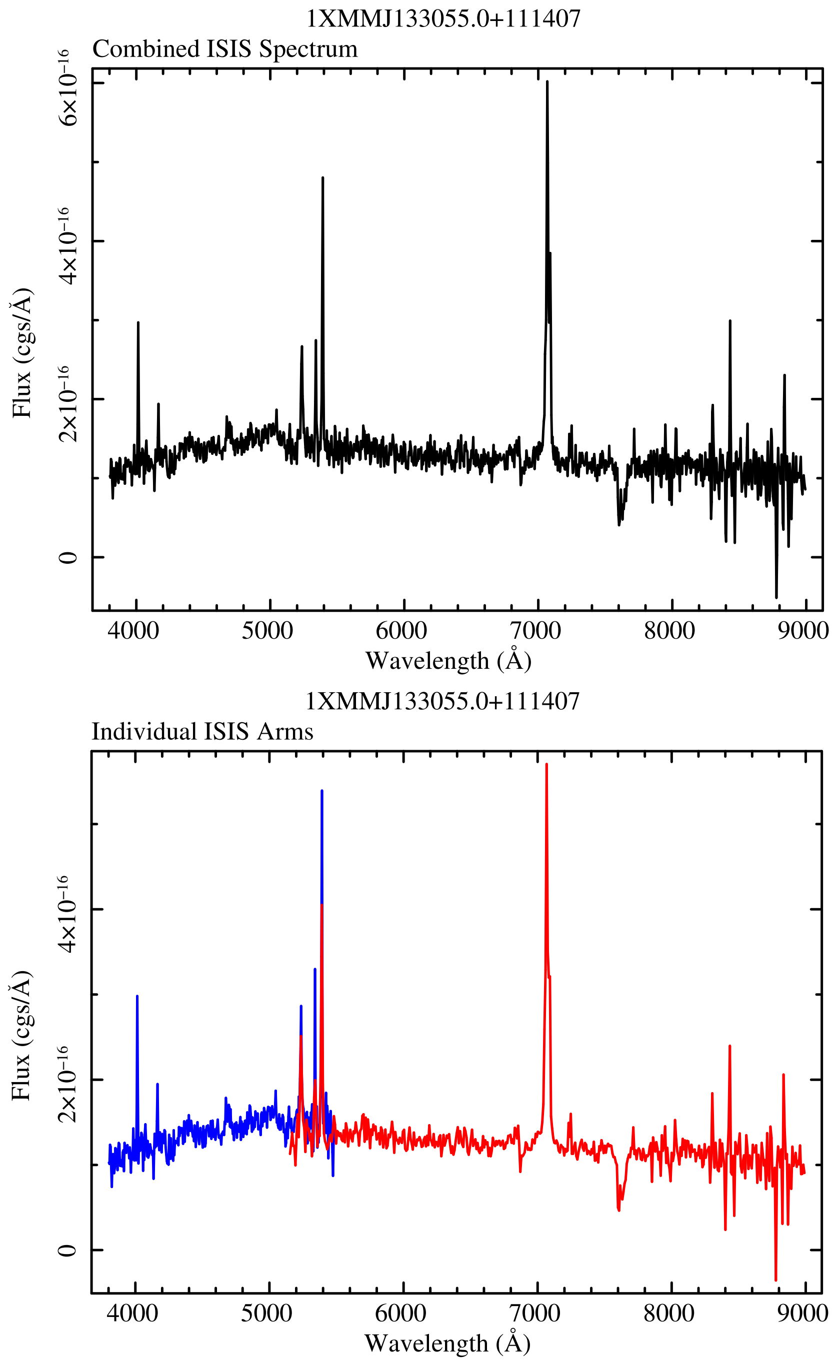

FIGURE 4.8: Flux calibrated, WHT ISIS optical spectra of 1XMM J133055.0+111407. Top: combined ISIS spectrum. Bottom: individual ISIS blue and red arm spectra. The narrow feature at ~ 8400 Å is due to a sky line that has not been properly subtracted from the source spectrum.

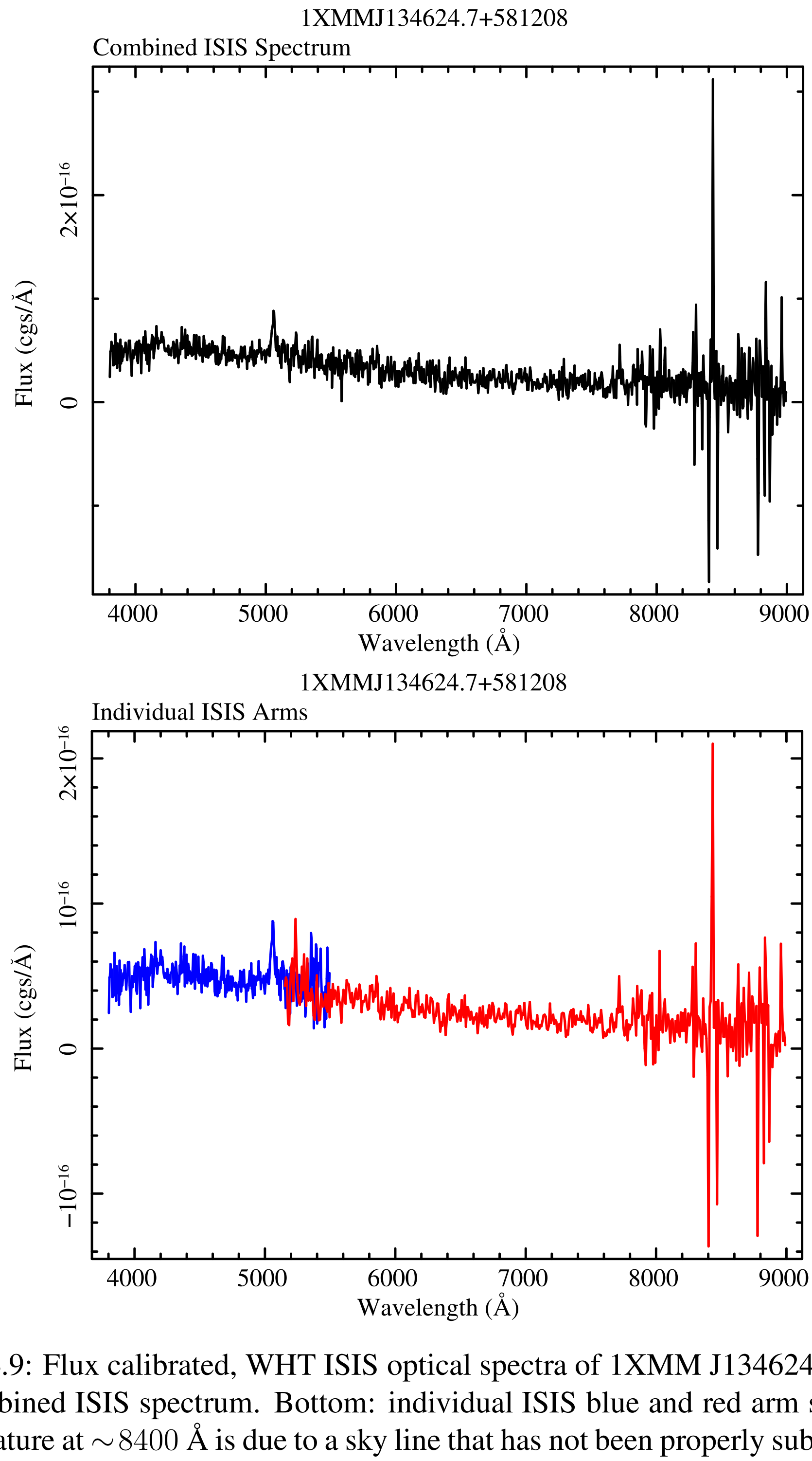

FIGURE 4.9: Flux calibrated, WHT ISIS optical spectra of 1XMM J134624.7+581208. Top: combined ISIS spectrum. Bottom: individual ISIS blue and red arm spectra. The narrow feature at ~ 8400 Å is due to a sky line that has not been properly subtracted from the source spectrum.

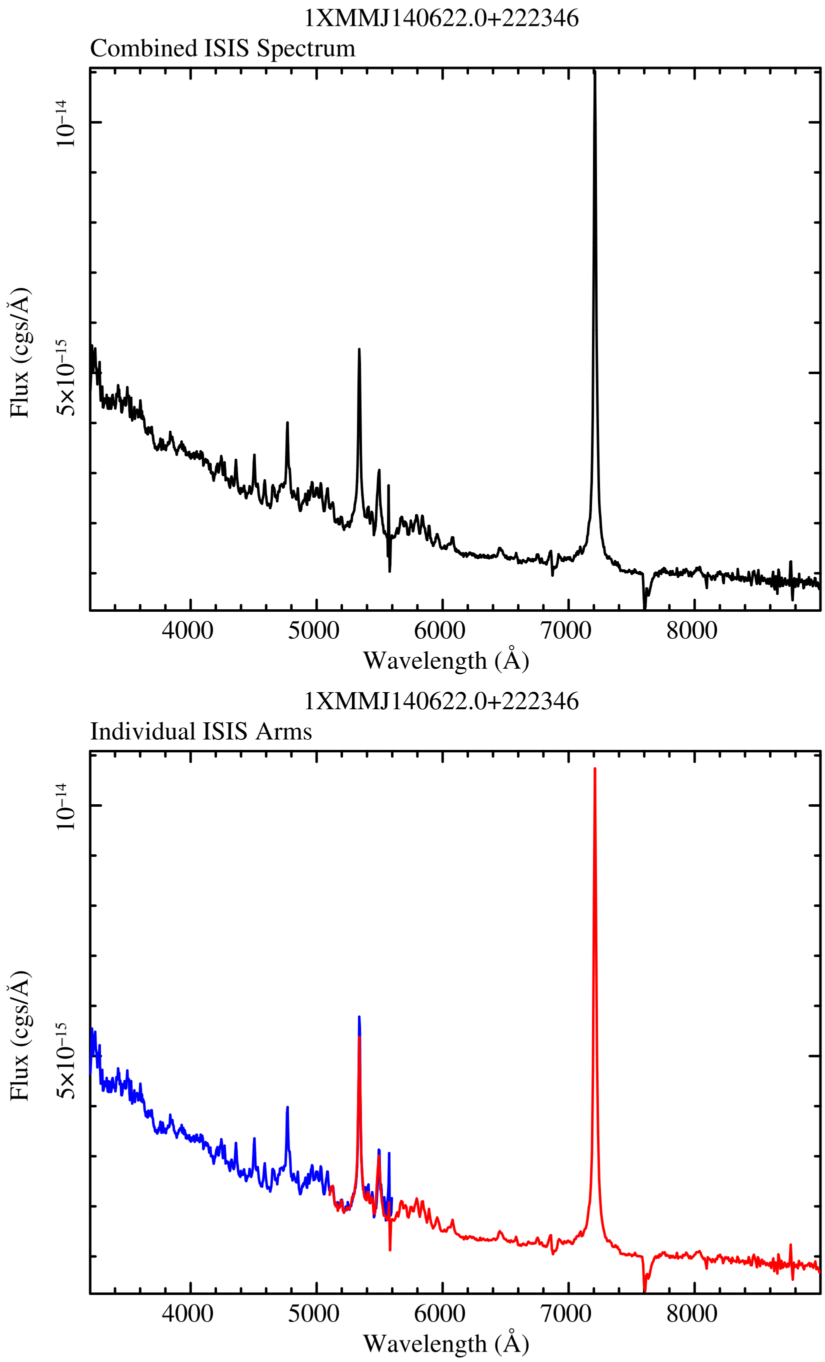

FIGURE 4.10: Flux calibrated, WHT ISIS optical spectra of 1XMM J140622.0+222346. Top: combined ISIS spectrum. Bottom: individual ISIS blue and red arm spectra.

Table 4.6: Optical Spectra Fitting Results

IAUNAME 1XMM	Type	Line ID	λ_c [Å]	$v_{\rm FWHM}$ [km s^{-1}]	Redshift
J021721.7−050630[a]	n/a	-	-	-	-
J022255.9−051352	AGN	Mg II	5170	2,402	0.848
J094349.1+465526	n/a	-	-	-	-
J095742.6+693732	n/a	-	-	-	-
J104519.5−011619	AGN	Mg II	5432	3,079	0.941
J120947.9+393043	n/a	-	-	-	-
J121035.1+393123	n/a	-	-	-	-
J123229.6+641114	AGN	Mg II	4878	2,009	0.743
J130200.1+274657[a]	eml	[O III]	5078	289	0.024
		[O III]	5126	264	
		[N II]	6703	299	
		[N II]	6740	373	
J133055.0+111407	AGN	[O II]	4015	464	0.077
		Hβ	5235	719	
		[O III]	5340	388	
		[O III]	5391	439	
		[N II] & Hα	7069	903	
J134624.7+581208	AGN	Mg II	5059	1,894	0.808
J140622.0+222346[a]	AGN	Hγ	4769	872	0.098
		Hβ	5339	1,079	
		[O III]	5493	1,738	
		Hα	7209	1,037	
J141711.0+522542	n/a	-	-	-	-
J152130.7+074917	n/a	-	-	-	-

Results from the spectroscopic observations of 14 of the 1XMM SSXs candidate counterparts. a – previously classified source. eml – emission line galaxy. For sources with multiple features, the lines are ordered in increasing wavelength.

increase the number of classified candidate counterparts in the 1XMM SSXs list from 17 to 22 ($\sim$42%), with AGN accounting for 11 ($\sim$21%) of these sources.

4.4 2XMM SSXs Sample

The second comprehensive *XMM-Newton* EPIC Serendipitous Source Catalogue (2XMM; Watson et al., 2008; Watson et al., 2009), again compiled by the SSC, was released to the public on the $22^{\rm nd}$ of August 2007. 2XMM consists of sources detected in $3{,}491$ *XMM-Newton* EPIC observations made between the $3^{\rm rd}$ February 2000 and the $31^{\rm st}$ March 2007. The unique area of sky covered by 2XMM is ~ 360 square degrees. All observations that were used in 2XMM were publicly available before the $1^{\rm st}$ of May 2007, although not all public observations before this date were included in 2XMM. The total number of sources within 2XMM is $246{,}897$, of which $191{,}870$ are unique. The median fluxes of the detected sources in the $0.2-12$ keV, $0.2-2$ keV and $2-12$ keV bands are $\sim 2.5\times10^{-14}$ erg s^{-1} cm^{-2}, $\sim 5.8\times10^{-15}$ erg s^{-1} cm^{-2} and $\sim 1.4\times10^{-14}$ erg s^{-1} cm^{-2}, respectively.

There are numerous changes between 1XMM and 2XMM, mostly due to different data processing techniques and the information provided for each source. However, out of all the various changes, only one is of concern here; the way in which the EPIC $0.2-12$ keV bandpass is divided. There are still five bands, however, the energy ranges have been changed slightly. This was done in an attempt to extract more information from the most sensitive 1XMM band ($0.5-2$ keV). The bands in 2XMM are quoted as: band 1 (b$1'$; $0.2-0.5$ keV), band 2 (b$2'$; $0.5-1$ keV), band 3 (b$3'$; $1-2$ keV), band 4 (b$4'$; $2-4.5$ keV) and band 5 (b$5'$; $4.5-12$ keV). Comparing the bands between the two catalogues, 2XMM bands b$1'$, b$4'$ and b$5'$ are equivalent to 1XMM bands b1, b3 and b4, respectively, while 1XMM band b2 is the sum of 2XMM bands b$2'$ and b$3'$.

4.4.1 Sample Selection

As in the case of the 1XMM SSXs sample (Section 4.2.1), a cut in the 2XMM EPN HR1 (the equivalent of the 1XMM HR1 value calculated using Equation 4.1 and 1XMM bands) was made as the first step in creating the sample selection. The 2XMM EPN HR1 values were created using the 2XMM b1′, b2′, and b3′ count rates. The HR1 selection criteria was the same for 2XMM as it was for 1XMM (Equation 4.2). The sample was then filtered further such that only sources with EPN b1′ DET_ML > 12 remained ($> 4\sigma$ detection). This resulted in a list of $2{,}055$ sources. Removing duplicate sources left a total of $1{,}911$ candidate SSXs. The SUMM_FLAG was not used to filter the 2XMM SSXs sample list as visual inspection of all $1{,}911$ sources was performed.

The task of visually inspecting each candidate SSXs from 2XMM was performed in conjunction with Dr. Anja Schröder. As with 1XMM, a source was deemed to be real based on the judgement of the individual concerned when viewing the X-ray images. Dr. Schröder produced a number of scripts to assist with the inspection process. In addition to the 2XMM b1′, b2′ and b3′ EPN images, EPN images were created from the energy bands $0.15-0.2$ keV and $0.25-2$ keV, respectively. This helped to distinguish real sources from spurious sources caused by detector noise and optical loading. After the visual inspection of all the sources, the final list contained a total of 212 SSXs deemed to be real. The list of the 212 SSXs can be found in Appendix A.1 (Table A.1).

4.4.2 Comparison of the 1XMM & 2XMM SSXs Samples

As the 1XMM SSXs sample selection and analysis was a precursor to performing the same analysis with 2XMM, it would be prudent to perform a check between the 1XMM SSXs sample list and the 2XMM SSXs sample list. Of the 53 1XMM SSXs, 48 were detected in 2XMM, with 26 of the 48 sources still classified as SSXs in the 2XMM. Of the remaining 5 1XMM SSXs not detected in 2XMM, 4 had their EPN 1XMM observational data sets included in 2XMM. Visual inspection of the 1XMM and 2XMM processed versions of the 4 EPN data sets show that there is no evidence of the sources in the 2XMM images and that they were on the limit of detection in the 1XMM images. These 4 sources do not lie on chip edges nor do they have any candidate counterparts reported in Tables 4.3 and 4.4. It is likely, due to the knowledge and experience gained through screening the 2XMM SSXs candidates, that the 4 sources would not have been included as SSXs if the visual screening of the 1XMM SSXs list were to be repeated. In the case of the fifth 1XMM SSXs that was not detected in 2XMM (1XMM J005555.6−274633), the 1XMM EPN data set was not included in 2XMM. However, visual inspection of the latest version of the pipeline products for this observation shows the source is still clearly visible in the EPN data set. It is unclear as to why the EPN data set for this source was not included in 2XMM.

As previously stated, there were 48 1XMM SSXs detected in 2XMM, of which, 26 were still classified (after visual screening) as SSXs in 2XMM. This means there were 22 1XMM SSXs no longer classified as SSXs in 2XMM. Of the 22 sources, 10 still fulfil both the 1XMM and 2XMM SSXs selection criteria using the EPN HR1, EPN b1 DET_ML and EPN b6 DET_ML values determined by the 2XMM processing. However, after the visual screening process of the 2XMM images, the 10 sources were deemed to be spurious or to be affected by optical loading and are therefore not true SSXs. The remaining 12 1XMM SSXs no longer classified as SSXs in 2XMM do not fulfil the 1XMM or 2XMM selection criteria using the EPN HR1, EPN b1 DET_ML and EPN b6 DET_ML values determined by the 2XMM processing. This would suggest that there is a difference between the processing techniques and detection software used to create 1XMM and 2XMM. This has lead to a better parameterisation of the sources' X-ray properties and it is this that has affected their selection as SSXs, rather than the slight difference between the 1XMM and 2XMM selection criteria (EPN b6 DET_ML > 8 for 1XMM and EPN b1 DET_ML > 12 for 2XMM) resulting in 1XMM SSXs to no longer be classified as a SSXs in 2XMM. Also, in the case of the 12 1XMM SSXs that are no longer classified as SSXs in 2XMM, their selection as SSXs in 2XMM would not have been affected if they had been observed more than once. This is because 2XMM contains the parameters of a source each time that source is detected. Therefore, the fact that the 12 sources are in 2XMM but do not make the 2XMM SSXs sample list means that their parameterisation has moved them out of the sample selection criteria.

The above comparison of the 2XMM and 1XMM SSXs lists suggests that the 2XMM SSXs sample is a robust sample with, at worst, a small number of spurious sources. This is unlike the 1XMM SSXs list, which may contain $\sim 10-50\%$ spurious or non-SSX sources. The SSXs population of the unique sources in 2XMM is $\sim 0.1\%$. This is consistent with the SSXs population of the unique sources in 1XMM ($\sim 0.1\%$) when using the conservative number of 26 definite 1XMM SSXs. If, instead, the initial value of 53 SSXs is used, a population of $\sim 0.2\%$ is calculated for the number of SSXs in 1XMM, which is a factor of two greater than the 2XMM SSXs population.

4.4.3 2XMM SSXs Sample Cross-Correlation

The 2XMM SSX source list was cross-correlated with SIMBAD, NED and SDSS DR6 (Adelman-McCarthy et al., 2008). Like the 1XMM SSXs cross-correlation, the search radius was set to 10 arc seconds. However, unlike the 1XMM searches, the initial results were filtered such that matches from the catalogue searches were only kept if the position of the candidate counterpart was within the smaller of either 5 arc seconds or three times the X-ray source positional error (the POSERR parameter in 2XMM). This was done to reduce the number of spurious matches returned by the searches. The results of the searches can be found in Appendix A.1 (Table A.2). A summary of the results can be found in Table 4.7. Of the 212 SSXs in 2XMM, 126 have candidate counterparts within either 5 arc seconds or three times the X-ray positional error, whichever is smaller. Of the 126 sources, 89 have a candidate counterpart in NED or SIMBAD and 18 of these 89 sources are an X-ray source of unknown nature. This means there are a total of 71 of the 212 2XMM SSXs with a classified candidate counterpart. Once again both Galactic and extragalactic sources were returned. A total of 24, 14, and 30, AGN, galaxies/emission line galaxies and stellar type objects, respectively, were returned as candidate counterparts to the 2XMM SSXs. The 24 AGN correspond to $\sim 11\%$, $\sim 19\%$ and $\sim 27\%$ (38%), of the total 212 2XMM SSXs population, the 126 2XMM SSXs with candidate counterparts, and the 89 2XMM SSXs with a candidate counterpart in SIMBAD or NED (71 not including the 'xs' candidates), respectively.

4.5 Discussion

Investigating SSXs as defined by the criteria given in Section 4.2.1 with *XMM-Newton* has yielded some interesting results. It has been shown that the objects that occupy this extreme region of parameter space have different characteristics and classifications. The cross-correlation of the SSXs with data from other catalogues suggests that SSXs are both Galactic and extragalactic in nature.

As cross-correlation has been performed with other catalogues, the completeness of the catalogues searched should be discussed. Completeness is defined by the limiting magnitudes of the catalogues used and the area of sky covered. As previously discussed, the two *XMM-Newton* catalogues have similar median fluxes of $\sim 3 \times 10^{-14}$ erg s^{-1} cm^{-2} for the $0.2 - 10$ keV band and cover $\sim$ 90 and $\sim$ 360 square degrees for 1XMM and

Table 4.7: 2XMM SSXs Cross-Correlation Summary

Results		Total
SIMBAD/NED		
Type	Redshift Range	
Stars	–	13
vs	–	5
CV	–	5
PN	–	3
INS	–	2
xb	–	1
HMXB	–	1
UvES	–	2
RS	–	1
eml/G	$0.552 - 0.991$	14
Sy1	$0.042 - 0.270$	7
QSOs	$0.533 - 1.273$	17
xs	–	18
Sub-Total		89
Number of SSXs with candidate counterparts including SDSS only matches		126
Number of SSXs with no candidate counterparts		86
Total		212

Summary of the 2XMM SSXs cross-correlation searches. Acronyms used: vs – Variable Star; CV - Cataclysmic Variable; PN – Planetary Nebula; INS – Isolated Neutron Star; xb – X-ray Binary; HMXB – High-Mass X-ray Binary; UvES – Ultraviolet excess Source; RS – Radio Source; eml/G – Emission Line Galaxy or Galaxy; Sy1 – Type 1 Seyfert Galaxy; QSO – Quasi Stellar Object; xs – X-ray Source of unknown nature.

2XMM, respectively. Comparing this to the optical catalogues; the SDSS DR3 covers ~ 5282 square degrees in the Northern hemisphere with a limiting r-band magnitude of 22.2 mag. The SDSS DR6 covers ~ 8000 square degrees, again in the Northern hemisphere, with a limiting r-band magnitude of 22.2 mag. The SC covers the entire sky and the data have a limiting magnitude of $\mathrm{B}_J = 22.5$ and $\mathrm{R} = 21.5$. The INT-WFS covers $200+$ square degrees with a typical depth of 25 mag in the bands U through to z. *XMM-Newton* has covered a small fraction of the sky when compared to the areas covered by optical surveys. As the overlap of the areas of sky observed by the deeper optical surveys and *XMM-Newton* increases, the number of sources with no candidate optical counterpart should decrease. This will allow the classification of a larger number of SSXs.

Having commented on the reliability of the search results, it is time to turn to the types of sources returned during the cross-correlation of the 2XMM SSXs. The Galactic sources returned were of no surprise and included known SSS. For example, the Galactic sources consisted of X-ray emitting stellar type objects, including CVs, INS and PN, which were predicted as discussed in Section 4.1.1.

Approximately 54% of the previously classified SSXs in 2XMM were extragalactic, which is consistent with the value of $\sim 53\%$ obtained for 1XMM SSXs. The extragalactic objects previously classified SSXs in 2XMM consist of AGN and galaxies/emission line galaxies. The AGN population of the previously identified sources ($\sim 27\%$) consists of QSOs and Sy1s, although what fraction of these sources are narrow line objects (e.g., NLS1s) is not yet known. It is likely that this fraction will be high due to the selection criteria used and the suspected mechanisms behind the super soft X-ray emission in AGN. For example, two of the targets analysed in Chapter 3, PG 1001+054 and PG 1440+356, were selected as SSXs in 2XMM. These two sources were selected for analysis in

Chapter 3 because they are suspected of having a high-accretion rate that is close to or above the Eddington limit, $\dot{M} \approx \dot{M}_{\rm Edd}$. PG $1001+054$ and PG $1440+356$ are narrow line QSOs with $v_{\rm FWHM}({\rm H}\beta) \lesssim 2200$ km s^{-1}. As discussed in Section 1.1.5, NLS1s (and narrow line QSOs) are suspected to contain a lower mass black hole (BH) that is accreting at a higher fraction of its Eddington luminosity when compared to their broad line counterparts (Boroson and Green, 1992; Pounds et al., 1995; Boller et al., 1996). Also, NLS1s have been dubbed ultra-soft Seyferts as they tend to have a steeper power-law photon-index, $\Gamma \sim 2.0-2.3$, when compared to Sy1s. It is also usual for NLS1s to have a strong SE, which is likely to result in NLS1s being selected as SSXs. Thus, it is expected that narrow line objects will account for a large fraction of the 2XMM SSXs AGN population. Puchnarewicz et al. (1992) optically identified 53 ($\sim 23\%$) of the 230 sources that made up the *Einstein* Ultra-soft survey (Cordova et al., 1992) as AGN with redshifts $0.1 \lesssim z \lesssim 0.9$. The authors find $\sim 50\%$ of the 53 AGN have line widths $v_{\rm FWHM}({\rm H}\beta) \lesssim 2000$ km s^{-1}, classifying them as NLS1s. In addition, Thomas et al. (1998) identified a sample of 397 soft, high Galactic latitude sources detected in the ROSAT All Sky Survey (RASS). RASS sources were included in their sample if they satisfied the following criteria: $|b| > 20$ degrees, HR1$_{\rm RASS} < 0$ and count rate > 0.5 counts s^{-1}. Thomas et al. found the AGN population of the sample to be 113 ($\sim 28\%$) with redshifts of $0 \lesssim z \lesssim 0.4$. Grupe et al. (2004b; 2004c) analysed high resolution optical spectra for 110 of the 113 sources found by Thomas et al. (1998). Like Puchnarewicz et al. (1992), Grupe et al. find 51 ($\sim 50\%$) of the 110 AGN have $v_{\rm FWHM}({\rm H}\beta) \lesssim 2000$ km s^{-1}, classifying them as NLS1s.

A review of the properties of NLS1s by Komossa (2008) cites a number of X-ray selected NLS1 samples: Grupe and Mathur (2004a) and Grupe et al. (2004b) report the fraction of NLS1s detected from the RASS bright soft X-ray sample of AGN to be 46%

and 51%, respectively. In comparison, Hasinger et al. (2000) found only 1 NLS1 when they analysed the optical spectra of a sample of 69 AGN detected in the ROSAT ultra-deep survey of the Lockman Hole. The fraction of X-ray selected NLS1s determined by the work reported here is greater than the typical fraction of NLS1s that are selected optically ($\sim 10 - 15\%$; Osterbrock and Pogge, 1985; Bian and Zhao, 2003b). Zhou et al. (2006) performed a search for NLS1s from ~ 2000 sources classified as QSOs or galaxies in the spectroscopic sample of the SDSS DR3. The authors report the fraction of NLS1s from the global population of broad line AGN to be 14%, consistent with previous surveys. However, Zhou et al. (2006) also show that this fraction is luminosity dependent; the fraction increases to $\sim 20\%$ for low-luminosity ($M_g \leqslant -22$ mag) objects. The samples cited here suggest that the observed fraction of NLS1s is biased dependent on luminosity and the wavelength used to create the sample. Therefore, non-biased samples are required to obtain the true fraction of AGN that are NLS1s. However, the results of this chapter suggest that the SSXs selection process is an efficient way to find NLS1s.

The current AGN population of the identified 2XMM SSXs ($\sim 27\%$) is consistent with the AGN populations of the samples reported by Puchnarewicz et al. (1992; $\sim 23\%$) and Thomas et al. (1998; $\sim 28\%$). It is possible that the AGN population of the 2XMM SSXs could increase as the unidentified candidate counterparts are classified (e.g., the AGN identified in Section 4.3.2). Figure 4.11 plots the SDSS r-band magnitude against the observed $0.2 - 12$ keV EPN flux, $f_{\rm X}$, for the 62 2XMM SSXs that returned only 1 match during the SDSS 10 arc second radius searches. The lines in Figure 4.11 indicate lines of constant X-ray to optical flux ratios. From top to bottom the dot-dashed lines represent $f_{\rm X} = 10 f_r$, $f_{\rm X} = f_r$ and $f_{\rm X} = 0.1 f_r$, where $f_r \equiv f_{\rm opt}$ and is defined in Equation 2.10. The dashed line labelled QSOsOS represents the typical mean value of the optical to X-ray flux ratio index, $\alpha_{\rm o,x} = 1.5$, determined for optically selected AGN

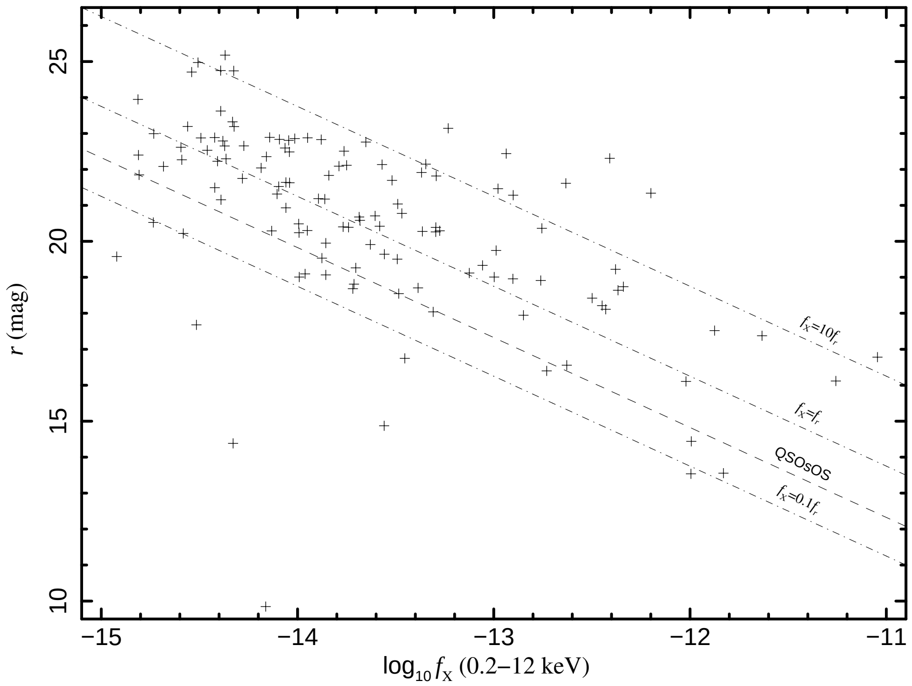

FIGURE 4.11: SDSS r magnitude against observed $0.2-12$ keV X-ray flux for the 62 SSXs with only one optical candidate counterpart from the SDSS DR6 within a 10 arc second radius search of the X-ray source position. The dot-dashed lines represent, from top to bottom, $f_{\rm X} = 10f_r$, $f_{\rm X} = f_r$ and $f_{\rm X} = 0.1f_r$, where $f_r \equiv f_{\rm opt}$ and is defined in Equation 2.10. The dashed line labelled QSOsOS represents the typical mean value of optical to X-ray flux ratio index, $\alpha_{\rm o,x} = 1.5$, determined for optically selected AGN (Green et al., 1995). This corresponds to an X-ray to optical flux ratio of $f_{\rm X}=0.27f_r$.

($f_{\rm X} = 0.27f_r$; Green et al., 1995). It can be seen in Figure 4.11 that the majority of the sources lie above the optically selected AGN line (marked QSOsOS). This would suggest that the majority of the SSXs with a single SDSS DR6 candidate counterpart are AGN. However, caution should be aired as the samples search an extreme region of parameter space. It is possible that exotic objects may be selected and wrongly classified. Optical spectroscopy of the candidate counterparts would allow the identification of the true AGN population of 2XMM SSXs, along with the detection of any exotic sources.

4.6 Conclusions

This chapter has looked at an extreme region of parameter space to search for the AGN population of SSXs. 1XMM was searched for SSXs as a pilot study for performing the same search in 2XMM. In 1XMM, a number of sources matched the SSXs criteria. These sources were then visually inspected to determine their reliability as a source. A final list of 53 SSXs in 1XMM remained. These sources were then cross-correlated with a number of catalogues at different wavelengths to search for candidate counterparts. A total of 40 sources had a candidate counterpart, of which 17 had been previously identified. A selection of 14 candidate counterparts were chosen to be observed with the WHT to gain optical spectra using the ISIS instrument on the WHT. Analysis of the optical spectra identified 5 of the unknown candidate counterparts. All 5 were classified as AGN. This increased the number of SSXs classified as AGN in 1XMM from 6 to 11, placing a lower limit of $\gtrsim 2\%$ on the population of SSXs AGN in 1XMM.

The same search criteria for the 1XMM SSXs sample was applied to 2XMM. The final list of SSXs in 2XMM, after visual inspection, contained a total of 212 sources ($< 1\%$ of the unique sources in 2XMM). As with the 1XMM SSXs sample, the source positions of the 2XMM SSXs were cross-correlated with other catalogues at different wavelengths. The number of previously identified AGN in the 2XMM SSXs sample was found to be 24. However, analysis of the 62 SSXs with only one SDSS DR6 candidate counterpart suggests that this number could be much more. Spectroscopic observations of the unclassified targets are needed to calculate the exact fraction. Comparison with similar studies suggests that 50% of the AGN population are NLS1s. This suggests that the SSXs selection process is an efficient way to find NLS1s.

Chapter 5

Summary

This thesis has looked at *XMM-Newton* observations of AGN in extreme regions of parameter space, in particular, super soft X-ray AGN, suspected high-accretion rate AGN and the AGN population of faint background X-ray sources.

5.1 A Deep X-ray View of the *XMM-Newton* Field Surrounding 3C 273

This chapter described the analysis of a deep-look (~ 500 ks) of the *XMM-Newton* FOV around the famous quasar 3C 273. The deep-look was created by mosaicing the many *XMM-Newton* EPIC calibration observations of 3C 273 taken over a period of ~ 8 years. Source detection was performed concurrently on the deep-look images created for each of the EPIC MOS detectors. This resulted in the detection of 136 faint background X-ray sources. Cross-correlation of the sources was carried out and for the SDSS DR6 candidate counterparts the probability of a unique match, $P_{\rm id}$, was calculated. 68 of the 136 sources were deemed to have a unique SDSS optical counterpart. The time averaged EPIC MOS spectra of the 17 brightest X-ray sources in the deep-look were analysed. 13 of the 17 sources were best modelled by a Galactic absorbed power-law, occasionally modified by absorption or emission intrinsic to the source. A further 3

sources were modelled by one or more *vmekal* components in XSPEC, confirming their previous classification as stellar objects in our Galaxy. The spectral fitting results of the remaining source was of the most interest. This source was well modelled by a multi-temperature plasma and included the detection of an iron emission line. This allowed a redshift of $z = 0.97 \pm 0.02$ to be determined for that source. The analysis of this source suggests that the source is a cluster of galaxies. Analysis of the X-ray properties of all the detected sources and the optical properties of the sources with unique SDSS matches suggest that $\gtrsim 70\%$ of the sources detected in the FOV surrounding 3C 273 are both type 1 and type 2 AGN.

5.2 Mass Loss from AGN

Chapter 3 looked at suspected high-accretion rate AGN and their role within the little understood phenomenon of high-ionisation, high-velocity X-ray outflows, which have been detected in a small number of AGN. Specifically, the *XMM-Newton* EPIC spectra of six narrow line type 1 AGN suspected of accreting at or above the Eddington limited accretion rate were analysed. The six targets were chosen by their position relative to the $M_{\rm BH} - {\rm H}\beta$ line width relation as determined by Wang (2003). The spectra were searched for the presence of Fe K band absorption features blueshifted relative to the systemic redshift of the host galaxy, as observed in X-ray spectra of sources with high-ionisation, high-velocity outflows such as PDS 456. No such features were detected in the EPIC spectra of the six targets. However, all of the targets display soft excess, with half of them displaying evidence of a warm absorber and one target displaying excess emission around the O VII triplet. The non-detection of a high-ionisation, high-velocity outflow implies that either PDS 456 type outflows are not very common or that orientation effects could prevent the observation of such outflows. In addition, the presence of such outflows within an object depends on additional parameters other than the accretion rate of the object.

5.3 Identifying the AGN Population of Super Soft X-ray Sources

This chapter used the first (1XMM) and second (2XMM) releases of the *XMM-Newton* EPIC Source Catalogues to search for super soft X-ray sources (SSXs). The AGN population of SSXs are likely to be high-accretion rate objects, e.g., NLS1s, which produce an excess of photons in the soft X-ray regime. The search for SSXs was not limited to AGN, as soft X-ray emitters can be found within our own Galaxy, e.g., cataclysmic variables and isolated neutron stars. The number of SSXs found in 1XMM and 2XMM were 57 and 212, respectively. These sample numbers are less than 1% of the unique sources in the respective catalogues. Cross-correlation and classification of the SSXs was performed and the global parameters of the AGN population were explored. As part of the cross-correlation of the 1XMM SSXs sample list, candidate counterparts for 14 of the SSXs sources were observed with the Intermediate dispersion Spectrograph and Imaging System (ISIS) instrument on the William Herschel Telescope (WHT). Only 7 of the target spectra had a signal-to-noise of high enough quality for spectral analysis to take place. Analysis of the optical spectra identified 5 of the unknown candidate counterparts as AGN. Using the optical and X-ray information of the 2XMM SSXs sample that returned only one possible SDSS candidate counterpart, the AGN population of the 2XMM SSXs sample is estimated to be $\gtrsim 30\%$. This is consistent with the estimated AGN population of the 1XMM SSXs sample ($\gtrsim 20\%$).

5.4 Future Work

There is future work specific to each of the three data analysis chapters discussed above. Firstly, optical spectroscopy of the candidate counterparts of the X-ray sources detected in the deep-look of the *XMM-Newton* FOV surrounding 3C 273 is required to definitively classify these objects. In addition, as the *XMM-Newton* mission continues and the number of calibration observations of 3C 273 increases, the new observations of 3C 273 should be added to the data sets described in Chapter 2 and be included in the data analysis. This will allow the detection of fainter background X-ray sources and more detailed X-ray spectral analysis of the brighter targets.

Secondly, the number of narrow line type 1 AGN observed in Chapter 3 (Mass Loss from AGN) should be increased and uniformly analysed. Reeves et al. (in prep) have begun such a study. The authors are analysing a large fraction of the *XMM-Newton* sample of narrow line type 1 AGN. This will allow the frequency of objects with high-ionisation, high-velocity outflows to be determined, which will in turn contribute to the understanding of this phenomenon. In addition, the search for high-ionisation, high-velocity outflows continues at the University of Leicester. O'Brien et al. (in prep) have been awarded *XMM-Newton* observing time to acquire data for RX J1230.8$+$0115. Also, O'Brien et al. (in prep) have analysed the *XMM-Newton* and *Suzaku* data taken of PKS 1549$-$79, an object which has undergone a recent merger and has evidence for an optical outflow. The X-ray data for PKS 1549$-$79 do not show any evidence of a high-ionisation, high-velocity outflow.

Finally, as incremental releases of the 2XMM catalogue become publicly available, along with the possible release of the third *XMM-Newton* EPIC Source Catalogue, the SSXs search should be carried out on the new data. This may increase the 2XMM SSXs sample. In addition, optical spectroscopy of the candidate counterparts is needed to definitively classify the observed SSXs.

The first and third data analysis chapters are survey chapters. The SSXs chapter finds rare, extreme objects and the deep-look chapter looks at the general population of the X-ray background in the *XMM-Newton* FOV around 3C 273. The SSXs selected AGN are suspected to be accreting at a high rate, which was the proposed property of AGN with high-ionisation, high-velocity outflows. Interestingly, two targets in the second data analysis chapter, PG 1001+054 and PG 1440+356, were selected as SSXs in the 2XMM SSXs sample search from the third data analysis chapter.

In addition to the proposed future work for the topics investigated in this thesis, proposed future X-ray missions will be able to improve upon our current understanding of SSXs, high-ionisation, high-velocity outflows and the X-ray background. One proposed mission in particular that will be of great importance is the *International X-ray Observatory* (IXO). The IXO will carry a number of next generation instruments, which will have the ability to probe the inner regions of AGN with better clarity. For example, the IXO microcalorimeter spectrometer (XMS) will provide an increased spectral resolution (better than 10 eV at the Fe K line $\sim 6.4-6.7$ keV; 2.5 eV across $0.3-7$ keV). In addition to the XMS, the wide-field instrument aboard the IXO will provide spatial and spectral resolution similar to the *XMM-Newton* EPIC instruments, ~ 5 arc seconds and $\Delta E = 150$ eV, respectively, within an 18 arc minute field of view, across $0.1-15$ keV. However, the throughput of the wide-field instrument (3 m^2 at 1.25 keV) will be $\gtrsim 3$ times larger than the throughput of the EPIC instruments.

Appendices

Appendix A

2XMM Super Soft X-ray Source Sample Information

A.1 2XMM Lists

The tables in this Appendix, Tables A.1 and A.2, contain the X-ray properties of the 2XMM SSXs sample and the results of the cross-correlation of the 2XMM SSXs positions with catalogues at other wavelengths, respectively. The contents of the tables are discussed in Sections 4.4.1 and 4.4.3, respectively. The searches for SSXs in 1XMM and 2XMM are discussed in Chapter 4.

Table A.1: X-ray Properties of the SSXs in 2XMM

IAUNAME 2XMM	R.A. [Degrees]	Dec [Degrees]	POSERR [arc seconds]	EPN HR1	EPN GTI [s]	EPN Total Counts
J000924.9−321339	2.354124	−32.227750	0.97	-0.788 ± 0.205	12360	72 ± 11
J001403.6−391029	3.515401	−39.174800	1.54	-0.695 ± 0.319	19775	31 ± 8
J001503.8−391458	3.766144	−39.249681	0.95	-0.920 ± 0.312	16630	39 ± 9
J001950.6−253800	4.960835	−25.633605	1.60	-0.521 ± 0.254	4415	32 ± 7
J003845.1+481538	9.688217	48.260566	1.48	-1.000 ± 0.234	5699	49 ± 8
J004154.2+410723	10.476017	41.123274	0.39	-0.762 ± 0.086	17669	313 ± 21
J004234.4+411809	10.643386	41.302718	0.36	-0.965 ± 0.248	47031	101 ± 18
J004242.3+411218	10.676445	41.205029	1.08	-0.737 ± 0.204	50840	144 ± 24
J004243.8+411754	10.682572	41.298539	0.43	-0.996 ± 0.129	26958	281 ± 26
J004247.1+411413	10.696660	41.237006	0.94	-1.000 ± 0.172	53383	198 ± 24
J004252.4+411540	10.718669	41.261246	0.22	-0.470 ± 0.014	22904	9166 ± 116
J004255.0+412045	10.729562	41.346003	0.75	-0.763 ± 0.347	13516	39 ± 11
J004259.2+411643	10.746762	41.278675	0.42	-1.000 ± 0.382	11401	47 ± 12
J004308.1+411820	10.783909	41.305721	1.05	-0.963 ± 0.082	23400	451 ± 26
J004318.8+412017	10.828454	41.338074	0.26	-0.666 ± 0.147	18783	141 ± 17
J004319.4+411756	10.830943	41.299059	0.38	-0.402 ± 0.031	7880	2103 ± 60
J004328.6+412140	10.869528	41.361268	1.06	-0.530 ± 0.241	24861	59 ± 13
J004718.6−252113	11.827805	−25.353695	0.70	-1.000 ± 0.351	21450	35 ± 9
J004755.3−251906	11.980531	−25.318425	0.60	-0.811 ± 0.166	24538	111 ± 14
J005412.9−373309	13.554113	−37.552714	0.32	-0.292 ± 0.093	15971	177 ± 16
J005455.0−374117	13.729471	−37.688170	0.29	-0.693 ± 0.041	24457	1254 ± 41
J005510.9−373854	13.795444	−37.648388	0.31	-0.642 ± 0.063	10202	620 ± 33

Table A.1: X-ray Properties of the SSXs in 2XMM (*Cont.*)

IAUNAME 2XMM	R.A. [Degrees]	Dec [Degrees]	POSERR [arc seconds]	EPN HR1	EPN GTI [s]	EPN Total Counts
J005512.8−373849	13.803370	−37.647140	0.70	−0.924±0.128	30490	155±15
J005520.3−374016	13.834615	−37.671383	0.66	−0.881±0.301	21046	35±8
J005834.7−360429	14.644920	−36.074976	0.88	−0.455±0.151	83854	158±21
J005912.1−750517	14.800738	−75.088159	1.05	−0.991±0.055	13366	740±29
J010147.5−715550	15.448148	−71.930686	0.84	−0.506±0.210	5390	49±9
J010257.4−215846	15.739519	−21.979608	0.41	−0.105±0.034	12244	1104±36
J011302.0−453021	18.258685	−45.506066	0.39	−0.140±0.028	34247	1633±44
J012324.0−583834	20.850053	−58.642813	0.82	−0.290±0.111	13617	138±15
J013304.6+302107	23.269488	30.352207	0.45	−0.872±0.177	2108	83±11
J013409.8+303221	23.541014	30.539423	0.85	−0.556±0.074	5013	270±17
J013646.3+154840	24.192992	15.811161	1.92	−1.000±0.393	9669	32±10
J013654.4−350952	24.226824	−35.164481	0.35	−0.157±0.003	38295	117381±346
J013914.4−543105	24.810378	−54.518175	0.56	−0.919±0.073	8976	405±22
J013955.7+061922	24.982294	6.322921	0.36	−0.310±0.010	14519	12454±114
J020348.4+295924	30.952070	29.990005	1.03	−0.325±0.040	1969	951±32
J021938.5−032507	34.910779	−3.418723	0.91	−0.416±0.101	1630	194±18
J022255.9−051352	35.732943	−5.231178	0.82	−0.366±0.112	13292	136±14
J022306.4−051300	35.776984	−5.216921	0.88	−0.615±0.296	6742	29±7
J022306.9−041511	35.778890	−4.253163	1.12	−1.000±0.397	5038	19±6
J022511.6−293226	36.298601	−29.540769	0.53	−0.317±0.072	12761	290±20
J023507.6+034357	38.781985	3.732662	0.57	−0.448±0.060	6080	407±22
J023821.8−521935	39.591024	−52.326465	1.91	−0.985±0.489	12657	18±8
J030707.8−000543	46.782754	−0.095402	1.98	−1.000±0.377	10483	33±9
J031505.6−550942	48.773534	−55.161770	0.41	−0.307±0.150	3570	77±10
J031722.8−663705	49.345120	−66.618174	0.44	−0.779±0.207	7581	48±8
J032159.8−370509	50.499462	−37.086008	0.48	−0.220±0.050	26245	619±31
J032432.7−292416	51.136495	−29.404499	0.55	−0.135±0.063	3674	298±18
J033017.3−031653	52.572150	−3.281623	1.00	−0.799±0.163	4954	83±10
J033226.4−274035	53.110383	−27.676618	0.16	−0.157±0.035	23030	1055±36
J033227.1−280124	53.113120	−28.023347	0.33	−0.342±0.065	17612	377±23
J033234.6−273426	53.144496	−27.574161	1.53	−0.509±0.235	23461	48±12
J033735.0−251805	54.396128	−25.301436	0.42	−0.080±0.033	19632	1371±41
J033742.8−252209	54.428511	−25.369391	0.62	−0.300±0.087	25172	270±21
J033843.5−353349	54.681257	−35.563680	1.08	−0.596±0.293	2863	46±9
J034314.8−094544	55.811858	−9.762456	0.59	−0.447±0.069	55236	378±24
J042001.9−502248	65.007965	−50.380096	0.20	−0.865±0.032	16851	1841±44
J042538.6−571436	66.411118	−57.243373	0.21	−0.124±0.055	4065	690±34
J042627.9−571309	66.616488	−57.219399	0.47	−0.159±0.054	9985	461±24
J042711.3−571656	66.797180	−57.282325	0.39	−0.254±0.088	6030	175±14
J043152.0−780010	67.967050	−78.002954	1.12	−0.591±0.217	2180	38±7
J043944.8−454042	69.936821	−45.678337	0.36	−0.343±0.014	21477	6968±87
J043949.5−680902	69.956555	−68.150618	1.01	−0.999±0.026	8871	3181±58
J045230.1−295335	73.125528	−29.893270	0.35	−0.069±0.006	9700	35464±191
J050803.4−684016	77.014301	−68.671336	1.38	−0.956±0.198	6864	71±10
J051541.3+010441	78.922486	1.078099	0.36	−0.720±0.010	20280	16982±133
J051724.9+460122	79.353879	46.022856	1.83	−1.000±0.374	11145	20±5
J051756.3+455804	79.484719	45.968048	2.10	−1.000±0.320	7420	32±7
J051857.8−453413	79.741183	−45.570319	1.50	−0.875±0.320	7672	33±9
J052016.0−692505	80.066972	−69.418265	1.51	−1.000±0.342	10754	33±8
J052159.3−362257	80.497497	−36.382610	0.44	−0.311±0.133	9844	90±11
J052418.9−334736	81.078751	−33.793335	2.06	−1.000±0.339	1832	29±7
J052650.1−700126	81.708940	−70.024001	1.00	−0.970±0.010	38673	20419±146
J054333.8−682220	85.890848	−68.372329	1.00	−0.788±0.007	8136	37993±197
J054717.0−510400	86.820967	−51.066816	1.44	−0.492±0.195	57167	68±12
J055531.7+220746	88.882233	22.129480	1.00	−0.980±0.011	6786	16937±131
J064804.6−441858	102.019511	−44.316210	0.29	−0.417±0.044	4439	724±28
J072024.9−312549	110.103913	−31.430542	0.14	−0.477±0.002	34186	219780±436
J073709.5+653306	114.289972	65.551922	0.69	−0.637±0.131	45867	160±19
J073721.8+653318	114.341238	65.555039	0.72	−0.457±0.111	47886	162±16
J073738.2+653630	114.409247	65.608446	0.51	−0.891±0.068	50307	487±24
J073739.5+653322	114.414715	65.556163	1.03	−0.947±0.235	43445	59±11
J080622.9+152730	121.595688	15.458604	0.25	−0.778±0.015	16811	8059±92
J080623.3−412231	121.597447	−41.375491	0.25	−0.418±0.007	16317	25349±161
J081035.5−471814	122.648046	−47.304100	2.68	−1.000±0.435	21782	22±8
J082150.0−423703	125.458677	−42.617585	1.85	−0.710±0.308	4528	186±46
J082411.9−430341	126.049683	−43.061434	2.71	−0.885±0.348	2920	121±31
J083526.9−262941	128.862205	−26.494825	1.41	−0.846±0.292	12650	47±11
J084937.4−453232	132.406201	−45.542493	2.05	−0.765±0.289	15899	128±29
J085618.4+380712	134.077039	38.120182	0.87	−0.657±0.126	8357	123±13
J085626.0+380520	134.108625	38.088911	0.38	−0.051±0.019	10942	3144±58
J090013.0−455734	135.054323	−45.959541	2.07	−1.000±0.268	5760	79±15
J090927.7+542128	137.365810	54.357884	0.63	−0.421±0.081	30542	261±19
J092053.8+370323	140.224497	37.056592	1.57	−0.854±0.350	27745	37±10
J092246.9+512037	140.695826	51.343853	0.35	−0.191±0.008	9957	17043±133
J094322.8+164113	145.845280	16.686985	0.77	−0.333±0.150	6462	69±9
J094349.0+465526	145.954505	46.924163	1.08	−0.658±0.180	19532	82±12
J094354.7+480734	145.977931	48.126368	0.51	−0.326±0.102	9767	157±15
J094404.3+480647	146.018191	48.113176	0.27	−0.103±0.025	9059	1952±47
J094409.6+480813	146.040266	48.136977	1.13	−0.505±0.190	8534	59±9
J094512.9+100000	146.304054	10.000030	2.28	−0.387±0.178	733	68±11
J094531.8+040235	146.382671	4.043116	1.65	−0.539±0.108	4939	138±13
J094610.7+095227	146.544596	9.874222	0.41	−0.189±0.034	17281	1093±36
J095542.0+690336	148.925004	69.060277	0.76	−0.429±0.102	3457	211±19
J095550.0+685911	148.958676	68.986543	0.83	−0.512±0.162	3352	73±10
J095910.3+020730	149.793143	2.125247	0.94	−1.000±0.359	9604	29±8
J095950.3+021410	149.959749	2.236247	2.42	−0.943±0.425	8194	20±7
J100211.7−192538	150.548890	−19.427239	0.40	−0.440±0.033	2838	1357±38

Table A.1: X-ray Properties of the SSXs in 2XMM (*Cont.*)

IAUNAME 2XMM	R.A. [Degrees]	Dec [Degrees]	POSERR [arc seconds]	EPN HR1	EPN GTI [s]	EPN Total Counts
J100218.9+325315	150.578756	32.887603	1.16	-0.874 ± 0.272	9687	36 ± 8
J100324.8+554330	150.853517	55.725092	1.80	-1.000 ± 0.456	7616	22 ± 8
J100420.0+051300	151.083620	5.216722	0.47	-0.382 ± 0.057	8733	515 ± 25
J100734.6−201733	151.894575	−20.292579	1.00	-0.806 ± 0.011	3623	14892 ± 123
J101341.8−000925	153.424563	−0.157203	0.84	-0.320 ± 0.149	4276	111 ± 14
J102255.3+195554	155.730562	19.931818	1.68	-0.828 ± 0.328	16027	43 ± 10
J102446.0−183832	156.191995	−18.642223	0.47	-0.108 ± 0.041	13628	689 ± 28
J103438.6+393828	158.660837	39.641292	0.35	-0.327 ± 0.007	3189	21924 ± 150
J104412.2+212936	161.051108	21.493347	0.44	-0.179 ± 0.073	10982	322 ± 23
J104459.6+214432	161.248678	21.742272	1.06	-0.677 ± 0.314	16304	50 ± 12
J104519.6−011618	161.331706	−1.271933	1.02	-0.303 ± 0.110	10356	137 ± 15
J104613.6+525554	161.557082	52.931717	0.36	-0.333 ± 0.013	7071	7179 ± 87
J105221.0+440439	163.087619	44.077584	0.36	-0.231 ± 0.054	4252	415 ± 21
J105252.7+572900	163.219695	57.483425	0.27	-0.442 ± 0.209	26407	104 ± 14
J110319.9+355750	165.833192	35.964083	0.35	-0.088 ± 0.005	26062	47030 ± 221
J110354.1+381751	165.975519	38.297717	0.25	-0.176 ± 0.082	9924	217 ± 17
J120016.4−031652	180.068632	−3.281321	0.84	-0.293 ± 0.105	7875	136 ± 13
J120122.0−185150	180.342065	−18.863947	0.40	-0.296 ± 0.087	7872	199 ± 16
J120947.8+393042	182.449210	39.511785	0.59	-0.472 ± 0.130	23507	142 ± 16
J121035.0+393123	182.645897	39.523193	0.34	-0.628 ± 0.052	31554	679 ± 30
J121839.4+470627	184.664542	47.107644	0.41	-0.422 ± 0.187	3385	55 ± 9
J122539.3+333349	186.413778	33.563700	1.00	-0.798 ± 0.373	9983	22 ± 6
J122542.3+333233	186.426374	33.542620	0.88	-1.000 ± 0.386	77883	51 ± 14
J122542.7+310541	186.428256	31.094930	0.81	-0.225 ± 0.107	1462	115 ± 11
J122543.6+333507	186.431840	33.585347	0.80	-1.000 ± 0.210	75818	91 ± 15
J122545.2+333103	186.438616	33.517714	0.45	-0.195 ± 0.077	66295	499 ± 38
J122617.6+332942	186.573525	33.495269	0.57	-1.000 ± 0.385	29560	126 ± 17
J122811.0+440338	187.045883	44.060656	0.49	-0.360 ± 0.055	10905	457 ± 23
J123019.8+075745	187.582867	7.962736	0.42	-0.096 ± 0.040	47663	943 ± 37
J123036.3+413802	187.651650	41.633970	1.48	-1.000 ± 0.427	11294	29 ± 9
J123103.2+110648	187.763370	11.113478	0.23	-0.192 ± 0.032	30413	1298 ± 40
J123104.6+142831	187.769340	14.475323	2.39	-0.999 ± 0.500	5120	24 ± 7
J123229.6+641115	188.123421	64.187528	0.31	-0.232 ± 0.058	8364	673 ± 38
J124049.0−015523	190.204435	−1.923081	0.66	-0.459 ± 0.111	12035	138 ± 14
J124112.5+331746	190.302187	33.296243	0.77	-0.288 ± 0.099	22752	185 ± 18
J124232.3+141728	190.634979	14.291201	0.58	-0.263 ± 0.073	29881	322 ± 22
J124236.7+323216	190.653305	32.537929	1.45	-0.729 ± 0.237	23213	49 ± 9
J125413.0+310923	193.554410	31.156405	0.56	-0.356 ± 0.107	5502	131 ± 13
J125702.3+220151	194.259650	22.031005	0.20	-0.946 ± 0.012	10478	13847 ± 119
J130200.1+274657	195.500624	27.782599	0.38	-0.632 ± 0.027	12410	2134 ± 49
J130540.3−101956	196.417959	−10.332429	1.40	-0.537 ± 0.257	8816	34 ± 7
J130848.1+212707	197.200613	21.451946	0.14	-0.168 ± 0.006	11369	29651 ± 175
J130903.9+213449	197.266350	21.580549	0.41	-0.340 ± 0.120	15602	145 ± 16
J130908.9+213715	197.287449	21.620939	0.71	-0.554 ± 0.214	12196	70 ± 13
J132342.2+482701	200.926057	48.450529	1.25	-0.337 ± 0.115	4369	111 ± 12
J132349.6+654148	200.956686	65.696790	0.25	-0.018 ± 0.006	11003	32270 ± 185
J133410.6+375956	203.544505	37.998976	0.32	-0.441 ± 0.086	22234	374 ± 29
J133935.6−003133	204.898600	−0.525886	0.32	-0.352 ± 0.036	5554	1007 ± 33
J133944.4−001451	204.935183	−0.247702	0.84	-0.492 ± 0.226	1814	46 ± 9
J134009.3+271839	205.039085	27.310970	0.43	-0.192 ± 0.075	1402	266 ± 19
J134815.7+264441	207.065599	26.744911	0.46	-0.191 ± 0.092	15214	202 ± 18
J134834.2+262205	207.142870	26.368220	0.28	-0.197 ± 0.009	47434	14770 ± 126
J134848.2+262219	207.201073	26.372048	0.31	-0.199 ± 0.020	24954	5054 ± 98
J135406.2−021034	208.525875	−2.176227	2.48	-0.469 ± 0.227	3359	35 ± 8
J140229.6+542346	210.623646	54.396246	1.08	-0.712 ± 0.220	16633	74 ± 13
J140244.9+541604	210.687267	54.267781	0.77	-0.828 ± 0.264	13917	49 ± 10
J140301.0+542341	210.754516	54.394770	0.66	-0.523 ± 0.182	20549	74 ± 12
J140301.1+542556	210.754956	54.432478	1.68	-0.884 ± 0.304	19932	39 ± 9
J140313.4+542009	210.806198	54.335885	0.67	-0.820 ± 0.288	8008	84 ± 19
J140332.2+542102	210.884233	54.350822	0.36	-0.607 ± 0.036	17360	1217 ± 37
J140333.2+541800	210.888527	54.300054	0.51	-0.302 ± 0.129	15799	119 ± 15
J140344.4+542807	210.935340	54.468743	0.59	-0.584 ± 0.178	13104	68 ± 11
J140621.8+222347	211.591106	22.396497	0.39	-0.279 ± 0.024	3075	2039 ± 46
J140856.7−034634	212.236626	−3.776197	1.06	-0.300 ± 0.135	8111	106 ± 13
J141711.0+522541	214.296044	52.428303	0.41	-0.517 ± 0.059	36221	504 ± 27
J142927.1−380409	217.363235	−38.069338	1.03	-0.571 ± 0.042	4367	940 ± 33
J144207.4+352622	220.531229	35.439697	0.23	-0.077 ± 0.003	13296	107217 ± 322
J145144.2+163657	222.934427	16.616111	0.60	-0.202 ± 0.059	7489	433 ± 25
J150244.3−420302	225.684850	−42.050652	2.05	-0.949 ± 0.347	5038	65 ± 16
J150351.5−415215	225.964837	−41.871027	0.90	-0.152 ± 0.038	17875	3812 ± 142
J150945.7+565936	227.440464	56.993477	1.06	-0.547 ± 0.157	7555	87 ± 12
J150948.6+333626	227.452725	33.607427	0.52	-0.211 ± 0.061	6304	352 ± 20
J151558.8−000154	228.995046	−0.031667	1.21	-0.423 ± 0.155	12310	89 ± 12
J151637.1−160911	229.154847	−16.153312	0.98	-0.621 ± 0.182	26995	80 ± 12
J151743.7+070122	229.432412	7.022951	0.49	-0.077 ± 0.030	7128	1383 ± 40
J152130.7+074916	230.377983	7.821200	0.38	-0.369 ± 0.023	18319	2585 ± 55
J153450.3+543000	233.709723	54.500041	0.61	-0.187 ± 0.056	5167	461 ± 25
J153557.0+543750	233.987798	54.630556	0.20	-0.070 ± 0.013	10096	7165 ± 89
J154332.5+535634	235.885472	53.942994	0.72	-0.382 ± 0.183	3098	53 ± 9
J155333.5+190051	238.389690	19.014374	0.67	-0.175 ± 0.079	1994	196 ± 15
J160141.0+664810	240.420999	66.802846	0.26	-0.704 ± 0.099	8977	186 ± 15
J160518.5+324918	241.327140	32.821678	0.16	-0.412 ± 0.003	25439	100645 ± 314
J162910.1+780441	247.292413	78.078060	0.38	-0.591 ± 0.051	1561	584 ± 25
J163819.0−642200	249.579383	−64.366718	1.20	-0.378 ± 0.110	7308	251 ± 27
J172912.1+703256	262.300666	70.548890	1.18	-0.309 ± 0.109	849	107 ± 11
J175833.3+663800	269.639006	66.633499	0.69	-0.235 ± 0.089	2183	154 ± 13
J180019.6+080503	270.081709	8.084384	1.24	-0.361 ± 0.095	10757	171 ± 15

Table A.1: X-ray Properties of the SSXs in 2XMM (*Cont.*)

IAUNAME 2XMM	R.A. [Degrees]	Dec [Degrees]	POSERR [arc seconds]	EPN HR1	EPN GTI [s]	EPN Total Counts
J180632.7+703221	271.636262	70.539373	0.87	-0.339 ± 0.157	7648	75 ± 10
J182140.5−273136	275.418769	−27.526783	0.60	-0.129 ± 0.056	4528	427 ± 22
J204351.8−672512	310.965980	−67.420135	0.61	-0.168 ± 0.076	6757	252 ± 18
J215735.6−695406	329.398657	−69.901730	1.35	-0.701 ± 0.226	6693	54 ± 10
J221605.9−174333	334.024891	−17.726024	1.86	-0.707 ± 0.335	24210	37 ± 10
J221719.0−354951	334.329565	−35.830962	0.39	-0.069 ± 0.025	10153	1952 ± 46
J221747.8−353800	334.449522	−35.633421	0.58	-0.307 ± 0.116	13853	161 ± 15
J223439.9−374259	338.666599	−37.716457	0.36	-0.085 ± 0.014	4010	5774 ± 80
J225733.2−363525	344.388577	−36.590554	0.58	-0.339 ± 0.068	13680	301 ± 19
J231439.2−424244	348.663539	−42.712229	0.32	-0.238 ± 0.052	18621	526 ± 26
J231818.7−422237	349.578244	−42.377126	0.40	-0.138 ± 0.027	61721	1923 ± 52
J232134.2+195217	350.392738	19.871411	0.37	-0.115 ± 0.020	14067	3049 ± 57
J234348.9−151721	355.953830	−15.289239	2.75	-0.232 ± 0.097	37431	1707 ± 140
J234349.7−151700	355.957138	−15.283389	0.37	-0.342 ± 0.020	39538	4290 ± 74
J234729.5+010113	356.873077	1.020434	0.66	-0.170 ± 0.078	7362	212 ± 16
J234753.6−281043	356.973538	−28.178880	0.63	-0.832 ± 0.120	23023	445 ± 41

List of sources in 2XMM that match the criteria for SSXs as defined in Section 4.4.1. The list is ordered by 'R.A.'. The 'IAUNAME 2XMM' column contains, when prefixed with "2XMM", the IAUNAME source name. 'R.A.' and 'Dec' are given in decimal degrees. 'POSERR', is the 1σ X-ray positional error in arc seconds. 'EPN HR1' is the EPN 2XMM HR equivalent to 1XMM HR1 defined in Equation 4.1 and is calulated using 1XMM bands. 'EPN GTI' is the good time interval exposure time for the EPN detector, in seconds, for the observation in which the source was detected. 'EPN Total Counts' is the total detected counts in the EPN broad-band ($0.2-12$ keV).

Table A.2: Cross-Correlation of 2XMM SSXs Sample List

IAUNAME 2XMM	SIMBAD DIST [as]	SIMBAD NAME TYPE	NED DIST [as]	NED TYPE NAME	z	SDSS DIST [as]	umag rmag	gmag zmag	imag z
J000924.9−321339	-	-	1.4	G 2dFGRS S434Z02	0.118	-	-	-	-
J001503.8−391458	-	-	0.7	XrayS NGC 0055:[SRW2006] 053	-	-	-	-	-
J004154.2+410723	0.7	M31N 2001-10f Nova	1.0	XrayS MESSIER 031:[PFH2005] 191	-	-	-	-	-
J004242.3+411218	0.6	[TC96] 94 Variable Star	2.8	XrayS CXOM31 J004242.1+411218	-	-	-	-	-
J004247.1+411413	0.3	CXOM31 J004247.1+411413 X-ray source	1.4	XrayS CXOM31 J004247.1+411413	-	-	-	-	-
J004252.4+411540	2.8	RX J0042.8+4115 X-ray source	2.9	V* CXOM31 J004252.5+411540	-	-	-	-	-
J004255.0+412045	0.9	M31N 1996-08b Nova	1.6	XrayS CXOM31 J004255.3+412045	-	-	-	-	-
J004259.2+411643	2.7	M31N 1995-11c Nova	2.6	XrayS CXOM31 J004259.3+411643	-	-	-	-	-
J004308.1+411820	1.9	[O2006] SSS 12 X-ray source	-	-	-	-	-	-	-
J004318.8+412017	3.8	RX J004318.6+412024 Cataclysmic Variable Star	3.8	V* CXOM31 J004318.8+412018	-	-	-	-	-
J004328.6+412140	2.3	[PFH2005] 456 X-ray source	2.2	Nova MESSIER 031:[H29] Nova 86	-	-	-	-	-
J005455.0−374117	0.8	XMMU J005455.0−374117 X-ray source	0.8	XrayS XMMU J005455.0−374117	-	-	-	-	-
J005510.9−373854	-	-	0.2	XrayS 1WGA J0055.1-3738	-	-	-	-	-
J005912.1−750517	0.3	LIN 358 Symbiotic Star	-	-	-	-	-	-	-
J010147.5−715550	2.6	AzV 281 Emission-line Star	-	-	-	-	-	-	-
J011302.0−453021	0.9	[GHA2004] 19 X-ray source	0.9	G [GHA2004] 1	1.208	-	-	-	-

Table A.2: Cross-Correlation of 2XMM SSXs Sample List (*Cont.*)

IAUNAME 2XMM	SIMBAD DIST [as]	 NAME TYPE	 DIST [as]	NED TYPE NAME	 z	SDSS DIST [as]	 umag rmag	 gmag zmag	 imag z
J013304.6+302107	2.4	XMMU J013304.7+302107 X-ray source	1.8	XrayS MESSIER 033:[PMH2004] 109	-	-	-	-	-
J013409.8+303221	3.0	CXOU J013409.9+303219 X-ray source	3.2	XrayS MESSIER 033:[PMH2004] 247	-	-	-	-	-
J013646.3+154840	-	-	3.6	XrayS CXOU J013646.1+154842	-	-	-	-	-
J013654.4−350952	0.2	2MASSI J0136544-350952 Seyfert 1 Galaxy	0.5	G 2MASSi J0136544-350952	0.289	-	-	-	-
J020348.4+295924	2.7	V* AI Tri Cataclysmic Var. AM Her type	2.4	V* RBS 027	-	-	-	-	-
J021938.5−032507	-	-	1.8	G SWIRE J021938.70-032508.2	0.435	-	-	-	-
J022255.9−051352	-	-	0.3	G SWIRE J022255.87-051351.7	0.846	-	-	-	-
J022511.6−293226	-	-	0.9	VisS 2QZ J022511.6−293227	-	-	-	-	-
J023507.6+034357	1.4	V* FS Cet White Dwarf	-	-	-	-	-	-	-
J031505.6−550942	-	-	2.3	G XMMU J031505.7−550942	0.501	-	-	-	-
J033226.4−274035	0.3	CXOCDFS J033226.6−274036 Active Galaxy Nucleus	0.5	QSO EIS J033226.51-274035.7	1.030	-	-	-	-
J033227.1−280124	0.6	[MBR2003] CDFS-H 4453 Galaxy	1.0	G COMBO-17 0579	0.552	-	-	-	-
J033234.6−273426	-	-	0.9	G COMBO-17 6303	1.182	-	-	-	-
J033843.5−353349	1.1	[MCJ93] NGC 1404 a Quasar	1.9	QSO FCSS J033843.5−353349	0.741	-	-	-	-
J042538.6−571436	0.5	RX J0425.6-5714 Cataclysmic Var. AM Her type	-	-	-	-	-	-	-
J043949.5−680902	0.9	1ES 0439-68.2 Cataclysmic Variable Star	1.2	XrayS RBS 056	-	-	-	-	-
J045230.1−295335	0.5	QSO B0450-2958 Seyfert 1 Galaxy	0.8	G 6dF J0452301-295335	0.286	-	-	-	-
J050803.4−684016	-	-	0.9	PN IRAS 05082-684	-	-	-	-	-
J051541.3+010441	0.8	V* V1309 Ori Cataclysmic Var. AM Her type	-	-	-	-	-	-	-
J052016.0−692505	0.8	XMMU J052016.0−692505 X-ray source	0.5	V* HV 0576	-	-	-	-	-
J052650.1−700126	2.8	NOVA LMC 1995 Nova	-	-	-	-	-	-	-
J054333.8−682220	-	-	2.3	XrayS RBS 067	-	-	-	-	-
J054717.0−510400	1.2	* bet Pic Star	-	-	-	-	-	-	-
J064804.6−441858	0.7	HD 49798 High Mass X-ray Binary	-	-	-	-	-	-	-
J072024.9−312549	1.6	1ES 0718-31.3 Star	-	-	-	-	-	-	-
J080622.9+152730	-	-	-	-	-	0.2	20.3 21.5	20.7 21.7	21.5
J085626.0+380520	-	-	-	-	-	0.5	19.6 19.1	19.4 18.6	19.1
J090927.7+542128	-	-	0.9	UvES SDSS J090927.74+542127.9	1.325	0.6	20.6 19.9	20.3 19.7	19.9
J092053.8+370323	-	-	-	-	-	0.9	22.1 19.6	21.1 19.3	19.6
J092246.9+512037	0.3	QSO B0919+515 Seyfert 1 Galaxy	0.1	QSO SBS 0919+51	0.160	0.3	17.6 16.9	17.4 16.8	16.9 0.160
J094322.8+164113	-	-	-	-	-	0.8	20.8 18.8	20.2 18.4	18.8
J094349.0+465526	-	-	-	-	-	0.6	23.2 19.3	21.6 18.9	19.3
J094354.7+480734	-	-	-	-	-	1.7	24.0 18.1	20.5 17.9	18.1
J094404.3+480647	0.8	[VV96] J094404.4+480644 Quasar	0.5	QSO SDSS J094404.41+480646.6	0.392	0.8	18.3 18.2	18.1 17.9	18.2 0.392
J094409.6+480813	1.1	SDSS J094409.76+480812.4 Quasar	0.4	QSO SDSS J094409.76+480812.4	1.111	1.2	19.4 19.0	19.2 19.0	19.0 1.111
J094512.9+100000	-	-	-	-	-	4.6	22.9 20.3	23.8 19.8	20.3
J094531.8+040235	-	-	-	-	-	0.7	22.4 20.1	21.5 20.4	20.1
J094610.7+095227	-	-	-	-	-	0.8	20.4 19.6	20.0 19.6	19.6
J095542.0+690336	1.1	[IW2001] H25 X-ray source	2.1	XrayS NGC 3031:[IW2001] H25	-	-	-	-	-
J095550.0+685911	1.4	[PR95] 50167 Object of unknown nature	3.3	HII NGC 3031:[HK83]289	-	-	-	-	-
J095910.3+020730	-	-	1.7	RadioS [SCS2004] J095910.30+020732.3	-	2.0	21.4 18.6	20.2 18.0	18.6

Table A.2: Cross-Correlation of 2XMM SSXs Sample List (*Cont.*)

IAUNAME 2XMM	SIMBAD DIST [as]	 NAME TYPE	NED DIST [as]	 TYPE NAME	z	SDSS DIST [as]	 umag rmag	 gmag zmag	 imag z
J100211.7−192538	0.7	RE J1002-19 Cataclysmic Var. AM Her type	-	-	-	-	-	-	-
J100218.9+325315	-	-	-	-	-	2.2	22.9 21.1	22.9 20.7	21.1
J100324.8+554330	-	-	-	-	-	2.6	22.8 19.8	21.6 19.6	19.8
J100420.0+051300	1.1	LEDA 29208 Galaxy	0.9	QSO PG 1001+05	0.161	1.0	16.6 16.1	16.4 16.2	16.1 0.160
J100734.6−201733	1.4	RX J1007.5-2017 Cataclysmic Var. AM Her type	-	-	-	-	-	-	-
J101341.8−000925	1.1	MGC 95012 Seyfert 1 Galaxy	0.1	QSO SDSS J101341.89-000925.7	0.277	0.2	19.8 18.5	19.3 18.1	18.5 0.277
J102255.3+195554	-	-	-	-	-	2.2	21.2 19.5	20.8 19.1	19.5
J102446.0−183832	0.8	NGC 3242 Planetary Nebula	0.3	PN NGC 324	-	-	-	-	-
J103438.6+393828	-	-	0.7	G KUG 1031+39	0.042	0.4	16.3 14.7	15.4 14.4	14.7 0.043
J104412.2+212936	-	-	-	-	-	0.6	20.7 20.4	20.6 20.2	20.4
J104459.6+214432	-	-	-	-	-	2.8	22.4 22.1	22.6 21.3	22.1
J104519.6−011618	0.1	2QZ J104519.6−011619 Quasar	0.2	QSO 2QZ J104519.6−011619	0.941	0.2	19.2 18.9	19.0 18.7	18.9
J104613.6+525554	0.3	RBS 901 Seyfert 1 Galaxy	0.2	QSO SDSS J104613.73+525554.2	0.503	0.3	17.7 17.5	17.5 17.5	17.5 0.503
J105221.0+440439	-	-	1.4	QSO SDSS J105220.92+440439.1	0.968	1.2	22.6 19.4	23.2 19.0	19.4
J105252.7+572900	0.7	RX J105252.9+572901 X-ray source	0.1	G 2MASX J10525269+5728597	0.204	0.5	20.0 17.1	18.6 16.8	17.1
J110354.1+381751	-	-	-	-	-	0.4	23.1 21.2	23.3 20.5	21.2
J120016.4−031652	-	-	0.9	UvES SDSS J120016.51-031651.9	1.725	1.0	21.0 20.5	20.8 20.4	20.5
J120947.8+393042	-	-	-	-	-	0.6	21.1 20.4	20.8 20.4	20.4
J121035.0+393123	-	-	-	-	-	0.2	22.0 19.1	20.5 18.8	19.1
J121839.4+470627	-	-	1.8	G 2MASX J12183945+4706275	0.094	1.6	18.8 16.4	17.6 16.2	16.4 0.094
J122539.3+333349	-	-	-	-	-	3.7	22.9 22.6	22.3 23.2	22.6
J122543.6+333507	-	-	-	-	-	0.8	21.6 21.9	21.8 22.0	21.9
J122617.6+332942	-	-	-	-	-	2.6	20.2 18.8	19.9 18.5	18.8
J122811.0+440338	0.9	RX J122811.1+440339 X-ray source	-	-	-	-	-	-	-
J123019.8+075745	-	-	-	-	-	0.6	21.3 20.7	21.1 20.2	20.7
J123103.2+110648	-	-	-	-	-	0.6	22.4 19.7	20.9 19.6	19.7
J123229.6+641115	0.7	2MASS J12322972+6411151 Quasar	0.7	QSO SDSS J123229.67+641115.1	0.743	0.7	18.3 17.9	18.0 17.8	17.9 0.743
J124049.0−015523	1.1	2QZ J124049.1−015524 Quasar	0.6	QSO SDSS J124049.11-015523.5	1.292	0.9	19.5 19.1	19.3 19.2	19.1
J124112.5+331746	-	-	-	-	-	1.1	23.0 20.9	24.4 20.8	20.9
J124232.3+141728	-	-	-	-	-	0.8	19.9 18.4	19.2 18.2	18.4
J125413.0+310923	-	-	-	-	-	1.0	20.8 20.1	20.4 19.9	20.1
J125702.3+220151	0.3	GSC 01455-01145 White Dwarf	0.4	WD* FSAO J125702.33+220152.6	-	1.0	13.3 14.6	13.2 14.4	14.6
J130200.1+274657	0.8	2MASX J13020015+2746579 Emission-line galaxy	0.9	G KUG 1259+28	7070.000	0.5	16.9 14.7	15.4 14.5	14.7
J130903.9+213449	-	-	-	-	-	0.2	23.3 22.4	23.4 23.1	22.4
J130908.9+213715	-	-	-	-	-	1.9	21.7 21.1	21.5 20.8	21.1
J132342.2+482701	2.8	SDSS J132341.97+482701.2 Galaxy	2.7	G SDSS J132341.97+482701.3	0.087	2.8	19.1 17.2	18.3 16.9	17.2 0.088
J132349.6+654148	0.6	QSO B1322+659 Seyfert 1 Galaxy	0.8	QSO PG 1322+65	0.168	0.7	16.2 15.7	16.1 15.9	15.7
J133410.6+375956	0.5	RX J1334.2+3759 Quasar	0.8	QSO RX J1334.2+375	0.386	0.3	20.7 19.6	20.4 19.3	19.6
J133935.6−003133	-	-	-	-	-	0.9	23.8 21.0	22.0 20.2	21.0
J133944.4−001451	4.0	MGC 49365 Quasar	3.8	QSO SDSS J133944.50-001451.5	1.268	4.1	19.4 19.0	19.1 19.1	19.0 1.269
J134009.3+271839	0.2	[CCS88] 1337.8+2733 Emission-line galaxy	0.6	G [CCS88] 133750.0+273348	0.327	1.1	19.0 18.4	18.7 17.9	18.4
J134815.7+264441	-	-	1.4	QSO 1RXS J134816.2+264415	0.930	1.2	19.6 19.2	19.5 19.0	19.2

Table A.2: Cross-Correlation of 2XMM SSXs Sample List (*Cont.*)

IAUNAME 2XMM	SIMBAD DIST [as]	 NAME TYPE	NED DIST [as]	 TYPE NAME	 z	SDSS DIST [as]	 umag rmag	 gmag zmag	 imag z
J134834.2+262205	-	-	0.7	G SDSS J134834.28+262205.9	0.918	0.5	19.1 18.7	18.9 18.5	18.7 0.918
J134848.2+262219	1.0	[VV96] J134848.3+262237 Quasar	0.7	G SDSS J134848.25+262219.3	0.595	0.3	18.8 18.2	18.4 18.2	18.2 0.595
J135406.2−021034	-	-	4.9	XrayS 1WGA J1354.0-0209	-	2.1	21.6 20.8	21.1 20.7	20.8
J140229.6+542346	-	-	2.9	XrayS XMMU J140229.5+542349	-	-	-	-	-
J140244.9+541604	-	-	2.5	XrayS XMMU J140244.9+541602	-	-	-	-	-
J140301.0+542341	0.4	[DK2003] M101-18 X-ray source	1.7	XrayS CXOU J140301.2+542342	-	-	-	-	-
J140313.4+542009	3.2	HGGK 673 HII (ionized) region	1.5	XrayS CXOU J140313.6+542010	-	-	-	-	-
J140333.2+541800	1.8	[DK2003] M101-104 HII (ionized) region	2.2	VisS CXOU J140333.3+541800	-	1.6	20.6 20.4	21.1 20.0	20.4
J140621.8+222347	-	-	-	-	-	0.9	16.3 15.7	16.0 15.9	15.7
J141711.0+522541	1.2	CFDF 14h 45989 X-ray source	-	-	-	1.2	24.7 19.4	21.6 18.9	19.4
J142927.1−380409	0.7	V* V895 Cen Cataclysmic Variable Star	-	-	-	-	-	-	-
J144207.4+352622	0.3	QSO B1440+356 Seyfert 1 Galaxy	0.7	G MRK 047	0.079	0.4	15.8 14.6	15.4 14.5	14.6
J145144.2+163657	-	-	-	-	-	0.8	19.8 18.7	19.1 18.6	18.7
J150948.6+333626	0.9	[VV2006c] J150948.7+333626 Seyfert 1 Galaxy	0.7	QSO SDSS J150948.65+333626.7	0.512	0.1	19.8 19.1	19.4 19.1	19.1 0.512
J151558.8−000154	-	-	-	-	-	1.2	19.7 17.4	18.6 17.2	17.4
J151743.7+070122	-	-	-	-	-	1.0	18.3 17.7	18.1 17.2	17.7 0.282
J152130.7+074916	-	-	-	-	-	0.3	22.4 19.5	21.1 19.2	19.5
J153450.3+543000	1.3	[VV2006c] J153450.2+542959 Active Galaxy Nucleus	0.2	QSO SDSS J153450.27+542959.6	0.289	0.3	20.0 19.1	19.7 18.6	19.1 0.289
J153557.0+543750	0.3	NSV 7163 Variable Star	-	-	-	0.2	7.5 9.9	10.0 6.7	9.9
J154332.5+535634	-	-	-	-	-	1.0	20.2 19.4	19.7 19.3	19.4
J155333.5+190051	-	-	-	-	-	0.6	23.0 21.0	21.9 20.6	21.0
J160141.0+664810	0.7	[OCC2002] AG Dra N1 Radio-source	0.7	V* RBS 154	-	-	-	-	-
J172912.1+703256	-	-	-	-	-	2.3	19.4 18.8	19.0 18.7	18.8
J175833.3+663800	1.3	NGC 6543 Planetary Nebula	1.8	PN NGC 654	-	-	-	-	-
J182140.5−273136	1.4	NOVA Sgr 1998 Nova	-	-	-	-	-	-	-
J223439.9−374259	1.0	CTS A11.37 Seyfert 1 Galaxy	-	-	-	-	-	-	-
J234729.5+010113	-	-	-	-	-	1.1	23.2 21.4	23.0 20.8	21.4

This table only contains the X-ray sources that had a match from at least one of the other catalogues. Where more than one candidate counterpart was returned only the closest one is reported here. The search criteria were that the offset of the candidate counterpart was below 5 arc seconds or within 3 times the X-ray positional error, whichever was smaller. The 'DIST' columns contain the offset of the candidate counterpart from the X-ray source position in arc seconds. Under the SIMBAD heading, the column titled 'NAME/TYPE' contains the name then the type of the candidate counterpart. Under the NED heading the column titled 'TYPE/NAME' contains the type then name of the candidate counterpart. The column labelled 'z' contains the reported redshift within NED. Under the SDSS heading are the 5 SDSS colour magnitudes along with the spectroscopic redshift if available.

Appendix B

Credits

The following statements are those suggested for use by the various missions, institutions and databases that this thesis has made use of.

Part of this work was based on observations obtained with XMM-Newton, an ESA science mission with instruments and contributions directly funded by ESA Member States and NASA.

This research has made use of data obtained from the Leicester Database and Archive Service at the Department of Physics and Astronomy, Leicester University, UK.

This publication makes use of data products from the Two Micron All Sky Survey, which is a joint project of the University of Massachusetts and the Infrared Processing and Analysis Center/California Institute of Technology, funded by the National Aeronautics and Space Administration and the National Science Foundation.

The Guide Star Catalogue-II is a joint project of the Space Telescope Science Institute and the Osservatorio Astronomico di Torino. Space Telescope Science Institute is operated by the Association of Universities for Research in Astronomy, for the National Aeronautics and Space Administration under contract NAS5-26555. The participation of the Osservatorio Astronomico di Torino is supported by the Italian Council for Research in Astronomy. Additional support is provided by European Southern Observatory, Space Telescope European Coordinating Facility, the International GEMINI project and the European Space Agency Astrophysics Division.

This research has made use of the SIMBAD database, operated at CDS, Strasbourg, France.

This research has made use of the NASA/IPAC Extragalactic Database (NED) which is operated by the Jet Propulsion Laboratory, California Institute of Technology, under contract with the National Aeronautics and Space Administration.

The data was made publically available through the Isaac Newton Groups' Wide Field Camera Survey Programme. The Isaac Newton Telescope is operated on the island of La Palma by the Isaac Newton Group in the Spanish Observatorio del Roque de los Muchachos of the Instituto de Astrofisica de Canarias

This research has made use of data obtained from the SuperCOSMOS Science Archive, prepared and hosted by the Wide Field Astronomy Unit, Institute for Astronomy, University of Edinburgh, which is funded by the UK Particle Physics and Astronomy Research Council.

Funding for the SDSS and SDSS-II has been provided by the Alfred P. Sloan Foundation, the Participating Institutions, the National Science Foundation, the U.S. Department of Energy, the National Aeronautics and Space Administration, the Japanese Monbukagakusho, the Max Planck Society, and the Higher Education Funding Council for England. The SDSS Web Site is http://www.sdss.org/.

The SDSS is managed by the Astrophysical Research Consortium for the Participating Institutions. The Participating Institutions are the American Museum of Natural History, Astrophysical Institute Potsdam, University of Basel, University of Cambridge, Case Western Reserve University, University of Chicago, Drexel University, Fermilab, the Institute for Advanced Study, the Japan Participation Group, Johns Hopkins University, the Joint Institute for Nuclear Astrophysics, the Kavli Institute for Particle Astrophysics and Cosmology, the Korean Scientist Group, the Chinese Academy of Sciences (LAMOST), Los Alamos National Laboratory, the Max-Planck-Institute for Astronomy (MPIA), the Max-Planck-Institute for Astrophysics (MPA), New Mexico State University, Ohio State University, University of Pittsburgh, University of Portsmouth, Princeton University, the United States Naval Observatory, and the University of Washington.

IRAF is distributed by the National Optical Astronomy Observatories, which are operated by the Association of Universities for Research in Astronomy, Inc., under cooperative agreement with the National Science Foundation.

Bibliography

Abazajian K, Adelman-McCarthy J K, Agüeros M A, Allam S S, Anderson K S J et al. 2005 *AJ* **129**, 1755–1759.

Abramowicz M A, Czerny B, Lasota J P and Szuszkiewicz E 1988 *ApJ* **332**, 646–658.

Adelman-McCarthy J K, Agüeros M A, Allam S S, Allende Prieto C, Anderson K S J et al. 2008 *ApJS* **175**, 297–313.

Allen J T, Hewett P C, Maddox N, Richards G T and Belokurov V 2010 *ArXiv e-prints* .

Antonucci R 1993 *ARA&A* **31**, 473–521.

Antonucci R R J and Miller J S 1985 *ApJ* **297**, 621–632.

Arnaud K A 1996 *in* G. H Jacoby and J Barnes, eds, 'Astronomical Data Analysis Software and Systems V' Vol. 101 of *Astronomical Society of the Pacific Conference Series* pp. 17–+.

Ashton C E, Page M J, Blustin A J, Puchnarewicz E M, Branduardi-Raymont G et al. 2004 *MNRAS* **355**, 73–81.

Bahcall J N, Kozlovsky B Z and Salpeter E E 1972 *ApJ* **171**, 467–+.

Balbus S A 2003 *ARA&A* **41**, 555–597.

Ballantyne D R, Iwasawa K and Fabian A C 2001 *MNRAS* **323**, 506–516.

Bautista M A and Kallman T R 2001 *ApJS* **134**, 139–149.

Becker R H, White R L, Gregg M D, Brotherton M S, Laurent-Muehleisen S A et al. 2000 *ApJ* **538**, 72–82.

Begelman M C 1978 *MNRAS* **184**, 53–67.

Begelman M C 2001 *ApJ* **551**, 897–906.

Begelman M C 2002 *ApJ* **568**, L97–L100.

Begelman M C, McKee C F and Shields G A 1983 *ApJ* **271**, 70–88.

Begelman M C and Meier D L 1982 *ApJ* **253**, 873–896.

Bentz M C, Peterson B M, Netzer H, Pogge R W and Vestergaard M 2008 *ArXiv e-prints* .

Bentz M C, Peterson B M, Pogge R W, Vestergaard M and Onken C A 2006 *ApJ* **644**, 133–142.

Bian W H and Zhao Y H 2003a *PASJ* **55**, 599–603.

Bian W and Zhao Y 2003b *ApJ* **591**, 733–740.

Bian W and Zhao Y 2004 *MNRAS* **347**, 607–612.

Blandford R D and McKee C F 1982 *ApJ* **255**, 419–439.

Blandford R D and Payne D G 1982 *MNRAS* **199**, 883–903.

Blustin A J, Page M J, Fuerst S V, Branduardi-Raymont G and Ashton C E 2005 *A&A* **431**, 111–125.

Boehringer H, Mullis C, Rosati P, Lamer G, Fassbender R et al. 2005 *The Messenger* **120**, 33–36.

Boller T, Brandt W N and Fink H 1996 *A&A* **305**, 53–+.

Boller T, Gallo L C, Lutz D and Sturm E 2002 *MNRAS* **336**, 1143–1146.

Bonning E W, Shields G A, Salviander S and McLure R J 2005 *ApJ* **626**, 89–94.

Boroson T A 2003 *ApJ* **585**, 647–652.

Boroson T A and Green R F 1992 *ApJS* **80**, 109–135.

Botte V, Ciroi S, di Mille F, Rafanelli P and Romano A 2005 *MNRAS* **356**, 789–793.

Botte V, Ciroi S, Rafanelli P and Di Mille F 2004 *AJ* **127**, 3168–3179.

Braito V, Reeves J N, Dewangan G C, George I, Griffiths R E et al. 2007 *ApJ* **670**, 978–991.

Brandt W N, Laor A and Wills B J 2000 *ApJ* **528**, 637–649.

Bregman J N and Lloyd-Davies E J 2007 *ApJ* **669**, 990–1002.

Brinkmann W, Wang T, Grupe D and Raeth C 2006 *A&A* **450**, 925–931.

Chartas G, Brandt W N and Gallagher S C 2003 *ApJ* **595**, 85–93.

Chartas G, Brandt W N, Gallagher S C and Garmire G P 2002 *ApJ* **579**, 169–175.

Chartas G, Saez C, Brandt W N, Giustini M and Garmire G P 2009 *ApJ* **706**, 644–656.

Chelouche D and Netzer H 2003 *MNRAS* **344**, 233–241.

Chen X and Taam R E 1993 *ApJ* **412**, 254–266.

Civano F, Comastri A and Brusa M 2005 *MNRAS* **358**, 693–704.

Civano F, Mignoli M, Comastri A, Vignali C, Fiore F et al. 2007 *A&A* **476**, 1223–1233.

Collin S, Kawaguchi T, Peterson B M and Vestergaard M 2006 *A&A* **456**, 75–90.

Comastri A, Mignoli M, Ciliegi P, Severgnini P, Maiolino R et al. 2002 *ApJ* **571**, 771–778.

Cordova F A, Kartje J F, Thompson, Jr. R J, Mason K O, Puchnarewicz E M et al. 1992 *ApJS* **81**, 661–681.

Crenshaw D M and Kraemer S B 1999 *ApJ* **521**, 572–576.

Crenshaw D M, Kraemer S B, Boggess A, Maran S P, Mushotzky R F et al. 1999 *ApJ* **516**, 750–768.

Crenshaw D M, Kraemer S B and George I M 2003 *ARA&A* **41**, 117–167.

Crummy J, Fabian A C, Gallo L and Ross R R 2006 *MNRAS* **365**, 1067–1081.

Dadina M and Cappi M 2004 *A&A* **413**, 921–927.

Dadina M, Cappi M, Malaguti G, Ponti G and de Rosa A 2005 *A&A* **442**, 461–468.

Dai X, Shankar F and Sivakoff G R 2008 *ApJ* **672**, 108–114.

Decarli R, Dotti M, Fontana M and Haardt F 2008a *MNRAS* **386**, L15–L19.

Decarli R, Labita M, Treves A and Falomo R 2008b *MNRAS* **387**, 1237–1247.

Della Ceca R, Maccacaro T, Caccianiga A, Severgnini P, Braito V et al. 2004 *A&A* **428**, 383–399.

den Herder J W, Brinkman A C, Kahn S M, Branduardi-Raymont G, Thomsen K et al. 2001 *A&A* **365**, L7–L17.

Denney K D, Watson L C, Peterson B M, Pogge R W, Atlee D W and other 2009 *ArXiv e-prints* .

Di Matteo T, Springel V and Hernquist L 2005 *Nature* **433**, 604–607.

Di Stefano R and Kong A K H 2003 *ApJ* **592**, 884–899.

Dickey J M and Lockman F J 1990 *ARA&A* **28**, 215–261.

Done C and Gierliński M 2005 *MNRAS* **364**, 208–216.

Dotani T, Assai K, Ebisawa K and Greiner J 2000 *Advances in Space Research* **25**, 375–378.

Elvis M 2000 *ApJ* **545**, 63–76.

Elvis M, Maccacaro T, Wilson A S, Ward M J, Penston M V et al. 1978 *MNRAS* **183**, 129–157.

Elvis M, Wilkes B J, McDowell J C, Green R F, Bechtold J et al. 1994 *ApJS* **95**, 1–68.

Eracleous M and Halpern J P 1994 *ApJS* **90**, 1–30.

Everett J E 2005 *ApJ* **631**, 689–706.

Everett J E and Ballantyne D R 2004 *ApJ* **615**, L13–L16.

Fabian A C 1999 *MNRAS* **308**, L39–L43.

Fabian A C, Miniutti G, Gallo L, Boller T, Tanaka Y et al. 2004 *MNRAS* **353**, 1071–1077.

Fabian A C, Miniutti G, Iwasawa K and Ross R R 2005 *MNRAS* **361**, 795–802.

Fabian A C, Zoghbi A, Ross R R, Uttley P, Gallo L C et al. 2009 *Nature* **459**, 540–542.

Falcke H and Biermann P L 1995 *A&A* **293**, 665–682.

Falcke H, Malkan M A and Biermann P L 1995 *A&A* **298**, 375–+.

Fanaroff B L and Riley J M 1974 *MNRAS* **167**, 31P–36P.

Farrah D, Lacy M, Priddey R, Borys C and Afonso J 2007 *ApJ* **662**, L59–L62.

Ferrarese L and Merritt D 2000 *ApJ* **539**, L9–L12.

Ferrarese L, Pogge R W, Peterson B M, Merritt D, Wandel A et al. 2001 *ApJ* **555**, L79–L82.

Fruscione A 1996 *ApJ* **459**, 509–+.

Gammie C F 1998 *MNRAS* **297**, 929–935.

Ganguly R, Brotherton M S, Cales S, Scoggins B, Shang Z et al. 2007 *ApJ* **665**, 990–1003.

Gaskell C M 1982 *ApJ* **263**, 79–86.

Gebhardt K, Bender R, Bower G, Dressler A, Faber S M et al. 2000a *ApJ* **539**, L13–L16.

Gebhardt K, Kormendy J, Ho L C, Bender R, Bower G et al. 2000b *ApJ* **543**, L5–L8.

George I M, Turner T J, Mushotzky R, Nandra K and Netzer H 1998 *ApJ* **503**, 174–+.

Ghosh K K, Swartz D A, Tennant A F, Wu K and Ramsey B D 2004 *ApJ* **607**, L111–L114.

Gibson R R, Jiang L, Brandt W N, Hall P B, Shen Y et al. 2009a *ApJ* **692**, 758–777.

Gibson R R, Marshall H L, Canizares C R and Lee J C 2005 *ApJ* **627**, 83–96.

Gierliński M and Done C 2004 *MNRAS* **349**, L7–L11.

Gierliński M and Done C 2006 *MNRAS* **371**, L16–L20.

Gillessen S, Eisenhauer F, Trippe S, Alexander T, Genzel R et al. 2009 *ApJ* **692**, 1075–1109.

Gioia I M, Maccacaro T, Schild R E, Wolter A, Stocke J T et al. 1990 *ApJS* **72**, 567–619.

Gower A C and Hutchings J B 1984 *AJ* **89**, 1658–1687.

Green P J, Schartel N, Anderson S F, Hewett P C, Foltz C B et al. 1995 *ApJ* **450**, 51–+.

Green P J, Silverman J D, Cameron R A, Kim D, Wilkes B J et al. 2004 *ApJS* **150**, 43–71.

Gregg M D, Becker R H, White R L, Helfand D J, McMahon R G et al. 1996 *AJ* **112**, 407–+.

Greiner J 1996 *in* J Greiner, ed., 'Supersoft X-Ray Sources' Vol. 472 of *Lecture Notes in Physics, Berlin Springer Verlag* pp. 285–+.

Greiner J 2000 *New Astronomy* **5**, 137–141.

Grupe D 2004c *AJ* **127**, 1799–1810.

Grupe D, Beuermann K, Thomas H C, Mannheim K and Fink H H 1998 *A&A* **330**, 25–36.

Grupe D and Mathur S 2004a *ApJ* **606**, L41–L44.

Grupe D, Thomas H C and Beuermann K 2001 *A&A* **367**, 470–486.

Grupe D, Wills B J, Leighly K M and Meusinger H 2004b *AJ* **127**, 156–179.

Hachisu I, Kato M and Nomoto K 1996 *ApJ* **470**, L97+.

Hall P B, Anderson S F, Strauss M A, York D G, Richards G T et al. 2002 *ApJS* **141**, 267–309.

Halpern J P 1984 *ApJ* **281**, 90–94.

Hamann F W, Barlow T A, Chaffee F C, Foltz C B and Weymann R J 2001 *ApJ* **550**, 142–152.

Hambly N C, MacGillivray H T, Read M A, Tritton S B, Thomson E B et al. 2001 *MNRAS* **326**, 1279–1294.

Hasinger G, Altieri B, Arnaud M, Barcons X, Bergeron J et al. 2001 *A&A* **365**, L45–L50.

Hasinger G, Lehmann I, Schmidt M, Gunn J E, Schneider D P et al. 2000 *New A Rev.* **44**, 497–501.

Hasinger G, Schartel N and Komossa S 2002 *ApJ* **573**, L77–L80.

Hawley J F and Krolik J H 2006 *ApJ* **641**, 103–116.

Hewett P C and Foltz C B 2003 *AJ* **125**, 1784–1794.

Ho L 1999 *in* 'ASSL Vol. 234: Observational Evidence for the Black Holes in the Universe' pp. 157–+.

Ho L C, Filippenko A V and Sargent W L 1995 *ApJS* **98**, 477–593.

Hohle M M, Haberl F, Vink J, Turolla R, Hambaryan V et al. 2009 *A&A* **498**, 811–820.

Hubbard A and Blackman E G 2006 *MNRAS* **371**, 1717–1721.

Hurkett C P, Vaughan S, Osborne J P, O'Brien P T, Page K L et al. 2008 *ApJ* **679**, 587–606.

Hutchings J B and Neff S G 1992 *AJ* **104**, 1–14.

XMM-Newton Survey Science Centre C 2003 *VizieR Online Data Catalog* **9037**, 0–+.

Jansen F, Lumb D, Altieri B, Clavel J, Ehle M et al. 2001 *A&A* **365**, L1–L6.

Jiménez-Benito L, Díaz A I, Terlevich R and Terlevich E 2000 *MNRAS* **317**, 907–921.

Kaastra J S, Mewe R, Liedahl D A, Komossa S and Brinkman A C 2000 *A&A* **354**, L83–L86.

Kaastra J S, Steenbrugge K C, Raassen A J J, van der Meer R L J, Brinkman A C et al. 2002 *A&A* **386**, 427–445.

Kalberla P M W, Burton W B, Hartmann D, Arnal E M, Bajaja E et al. 2005 *A&A* **440**, 775–782.

Kaspi S and Behar E 2006 *ApJ* **636**, 674–679.

Kaspi S, Brandt W N, Netzer H, Sambruna R, Chartas G et al. 2000a *ApJ* **535**, L17–L20.

Kaspi S, Maoz D, Netzer H, Peterson B M, Vestergaard M et al. 2005 *ApJ* **629**, 61–71.

Kaspi S, Smith P S, Netzer H, Maoz D, Jannuzi B T et al. 2000b *ApJ* **533**, 631–649.

Kato Y 2007 *Ap&SS* **307**, 11–15.

Kato Y, Mineshige S and Shibata K 2004 *ApJ* **605**, 307–320.

Khachikian E Y and Weedman D W 1974 *ApJ* **192**, 581–589.

King A 2003 *ApJ* **596**, L27–L29.

King A R and Pounds K A 2003 *MNRAS* **345**, 657–659.

Komossa S 2008 *in* 'Revista Mexicana de Astronomia y Astrofisica Conference Series' Vol. 32 of *Revista Mexicana de Astronomia y Astrofisica Conference Series* pp. 86–92.

Kormendy J and Richstone D 1995 *ARA&A* **33**, 581–+.

Krolik J H and Kriss G A 1995 *ApJ* **447**, 512–+.

Krolik J H and Kriss G A 2001 *ApJ* **561**, 684–690.

Laor A, Fiore F, Elvis M, Wilkes B J and McDowell J C 1997 *ApJ* **477**, 93–+.

Leighly K M 1999*a* *ApJS* **125**, 297–316.

Leighly K M 1999*b* *ApJS* **125**, 317–348.

Livio M 2003 *ArXiv Astrophysics e-prints* .

Long K S, Helfand D J and Grabelsky D A 1981 *ApJ* **248**, 925–944.

Magdziarz P and Zdziarski A A 1995 *MNRAS* **273**, 837–848.

Marconi A, Axon D J, Maiolino R, Nagao T, Pastorini G et al. 2008 *ApJ* **678**, 693–700.

Markowitz A, Reeves J N and Braito V 2006 *ApJ* **646**, 783–800.

Marshall H L, Edelson R A, Vaughan S, Malkan M, O'Brien P et al. 2003 *AJ* **125**, 459–464.

Marshall H L, Fruscione A and Carone T E 1995 *ApJ* **439**, 90–97.

Mason K O, Breeveld A, Much R, Carter M, Cordova F A et al. 2001 *A&A* **365**, L36–L44.

Mathur S, Kuraszkiewicz J and Czerny B 2001 *New Astronomy* **6**, 321–329.

McKernan B, Yaqoob T and Reynolds C S 2004 *ApJ* **617**, 232–239.

McKernan B, Yaqoob T and Reynolds C S 2007 *MNRAS* **379**, 1359–1372.

McLean B J, Greene G R, Lattanzi M G and Pirenne B 2000 *in* N Manset, C Veillet and D Crabtree, eds, 'Astronomical Data Analysis Software and Systems IX' Vol. 216 of *Astronomical Society of the Pacific Conference Series* pp. 145–+.

McLure R J and Dunlop J S 2001 *MNRAS* **327**, 199–207.

McMahon R G, Irwin M J and Maddox S J 2000 *VizieR Online Data Catalog* **1267**, 0–+.

McMahon R G, Walton N A, Irwin M J, Lewis J R, Bunclark P S et al. 2001 *New Astronomy Review* **45**, 97–104.

Meurs E J A and Unger S W 1991 *A&A* **252**, 63–68.

Mineshige S, Kawaguchi T, Takeuchi M and Hayashida K 2000 *PASJ* **52**, 499–508.

Mitsuda K, Bautz M, Inoue H, Kelley R L, Koyama K et al. 2007 *PASJ* **59**, 1–7.

Monet D G, Levine S E, Canzian B, Ables H D, Bird A R et al. 2003 *AJ* **125**, 984–993.

Murray N and Chiang J 1995 *ApJ* **454**, L105+.

Murray N and Chiang J 1997 *ApJ* **474**, 91–+.

Murray N, Quataert E and Thompson T A 2005 *ApJ* **618**, 569–585.

Mushotzky R F and Wandel A 1989 *ApJ* **339**, 674–688.

Nandra K, O'Neill P M, George I M and Reeves J N 2007 *MNRAS* **382**, 194–228.

Nandra K and Pounds K A 1994 *MNRAS* **268**, 405–+.

Neff S G and Hutchings J B 1992 *AJ* **103**, 1746–1760.

Nelson C H 2000 *ApJ* **544**, L91–L94.

Nelson C H and Whittle M 1995 *ApJS* **99**, 67–+.

Nelson C H and Whittle M 1996 *ApJ* **465**, 96–+.

Netzer H 2003 *ApJ* **583**, L5–L8.

O'Brien P T, Reeves J N, Simpson C and Ward M J 2005 *MNRAS* **360**, L25–L29.

Ohsuga K, Mineshige S, Mori M and Umemura M 2002 *ApJ* **574**, 315–324.

Oke J B 1990 *AJ* **99**, 1621–1631.

Osterbrock D E and Pogge R W 1985 *ApJ* **297**, 166–176.

Paerels F B S and Kahn S M 2003 *ARA&A* **41**, 291–342.

Paerels F, Mori K, Motch C, Haberl F, Zavlin V E et al. 2001 *A&A* **365**, L298–L301.

Page K L, Reeves J N, O'Brien P T, Turner M J L and Worrall D M 2004 *MNRAS* **353**, 133–142.

Papadakis I E, Brinkmann W, Page M J, McHardy I and Uttley P 2007 *A&A* **461**, 931–942.

Park T, van Dyk D A and Siemiginowska A 2008 *ApJ* **688**, 807–825.

Peterson B M 1993 *PASP* **105**, 247–268.

Peterson B M 1997 *An Introduction to Active Galactic Nuclei* An introduction to active galactic nuclei, Publisher: Cambridge, New York Cambridge University Press, 1997 Physical description xvi, 238 p. ISBN 0521473489.

Peterson B M, Ferrarese L, Gilbert K M, Kaspi S, Malkan M A et al. 2004 *ApJ* **613**, 682–699.

Porquet D, Reeves J N, O'Brien P and Brinkmann W 2004 *A&A* **422**, 85–95.

Pounds K A, Done C and Osborne J P 1995 *MNRAS* **277**, L5–L10.

Pounds K A, King A R, Page K L and O'Brien P T 2003b *MNRAS* **346**, 1025–1030.

Pounds K A and Page K L 2006 *MNRAS* **372**, 1275–1278.

Pounds K A and Reeves J N 2009 *MNRAS* **397**, 249–257.

Pounds K A, Reeves J N, King A R, Page K L, O'Brien P T et al. 2003a *MNRAS* **345**, 705–713.

Pounds K A, Reeves J N, Page K L and O'Brien P T 2004a *ApJ* **605**, 670–676.

Pounds K A, Reeves J N, Page K L and O'Brien P T 2004b *ApJ* **616**, 696–706.

Pounds K and Vaughan S 2000 *New Astronomy Review* **44**, 431–433.

Prieto M A, Pérez García A M and Rodríguez Espinosa J M 2001 *A&A* **377**, 60–65.

Proga D 2003 *ApJ* **585**, 406–417.

Proga D and Kallman T R 2004 *ApJ* **616**, 688–695.

Proga D, Stone J M and Kallman T R 2000 *ApJ* **543**, 686–696.

Protassov R, van Dyk D A, Connors A, Kashyap V L and Siemiginowska A 2002 *ApJ* **571**, 545–559.

Puchnarewicz E M, Mason K O, Cordova F A, Kartje J, Brabduardi A A et al. 1992 *MNRAS* **256**, 589–623.

Read A, Saxton R, Esquej P, Freyberg M and Altieri B 2006 *PASJ* **58**, L47–L50.

Rees M J 1984 *ARA&A* **22**, 471–506.

Reeves J, Done C, Pounds K, Terashima Y, Hayashida K et al. 2008 *MNRAS* **385**, L108–L112.

Reeves J N, O'Brien P T, Braito V, Behar E, Miller L et al. 2009 *ApJ* **701**, 493–507.

Reeves J N, O'Brien P T and Ward M J 2003 *ApJ* **593**, L65–L68.

Reeves J N and Turner M J L 2000 *MNRAS* **316**, 234–248.

Reeves J N, Wynn G, O'Brien P T and Pounds K A 2002 *MNRAS* **336**, L56–L60.

Reichard T A, Richards G T, Hall P B, Schneider D P, Vanden Berk D E et al. 2003 *AJ* **126**, 2594–2607.

Reynolds C S 1997 *MNRAS* **286**, 513–537.

Richards G T, Vanden Berk D E, Reichard T A, Hall P B, Schneider D P et al. 2002 *AJ* **124**, 1–17.

Rosner R, Golub L and Vaiana G S 1985 *ARA&A* **23**, 413–452.

Ross R R and Fabian A C 2005 *MNRAS* **358**, 211–216.

Ross R R, Fabian A C and Young A J 1999 *MNRAS* **306**, 461–466.

Rush B and Malkan M A 1996 *ApJ* **456**, 466–+.

Rutledge R E, Brunner R J, Prince T A and Lonsdale C 2000 *ApJS* **131**, 335–353.

Rutledge R E and Sako M 2003 *MNRAS* **339**, 600–606.

Sako M, Kahn S M, Behar E, Kaastra J S, Brinkman A C et al. 2001 *A&A* **365**, L168–L173.

Sanders D B, Soifer B T, Elias J H, Neugebauer G and Matthews K 1988 *ApJ* **328**, L35–L39.

Santos J S, Rosati P, Gobat R, Lidman C, Dawson K et al. 2009 *A&A* **501**, 49–60.

Saxton R D, Read A M, Esquej P, Freyberg M J, Altieri B et al. 2008 *A&A* **480**, 611–622.

Schartel N, Rodríguez-Pascual P M, Santos-Lleó M, Clavel J, Guainazzi M et al. 2005 *A&A* **433**, 455–465.

Schneider D P, Hall P B, Richards G T, Strauss M A, Vanden Berk D E et al. 2007 *AJ* **134**, 102–117.

Schneider D P, Hall P B, Richards G T, Vanden Berk D E, Anderson S F et al. 2005 *AJ* **130**, 367–380.

Schwope A, Hasinger G, Lehmann I, Schwarz R, Brunner H et al. 2000 *Astronomische Nachrichten* **321**, 1–52.

Seyfert C K 1943 *ApJ* **97**, 28–+.

Shakura N I and Syunyaev R A 1973 *A&A* **24**, 337–355.

Shen Y, Greene J E, Strauss M A, Richards G T and Schneider D P 2008 *ApJ* **680**, 169–190.

Shields G A, Gebhardt K, Salviander S, Wills B J, Xie B et al. 2003 *ApJ* **583**, 124–133.

Shuder J M and Osterbrock D E 1981 *ApJ* **250**, 55–65.

Sikora M, Stawarz Ł and Lasota J P 2007 *ApJ* **658**, 815–828.

Silk J and Rees M J 1998 *A&A* **331**, L1–L4.

Simpson C, Ward M, O'Brien P and Reeves J 1999 *MNRAS* **303**, L23–L28.

Singh K P, Barrett P, White N E, Giommi P and Angelini L 1995 *ApJ* **455**, 456–+.

Skrutskie M F, Cutri R M, Stiening R, Weinberg M D, Schneider S et al. 2006 *AJ* **131**, 1163–1183.

Sobolewska M A and Done C 2007 *MNRAS* **374**, 150–158.

Stocke J T, Morris S L, Gioia I M, Maccacaro T, Schild R et al. 1991 *ApJS* **76**, 813–874.

Stocke J T, Morris S L, Weymann R J and Foltz C B 1992 *ApJ* **396**, 487–503.

Strüder L, Briel U, Dennerl K, Hartmann R, Kendziorra E et al. 2001 *A&A* **365**, L18–L26.

Tanaka Y, Boller T, Gallo L, Keil R and Ueda Y 2004 *PASJ* **56**, L9–L13.

Tanaka Y, Inoue H and Holt S S 1994 *PASJ* **46**, L37–L41.

Tananbaum H, Avni Y, Branduardi G, Elvis M, Fabbiano G et al. 1979 *ApJ* **234**, L9–L13.

Tananbaum H, Avni Y, Green R F, Schmidt M and Zamorani G 1986 *ApJ* **305**, 57–67.

Thomas H, Beuermann K, Reinsch K, Schwope A D, Truemper J et al. 1998 *A&A* **335**, 467–478.

Tody D 1986 *in* D. L Crawford, ed., 'Instrumentation in astronomy VI; Proceedings of the Meeting, Tucson, AZ, Mar. 4-8, 1986. Part 2 (A87-36376 15-35). Bellingham, WA, Society of Photo-Optical Instrumentation Engineers, 1986, p. 733.' Vol. 627 of *Presented at the Society of Photo-Optical Instrumentation Engineers (SPIE) Conference* pp. 733–+.

Tolea A, Krolik J H and Tsvetanov Z 2002 *ApJ* **578**, L31–L35.

Tombesi F, Cappi M, Reeves J N, Palumbo G G C, Yaqoob T et al. 2010a *ArXiv e-prints* .

Tombesi F, Sambruna R M, Reeves J N, Braito V, Ballo L et al. 2010b *ApJ* **719**, 700–715.

Tran H D, Miller J S and Kay L E 1992 *ApJ* **397**, 452–456.

Tremaine S, Gebhardt K, Bender R, Bower G, Dressler A et al. 2002 *ApJ* **574**, 740–753.

Truemper J 1982 *Advances in Space Research* **2**, 241–249.

Trump J R, Hall P B, Reichard T A, Richards G T, Schneider D P et al. 2006 *ApJS* **165**, 1–18.

Turner M J L, Abbey A, Arnaud M, Balasini M, Barbera M et al. 2001 *A&A* **365**, L27–L35.

Turner T J and Pounds K A 1988 *MNRAS* **232**, 463–471.

Turnshek D A, Bohlin R C, Williamson, II R L, Lupie O L, Koornneef J et al. 1990 *AJ* **99**, 1243–1261.

Tytler D and Fan X M 1992 *ApJS* **79**, 1–36.

Ulvestad J S, Antonucci R R J and Barvainis R 2005 *ApJ* **621**, 123–129.

van den Heuvel E P J, Bhattacharya D, Nomoto K and Rappaport S A 1992 *A&A* **262**, 97–105.

Vaughan S, Reeves J, Warwick R and Edelson R 1999 *MNRAS* **309**, 113–124.

Vaughan S and Uttley P 2008 *MNRAS* **390**, 421–428.

Veilleux S, Cecil G and Bland-Hawthorn J 2005 *ARA&A* **43**, 769–826.

Vestergaard M 2002 *ApJ* **571**, 733–752.

Vestergaard M and Peterson B M 2006 *ApJ* **641**, 689–709.

Voges W, Aschenbach B, Boller T, Bräuninger H, Briel U et al. 1999 *A&A* **349**, 389–405.

Wandel A 2002 *ApJ* **565**, 762–772.

Wandel A 2004 *in* T Storchi-Bergmann, L. C Ho and H. R Schmitt, eds, 'The Interplay Among Black Holes, Stars and ISM in Galactic Nuclei' Vol. 222 of *IAU Symposium* pp. 65–69.

Wandel A, Peterson B M and Malkan M A 1999 *ApJ* **526**, 579–591.

Wang J M 2003 *AJ* **125**, 2859–2864.

Wang J M and Netzer H 2003 *A&A* **398**, 927–936.

Wang J M, Szuszkiewicz E, Lu F J and Zhou Y Y 1999 *ApJ* **522**, 839–845.

Wang J M and Zhou Y Y 1999 *ApJ* **516**, 420–424.

Wang T, Brinkmann W and Bergeron J 1996 *A&A* **309**, 81–96.

Wang T G, Brinkmann W, Yuan W, Wang J X and Zhou Y Y 2000 *ApJ* **545**, 77–85.

Wang T and Lu Y 2001 *A&A* **377**, 52–59.

Watson L C, Mathur S and Grupe D 2007 *AJ* **133**, 2435–2441.

Watson M G, Augueres J L, Ballet J, Barcons X, Barret D et al. 2001 *A&A* **365**, L51–L59.

Watson M G, Schroder A C, Fyfe D, Page C G, Lamer G et al. 2008 *VizieR Online Data Catalog* **349**, 30339–+.

Watson M G, Schröder A C, Fyfe D, Page C G, Lamer G et al. 2009 *A&A* **493**, 339–373.

Weinstein M A, Richards G T, Schneider D P, Younger J D, Strauss M A et al. 2004 *ApJS* **155**, 243–256.

Weymann R J, Morris S L, Foltz C B and Hewett P C 1991 *ApJ* **373**, 23–53.

White R L, Becker R H, Gregg M D, Laurent-Muehleisen S A, Brotherton M S et al. 2000 *ApJS* **126**, 133–207.

Wilkes B J 2001 *New Astronomy Review* **45**, 641–648.

Wills B J, Shang Z and Yuan J M 2000 *New Astronomy Review* **44**, 511–517.

Wilms J, Allen A and McCray R 2000 *ApJ* **542**, 914–924.

Woo J H and Urry C M 2002 *ApJ* **579**, 530–544.

Yun M S, Reddy N A and Condon J J 2001 *ApJ* **554**, 803–822.

Zheng W, Kriss G A, Wang J X, Brotherton M, Oegerle W R et al. 2001 *ApJ* **562**, 152–159.

Zheng W and Malkan M A 1993 *ApJ* **415**, 517–+.

Zhou H, Wang T, Yuan W, Lu H, Dong X et al. 2006 *ApJS* **166**, 128–153.

Zoghbi A, Fabian A C and Gallo L C 2008 *MNRAS* **391**, 2003–2008.